ABSTRACT

Title of Dissertation: Microwave Nonlinearities in Photodiodes

Keith Jake Williams, Doctor of Philosophy, 1994

Dissertation directed by: Dr. Mario Dagenais
Professor of Electrical Engineering

The nonlinearities in p-i-n photodiodes have been measured and numerically modeled. Harmonic distortion, response reduction, and sinusoidal output distortion measurements were made with two single-frequency offset-phased-locked Nd:YAG lasers, which provided a source dynamic range greater than 130 dB, a 1 MHz to 50 GHz frequency range, and optical powers up to 10 mW.

A semi-classical approach was used to solve the carrier transport in a one-dimensional p-i-n photodiode structure. This required the simultaneous solution of three coupled nonlinear differential equations: Poisson's equation and the hole and electron continuity equations. Space-charge electric fields, loading in the external circuit, and absorption in undepleted regions next to the intrinsic region all contributed to the nonlinear behavior described by these equations.

Numerical simulations were performed to investigate and isolate the various nonlinear mechanisms. It was found that for intrinsic region electric fields below 50 kV/cm, the nonlinearities were influenced primarily by the space-charge electric-field-induced change in hole and electron velocities. Between 50 and 100 kV/cm, the nonlinearities were found to be influenced primarily by changes in electron velocity for frequencies

above 5 GHz and by p-region absorption below 1 GHz. Above 100 kV/cm, only p-region absorption could explain the observed nonlinear behavior, where only 8 to 14 nm of undepleted absorbing material next to the intrinsic region was necessary to model the observed second harmonic distortions of -60 dBc at 1 mA.

Simulations were performed at high power densities to explain the observed response reductions and time distortions. A radially inward component of electron velocity was discovered, and under certain conditions, was estimated to have the same magnitude as the axial velocity. The model was extended to predict that maximum photodiode currents of 50 mA should be possible before a sharp increase in nonlinear output occurs. For capacitively-limited devices, the space-charge-induced nonlinearities were found to be independent of the intrinsic region length, while external circuit loading was determined to cause higher nonlinearities in shorter devices. Simulations indicate that second harmonic improvements of 40 to 60 dB may be possible if the photodiode can be fabricated without undepleted absorbing regions next to the intrinsic region.

Microwave Nonlinearities in Photodiodes

by

Keith Jake Williams

Dissertation submitted to the Faculty of the Graduate School
of The University of Maryland in partial fulfillment
of the requirements for the degree of
Doctor of Philosophy
1994

U MD Electrical Engineering Dept.

Advisory Committee:

Professor Mario Dagenais, Advisor
Professor Christopher Davis
Professor Marty Peckerar
Professor Aristos Christou
Dr. Ronald Esman
Dr. Lew Goldberg

ACKNOWLEDGEMENTS

I would like to thank the members on my dissertation committee for giving their precious time: my advisor, Dr. Mario Dagenais, Dr. Christopher Davis, Dr. Marty Peckerar, Dr. Aristos Christou, Dr. Ronald Esman, and Dr. Lew Goldberg. I would also like to thank NRL Code 5750 for the use of their Convex computer, the NRL Center for Computational Science for the use of their Cray Computer, Dr. John Bowers of the University of California Santa Barbara for useful discussions, Dr. Greg Olsen and Epitaxx for detectors, and Dr. Joseph F. Weller for his support. Special appreciation is extended to Dr. Ronald Esman for enlightening discussions and proofreading of the manuscript, and to my wife, Vicki, for her support, especially during the preparation of the manuscript.

TABLE OF CONTENTS

LIST OF FIGURES

I. INTRODUCTION

Nonlinear distortion in optical systems has been studied by many researchers.[1-10] Although most of the research in the nonlinear behavior of these systems has been concentrated on sources,[1-4] for example laser diodes and external modulators, there has been a limited amount of work done concerning the nonlinearities in receivers.[5-11] One important receiver component, the p-i-n photodiode (PD), has received very little attention. The reason for this lack of work on the p-i-n PD has been two-fold, 1) the devices were assumed to be very linear devices if the electric field is kept high enough in the intrinsic (depletion) region to cause the carrier velocities to saturate, and 2) source nonlinearities limited measurement dynamic range.

Nevertheless, nonlinear behavior in PDs can be an important limiting factor in high-fidelity analog and digital communication systems. CATV applications requiring studio quality video transmission strive for harmonic distortion (HD) and inter-modulation distortion products (IMD) between -60 and -80 dBc. Also, many radar and electronic warfare systems require HD or IMD levels of -50 dBc or better.

Many fiber-optic systems are now taking advantage of recently available high optical power sources for increased performance. For instance, heterodyne detection takes advantage of high local oscillator power to obtain shot-noise-limited performance in PDs. Optical preamplifiers, both Erbium doped fiber amplifiers and semiconductor optical amplifiers, are used to reduce system link loss. Using high power optical sources with external modulators also lowers system link loss by increasing the modulated optical power without increasing the drive microwave power. Of course, harmonics traditionally grow with a power-law behavior, for example second harmonics will grow proportional to the square of optical power, third harmonics will grow proportional to the cube of optical power, etc. Thus nonlinearities become more important in systems with high incident optical powers. All of these basic optical systems will be affected, if not limited, by the nonlinearities in the common component – the PD. Hence, it is extremely important to understand the nonlinear behavior in p-i-n PDs so that steps can be taken to minimize it, and so that the fundamental limits of devices can be explored.

Nonlinearities will exist at some level in PDs for many reasons. It is usually a poor assumption that an electric field which is high enough to saturate the carrier velocities will yield, by itself, high linearity. Saturated carrier velocities are only one of the many assumptions that are required to linearize the equations that describe the transport of carriers in PDs. The exclusion of electric field dependence of the diffusion constants, electric field screening due to high space-charge densities, highly-doped (undepleted) absorbing regions where electric fields are low, trap sites, recombination, heterojunctions, and non-zero load resistances all add nonlinear terms to the transport equations. This study concentrates on five of these effects: 1) Generation in highly-doped absorbing regions where the electric field is low, 2) diffusion, 3) recombination, 4) the effects of space-charge induced electric field screening, and 5) load resistance. These effects will be analyzed for their relative contribution to the nonlinear behavior in PDs.

A sample of the harmonic data obtained from a commercial p-i-n PD is shown in figure 1.1. The device in figure 1.1 has a 3-dB bandwidth

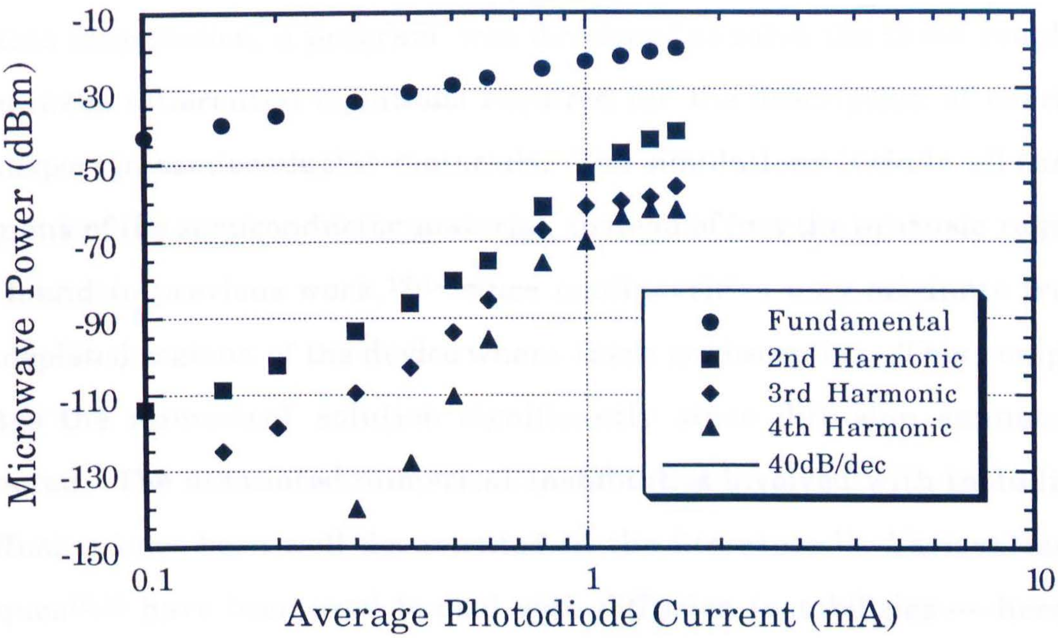

Figure 1.1 Measured fundamental and harmonic power of a p-i-n photodiode at a fundamental frequency of 1 GHz.

of 22 GHz with a 0.95-μm long intrinsic region. The applied bias was -2 V and the device was pigtailed with a single mode optical fiber. From the figure, the device displays two distinct regions of nonlinear behavior. For average PD currents below 300 to 500 μA, the growth in harmonic power approximately follows power-laws; however, for average PD currents above 500 μA, the growth in harmonic power deviates significantly from a power-law behavior.

The overall scope of this dissertation is three-fold: demonstration of a technique for wide dynamic range (>130 dB) measurement of device nonlinearities, the modeling (physics) of photodetector carrier transport, and the obtaining of new insight into PD operation by relating nonlinearities from the simulation output to measured output. The second part of this work, device modeling, will help to predict and determine the limits of the nonlinear behavior. To carry out the numerical simulation portion of this dissertation, a program was developed to solve the three coupled nonlinear differential equations required for the description of carrier transport in semiconductor materials. The simulations include all three regions of the semiconductor material, instead of just the intrinsic region as found in previous work,[12-14] since nonlinearities may originate from undepleted regions of the device where there is absorption. This complicates the numerical solution significantly since diffusion cannot be ignored. The associated numerical instabilities involved with including diffusion have been well documented in the literature.[15] Various techniques[15,16] have been used to deal with diffusion instabilities — here a new technique is introduced which is based on basic solid state physics.

The simulations are first used to accurately model and understand device nonlinear behavior. After adequate agreement has been obtained between experiments and simulations, the various properties of the device, such as recombination, carrier mobilities, absorption in undepleted semiconductor regions, the intrinsic properties of InGaAs, and the intrinsic region length are modified to determine their relative contributions to the nonlinear behavior for various PD operating conditions.

The work presented in the following eight chapters provides the first comprehensive study of the nonlinear behavior in p-i-n PDs and reveals that nonlinearities in certain devices can be quite high even when illuminated with low to medium power levels. Also, operation under high power densities is found to cause not only harmonic distortion, but also response reduction and phase distortions.

Chapter II outlines the various methods for measurement of harmonic levels in PDs or other photosensitive devices.

Chapter III reviews the physics governing PD carrier transport and the associated nonlinear transport equations. Specific properties of InGaAs and InP materials, including diffusion constants and the electric field dependence of the carrier drift velocities, are covered along with the structure of the p-i-n PDs under investigation here.

Chapter IV discusses the numerical methods employed to solve the set of nonlinear equations governing carrier transport (Poisson's equation and the carrier continuity equations) in one spatial dimension. Special attention is paid to specific limitations on the diffusion current derived from first principles rather than using numerical treatments.

Chapter V presents measurement data with simulation results and analysis to sort out the various nonlinear mechanisms and their contribution to PD nonlinearity in various regions of PD applied voltage.

Chapter VI presents additional data with simulation results and analysis pertaining to nonlinearities in several photodiodes under moderate power densities where the generated carrier densities are low enough not to cause the intrinsic region electric field to collapse.

Chapter VII presents high power density measurements and simulations of a device where the generated carrier densities are high enough to screen the intrinsic region electric field.

Chapter VIII investigates ways of reducing PD nonlinearity and ways to increase the maximum PD current before the effects investigated in Chapter VII occur.

Chapter IX gives conclusions. It summarizes the main results of this research and discusses suggestions for further work.

1. W. Susaki, "Recent Progress in superlinear InGaAsP Laser Diodes," OFC 91, Paper WG5, p. 92.
2. A. H. Gnauck, *et al.*, "Comparison of Direct and External Modulation for CATV Lightwave Transmission at 1.5μm Wavelength," *Electron. Lett.*, **28**, p. 1875, 1992.
3. G. E. Bodeep and T. E. Darcie, "Comparison of Second- and Third-Order Distortion in Intensity Modulated InGaAsP Lasers and a $LiNbO_3$ External Modulator," OFC 89, Paper WK2.
4. R. B. Childs and V. A. O'Byrne, "Predistortion Linearization of Directly Modulated DFB Lasers and External Modulators for AM Video Transmission," OFC 90, Paper WH6.
5. R.D. Esman and K.J. Williams, "Measurement of Harmonic Distortion in Microwave Photodetectors," *IEEE Photon. Tech. Lett.*, **PTL-2**, p. 502, 1990.
6. K. J. Williams and R. D. Esman, "Observation of Photodetector Nonlinearities," *Electron. Lett.*, **28**, p. 731, 1992.
7. M. Dentan and B. de Cremoux, "Numerical Simulation of the Nonlinear Response of a p-i-n Photodiode Under High Illumination," *J. of Lightwave Tech.*, **JLT-8**, p. 1137, 1990.
8. R. R. Hayes and D.L. Persechini, "Nonlinearity of p-i-n Photodetectors," *IEEE Photonics Tech. Lett.*, **PTL-5**, p. 70, 1993.
9. T. Ozeki and E. H. Hara, "Measurements of Nonlinear Distortion in Photodiodes," *Electron. Lett.*, **12**, p. 80, 1976.
10. D. Kuhl, et al., "Influence of Space Charges on the Impulse Response of InGaAs Metal-Semiconductor-Metal Photodetectors," *J. of Lightwave Tech.*, **JLT-10**, p. 753, 1992.

11. A. R. Williams, *et al.*, "High Frequency Saturation Measurements of an InGaAs/InP Waveguide Photodetector," *Electron. Lett.*, **29**, p. 1298, 1993.

12. G. Lucovsky, *et al.*, "Transit-Time Considerations in p-i-n Diodes," *J. of Appl. Physics*, **35**, p. 622, 1964.

13. R. Sabella and S. Merli, "Analysis of InGaAs p-i-n Photodiode Frequency Response," *IEEE J. of Quantum Elec.*, **JQE-29**, p. 906, 1993.

14. J.M. Zhang and D.R. Conn, "State-Space Modeling of the PIN Photodetector," *J. of Lightwave Tech.*, **JLT-10**, p. 603, 1992.

15. S.J. Polak, *et al.*, "Semiconductor Device Modeling from the Numerical Point of View," *Intl. J. for Numerical Methods in Eng.*, **24**, p. 763, 1987.

16. H. Yi, *et al.*, "Novel Method to Control Numerical Solution Oscillation of Diffusion-Drift Equation," *Electron. Lett.*, **26**, p. 1487, 1990.

II. MEASUREMENT SYSTEM

To fully characterize and analyze the nonlinear behavior in PDs, an amplitude modulated source free from harmonic content is essential. A measure of the source quality is its dynamic range or the range of optical power for which optical nonlinearities in the source can be neglected. In order to simulate a wide variety of current optical systems, the source also must have a modulation depth that is variable from very low values for multichannel systems to values at least greater than 50% for single channel systems.

The direct modulation of laser diodes is a poor candidate as a source for testing nonlinearities in PDs. This source presents some very difficult problems for manufacturers wishing to construct devices with high dynamic range. Several researchers[1-5] have measured and analyzed the dynamic range of laser diodes and their results have shown that a dynamic range of 60 dB or better for both HD and IMD is difficult when the optical modulation depth (OMD) is greater than 4%. For 50% modulation depths, values of HD and IMD are a disappointing 20 dB.[6] Light emitting diodes (LEDs) have been used[7] to study the nonlinearities in avalanche photodiodes. However, this measurement technique[7] requires several assumptions about the relationship between actual harmonic levels and the intermodulation or second order products measured. Additionally it provides only about 60 dB dynamic range.

External modulation of a CW optical source with a Mach-Zehnder (MZ) electro-optic modulator is another possible source for testing the nonlinear behavior in PDs. The modulator, biased at quadrature to maximize the linearity of the sinusoidal transfer characteristic, produces an amplitude modulated optical output according to the applied electrical signal input. Since the light output from the modulator is proportional to the sine of the input voltage, a large modulation signal causes harmonics of the modulation frequency f to appear in the optical output. The amplitude of these harmonics is described by a Bessel function expansion of $\sin(m\sin(\omega t)+\phi)$, where $\omega = 2\pi f$. The power in the harmonics of f depend quite heavily on the modulation depth m and bias point ϕ; however, these nonlinearities have been measured by several researchers[2-6,8] (for m = 0.02) to be as low as -55 dBc for IMD and -85 dBc for HD. By utilizing modulator linearizing circuits,[4] slightly better results of -65 dBc have been achieved for IMD. As the MZ modulation depth approaches 50%, values of HD and IMD approach 20 dB.[6,9] Therefore the use of externally modulated sources for reliable measurements of PD nonlinear properties is very limited.

Recently, an attractive new source[10,11] has been developed for the testing of nonlinearities in photodiodes. This new source meets every requirement of the ideal source for testing PDs due to its unique way of generating the frequency f. Such a source is used for this work and is based on heterodyning two single frequency lasers. This source creates a microwave signal at the frequency f by mixing two optical frequencies separated by f and has no inherent mixing components to create frequencies at integer multiples of f.

Consider the case of two single frequency lasers with electric fields, $E_1(t) = E_{o1}\cos(\omega_1 t+\phi_1)$ and $E_2(t) = E_{o2}\cos(\omega_2 t+\phi_2)$, incident on and heterodyned in a photodetector as shown in figure 2.1. The resulting time-

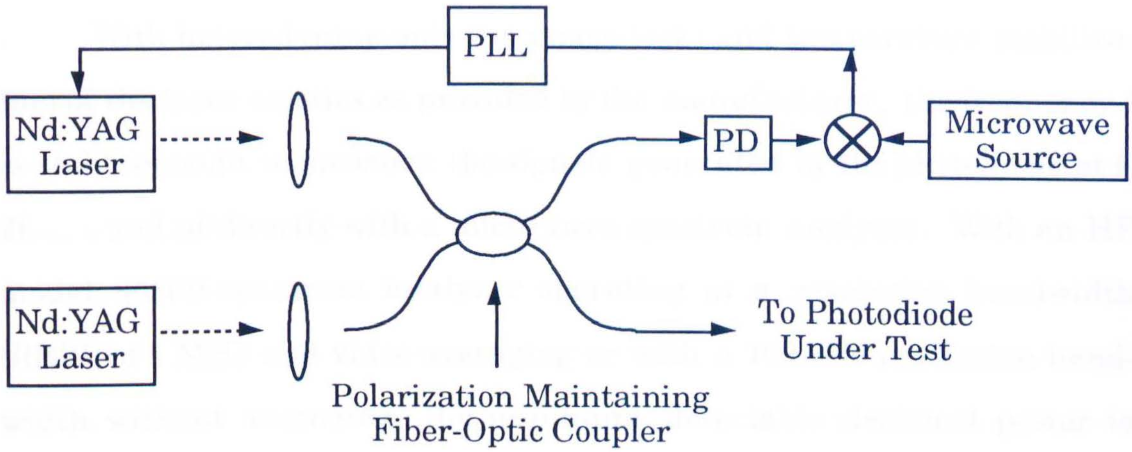

Figure 2.1 Heterodyne laser system for photodiode nonlinearity measurements. The individual laser powers can be adjusted to yield modulation depths from 0 to 100%.

average current generated by an ideal detector is proportional to the square of the total electric field and is given by:

$$I(t) \propto \frac{\left(E_{o1}^2 + E_{o2}^2\right)}{2} + E_{o1}E_{o2}\cos(\omega_1 t - \omega_2 t + \phi_1 - \phi_2)\ . \qquad (2.1)$$

The first term in equation 2.1 is the average PD current while the second term is a signal at the frequency ω_1-ω_2. If the frequencies are adjusted such that ω_1-ω_2 = $2\pi f$ is a microwave or RF frequency, the heterodyned signal can be detected by a PD. Notice that since there is no term in equation 2.1 that contains an integer multiple of f, the source is completely free of nonlinearities. However, without a phase-lock-loop (PLL), the beatnote will exhibit a linewidth approximately twice that of the laser linewidth. Commercial Lightwave Electronics model 120 single-frequency lasers are ideal candidates for heterodyning since they are available with very narrow linewidths (<100 kHz). Additional essential features are output powers up to 150 mW at 1319 nm and tunability over 50 GHz.

With heterodyning only (no phase-lock) and temperature stabilization of the laser cavities as provided by the manufacturer, the frequency f is stable enough to measure the signals generated by the photodiode at f, 2f, ... , and nf directly with a microwave spectrum analyzer. With an HP model 8566B spectrum analyzer operating at a resolution bandwidth (RBW) of 1 MHz and video averaging or with a 100 kHz resolution bandwidth without averaging, the minimum detectable electrical power is approximately -90 dBm. The RBW must be set sufficiently higher than its minimum of 10 Hz because of the frequency drift (1 MHz/min) and linewidth (1 to 50 kHz) of the lasers and associated beatnote. Additionally, at an upper PD current limit of 2.5 mA, the microwave power generated at the fundamental frequency f is approximately -10 dBm. This results in an 80 dB dynamic range, which represents a 15 to 60 dB improvement (depending on the modulation depth) over the direct modulation of laser diodes or the external modulation of lasers with a MZ modulator approaches.

A higher dynamic range for the heterodyne system (figure 2.1) can be obtained by offset-phase-locking the two lasers. Phase-locking[12,13] the two lasers at the difference frequency f produces a spectrally pure beat note with negligible linewidth (< 1 Hz) and drift. The RBW can then be reduced to less than 1 Hz, allowing the detection of electrical signals with signal powers of -140 dBm (10 Hz RBW, HP8566B) and below, depending on the spectrum analyzer. This increases the dynamic range of the measurement system to 130 dB, a value unsurpassed by any other PD nonlinearity measurement technique.

To test a PD, the single mode fiber-optic output of the source in figure 2.1 can be used in two ways. It can be fused directly to the fiber-optic pigtail of a fiber-coupled PD or it can be used with laboratory-mounted unpigtailed PDs as shown in figure 2.2. The output Gaussian beam from the fiber is collimated with a spherical lens and is focused with a second spherical lens onto the PD under test. With identical focusing and collimating lenses, a spot size equal to the spot size of the light in the fiber (approximately 10 μm) will be incident on a PD placed in the focal plane of the focusing lens. With another combination of focusing lenses[10] the minimum spot size can be reduced allowing higher power densities inside the photodiode. Larger spot sizes can also be achieved by translating the PD in the Z direction (defocusing) as shown in figure 2.2.

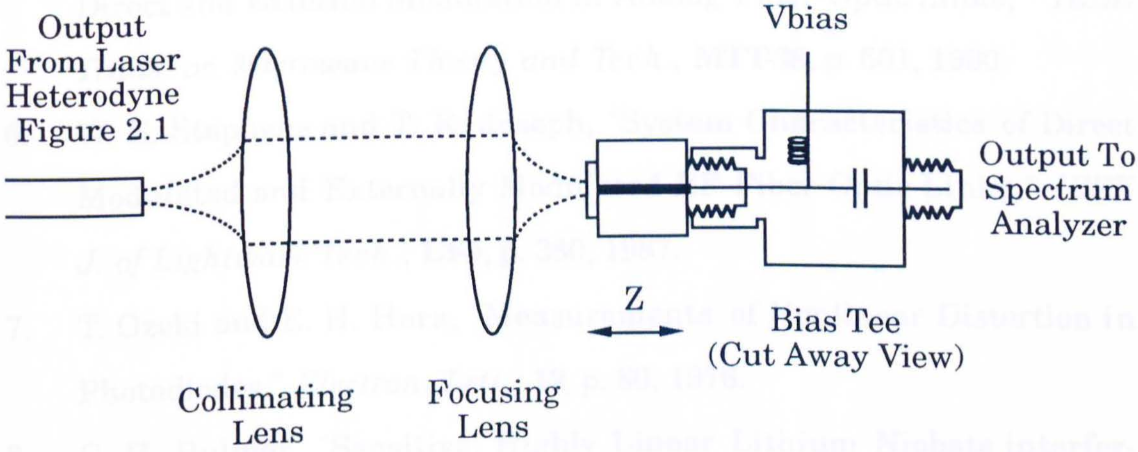

Figure 2.2 Lens coupling system with a variable optical spot size for use with laboratory mounted devices.

1. W. Susaki, "Recent Progress in superlinear InGaAsP Laser Diodes," OFC 91, Paper WG5, p. 92.

2. A. H. Gnauck, *et al.*, "Comparison of Direct and External Modulation for CATV Lightwave Transmission at 1.5μm Wavelength," *Electron. Lett.*, **28**, p. 1875, 1992.

3. G. E. Bodeep and T. E. Darcie, "Comparison of Second- and Third-Order Distortion in Intensity Modulated InGaAsP Lasers and a $LiNbO_3$ External Modulator," OFC 89, Paper WK2.

4. R. B. Childs and V. A. O'Byrne, "Predistortion Linearization of Directly Modulated DFB Lasers and External Modulators for AM Video Transmission," OFC 90, Paper WH6.

5. C. H. Cox, *et al*,. "An Analytic and Experimental Comparison of Direct and External Modulation in Analog Fiber-Optic Links," *IEEE Trans. on Microwave Theory and Tech.*, **MTT-38**, p. 501, 1990.

6. W. E. Stephens and T. R. Joseph, "System Characteristics of Direct Modulated and Externally Modulated RF Fiber-Optic Links," *IEEE J. of Lightwave Tech.*, **LT-5**, p. 380, 1987.

7. T. Ozeki and E. H. Hara, "Measurements of Nonlinear Distortion in Photodiodes," *Electron. Lett.*, **12**, p. 80, 1976.

8. C. H. Bulmer, "Sensitive, Highly Linear Lithium Niobate interferometers for Electromagnetic Field Sensing," *Appl. Phys. Lett.*, **53**, p. 2368, 1988.

9. B. H. Kolner and D. W. Dolfi, "Intermodulation Distortion and Compression in an Integrated Electrooptic Modulator," *Applied Optics*, **26**, p. 3676, 1987.

10. R.D. Esman and K.J. Williams, "Measurement of Harmonic

Distortion in Microwave Photodetectors," *IEEE Photon. Tech. Lett.*, **PTL-2**, p. 502, 1990.

11. K. J. Williams and R. D. Esman, "Observation of Photodetector Nonlinearities," *Electron. Lett.*, **28**, p. 731, 1992.
12. K. J. Williams, "Offset Phase Locking of Nd:YAG Nonplanar Ring Lasers," MS Thesis, Univ. of Maryland, 1989.
13. K.J. Williams, *et al.*, "6-34 GHz Offset Phase Locking of Nd:YAG 1319 nm Nonplanar Ring Lasers," *Electron. Lett.*, **25**, p. 1242, 1989.

III. PHOTODIODE DEVICE PHYSICS

Generalized Transport Equations

The basic equations governing carrier transport in any semiconductor region are Poisson's equation and the carrier continuity equations. Poisson's equation relates the potential Ψ, to the charge distribution inside any region and is given by:

$$-\nabla \cdot \nabla \Psi = \frac{q}{\varepsilon}(p - n + N_d - N_a) \ , \tag{3.1}$$

where $\Psi = \Psi(x,y,z,t)$ is the potential at the position (x,y,z) at some time t, p $= p(x,y,z,t)$ is the hole density, $n = n(x,y,z,t)$ is the electron density, N_a is the density of ionized acceptor dopants present in the crystal, N_d is the density of ionized donor dopants present in the crystal, q is the unit of charge (here positive), and ε is the permitivity of the semiconductor material. The electric field, $E = E(x,y,z,t)$, in the semiconductor region is given by the negative gradient of the potential Ψ and when substituted into Poisson's equation (3.1) yields Gauss's Law which is given by:

$$\nabla \cdot E = \frac{q}{\varepsilon}(p - n + N_d - N_a) \ . \tag{3.2}$$

The continuity equations for holes and electrons control the conservation of carriers in any volume. With a mid-bandgap approximation for the recombination centers,[1] the continuity equations are given by:

$$\frac{\partial p}{\partial t} = G - \frac{pn - n_i^2}{(p + n + 2n_i)\tau_p} - \frac{1}{q}\nabla \cdot J_p \ , \tag{3.3}$$

$$\frac{\partial n}{\partial t} = G - \frac{pn - n_i^2}{(p + n + 2n_i)\tau_n} + \frac{1}{q}\nabla \cdot J_n \ , \tag{3.4}$$

where $G = G(x,y,z,t)$ is the generation of carriers in the volume, τ_p and τ_n are the hole and electron recombination times, respectively, and n_i is the intrinsic carrier density. J_p and J_n are the hole and electron currents, respectively, which are expressed as:

$$J_p = J_{pdrift} + J_{pdiff} , \tag{3.5}$$

$$J_n = J_{ndrift} + J_{ndiff} , \tag{3.6}$$

where J_{pdrift} and J_{ndrift} are the hole and electron drift currents, respectively, and J_{pdiff} and J_{ndiff} are the hole and electron diffusion currents, respectively. The total current in the semiconductor region is the sum of the hole and electron currents (equations 3.5 and 3.6) with the addition of the displacement current and is given by:

$$J = J_p + J_n + \varepsilon \frac{\partial E}{\partial t} . \tag{3.7}$$

Equations 3.2 to 3.4 describe the carrier flow within a semiconductor region and solutions to a particular problem require the simultaneous solution of these coupled equations with the appropriate boundary conditions and the particular expressions for the currents (equations 3.5 and 3.6). In particular, photodiodes made with InGaAs and InP material will be considered here.

p-i-n Photodiode Structure

The basic photodiode structure under investigation here (figure 3.1) is either a single or double heterojunction device made from InP and InGaAs. InGaAs lattice-matched to InP has a bandgap[2] of 0.75 eV at 300 K and is sensitive to optical radiation if the wavelength is 1650 nm or shorter. InP, however, has a bandgap[2] of 1.35 eV at 300 K and is sensitive only to radiation having a wavelength of 920 nm or shorter. Therefore these are an ideal pair of semiconductor materials for detection of radiation in the 1300-nm to 1550-nm wavelength range, a region of importance for low-loss optical fiber communication systems.

The generic device (figure 3.1) under investigation is composed of a highly-doped n-InP substrate, an intrinsic layer of unintentionally-doped n-InGaAs, and a degenerately-doped p-InP or p-InGaAs cap layer. The

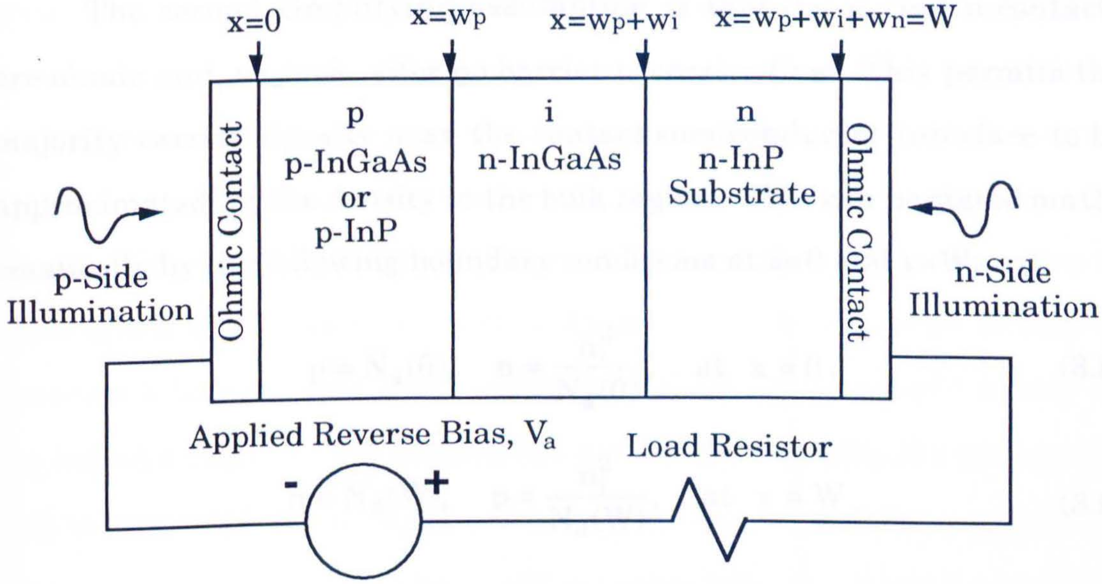

Figure 3.1 Simple model of a p-i-n photodiode structure.

incident light is assumed to pass through an aperture in either the n- or p-side ohmic contact of the device. Actual devices may take on many forms such as planar or mesa[3,4] structures. However, the simplified model will allow many of the physical mechanisms responsible for PD nonlinearities (NL) to be studied.

Simplifying Assumptions

Throughout this work, several simplifying assumptions on the behavior and physical properties of the device in figure 3.1 will be made by eliminating unknown or little known aspects of the device. The validity of any such assumptions is deemed appropriate if sufficient agreement is obtained between experimental measurements and the simulated results. A one-dimensional (one spatial dimension) analysis will be considered here. This will allow some aspects of the device NL to be studied, however; as will be explained later, two-dimensional simulations will be required to further study device nonlinear behavior.

The second simplifying assumption is that the p- and n-contacts are ohmic and, as such, offer no barrier to carrier flow. This permits the majority carrier density near the contact/semiconductor interface to be approximated[5] by the density in the bulk region. This can be stated mathematically by the following boundary conditions at x=0 and x=W:

$$p = N_a(0), \quad n = \frac{n_i^2}{N_a(0)}, \quad \text{at} \quad x = 0, \tag{3.8}$$

$$n = N_d(W), \quad p = \frac{n_i^2}{N_d(W)}, \quad \text{at} \quad x = W. \tag{3.9}$$

An additional boundary condition is needed for the solutions of equations 3.2 to 3.4. This boundary condition relates the given applied voltage V_a and the built-in diffusion potential V_{bi} to the electric field in the semiconductor region and is given by:

$$V_a + V_{bi} = -\int_{x=0}^{x=W} E dx \, , \tag{3.10}$$

with the built-in potential given by the usual expression:

$$V_{bi} = \frac{kT}{q} \ln\left\{\frac{N_a(0) N_d(W)}{n_i^2}\right\}, \tag{3.11}$$

where k is Boltzmann's constant and T is the absolute temperature. Note that in equations 3.10 and 3.11, the heterojunction potential steps have been omitted in the formulation of the potential and electric field. This is equivalent to treating the device (from the point of view of the electric field) as a homojunction p-i-n diode. The transport of carriers across the heterojunction(s) will be discussed in the next section.

The light incident on the detector (figure 3.1) enters either through an opening in the p-side or the n-side contact depending on device construction. For the purposes here, the incident contact surface is assumed to be anti-reflection coated and thus 100% of the incident light enters the semiconductor material. The generation rate G (eqns 3.3 and 3.4) can be expressed as the absorption of photons at a position x multiplied by the time dependence of the generated light. The absorption is exponential in the regions where a single photon has enough energy to generate a hole-electron pair, which for 1300 to 1550-nm light is only in the InGaAs regions. For single-pass p-side illumination, the generation rate is expressed as:

$$G(x,t) = G_o(t)e^{-\alpha x} \quad , \tag{3.12}$$

where $G_o(t)$ is the time-dependent generation rate per volume and α is the absorption coefficient for InGaAs. For single-pass n-side illumination, the generation rate is expressed as:

$$G(x,t) = G_o(t)e^{-\alpha(w_p+w_i-x)} \quad , \tag{3.13}$$

where $x = (w_p+w_i)$ is the InP/InGaAs interface (figure 3.1).

The band diagram of the device is shown in figure 3.2, where a p-InGaAs cap layer is assumed with a reverse bias voltage of a few volts. The InGaAs/InP heterojunction depicted in figure 3.2 has a valence band

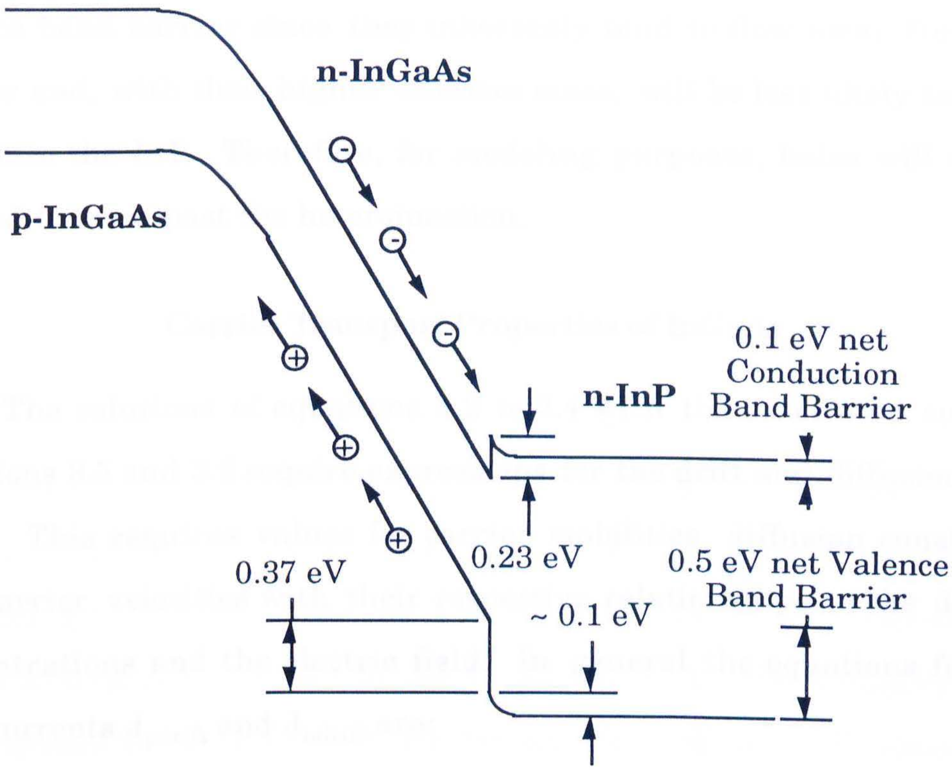

Figure 3.2 A depiction of the photodiode band diagram.

discontinuity[6] of 0.37 eV and a conduction band discontinuity[6] of 0.23 eV. The reduction in the conduction band discontinuity and the increase in the valence bands discontinuity of approximately 0.1 eV is the result of the difference in the doping of the intrinsic n-InGaAs, $N_d = 10^{15}$ cm^{-3}, and the n-InP, $N_d = 10^{17}$ cm^{-3}. The band discontinuities are barriers to current flow and their effect is to trap carriers.[7] Here the effects of the heterojunctions will be reduced because of several approximations.

Electrons will be allowed to flow without restriction across the conduction band barrier since, near the 0.1 eV barrier, the electron can have significant velocity (energy) towards the barrier due to the high electric field and, with a low effective mass, may travel across the barrier without restriction. Holes on the other hand will not tend to flow across the 0.5 eV valence band barrier since they inherently tend to flow away from the barrier and, with their higher effective mass, will be less likely to penetrate into the InP. Therefore, for modeling purposes, holes will not be allowed to move past the heterojunction.

Carrier Transport Properties of InGaAs

The solutions of equations 3.2 to 3.4 with the associated current equations 3.5 and 3.6 require expressions for the drift and diffusion currents. This requires values for carrier mobilities, diffusion constants, and carrier velocities with their respective relationships to the doping concentrations and the electric field. In general the equations for the drift currents J_{pdrift} and J_{ndrift} are:

$$J_{pdrift} = -qpv_p(E) \ , \tag{3.14}$$

$$J_{ndrift} = qnv_n(E) \ , \tag{3.15}$$

where $v_p(E)$ and $v_n(E)$ are the electric-field-dependent hole and electron drift velocities, respectively. For electric fields below 4 kV/cm for electrons and below 20 kV/cm for holes, the drift velocities are the usual expressions of mobility times the electric field. However, for high speed operation, it is desirable to operate the device with electric fields high enough to saturate both carrier velocities to minimize the carrier transit times. To model a particular device, it is necessary to utilize the entire velocity-versus-field relationships for the drift velocities because carriers will be in regions of the device where the electric field may be high enough to saturate carrier velocities (intrinsic region) and in regions where the fields are low (contacts and interface regions).

The electron velocity versus electric field has been measured[8] for various samples of InGaAs at electric fields from 10 to 100 kV/cm. An empirical expression is used to describe $v_n(E)$ for electrons in InGaAs:

$$v_n(E) = \frac{E(\mu_n + v_{nhf}\beta|E|)}{1+\beta E^2} , \tag{3.16}$$

where μ_n is the electron low-field mobility in InGaAs, v_{nhf} is the high field electron velocity, and β is a fitting parameter.

Equation 3.16 is plotted in figure 3.3 for electron mobilities of 10,000 and 8,000 cm^2/Vs with the experimental data from reference [8]. The corresponding fitted parameters are $\beta = 1.0 \times 10^{-7}$ and 0.8×10^{-7}, respectively, and in both cases $v_{nhf} = 5.4 \times 10^6$ cm/s. Equation 3.16 differs slightly from the empirical formula given by Dentan and de Cremoux.[9] Equation 3.16 was chosen because it provides a better fit to the experimental data[8] from 20 to 100 kV/cm, even though it fails to give a high enough peak electron

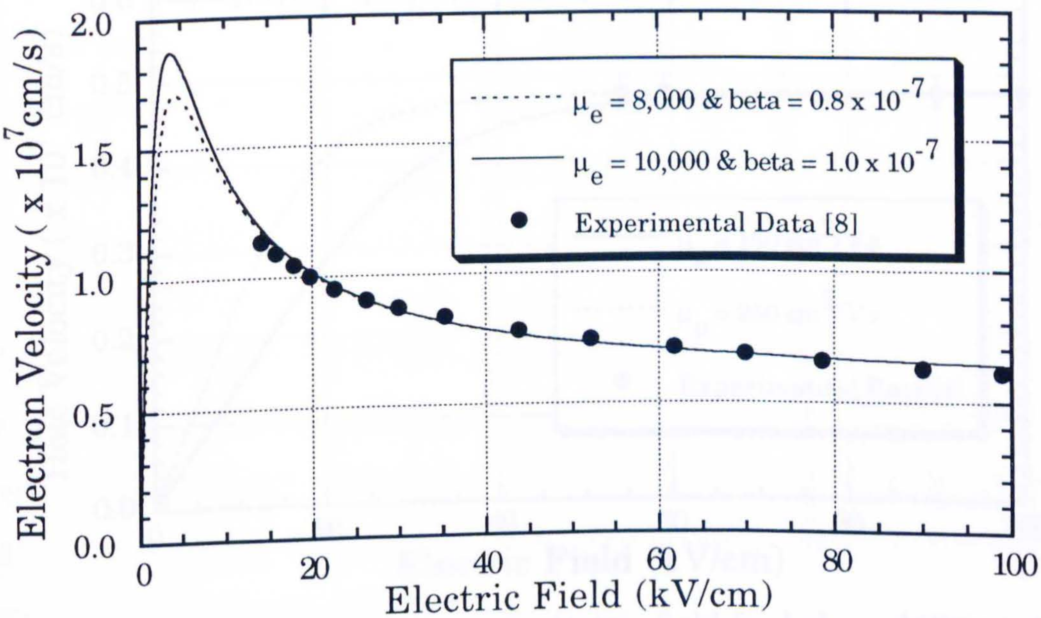

Figure 3.3 Electron velocity versus electric field for electron mobilities of 8,000 and 10,000 cm^2/Vs. Experimental data from Reference [8].

velocity. For simulation purposes, the low-field electron mobility used will be between 6,000 and 10,000 cm^2/Vs since the measured values in different semiconductor samples vary between 6,000 and 10,500 cm^2/Vs.[2]

The electric field dependence of the hole velocity in InGaAs has not received as much attention as the electron velocity; however, measurements have been made for the saturated hole velocity.[4] A high-field hole velocity of v_{phf} = 4.8 x 10^6 cm/s may be used with the following empirical formula:

$$v_p(E) = \frac{\mu_p v_{phf} E}{\left(v_{phf}^4 + \mu_p^4 E^4\right)^{1/4}} \tag{3.17}$$

to analytically describe the hole velocity versus electric field (figure 3.4) for hole mobilities of 150 and 250 cm^2/Vs.

The value for the hole mobility used in our studies is between 50 to

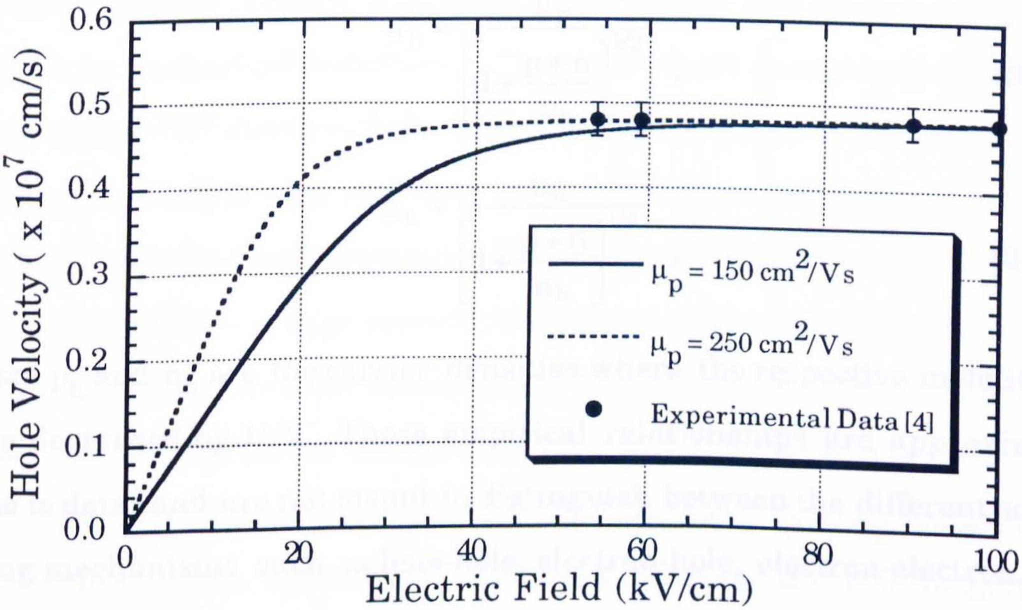

Figure 3.4 Hole velocity versus electric field for hole mobilities of 150 and 250 cm^2/Vs. Experimental data from Reference [4].

80 percent of the only reported[10] (300 cm^2/Vs) value in the literature. This is reasonable considering the fact that the electron mobility varies appreciably from sample to sample. The exact electric field dependence of the hole mobility in InGaAs below 50 kV/cm has not yet been measured. For example, the hole mobility in equation 3.17 needs to be at least 10% lower for a best fit to the empirical formula of Dentan and de Cremoux[9] below 50 kV/cm. Therefore, the hole mobility will be left as an adjustable parameter for this study so long as the values used are within the 150-300 cm^2/Vs range.

It has also been reported[2] that the carrier mobilities decrease as the doping densities exceed 10^{16} /cm^3 due to ionized impurity or free carrier scattering. To incorporate this information into the transport equations, the hole and electron mobilities will be reduced by the following empirical relationships:

$$\mu_p' = \frac{\mu_p}{\left[1+\dfrac{p+n}{p_h}\right]^{1/2}}, \tag{3.18}$$

$$\mu_n' = \frac{\mu_n}{\left[1+\dfrac{p+n}{n_h}\right]^{1/2}}, \tag{3.19}$$

where p_h and n_h are the carrier densities where the respective mobilities have decreased by $1/\sqrt{2}$. These empirical relationships are approximations to data[2] and are not meant to distinguish between the different scattering mechanisms such as hole-hole, electron-hole, electron-electron, or carrier-ionized-dopant scattering.

Diffusion Current Limitations

Limitations on the diffusion current has not received much attention in the literature with the exception of several[11,12] numerical treatments. The diffusion current for electrons is typically expressed as:

$$J_{ndiff} = qD_n \frac{\partial n}{\partial x} \quad . \tag{3.20}$$

This equation implies that, as the carrier density gradient increases, the diffusion current will increase without bound. This will certainly not occur in any semiconductors since carrier scattering and thermal velocity limitations will limit the carriers effective velocity whether the carrier moves by drift or diffusive mechanisms.

When equations 3.5 and 3.6, containing the diffusion terms, are substituted into the continuity equations 3.3 and 3.4, the three coupled differential equations become second order in x. The resulting drift-diffusion problem becomes analytically untractable and leads to instabilities[11,12] in numerical solutions. To avoid these complexities, many researchers[9,13-15] disregard the diffusion terms in the continuity equations and solve drift-only problems in regions where the diffusion terms are believed to be less important. This is rationalized[13] with the argument that once the voltage exceeds kT/q, the contribution of the diffusion current to the total current is negligible. While this may be true, carrier diffusion is crucial for an accurate determination of the internal PD electric field which depends on the charge location, itself a strong function of the diffusion terms. Additionally, reference [13] assumes that the generated carrier densities are small such that the electric field is not perturbed, which may not be true for the high incident powers under consideration here. In fact, the basic solution to a p-n junction under dark conditions (zero total current) requires the delicate balance between the drift and diffusion currents.

To circumvent the added complexity of the diffusion terms, researchers[13-15] have limited their modeling to the intrinsic region only or divided the problem up into distinct regions. In this study, the diffusion terms will not be neglected. Although this adds considerable computation time to the simulations, a complete treatment of diffusion is necessary since an accurate description of the electric field is important for high power effects as will be demonstrated in Chapter VII.

Equation 3.20 therefore needs to be modified for the effects of velocity saturation. The expression for the diffusion constant for non-degenerate semiconductors is given by the Einstein relationship:

$$D = \frac{kT}{q}\mu \quad . \tag{3.21}$$

The dependence of the diffusion constant with electric field is linked to the mobility since kT/q is constant at a given carrier temperature. An expression for the mobility as a function of electric field for electrons in materials with intravalley scattering (GaAs, InGaAs, InP, and etc.) is given by Boer[17] (eqn 33.23). Although the exact characteristic of electrons in InGaAs is not known, the dependence from equation (33.23)[17] suggests that at high fields, the mobility has a $1/E$ dependence. Experimental verification of the diffusion constant versus electric field is difficult to measure since the diffusion current is masked by the drift current at high fields. However, theoretical calculations[18-21] in InP and GaAs result in diffusion constants with a $1/E^{\xi}$ dependence where ξ is between 0.5 to 1, depending on carrier temperature and model assumptions. Additionally these calculations predict a diffusion constant peak near an electric field where the drift velocity peaks. From the results in GaAs and InP, an estimation of the diffusion constant will be made for electrons in InGaAs and will be expressed as:

$$D_n = \frac{\frac{kT}{q}\mu(E=0)}{\left\{1-2\left(\frac{E}{E_p}\right)^2+\frac{4}{3}\left(\frac{E}{E_p}\right)^3\right\}^{1/4}} , \tag{3.22}$$

where E_p is the electric field where the diffusion constant peaks and $\mu(E=0)$ is given by equation 3.19. The polynomial and its coefficients in the denominator of equation 3.22 were chosen to portray the behavior of the diffusion constant[18-21] in GaAs and InP in three respects: 1) the slope of the diffusion constant at $E = 0$ is zero, 2) the peak in the diffusion constant is approximately 130% of its value at $E = 0$ at a field near the drift velocity peak, and 3) the characteristic roll off at high electric fields is $\xi = 0.75$. Equation 3.22 is plotted in figure 3.5 with $E_p = 4$ kV/cm.

The diffusion constant for holes has not received much attention in the literature. Since the hole does not experience a velocity peak at a particular electric field (scattering into a higher-effective-mass valley), the hole diffusion constant can be approximated by the following expression:

$$D_p = \frac{kT}{q}\frac{v_p(E)}{E} , \tag{3.23}$$

where $v_p(E)$ is given by equation 3.17. Equation 3.23 is also plotted in figure 3.5. Note that the diffusion constant for electrons is 20 to 50 times greater than that of the hole for $E < 100$ kV/cm. Equations 3.22 and 3.23

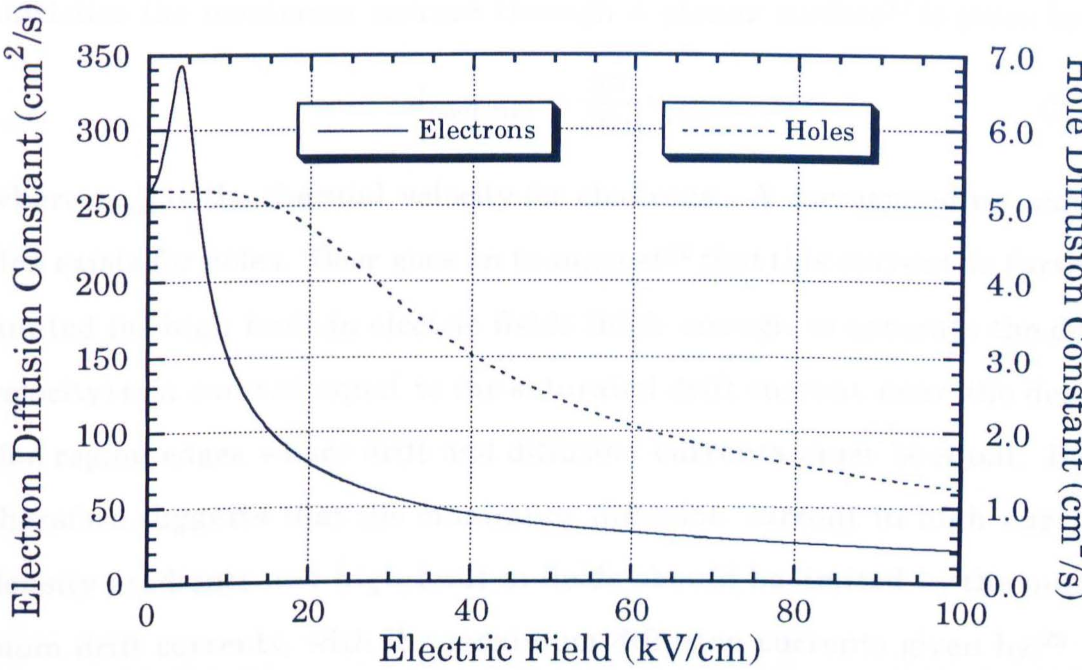

Figure 3.5 Hole and electron diffusion constants versus electric field according to equations 3.22 and 3.23.

are only estimates for the diffusion constants and, as will be discussed shortly, further reductions in the diffusion current will be required.

Even with the diffusion constant limitations implied by equations 3.22 and 3.23, the diffusion current and effective diffusion carrier "velocity" can quickly exceed the thermal velocity or the saturated carrier velocities. Boer has analyzed diffusion[5,17,22,23] and applied his results to semiconductors. His work leads to the hypothesis that, since diffusion is derived from the difference between two random walk currents[22] (a forward and reverse current), as the carrier density gradient becomes increasingly high, the contribution of the reverse current is negligible compared to the forward current. The maximum diffusion current therefore, is the maximum forward current which is expressed as the Richardson-Dushman current.[23] For carriers following Boltzmann statistics the maximum current through a planar surface[17] is given by:

$$J_{ndiff,max} = \frac{qn}{\sqrt{6\pi}} v_{rms} \ , \tag{3.24}$$

where v_{rms} is the thermal velocity for electrons. A corresponding equation exists for holes. Boer goes on to suggest[22] that this current is further limited for high built-in electric fields (high enough to saturate the drift velocity) to a current equal to the saturated drift current near the depletion region edges where drift and diffusion currents must be equal. Boer therefore suggests that the maximum diffusion current in high carrier density gradients and high built-in fields should be limited by the maximum drift currents, with the maximum diffusion currents given by:[22]

$$J_{ndiff,max} = qnv_{ndiff\text{-}sat} \ , \tag{3.25}$$

$$J_{pdiff,max} = qpv_{pdiff\text{-}sat} \ , \tag{3.26}$$

where $v_{ndiff\text{-}sat}$ and $v_{pdiff\text{-}sat}$ are the saturated diffusion "velocities" and in some sense are equal or nearly equal[22] to the saturated drift velocities.

The Nonlinear Transport Equations

Gauss's law (eqn. 3.2) combined with the continuity equations (3.3 and 3.4) with the appropriate substitutions for the currents J_n and J_p, (eqns 3.5 and 3.6), and the expressions for the drift currents, (eqns 3.14 and 3.15), yield the three simplified transport equations:

$$\nabla \cdot E = \frac{q}{\varepsilon}(p - n + N_d - N_a) \ , \tag{3.27}$$

$$\frac{\partial p}{\partial t} = G - \frac{pn - n_i^2}{(p + n + 2n_i)\tau_p} - v_p \frac{\partial p}{\partial x} - p\frac{\partial v_p}{\partial x} - \frac{1}{q}\frac{\partial J_{pdiff}}{\partial x} \ , \tag{3.28}$$

$$\frac{\partial n}{\partial t} = G - \frac{pn - n_i^2}{(p + n + 2n_i)\tau_n} + v_n \frac{\partial n}{\partial x} + n \frac{\partial v_n}{\partial x} + \frac{1}{q}\frac{\partial J_{ndiff}}{\partial x} \quad , \tag{3.29}$$

where the diffusion current has not been simplified but may be reduced with the help of equations 3.25 and 3.26. Equations 3.27 to 3.29 are linear only if the following three conditions are satisfied:

1) The carrier velocities, v_n and v_p, are independent of the carrier densities, n and p.

2) The diffusion current terms in equations 3.28 and 3.29 are linear with carrier density.

3) The recombination terms are simplified or neglected.

Since the carrier velocities are related to the electric field via equations 3.16 and 3.17 and are further related to the carrier densities via equation 3.27, the first condition is satisfied only when the electric field is not effected in the PD due to the generated carrier densities; however, this does not restrict the velocities from being functions of position or time. This approximation is the low-level-injection condition.

To define the low-level-injection condition, let the total hole and electron concentrations be defined as follows:

$$p = p_o + p' \quad , \tag{3.30}$$

$$n = n_o + n' \quad , \tag{3.31}$$

where p_o and n_o are the dark-condition carrier concentrations and p' and n' are the excess carrier concentrations due to the incident light. Gauss's law (eqn. 3.27) can then be expressed as:

$$\nabla \cdot E \;=\; \frac{q}{\varepsilon}\left(p_o + p' - n_o - n' + N_d - N_a\right) \;. \tag{3.32}$$

The electric field can then be expressed as the sum of a dark electric field (E_{dark}) and a space charge electric field (E_{sc}) given by:

$$E = E_{dark} + E_{sc} \quad , \tag{3.33}$$

which allows Gauss's law to be divided into two equations; one equation describing E_{dark} and the other describing E_{sc}, given by:

$$\nabla \cdot E_{dark} = \frac{q}{\varepsilon}(p_o - n_o + N_d - N_a) \ , \tag{3.34}$$

$$\nabla \cdot E_{sc} = \frac{q}{\varepsilon}\left(p' - n'\right) . \tag{3.35}$$

Low-level-injection is defined when $p' << p_o$, $n' << n_o$, and $p' \approx n'$. Operating in the low-level-injection condition therefore allows $E_{sc} \approx 0$, or equivalently, it assumes that the electric field is unchanged from its value under otherwise dark conditions. To a first approximation, this breaks the connection between the electric field and the carrier velocities.

The second condition is satisfied only if the diffusion constants are independent of the carrier densities. The carrier velocities and diffusion constants may be functions of the generated carrier densities by the following mechanisms:

1) Space-charge fields, which violate the low-level-injection conditions, result in carrier-density-dependent electric fields. This can result in changes in the electron velocity via equation 3.16, changes in the hole velocity via equation 3.17, and changes in the diffusion constants via equations 3.22 and 3.23.

2) The flow of current in the p-region, being directly proportional to the electric field, modifies the carrier velocities of the generated carriers in this region.

3) Lower carrier mobilities via equations 3.18 and 3.19 from scattering at high carrier densities can modify the carrier velocities and the diffusion constants with increasing carrier densities.

4) Photodiode potential drops from current flow in the external load resistance lowers the internal electric field and results in carrier-density-dependent carrier velocities.

5) Saturation of trap sites.

6) Carrier flow near or across the heterojunctions.

7) The generated carriers not reaching their steady-state velocities instantly due to their finite acceleration and scattering times.

The relative contribution of the first four of these conditions to PD nonlinear behavior will be the focus Chapters V through VIII.

The solution to the transport equations (3.27 to 3.29) thus requires the substitutions of the appropriate equations given throughout this chapter and results in a system of three coupled nonlinear differential equations for the currents in a p-i-n PD. In principle, using these equations with the boundary conditions (3.8 to 3.11), the resulting system of equations can be solved. Analytical solutions for equations 3.27 to 3.29 are extremely difficult and have led to numerous numerical solutions.[9,11,12,14,15,24,25] Chapter IV will discuss the approach taken here to solve this system of equations as well as presenting the resultant physical approach for the diffusion current limitations, which was proposed in equations 3.25 and 3.26.

1. S.M. Sze, "Physics of Semiconductor Devices," 2nd Edition, John Wiley and Sons, pp. 35-51, 1981.
2. T.P. Pearsall, Editor, "GaInAsP Alloy Semiconductors", John Wiley and Sons, p.456, 1982.
3. Y.G. Wey, *et al.*, "Ultrafast Graded Double-Heterostructure GaInAs/ InP Photodiode," *Appl. Physics Lett.*, **58**, p. 2156, 1991.
4. P. Hill, *et al.*, "Measurement of Hole Velocity in n-Type InGaAs," *Appl. Physics Lett.*, **50**, p. 1260, 1987.
5. K.W. Boer, "Survey of Semiconductor Physics," Van Nostrand Reinhold, New York, Volume II, p. , 1992.
6. K.W. Boer, "Survey of Semiconductor Physics," Van Nostrand Reinhold, New York, Volume II, p. 316, 1992.
7. J.E. Bowers and C.A. Burrus,"Ultrawide-Band Long-Wavelength p-i-n Photodetectors," *J. of Lightwave Tech.*, **JLT-5**, p. 1339, 1987.
8. T.H. Windhorn, *et al.*, "The Electron Velocity-Field Characteristic for n-InGaAs at 300K," *IEEE Electron Device Lett.*, **EDL-3**, p. 18, 1982.
9. M. Dentan and B. de Cremoux, "Numerical Simulation of the Nonlinear Response of a p-i-n Photodiode Under High Illumination," *J. of Lightwave Tech.*, **JLT-8**, p. 1137, 1990.
10. T.P. Pearsall, *et al.*, "Electron and Hole Mobilities in GaInAs," *Gallium Arsenide and Related Compounds 1980*, p. 639, 1981.
11. H. Yi, *et al.*, "Novel Method to Control Numerical Solution Oscillation of Diffusion-Drift Equation," *Electron. Lett.*, **26**, p. 1487, 1990.
12. R.E. Bank, *et al.*, "Numerical Methods for Semiconductor Device Simulation," *IEEE Trans. on Electron Devices*, **ED-30**, p. 1031, 1983.

13. G. Lucovsky, *et al.*, "Transit-Time Considerations in p-i-n Diodes," *J. of Appl. Physics*, **35**, p. 622, 1964.

14. R. Sabella and S. Merli, "Analysis of InGaAs p-i-n Photodiode Frequency Response," *IEEE J. of Quantum Elec.*, **JQE-29**, p. 906, 1993.

15. J.M. Zhang and D.R. Conn, "State-Space Modeling of the PIN Photodetector," *J. of Lightwave Tech.*, **JLT-10**, p. 603, 1992.

17. K.W. Boer, "Survey of Semiconductor Physics," Van Nostrand Reinhold, New York, Volume I, 1990.

18. P.E. Bauhahn, *et al.*, "Comparison of the Hot Electron Diffusion Rates for GaAs and InP," *Electron. Lett.*, **9**, p. 460, 1973.

19. C. Hammar and B. Vinter, "Diffusion of Hot Electrons in n-Indium Phosphide," *Electron. Lett.*, **9**, p. 9, 1973.

20. W. Fawcett and G. Hill, "Temperature Dependence of the Velocity-Field Characteristic of Electrons in InP," *Electron. Lett.*, **11**, p. 80, 1975.

21. P.S. Cheung and C.J. Hearn, "The Diffusion of Electrons in Semiconductors in High Electric Fields," *J. of Physics C: Solid State Physics*, **5**, p. 1563, 1972.

22. K.W. Boer, "High-Field Carrier Transport in Inhomogeneous Semiconductors," *Ann. der Physik*, p. 371, 1985.

23. S. Dushman, *Rev. Modern Physics*, **2**, p. 381, 1930.

24. O. Heinreichsberger, *et al.*, "Fast Iterative Solution of Carrier Continuity Equations for Three-Dimensional Device Simulation," *SIAM J. of Sci. Stat. Comput.*, **13**, p. 289, 1992.

25. A. Yoshii, *et al.*, "Investigation of Numerical Algorithms in Semiconductor Device Simulation," *Solid State Elec.*, **30**, p. 813, 1987.

IV. NUMERICAL TECHNIQUES

Introduction

Solutions to the transport equations outlined in Chapter III have been limited to numerical treatments with the exception of some simple one-dimensional (1-D) problems. A sample of the overwhelming number of papers on numerical techniques for semiconductor device simulation are given in references [1]-[9]. The appropriate choice of numerical technique for the solution of the transport equations is not straight forward and each method has its advantages and disadvantages.

Several numerical methods were considered including the finite difference, finite element, and iterative methods. Iterative and finite element methods are usually considered two-dimensional (2-D) methods and since the extension of this work to 2-D was not pursued, these methods were not used. Initial solutions with the finite difference method using a two-point difference resulted in poor accuracy and numerical instabilities. After some time modeling only the intrinsic region, an open-loop time-step solution was chosen over the finite difference method. Although this method may not be the most efficient (computationally), it promised to give accurate and satisfactory results. A block diagram of the algorithm is given in figure 4.1. The PD (figure 3.1) is divided into m slices or bins, not necessarily of the same width. A piecewise-constant approximation for the carrier densities is utilized in each slice as shown in figure 4.2.

The algorithm begins by solving the steady-state transport equations with a given constant (possibly zero) generation function. The main

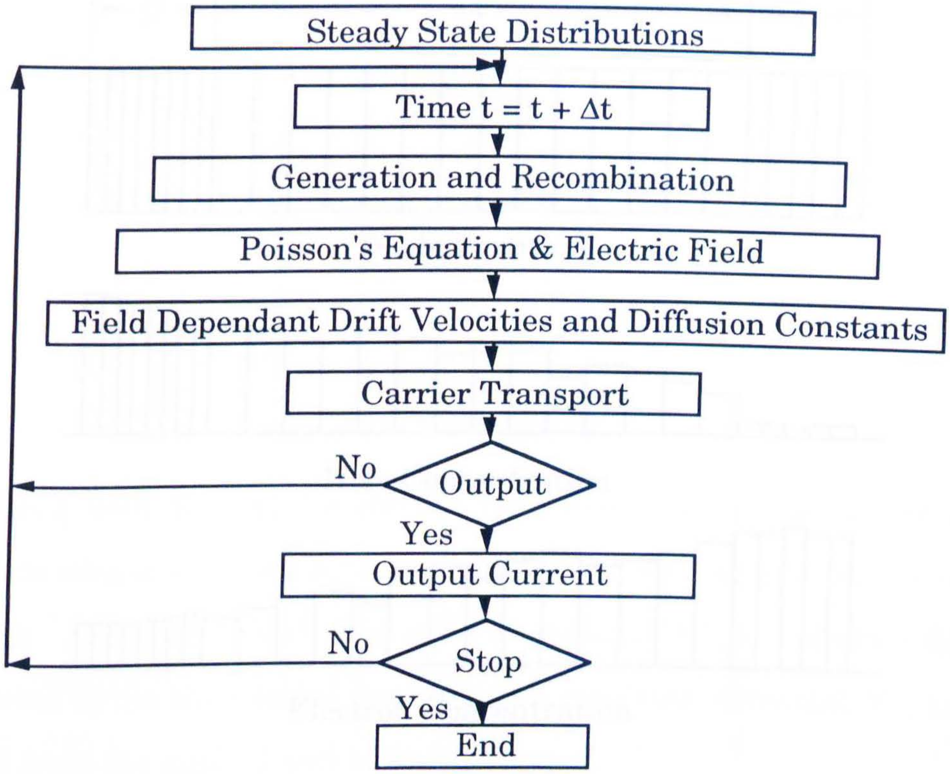

Figure 4.1 Algorithm Flow Chart

loop (figure 4.1) begins by adjusting the carrier densities via generation and recombination during the time Δt and, with the new carrier densities, then recalculates the electric field at the bin interfaces via a solution of Poisson's equation. Following the evaluation of a new electric field, new values for the carrier velocities and diffusion constants are calculated at the bin interfaces. The carriers are then allowed to move during Δt from their respective bins according to their new velocities and diffusion constants. If no output (current) is desired, the loop repeats itself for a predetermined time. The algorithm is open-loop[10] because the solution of the transport equations at the time t requires information about the carrier densities at the time $t - \Delta t$ only once and does not iteratively solve

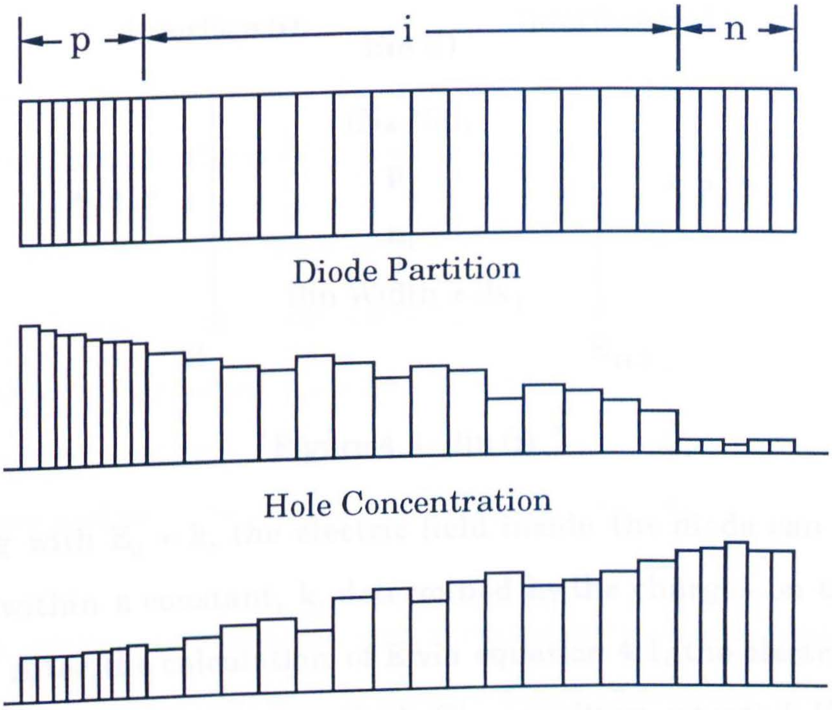

Figure 4.2 Diode Partitions and Carrier Approximations

for variables at time t. Specifics outlining each of the algorithm steps will be presented in the next few sections.

Solving Poisson's Equation

The solutions to Poisson's equation (eqn. 3.1) or, equivalently to the differential form of Gauss's law (eqn. 3.2) using a piecewise-constant approximation for the carrier densities is a simple calculation for a given boundary condition (eqn. 3.9) as follows. Referring to figure 4.3 and assuming a forward-difference approximation for the derivative in equation 3.2, the electric field at the interface i+1, E_{i+1}, is related to E_i by:

$$E_{i+1} = dE + E_i = \frac{q}{\varepsilon}(p_i - n_i + (N_d - N_a)_i)dx_i + E_i \quad . \tag{4.1}$$

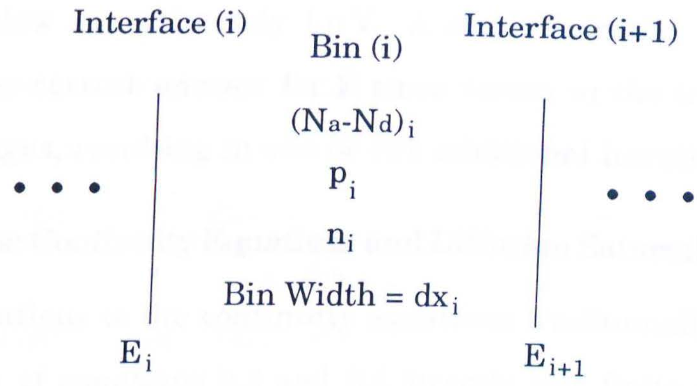

Figure 4.3 Bin (i)

Beginning with $E_0 = k$, the electric field inside the diode can be determined to within a constant, k, determined by the charges on the ohmic contacts. After the calculation of E via equation 4.1, the electric field is integrated by the trapezoidal method. The resulting potential, V_E, is subtracted from the applied and built-in voltages:

$$V_{error} = V_E - (V_a + V_{bi}) \ . \tag{4.2}$$

The resulting error potential, V_{error}, is due to charge on the ohmic contacts, since the field inside the contacts is uniquely determined (to within a constant) by equation 4.1, and the potential between the contacts must be equal to the applied and built-in voltages. Therefore an image charge is placed on the contacts, which results in an additional constant electric field component through the diode and is given by:

$$E_{add} = \frac{V_{error}}{W} \ , \tag{4.3}$$

where W is the separation between the ohmic contacts. The additional electric field is added to the field at each interface, which is equivalent to beginning the solution of equation 4.1 with $E_0 = k + E_{add}$. The integration of E is repeated with the calculation of a new error potential, until the error falls below approximately 1 μV. A single iteration will not necessarily give the correct answer for E since terms in the integration of E can change signs, resulting in one or two additional iterations.

The Continuity Equations and Diffusion Saturation

The solutions to the continuity equations traditionally have meant the expansion of equations 3.3 and 3.4 directly into finite differences or other numerical methods. Here the approach is to reanalyze the continuity equations and to carry out their solutions by the way in which they are created.

The continuity equations are a mathematical description of the conservation of carriers within a given volume. Consider the bins (i-1), (i), and (i+1) in figure 4.4. The change in carrier density within bin(i) is equal to the number of carriers entering the bin minus the number of carriers leaving the bin. The physical mechanisms for carriers entering bin(i) are generation within bin(i), carrier drift from bin(i-1) and bin(i+1) into bin(i), and carrier diffusion from bin(i-1) and bin(i+1) into bin(i). The physical mechanisms for carriers leaving bin(i) are recombination

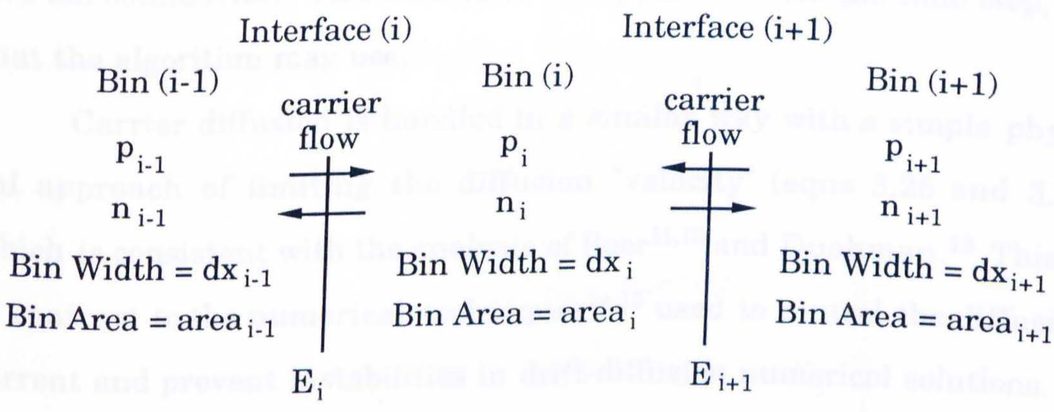

Figure 4.4 Bins (i-1), (i), and (i+1)

within bin(i), carrier drift from bin(i) into bin(i-1) and bin(i+1), and carrier diffusion from bin(i) into bin(i-1) and bin(i+1). Therefore, during every time step Δt, the carrier densities in each bin are recalculated based on generation, recombination, and carrier movement.

The carrier flow due to the drift current at interface (i) is evaluated with the following simple expressions. Consider the case when the drift velocity at interface (i) is such that electrons will tend to flow out of bin(i) and into bin(i+1), the number of carriers that flow during time Δt into bin(i+1) is just:

$$\Delta n = n_i v_{i+1} \mathrm{area}_i \Delta t \quad . \tag{4.4}$$

The drift terms in the continuity equations are thus treated by calculating the number of carriers that move through interface (i), using equation 4.4, and by adding and subtracting those carriers (divided by the volume) from their respective bins. In the limit of this simple physical model, the distance that the carriers travel in a single time step may not be any larger than the maximum of the velocity times the smaller of the leaving or entering bin widths, in order to keep the carriers from moving across two bin boundaries. This results in an upper limit for the time step, Δt, that the algorithm may use.

Carrier diffusion is handled in a similar way with a simple physical approach of limiting the diffusion "velocity" (eqns 3.25 and 3.26) which is consistent with the analysis of Boer[11,12] and Dushman.[13] This is in contrast to the numerical techniques[14,15] used to control the diffusion current and prevent instabilities in drift-diffusion numerical solutions.

Following the analysis of Boer,[12] the diffusion current is derived by the difference in carrier flow from one position in space to another as shown in figure 4.5. These currents can be expressed[12] as forward and reverse currents due to their Brownian motion as:

$$\vec{J}_{ndiff} = q\left(n_o - \frac{dn}{2}\right)\frac{v_{rms}^2}{3}\frac{\tau_n}{dx} \quad , \tag{4.5}$$

$$\bar{J}_{ndiff} = q\left(n_o + \frac{dn}{2}\right)\frac{v_{rms}^2}{3}\frac{\tau_n}{dx} \quad , \tag{4.6}$$

where τ_n is the mean time between collisions. The net diffusion current is the difference between equations 4.5 and 4.6 and is given by:

$$J_{ndiff} = q\frac{v_{rms}^2 \tau_n}{3}\frac{dn}{dx} \quad . \tag{4.7}$$

The diffusion constant is therefore defined as:

$$D_n = \frac{v_{rms}^2 \tau_n}{3} \quad . \tag{4.8}$$

The maximum diffusion current (eqn. 3.24) is derived from equations 4.5 and 4.6 assuming that for high carrier density gradients the reverse current (eqn. 4.6) vanishes. If the distance dx is set equal to the mean free path, $dx = v_{rms}\tau_n$, equation 3.24 is obtained.

A direct analogy between the discrete nature of a numerical solu-

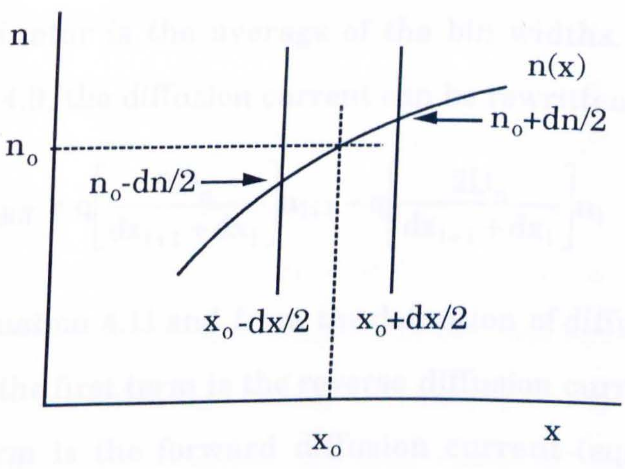

Figure 4.5 Illustration for the derivation of the diffusion current. From Ref. [11]

tion and the derivation for diffusion can be presented with a simple model. Given the carrier densities between bins (i) and (i+1) in figure 4.6,

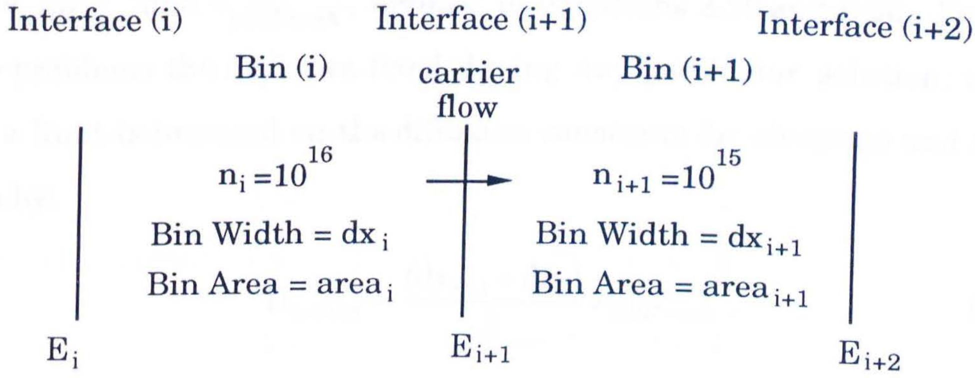

Figure 4.6 Electron diffusion between bins (i) and (i+1).

the diffusion current is expressed with equations 4.7 and 4.8 as:

$$J_{ndiff} = qD_n \frac{dn}{dx} \quad . \tag{4.9}$$

The derivative of the carrier density in finite arithmetic can be expressed by the forward difference formula as:

$$\frac{dn}{dx} = \frac{(n_{i+1} - n_i)}{\left(\frac{dx_{i+1} + dx_i}{2}\right)} \quad , \tag{4.10}$$

where the denominator is the average of the bin widths. Substituting equation 4.10 into 4.9, the diffusion current can be rewritten as:

$$J_{ndiff} = q\left[\frac{2D_n}{dx_{i+1} + dx_i}\right] n_{i+1} - q\left[\frac{2D_n}{dx_{i+1} + dx_i}\right] n_i \quad . \tag{4.11}$$

By inspection of equation 4.11 and from the definition of diffusion current (eqns. 4.5 and 4.6), the first term is the reverse diffusion current (eqn. 4.6) and the second term is the forward diffusion current (eqn. 4.5). The expressions in brackets are interpreted as the effective diffusion "velocities" for discrete problems. For arbitrary carrier density gradients, the term in the brackets must be limited by the maximum diffusion velocities, $v_{ndiff\text{-}max}$ and $v_{pdiff\text{-}max}$, defined in equations 3.25 and 3.26. For discrete problems the dx_i's are fixed during any particular solution; therefore, a limit is imposed on the diffusion constants for electrons and holes given by:

$$D_{n\text{-}max} = \frac{(dx_{i+1} + dx_i)}{2} v_{ndiff-sat} \,, \tag{4.12}$$

$$D_{p\text{-}max} = \frac{(dx_{i+1} + dx_i)}{2} v_{pdiff-sat} \,. \tag{4.13}$$

If one were to mistakenly ignore the limits of equations 4.12 and 4.13 the calculation of the diffusion current between two adjacent bins can be significantly overestimated. For example, let a 2 micron p-i-n PD be equally divided into 200 bins, resulting in a bin width of 1.0×10^{-6} cm. At a position in the PD where the electric field is 10 kV/cm, the electron drift velocity is (eqn. 3.16) approximately 1.3×10^{7} cm/s. The electron diffusion constant at 10 kV/cm is estimated (eqn. 3.22) to be 150 cm^2/Vs. The maximum diffusion constant allowed (eqn. 4.12) is 13 cm^2/Vs, assuming the maximum diffusion velocity is equal to the drift velocity in the bin. Therefore if one were to ignore the limitations on the diffusion constant imposed by equation 4.12, the diffusion current between bins would be overestimated by a factor of 150/13 or greater than 11 times. Bin widths of 10^{-7} cm are desired to improve numerical accuracy and so could result in an overestimation in the diffusion current by over 100 times.

For the purposes of this study, the maximum diffusion velocities (eqns. 4.12 and 4.13) will be set equal to the saturated drift velocities.

Carrier diffusion will be carried out through the calculation of diffusion current (eqn. 4.11) with a corresponding expression for holes. An expression similar to one used for calculating the drift carrier movement (eqn. 4.4) is used to calculate the diffusion carrier movement during Δt. This is believed to be the first time that the diffusion constants and hence the diffusion currents have been limited by physical considerations when finding the numerical solution of drift-diffusion problems.

Calculations of Output Current

The current, being the externally measured quantity, is calculated from equation (3.7) as:

$$J = \frac{1}{(x_2 - x_1)} \int_{x_1}^{x_2} \left(J_n + J_p + \varepsilon \frac{\partial E}{\partial t} \right) dx \quad , \tag{4.14}$$

where x_1=0 and x_2=W are points for the device in figure 3.1. The third term in the integral is the displacement current. If the load resistance is neglected for the device in figure 3.1, the displacement term is zero due to the constant-voltage conditions between the ohmic contacts. For a real device this is not the case since a 50 Ω resistive load exists for the frequencies of interest here. However, to distinguish between internal and external PD nonlinear mechanisms, the load resistance will normally be excluded. Any additional nonlinearities caused by the load resistance will be discussed in Chapters V and VIII.

To achieve greater than 140 dB of dynamic range for computing PD harmonics, the current needs to be calculated with seven significant digits. The representation of a real number as an IEEE 32-bit (single precision) number is unsuitable since the number only has approximately seven significant digits and each numerical operation may reduce the precision. This level of accuracy therefore requires 64-bit computation.

A Linear Approximation for the Gaussian

The solution to the transport equations (eqns 3.2 to 3.4), in one-spatial-dimension requires a 1-D approximation for the Gaussian distribution of the generated carriers. If the problem was linear, the radius of the corresponding approximating 1-D function would not affect the calculated current, so long as the total incident power remains the same. The situation is more complicated for nonlinear problems. By approximating the Gaussian radial intensity (I) with a constant value out to some radius r_0, the approximating intensity near the center of the Gaussian is lower than the actual intensity while the approximating intensity at r_0 is greater than the actual intensity. If the approximating radius r_0 is too small, the device NL will be overestimated and *vice versa*.

Often the effective radius of the Gaussian is chosen[16] to be the e^{-2} radius as shown in figure 4.7. As can see from the figure, about the same amount of the Gaussian intensity is above the linear function as below. The choice of the e^{-2} approximating radius is derived from the effective area equation which is the square of the integral of the intensity divided by the integral of the intensity squared, both integrated from $r = 0$ to $r =$ infinity. For effects which are linearly related to the intensity, this is a good approximation, however the NL here are proportional to higher powers of the intensity, therefore requiring a smaller effective spot size.

For example, Raman processes, where the Raman gain is proportional to the electric field cubed ($I^{3/2}$), use the e^{-1} intensity spot size as the effective spot size.[17] This is shown in figure 4.8 where $I^{3/2}$ is plotted with

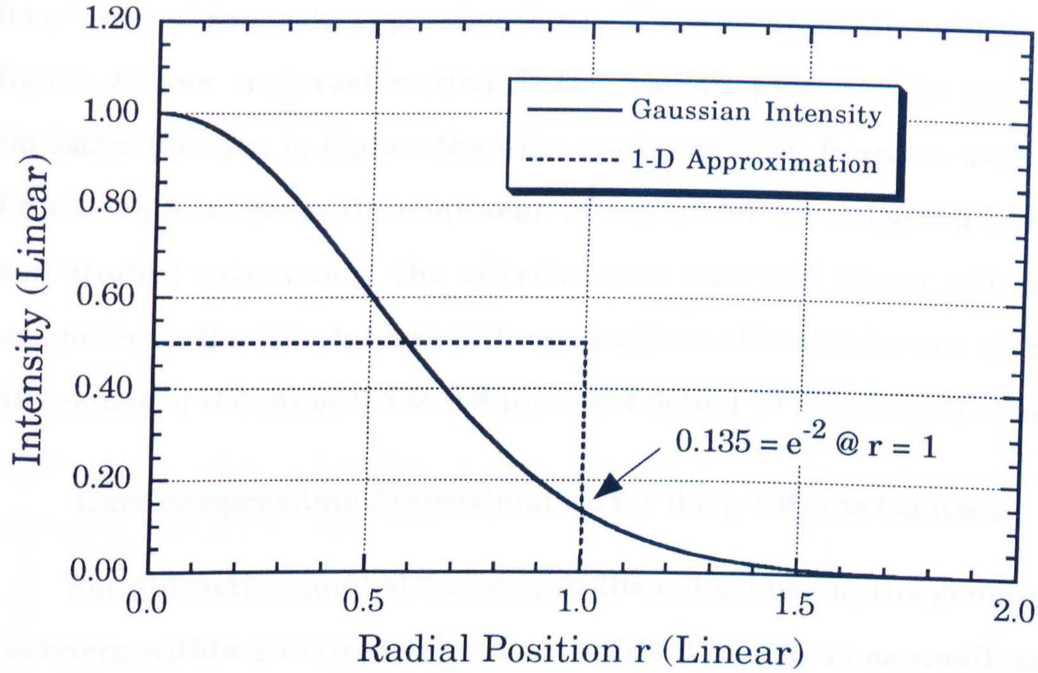

Figure 4.7 Intensity versus normalized radius for a Gaussian and the approximating 1-D function. Both functions yield the same total power.

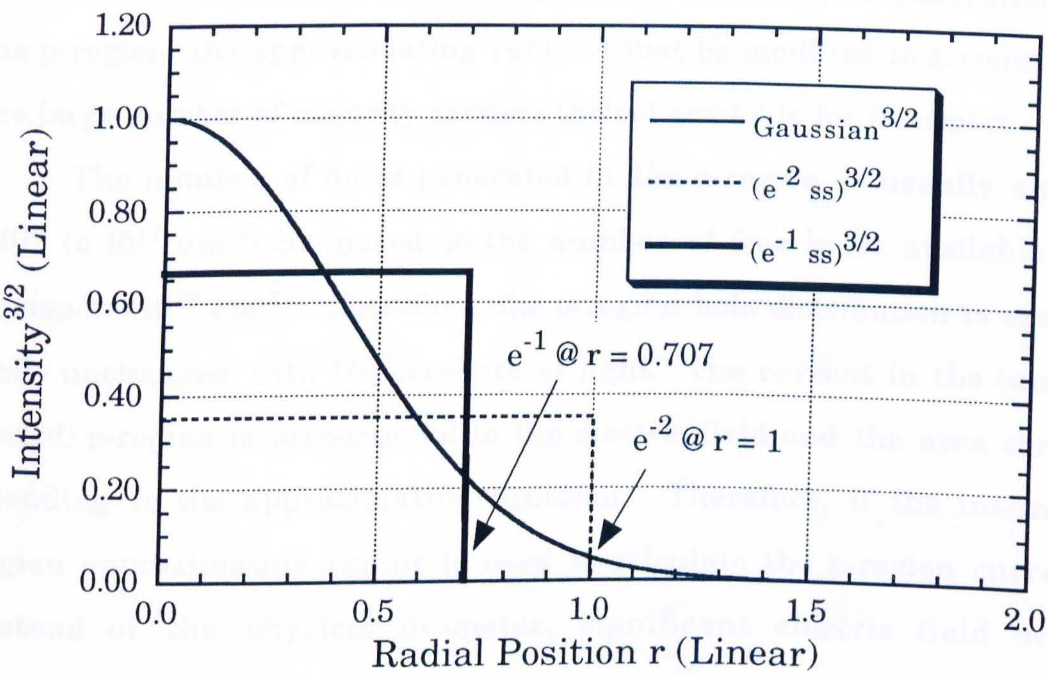

Figure 4.8 $\text{Intensity}^{3/2}$ versus radial position for a Gaussian and the e^{-2} and e^{-1} approximating functions.

the e^{-1} and e^{-2} intensity approximations. If the e^{-2} approximation is used (figure 4.8) an underestimation of the Raman gain results since the Gaussian function is higher than the approximating function over most of the e^{-2} radius. Since the nonlinear effects under investigation have not been studied extensively, the effective spot size will be an adjustable parameter in the simulations so long as reasonable results are obtained with values in the range 0.5 to 0.8 times the actual e^{-2} intensity spot size.

Carrier Spreading Approximation for the p-InGaAs Contact

For diffraction limited focusing of the optical beam, the generation of carriers within a PD may take place within dimensions as small as the wavelength. For generation in the intrinsic region, an approximation was made in the previous section for the radius of the generated carrier distribution based on the incident spot size. However, for generation in the p-region, the approximating radius must be modified to account for the large number of majority carriers (holes) available for transport.

The number of holes generated in the p-region is usually small (10^{16} to 10^{17} cm^{-3}) compared to the number of free holes available for transport (10^{19} cm^{-3}). Therefore, the p-region hole distribution is essentially unchanged with the presence of light. The current in the (undepleted) p-region is proportional to the electric field and the area corresponding to the approximating function. Therefore, if the intrinsic region approximating radius is used to calculate the p-region current instead of the physical diameter, significant electric field overestimations result. For example, let a 5-μm e^{-2} intensity optical beam be incident on a PD with a 1.0-μm long p-region having a 35 μm physical diameter. If an approximating radius of 3 μm (60%) is utilized throughout the 1.0 μm cap layer instead of the 35 μm physical diameter, the electric field and hence the series resistance in this region would be overestimated by 135 times (the ratio of the two areas). The over-estimated electric field will thus cause the p-region generated electrons (minority carriers) to have a velocity 135 times greater than their actual velocity. Therefore, to account for the large number of available holes in the p-region, an expansion function will be used to model the hole distribution just inside the p-i interface.

One approximating function is plotted in figure 4.9. The approximating diameter (see pg. 45) for the incident Gaussian beam is utilized for the beam diameter in the intrinsic region up to the edge of the depletion region. From the edge of the depletion region to the p-contact, where

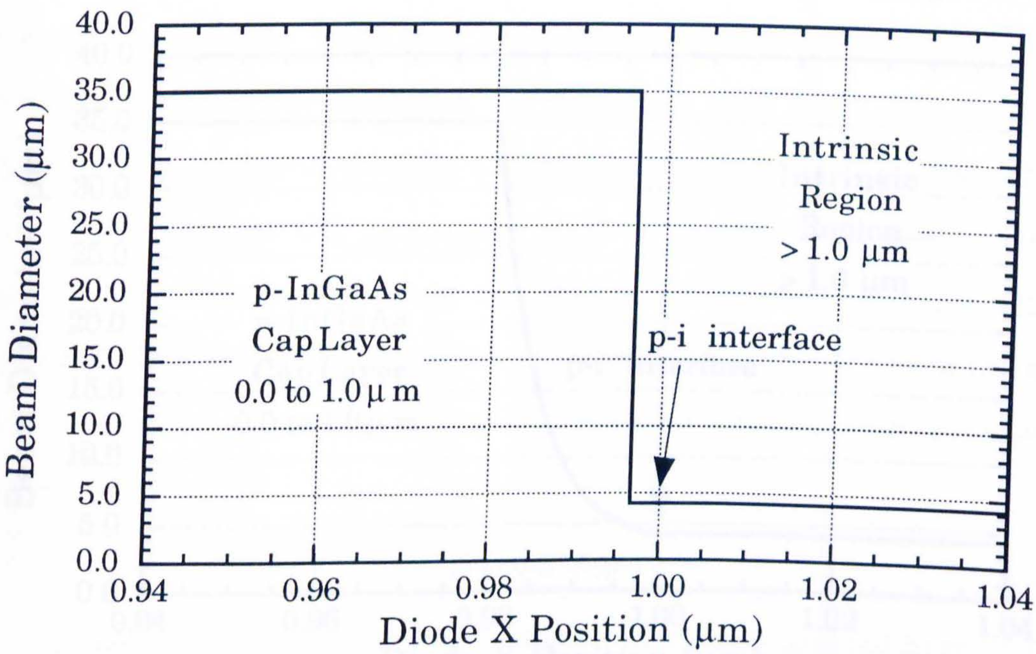

Figure 4.9 Beam diameter versus position for estimating the hole spreading in the p-region.

the injected hole density into the p-region is negligible compared to the majority carrier density, the approximating beam diameter is the physical diameter of the p-region. This function best describes the actual transport into the contact since the junction is abrupt (an assumption) resulting in a sharp transition between the depleted i-region and the undepleted p-region. However, the use of this beam diameter function leads to a large discontinuity in the calculated current between these two regions, even when bin widths of a few Angstroms are used.

When the beam diameter for holes was not allowed to change by more than 20% from bin to bin to minimize discontinuities, the error incurred in the calculated current (dc conditions) near the p-i interface was observed to fall below 2% in any particular bin. Figure 4.10 shows an example of this type of approximating function for a 35 μm diameter PD consisting of a 1.0 μm p-type cap layer. The holes traveling from the

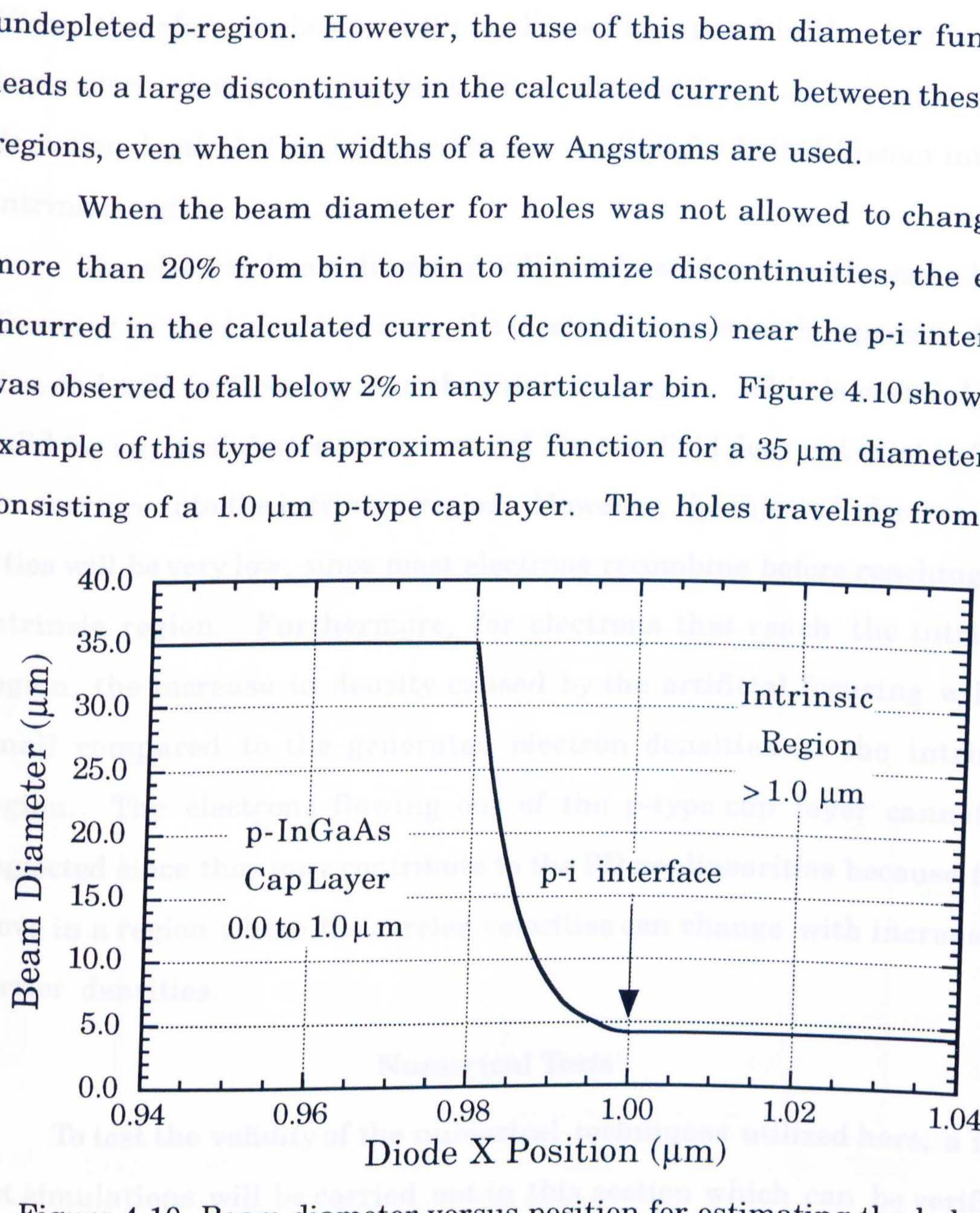

Figure 4.10 Beam diameter versus position for estimating the hole spreading in the p-region.

intrinsic region to the p-region are allowed to expand from their generated diameter, 4.2 μm for this example, to the 35 μm physical diameter. The electric field remains high just inside the p-i interface due to the depletion depth into the p-region, so little spreading is allowed from 1.0 to 0.995 μm. After 0.995 μm, the electric field quickly decreases to below 10 V/cm, therefore the beam width is allowed to expand in this region. The expansion takes place in about 5 nm, derived from an estimate of the depletion depth (1-2 nm) plus a few nm to allow for hole diffusion into the intrinsic region.

The electron beam diameter will be adjusted to have the same beam diameter as the holes; however, the electron travels in the opposite direction and will be focusing into the intrinsic region. This is certainly not valid for any real device since a radial electric field does not exist to focus the carriers into the intrinsic region. However, the injected electron densities will be very low, since most electrons recombine before reaching the intrinsic region. Furthermore, for electrons that reach the intrinsic region, the increase in density caused by the artificial focusing will be small compared to the generated electron densities in the intrinsic region. The electrons flowing out of the p-type cap layer cannot be neglected since they may contribute to the PD nonlinearities because they move in a region where the carrier velocities can change with increasing carrier densities.

Numerical Tests

To test the validity of the numerical techniques utilized here, a few test simulations will be carried out in this section which can be verified by easily obtained analytical results. The following results are obtained with the algorithm, written in FORTRAN, from a PD that will be modeled and studied extensively in the next two chapters, a mesa type p-i-n PD. The device consists of a 1.0-μm long p-GaInAs contact layer ($N_a \sim 7 \times 10^{18}$ cm^{-3}), a 0.95-μm long n-GaInAs intrinsic layer ($N_d \sim 5 \times 10^{15}$ cm^{-3}), and an n-InP buffer layer ($N_d \sim 2 \times 10^{17}$ cm^{-3}). Additional properties of this device can be found in Chapter VI.

For the first test, the PD will be reversed biased (all efficient p-i-n PDs are reversed biased) with -5 V and operated under dark (Gen = 0 and with no thermal generation) conditions. The total current should be very small through the device, governed only by the injected minority carrier density at the contacts which is quite small due to the high doping densities. Figure 4.11 shows the simulated PD carrier densities and electric field under the conditions where the diffusion from each ohmic contact of the device is observed along with a sudden change in the carrier densities near the edges of the intrinsic region due to the sudden increase in car-

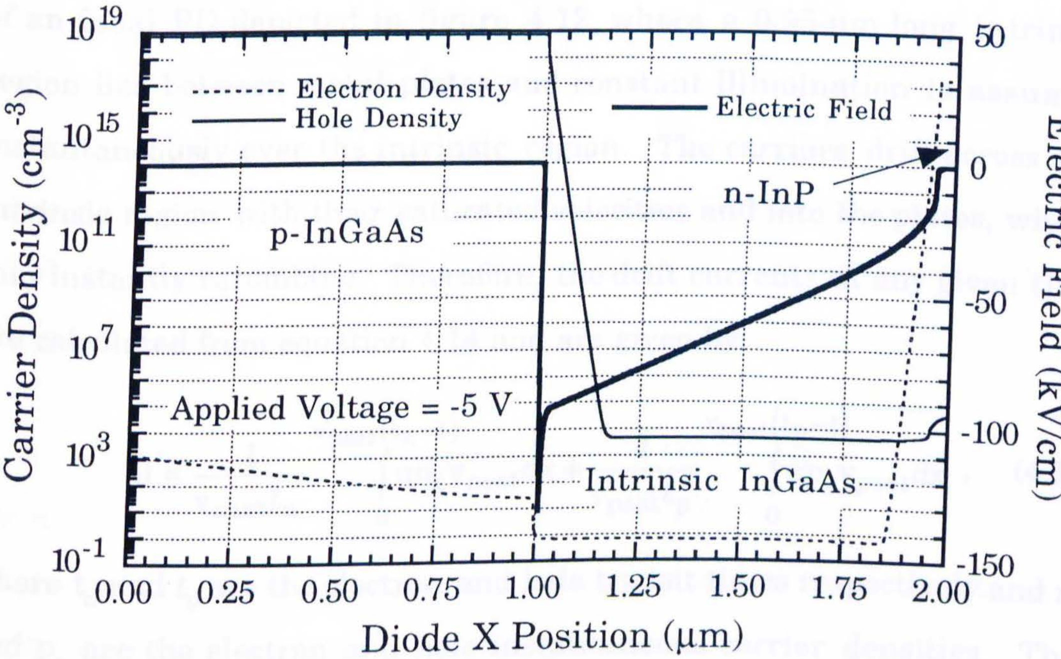

Figure 4.11 Carrier densities and electric field under dark conditions.

rier velocity from the high electric field.

The figure also shows the diffusion of carriers from their nominal values in the highly-doped layers into the depletion region as nearly straight lines (on a log scale) representing an exponential behavior of the carrier density near the edge of the depletion region. The figure also shows that the electric field rapidly increases near the edges of the intrinsic region and is approximately equal to zero in the contact layers. The slope of the electric field in the intrinsic region agrees with Gauss's Law where the change in the electric field is proportional to the ionized dopants in the intrinsic region having a density of 5×10^{15} cm^{-3}. The total current out of the modeled PD in figure 4.11 was less than 10^{-10} amps which demonstrates the degree of equality of the drift and diffusion current components near the edges of the depletion region.

In a second test, the ideal transit time response is used to check the algorithm output. The output can be compared to the analytical solution of an ideal PD depicted in figure 4.12, where a 0.95-μm long intrinsic region lies between metal plates and constant illumination is assumed instantaneously over the intrinsic region. The carriers drift across the intrinsic region with their saturated velocities and into the plates, where they instantly recombine. Therefore, the drift currents at any given time are calculated from equation 4.14 and are given by:

$$J = \frac{1}{v_{nsat} t_n} \int_0^{v_{nsat}(t_n - t)} q n_c v_{nsat} dx + \frac{1}{v_{psat} t_p} \int_0^{v_{psat}(t_p - t)} q p_c v_{psat} dx \;, \qquad (4.15)$$

where t_n and t_p are the electron and hole transit times respectively and n_c and p_c are the electron and hole instantaneous carrier densities. This reduces to the triangular responses shown in the first column of figure

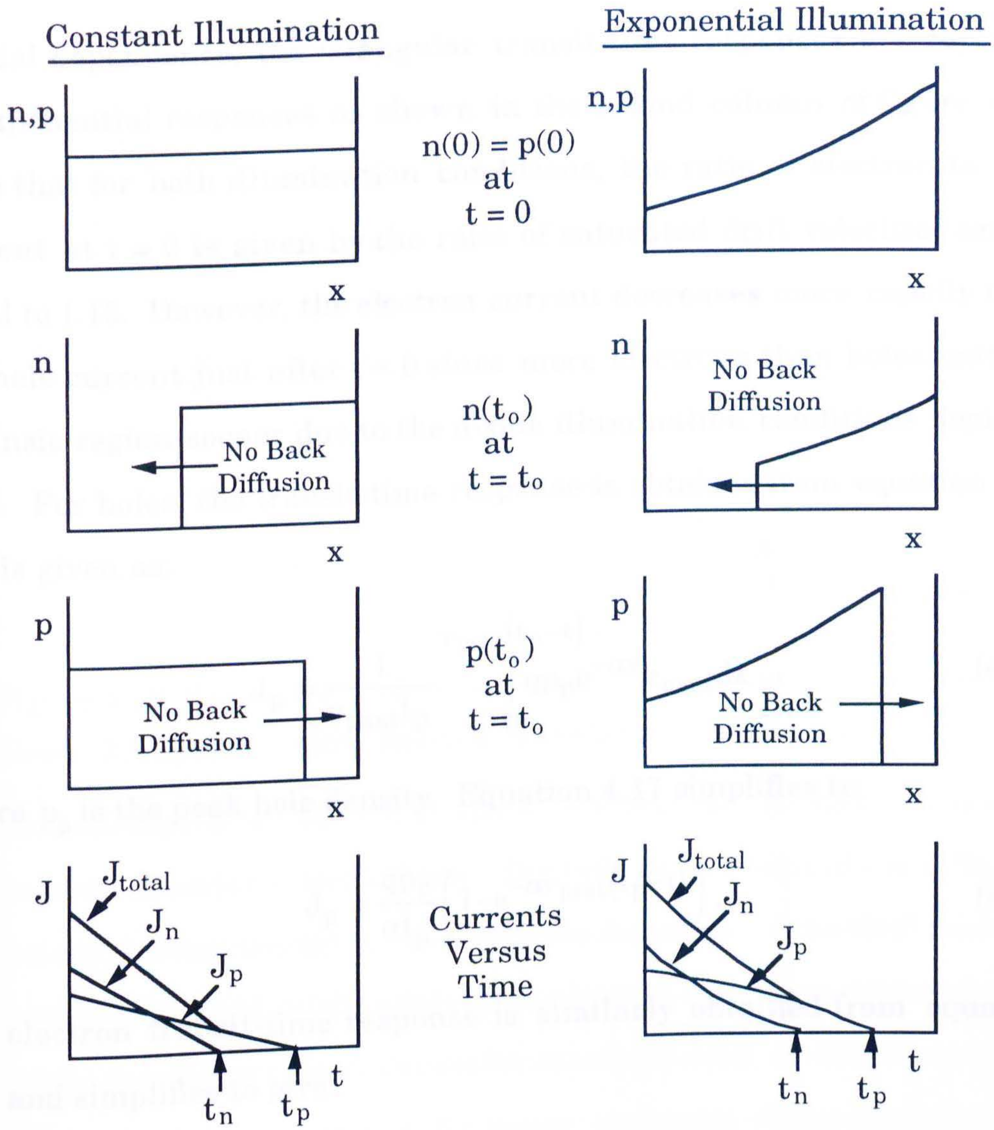

Figure 4.12 Carrier densities and transit time currents for constant and exponential illumination. In all cases, no carrier diffusion is assumed.

4.12 and expressed as:

$$J = \frac{qn_c v_{nsat}(t_n - t)}{t_n} + \frac{qp_c v_{psat}(t_p - t)}{t_p} \quad , \tag{4.16}$$

where the first term is the electron contribution and the second term is the hole contribution to the total current.

Since real devices absorb light and generate carriers with an exponential dependence, the triangular transit-time responses are replaced by exponential responses as shown in the second column of figure 4.12. Note that for both illumination conditions, the ratio of electron to hole current at t = 0 is given by the ratio of saturated drift velocities and is equal to 1.15. However, the electron current decreases more rapidly than the hole current just after t = 0 since more electrons than holes exit the intrinsic region sooner due to the n-side illumination conditions depicted here. For holes, the transit-time response is obtained from equation 4.14 and is given as:

$$J_p = \frac{1}{v_{psat} t_p} \int_0^{v_{psat}(t_p - t)} q p_p e^{-\alpha x} v_{psat} dx \quad , \tag{4.17}$$

where p_p is the peak hole density. Equation 4.17 simplifies to:

$$J_p = \frac{q p_p}{\alpha t_p} \left(1 - e^{-\alpha v_{psat}(t_p - t)} \right) . \tag{4.18}$$

The electron transit-time response is similarly obtained from equation 4.14 and simplifies to give:

$$J_n = \frac{q n_p}{\alpha t_n} \left(e^{-\alpha v_{nsat} t} - e^{-\alpha v_{nsat} t_n} \right) \quad , \tag{4.19}$$

where $n_p = p_p$ is the peak electron density. Equations 4.18 and 4.19 are plotted in the lower right hand curve of figure 4.12.

The simulated currents from the intrinsic region (that is the comparison of interest) of the PD under test are shown in figure 4.13 with the calculated results from equations 4.18 and 4.19. The model PD was pulsed from dark conditions at t = 0, with a flat pulse of light from t = 0 to t = 10^{-15} s. It can clearly be seen that the hole and electron currents follow

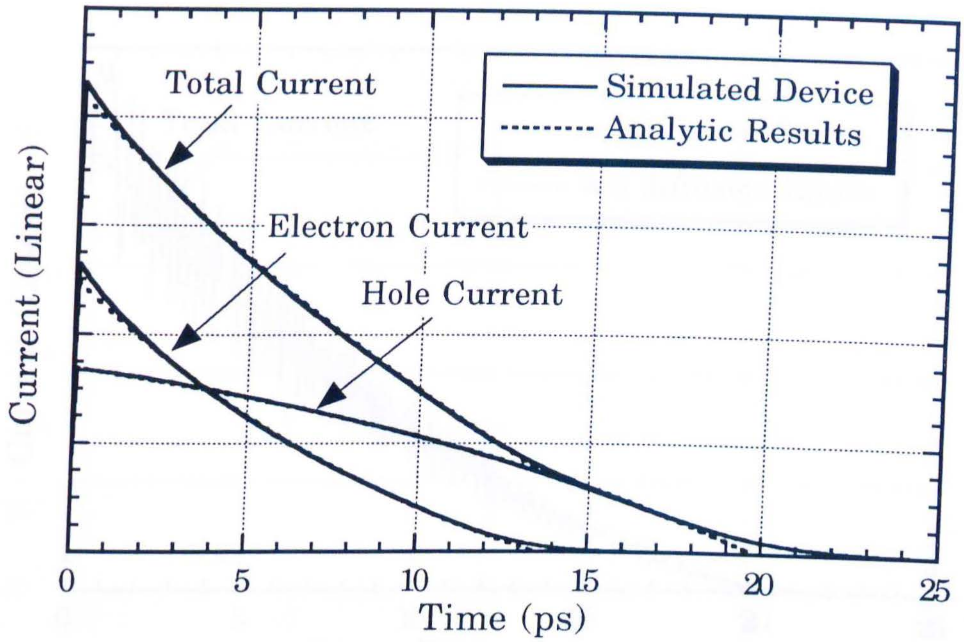

Figure 4.13 Simulated and analytical impulse response of the test diode. Analytical results based on equations 4.20 and 4.21.

the relationships of equation 4.18 and 4.19 except for the small tails near the respective carrier transit times. The tails are a result of the diffusion of carriers during transit in the opposite direction of the drift motion, which was neglected in the analysis leading to equations 4.18 and 4.19. The high density gradient causes a small portion of the carriers to remain in the intrinsic region for many multiples of the transit time, although the associated current is small compared to the total current. An example of the transit time response when the diffusion velocity limitations formulated here and in Chapter III are not implemented is plotted in figure 4.14. Although the overall shape of the transit time response is accurate, the noise due to the oscillating hole densities in the p-contact cause the current to oscillate.

To test the simulation under steady-state conditions, a constant photocarrier generation rate equivalent to 50 μA of average PD current is

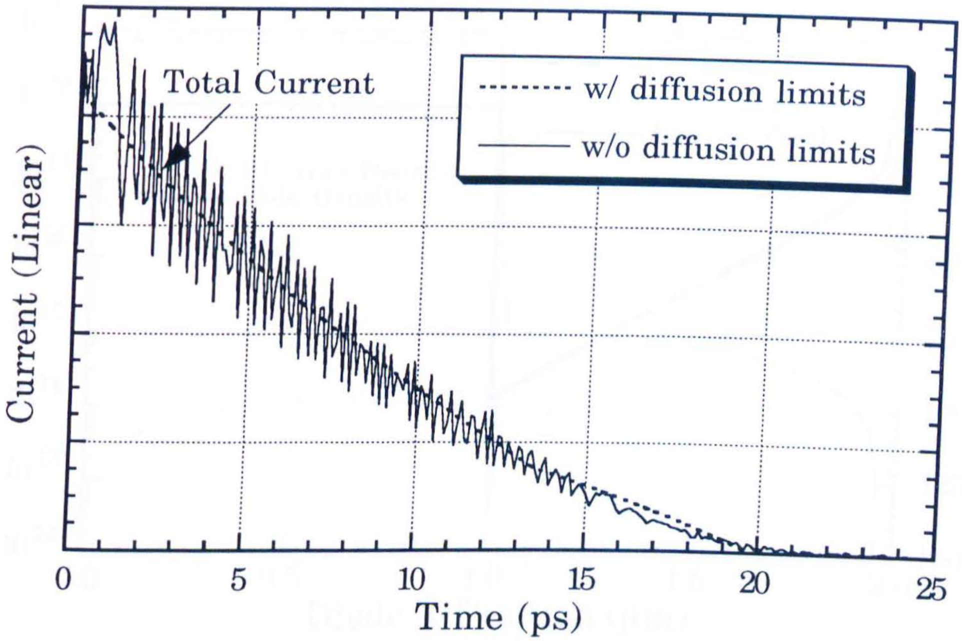

Figure 4.14 Simulated impulse response of the model PD. Modeled with and without restrictions on the carrier diffusion velocities.

used. The carrier densities and electric field are plotted in figure 4.15 and are computed until the total current reaches a steady-state (1 part in 10^6). Figure 4.15 shows the diffusion of electrons into the p-contact as well as a slight dip in the electron density just before the electrons enter the n-contact due to the increase in electron velocity at electric fields below 20 kV/cm. The hole density is higher near the p-InGaAs contact since holes flow to the left in the figure. The effect of the heterojunction is clearly seen at X = 1.95 μm for holes since here it was assumed that the hole could not travel over the 0.5 eV heterojunction barrier, hence a very low hole density for x greater than 1.95 μm.

Although the previous tests are not absolute proof that the numerical simulations are working properly, the ultimate test of the utility of the program will be the accuracy at which it provides results which agree

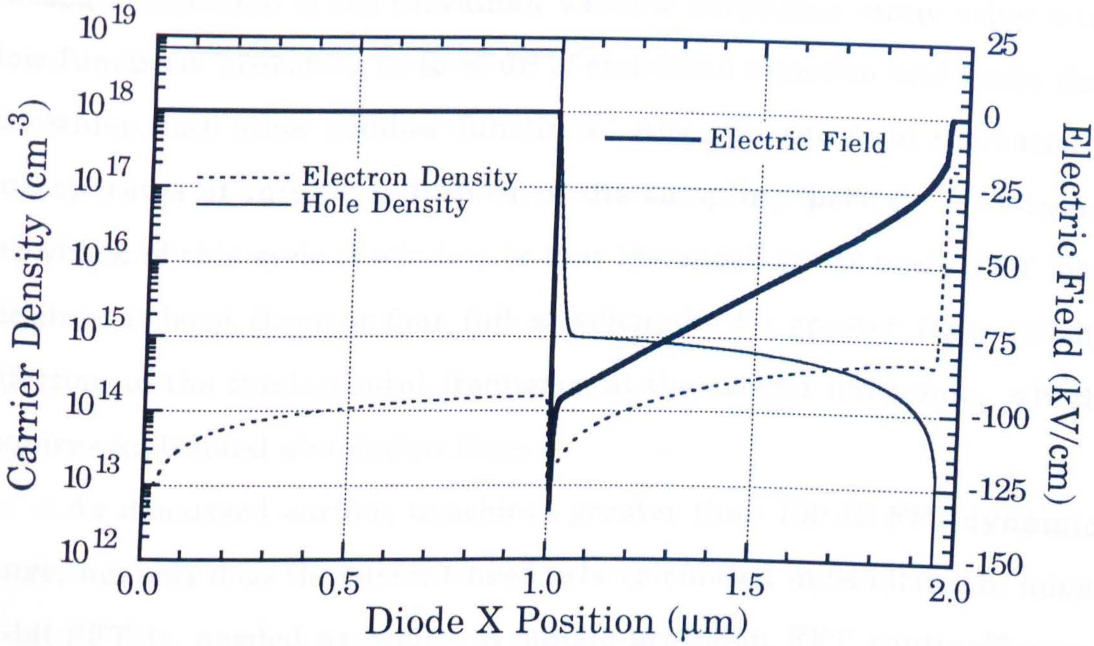

Figure 4.15 Carrier densities and electric field under steady-state conditions. Average PD current = 50 μA. Applied voltage = -5 V.

with the experiments of the next three chapters. Although some error is expected from the assumptions made here such as the carrier spreading in the p-contact, if results are in close agreement with experiment, alterations to the physical characteristics of the model PD will be made to investigate the origin(s) of PD nonlinearities.

To simulate PD nonlinearities at all voltages, the model diode is excited with a constant photocarrier generation function until the current reaches a steady state (1 part in 10^6) at which time a sinusoidal signal stimulates the device for a number of wavelengths. For Hanning or Hamming windows, only a single wavelength is necessary; however, these windows have very low off-peak rejection, resulting in false calculations of actual signal NL caused by leakage into the main lobe of the FFT filter. To ensure minimal leakage, a Blackman window[19] is used. The passband rejection of the Blackman window surpasses many other window functions providing 60 to 80 dB of stop-band rejection and nulls that are wider than other window functions. Also, the rejection increases if one operates at integer multiples of the sampling period. The main drawback of this style of window is that the width of the main FFT lobe requires at least three or four full wavelengths for greater than 100 dB rejection of the fundamental frequency at the second harmonic, which requires additional simulation time.

As discussed earlier, to achieve greater than 100 dB FFT dynamic range, not only does the current need to be calculated in 64 bit math, but a 64-bit FFT is needed as well. A single-precision FFT routine[20] was rewritten for double-precision use. Additionally, since no external capacitor circuit was included in the simulated diode, instantaneous changes in current creates aliasing from high frequency components in the simulated output, and so a digital pre-filter is required to ensure accurate FFT results. The FFT, windowing, and digital filter programs provide approximately 115, 125, and 133 dBc of second, third, and fourth harmonic dynamic range, respectively.

To accurately model these devices, as many diode bins as possible would be desirable; however, computation time considerations will limit the number of bins simulated. 384 bins were chosen since it is a multiple of 128 and 64 which allows efficient full-vector-length vectorization on the three vector computers used throughout this study, while yielding sufficient accuracy as will be evident from the results in Chapter V. The main computer utilized in this work, a Convex C-3820, has a vector length of 128 and offers 125 MFlops peak per-processor double precision

(IEEE 64 bit) performance. Highly vectorized and efficient algorithms achieve almost 50% efficiency on vector machines; this algorithm obtained an estimated 40% efficiency (50 MFlops). Some computing time was also obtained on two other vector computers both of which have vector lengths of 64. For this algorithm, a Cray YMP-EL yielded 10 - 15 MFlops of 64-bit performance, and a Cray YMP-C90 yielded 100 - 150 MFlops of 64-bit performance with this algorithm, both about 40-45% of their peak per-processor performances. Several scaler personal computers were tested for their throughput with this algorithm and it was found that the Macintosh Quadra 950 (33 MHz Motorola 68040) and an IBM clone (50 MHz Intel 486) both achieved about 1.5 MFlops of performance. The program requires approximately 1 hour of CPU time per 4 ns (384 bins) of simulation time on a 10 MFlop throughput machine. An estimation of the computer time required to calculate the harmonic content versus average PD current for five different currents at a fundamental frequency of 1 GHz, requires about six to eight full wavelengths of time output to achieve greater than 100 dB FFT dynamic range. Eight wavelengths multiplied by five power levels equals 40 ns of simulation time or about 10 hours of CPU time on a 10 MFlop machine or equivalently 67 hours on a 50 MHz Intel 486 machine. The total number of floating point operations (MFlops) used throughout this study for program debugging and production simulations equates to approximately 360,000,000 MFlops. This is equivalent to 99 years of computer time on a Digital Equipment VAX 11/780 (1980) and 569 years of computer time on a IBM 8 MHz 286 (1985).

1. M. Dentan and B. de Cremoux, "Numerical Simulation of the Nonlinear Response of a p-i-n Photodiode Under High Illumination," *J. of Lightwave Tech.*, **JLT-8**, p. 1137, 1990.
2. R. Sabella and S. Merli, "Analysis of InGaAs p-i-n Photodiode Frequency Response," *IEEE J. of Quantum Elec.*, **JQE-29**, p. 906, 1993.
3. J.M. Zhang and D.R. Conn, "State-Space Modeling of the PIN Photodetector," *J. of Lightwave Tech.*, **JLT-10**, p. 603, 1992.
4. U. Ascher, *et al.*, "Conditioning of the Steady State Semiconductor Device Problem," *SIAM J. of Applied Math.*, **49**, p. 165, 1989.
5. O. Heinreichsberger, *et al.*, "Fast Iterative Solution of Carrier Continuity Equations for Three-Dimensional Device Simulation," *SIAM J. of Sci. Stat. Comput.*, **13**, p. 289, 1992.
6. H.K. Gummel, "A Self-Consistent Iterative Scheme for One-Dimensional Steady State Transistor Calculations," *IEEE Trans. on Electron Devices*, , **ED-11**, p. 455, 1964.
7. A. Yoshii, *et al.*, "Investigation of Numerical Algorithms in Semiconductor Device Simulation," *Solid State Elec.*, **30**, p. 813, 1987.
8. C.S. Rafferty, *et al.*, "Iterative Methods in Semiconductor Device Simulation," *IEEE Trans. on Electron Devices*, **ED-32**, p. 2018, 1985.
9. R.E. Bank, *et al.*, "Numerical Methods for Semiconductor Device Simulation," *IEEE Trans. on Electron Devices*, **ED-30**, p. 1031, 1983.
10. L.B. Rall, "Computational Solution of Nonlinear Operator Equations," Krieger Publishing, Huntington, NY, 1979.
11. K.W. Boer, "High-Field Carrier Transport in Inhomogeneous Semiconductors," *Ann. der Physik*, p. 371, 1985.

12. K.W. Boer, "Survey of Semiconductor Physics," Van Nostrand Reinhold, New York, Volume I, 1990.

13. S. Dushman, *Rev. Modern Physics*, **2**, p. 381, 1930.

14. H. Yi, *et al.*, "Novel Method to Control Numerical Solution Oscillation of Diffusion-Drift Equation," *Electron. Lett.*, **26**, p. 1487, 1990.

15. S.J. Polak, *et al.*, "Semiconductor Device Modeling from the Numerical Point of View," *Intl. J. for Numerical Methods in Eng.*, **24**, p. 763, 1987.

16. A. Yariv, "Optical Electronics," Holt, Rinehart and Winston, 1985.

17. R.H. Stolen and E.P. Ippen, "Raman Gain in Glass Optical Waveguides," *Appl. Physics Lett.*, **22**, p. 276, 1973.

18. R.B. Adler, *et al.*, "Introduction to Semiconductor Physics," John Wiley and Sons, pp. 173-180, 1964.

19. H. Baher, "Analog and Digital Signal Processing," John Wiley and Sons, 1990.

20. W.H. Press, *et al.*, "Numerical Recipes The Art of Scientific Computing," Cambridge University Press, pp. 397-407, 1989.

V. DETERMINATION OF DOMINANT NONLINEAR MECHANISMS

Introduction

In this chapter, p-i-n photodiode (PD) nonlinearities (NL) are investigated to determine the dominant nonlinear mechanisms for various regions of applied PD voltage and frequency. The basic device structure under investigation in this chapter is a single-heterostructure[1] mesa-type device with a 0.95-μm long intrinsic region. This chapter will only analyze a subset of the measurement and simulation data obtained on this device to study the basic nonlinear behavior of p-i-n PDs. Additional information for this device can be found in Chapter VI.

Determination of the device parameters which dictate PD NL is an immense problem due to the numerous mechanisms (Chapter III) which result in nonlinear behavior. However, significant insight into PD NL can be obtained from the vast amount of available measurement data of PD harmonic distortion by dissection versus applied voltage and frequency. For example, figures 5.1, 5.2, 5.3, and 5.4 show the NL of the PD operating at 1 mA of average PD current with a modulation depth of 100% at frequencies of 100 MHz, 1 GHz, 5 GHz, and 10 GHz, respectively, where several trends are observed:

1) Above a given applied voltage, which depends on frequency, the NL content is nearly independent of voltage.

2) The minimum value of the second harmonic (-92, -88, -87 , and -92 dBm at 100 MHz, 1 GHz, 5 GHz, and 10 GHz, respectively) at high applied voltages is nearly independent of frequency.

3) The trends of the third and fourth harmonics at higher applied volt-

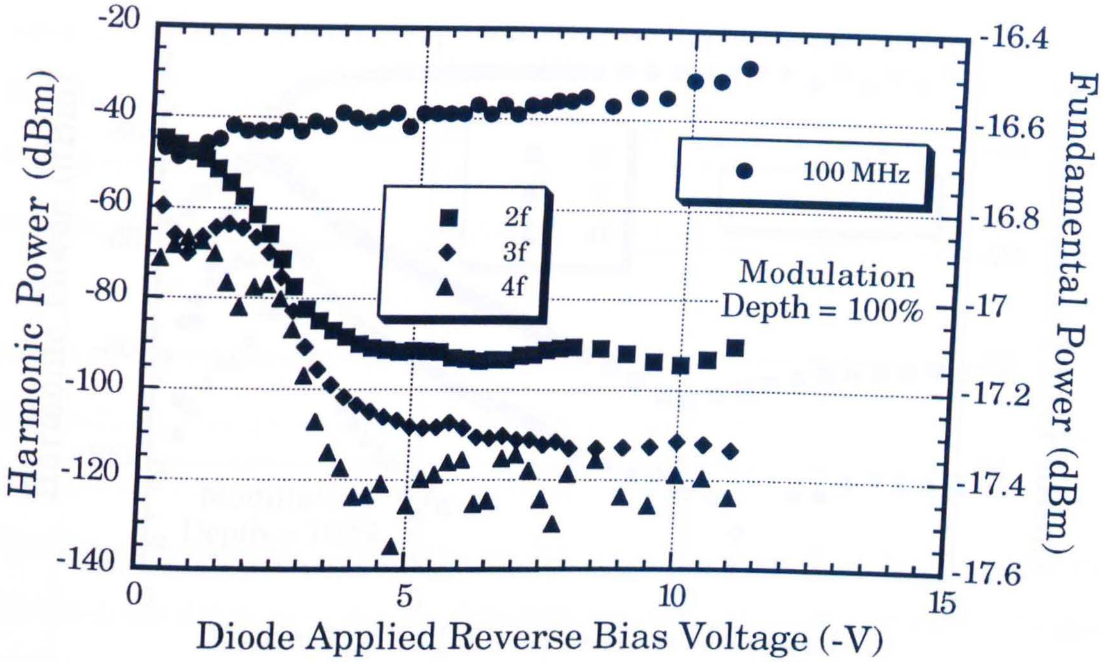

Figure 5.1 Measured fundamental and harmonic power versus detector applied reverse bias voltage at 100 MHz. Fiber pigtailed. Average detector current = 1 mA.

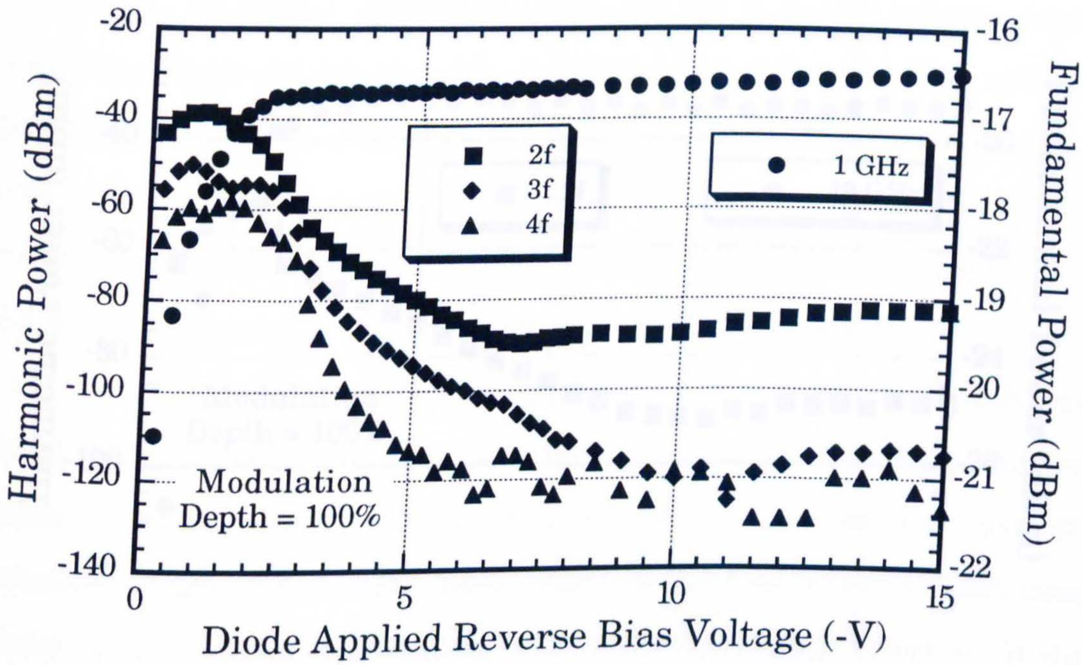

Figure 5.2 Measured fundamental and harmonic power versus detector applied reverse bias voltage at 1 GHz. Fiber pigtailed. Average detector current = 1 mA.

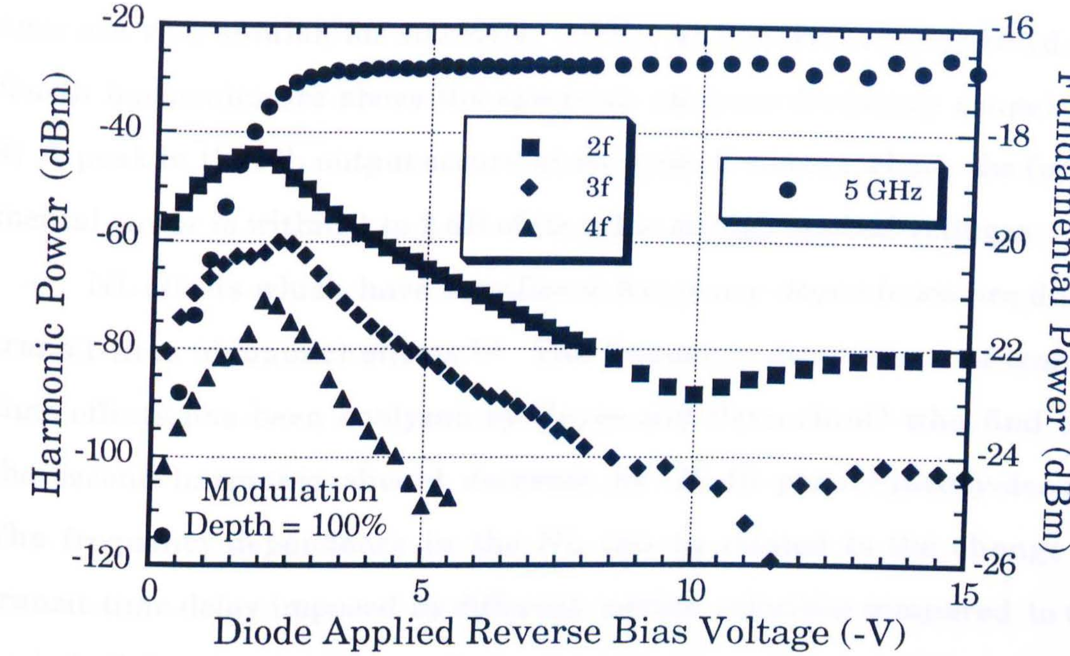

Figure 5.3 Measured fundamental and harmonic power versus detector applied reverse bias voltage at 5 GHz. Fiber pigtailed. Average detector current = 1 mA.

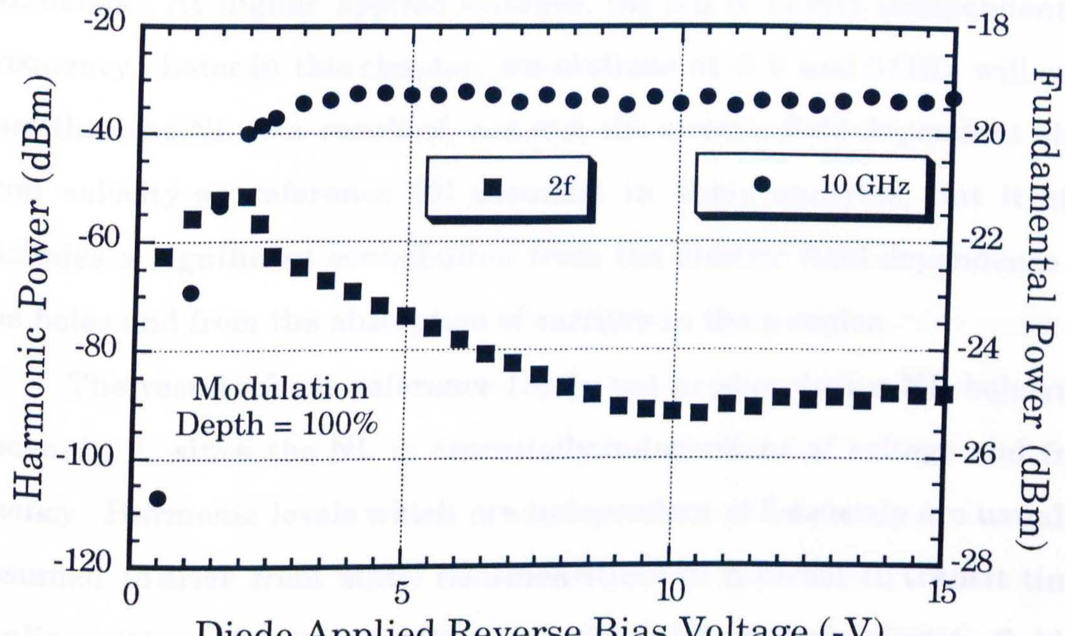

Figure 5.4 Measured fundamental and harmonic power versus detector applied reverse bias voltage at 10 GHz. Fiber pigtailed. Average detector current = 1 mA.

ages are very similar for 100 MHz, 1 GHz, and 5 GHz (10 GHz third and fourth harmonics are above the spectrum analyzer frequency range).

4) A peak in the NL output occurs at an applied voltage where the fundamental power is within 1 to 2 dB of its value at high applied voltages.

NL effects which have significant frequency dependence are due to transit-time (dynamic) effects.[2,3] The frequency dependence of transit-time effects has been analyzed by Hayes and Persechini[3] who find that the second harmonic should decrease by -20 dB per-frequency-decade. The frequency dependence in the NL can be related to the change in transit-time delay imposed by different carrier velocities compared to the period of the signal. The analysis presented in reference [3] accurately describes the PD NL data in figures 5.1 to 5.4 only in the region of applied voltages from -3 to -5 V, where significant frequency dependence in the NL exists. At higher applied voltages, the NL is nearly independent of frequency. Later in this chapter, simulations at -5 V and 5 GHz will suggest that the NL is a result of, not just the electric-field-dependent electron velocity as reference [3] assumes in their analysis, but it also includes a significant contribution from the electric field dependence of the holes and from the absorption of carriers in the p-region.

The results from reference [3] do not predict device NL behavior above -10 V, since the NL is essentially independent of voltage and frequency. Harmonic levels which are independent of frequency are usually assumed to arise from static nonlinearities[3] in contrast to transit time nonlinearities. An investigation into these NL at high electric fields, which dominate practical systems will be analyzed in this chapter to determine their true origin.

The "window" provided by the voltage and frequency dependence of the nonlinearities will be used to examine and separate the various nonlinear mechanisms. For the purposes here, the nonlinearities at 1 and 5 GHz will be simulated at applied voltages of -5, -10 and -15 V. At -5 V, the second harmonic of both frequencies is decreasing with increasing (negative) voltage. At -10 V, the second harmonic of 1 GHz has been at its minimum for several Volts and the second harmonic of 5 GHz has just reached the transition between the decreasing portion of the curve and the region where the second harmonic remains unchanged. At -15 V, the second harmonic of both frequencies have been at their respective minimums for several Volts. The following study will begin by fitting the modeled PD NL to the measurement data at -5 V. After good agreement is obtained, the various nonlinear mechanisms will be altered or removed to determine which mechanism(s) dictate PD nonlinear behavior. The study will continue at -10 and -15 V to describe the behavior observed in the data from figures 4.1 to 4.4.

Five Volt Measurements and Simulations

To study the dependence of the generated harmonics with incident optical power, the phase-locked lasers in figure 2.1 are adjusted such that they have equal amplitude and that their polarizations are aligned to yield a 100% modulation depth. Since the lasers do not generate frequencies at multiples (harmonics) of the fundamental frequency f, the measurement of the PD nonlinearities is obtained by simply measuring the harmonic power at the frequencies 2f, 3f, and etc. Measurements of the second and third harmonics are usually enough for most systems applications and the intermodulation products can, in some instances, be derived from the third harmonic. Measuring and simulating terms up to order four will increase our confidence in the third harmonic results.

The measurement data for the 0.95 μm device at frequencies of 1 and 5 GHz are plotted in figures 5.5 and 5.6, respectively. The modulation depth is 100%, the applied voltage is -5 V, and the device is fiber pigtailed, so the estimated e^{-2} incident spot size is 10 μm. From figures 5.5 and 5.6, two main tendencies for this device are observed. For a given average optical power (or, equivalently, average current), the harmonic power increases as the frequency increases. For example, at 1 mA, the second harmonic increases from -80 dBm to -65 dBm as the frequency increases from 1 GHz to 5 GHz. The second tendency is the deviation from power-law growth of the harmonic power as the average PD current

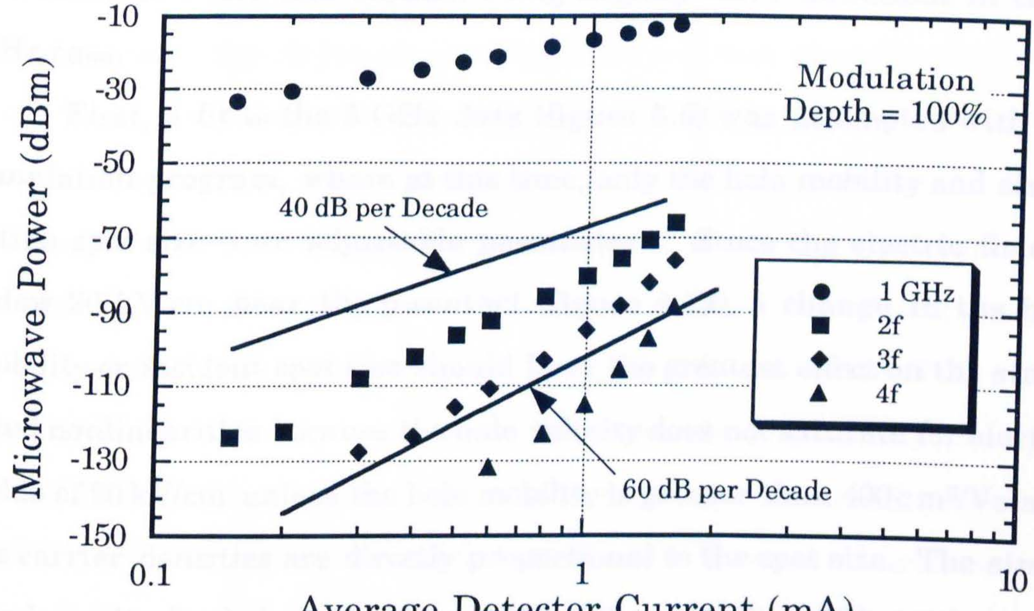

Figure 5.5 Measured fundamental and harmonic power versus average detector current at 1 GHz. Applied voltage = -5 V. Fiber pigtailed. 40 dB and 60 dB per decade tendancies included.

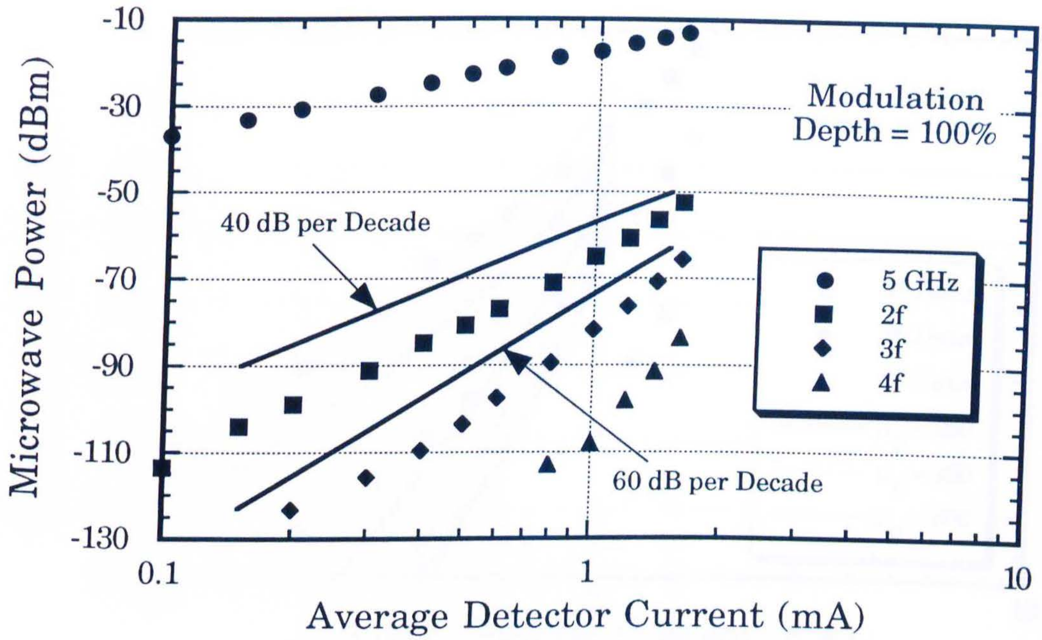

Figure 5.6 Measured fundamental and harmonic power versus average detector current at 5 GHz. Applied voltage = -5 V. Fiber pigtailed. 40 and 60 dB per decade tendancies included.

increases to 1 mA and beyond, being slightly more noticeable in the 1 GHz case.

First, a fit to the 5 GHz data (figure 5.6) was attempted with the simulation program, where at this time, only the hole mobility and simulation spot size were adjustable parameters. Since the electric field is below 20 kV/cm near the n-contact (figure 4.13), a change in the hole mobility or incident spot size should have the greatest effect on the simulated nonlinearities because the hole velocity does not saturate for electric fields of 20 kV/cm unless the hole mobility is greater than 400 cm^2/Vs and the carrier densities are directly proportional to the spot size. The simulated results for hole mobilities of 200, 230, and 260 cm^2/Vs with a spot size of 5.0 μm is shown in figure 5.7. The simulated data shows that while the second harmonic data is slightly underestimated, the third and

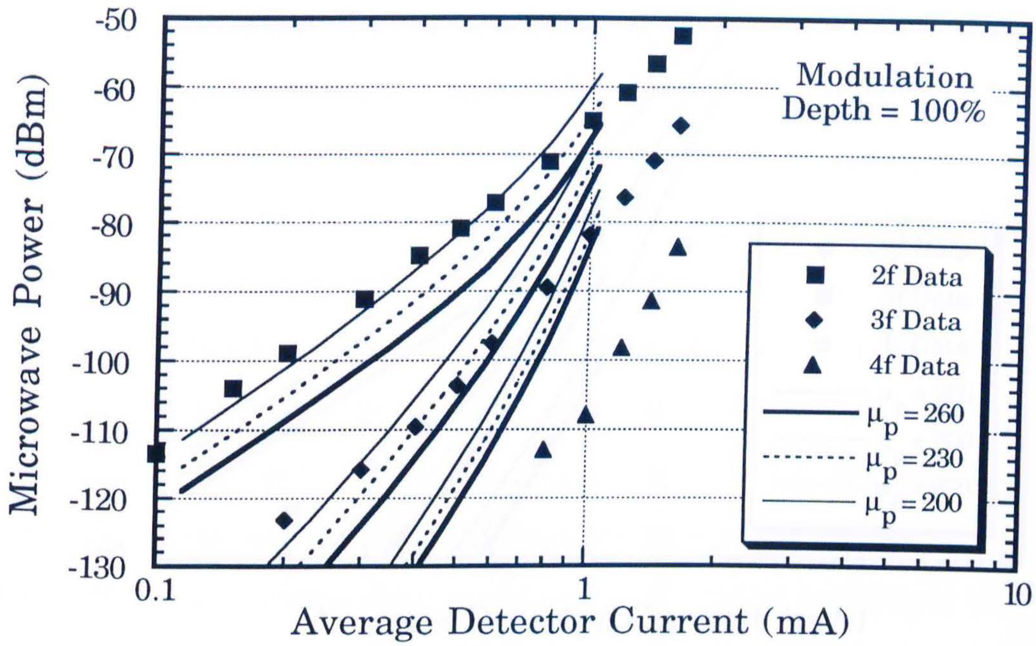

Figure 5.7 Measured and simulated harmonic power at 5 GHz. Simulated spot size = 5 μm with hole mobilities of 200, 230, and 260 cm^2/Vs. Measurement data from figure 5.6.

fourth harmonics are overestimated. Figure 5.8 plots the simulation results with a slightly larger spot size of 6.0 μm with the same three hole mobilities. Note that now, the second and third harmonics are slightly underestimated and the fourth harmonic is still overestimated. From the trends of figures 5.7 and 5.8, increasing the spot size to 7.0 μm and decreasing the hole mobility should yield better fits to the measured data. The simulated data for hole mobilities of 100, 150, and 200 cm^2/Vs with a spot size of 7.0 μm is shown in figure 5.9. Here the simulated data for the second and third harmonics, with a hole mobility of 150 cm^2/Vs, fits quite well to the experimental data, while the fourth harmonic is still slightly overestimated. Although the best fit hole mobility is about 1/2 that of a measured sample[4] of InGaAs, it is not so unrealistic, since measured values of electron mobility[4] for InGaAs also vary by 50% depending on the

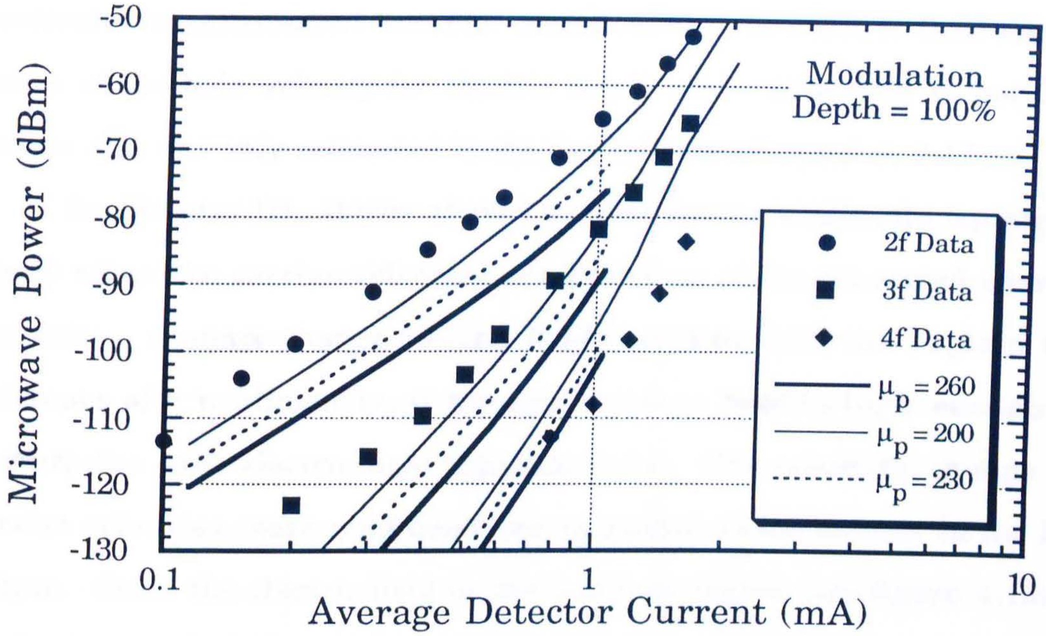

Figure 5.8 Measured and simulated harmonic power at 5 GHz. Simulated spot size = 6 μm with hole mobilities of 200, 230, and 260 cm^2/Vs. Measurement data from figure 5.6.

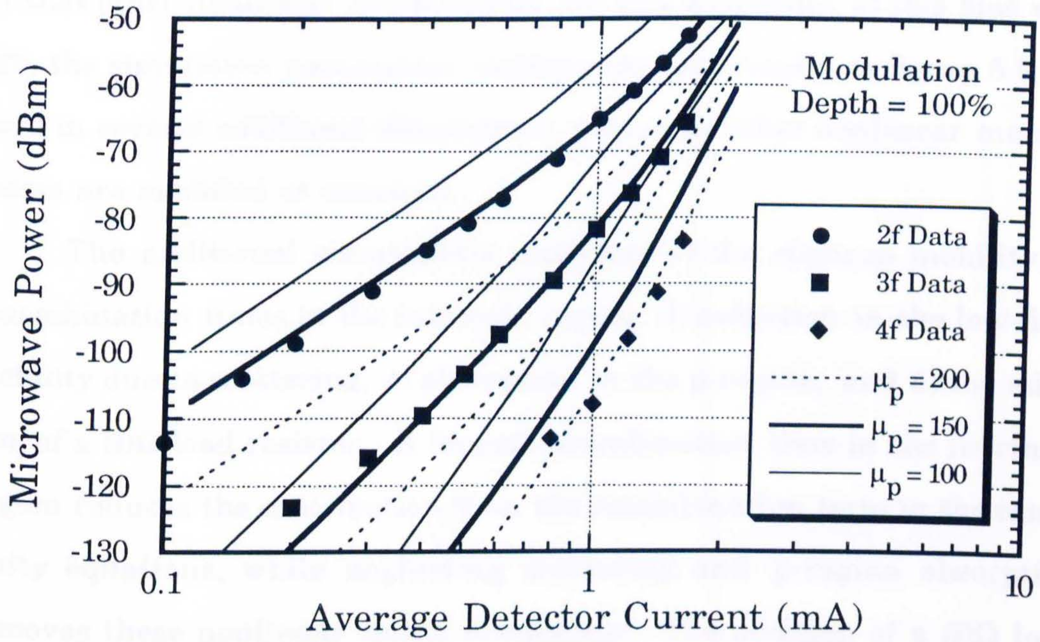

Figure 5.9 Measured and simulated harmonic power at 5 GHz. Simulated spot size = 7 μm with hole mobilities of 100, 150, and 200 cm^2/Vs. Measurement data from figure 5.6.

particular measurement sample. Additionally, the electric field dependence of the hole velocity for electric fields below 50 kV/cm is not well known and was only estimated in the formulation of equation 3.17.

In Chapter III, it was shown that nonlinear continuity equations result when the carrier velocities are functions of the generated carrier densities. A space-charge electric field (equation 3.35) can explain the existence of a nonlinearity, if the space-charge field is high enough to perturb the dark electric field (equation 3.34). The resulting change in carrier velocities cause nonlinearities measured as harmonics in the PD output. Since the electric field in the intrinsic region (see figure 4.13) is not high enough (10 to 20 kV/cm with -5 V applied voltage) to saturate the hole or electron velocities near the n-contact, a photogenerated space-charge electric field will cause a change in the carrier velocities. To verify that other nonlinear mechanisms are less important at this bias voltage, the simulation parameters yielding the best results in figure 5.9 are used in several additional simulations where the other nonlinear mechanisms are modified or removed.

The additional simulations consider: 1) the electron mobility, 2) recombination times in the intrinsic region, 3) reduction in the low-field mobility due to scattering, 4) absorption in the p-region, and 5) the addition of a 50Ω load resistor. A longer recombination time in the intrinsic region reduces the contribution from the recombination term in the continuity equations, while neglecting scattering and p-region absorption removes these nonlinear terms completely. The addition of a 50Ω load resistor will add to the NL by lowering the applied potential due to current flow through the load resistance. This modifies the internal electric field and hence the carrier velocities. A change in the electron mobility should not cause a change in the NL, even though the electron may contribute significantly to the overall NL, since the velocity dependence versus electric field above 20 kV/cm is a weak function of the electron mobility as can be seen in figure 3.3.

The simulation parameters for the best-fit results of figure 5.9 are utilized with the above five modifications. The nonlinear mechanisms are changed one at a time to compare their relative contributions to the total device NL, with the results plotted in figure 5.10. The simulation results in figure 5.10 were obtained by reducing the electron mobility 40% to 6,000 cm^2/Vs, neglecting mobility reduction (scattering), neglecting absorption in the p-region, increasing the recombination time in the intrinsic region from 2 ns to 2 μs, and adding a 50Ω load resistance to the

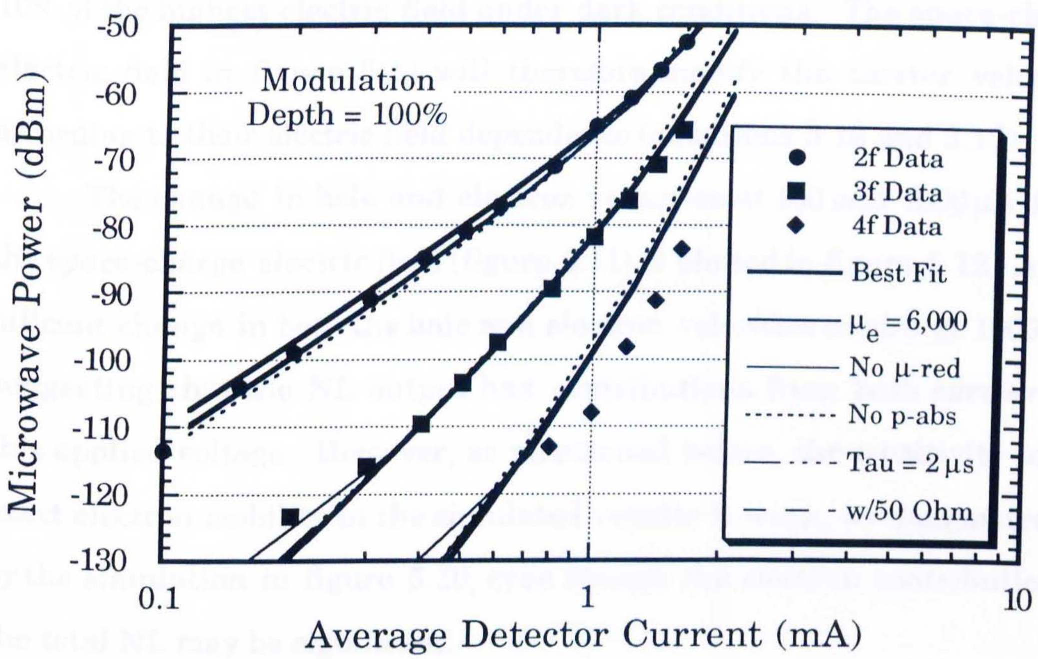

Figure 5.10 Harmonic power at 5 GHz. Best-fit simulation modified with $\mu_e = 6{,}000\ cm^2/Vs$, increasing the i-region recombination time, omitting scattering and p-region absorption, and adding a 50 Ohm load.

PD output circuit. As can be seen, little change in the simulated NL results from varying these additional nonlinear mechanisms. Therefore, we conclude that the NL is most sensitive to the hole mobility and the spot size at this particular applied bias.

In Chapter III the NL was assumed to arrive from the existence of a space-charge electric field causing a carrier density dependence in the carrier velocities. To obtain the relative size of the space-charge electric field compared to the dark electric field, the simulated diode was illuminated with a constant level of light equivalent to 0, 100, and 1000 μA of current with a constant spot size of 7.0 μm. The space-charge electric fields at 100 and 1000 μA are simply the difference between the electric field at 0 μA and their respective high-current electric fields. These resulting space-charge fields (figure 5.11) can be significant, as much as 10% of the highest electric field under dark conditions. The space-charge electric field in figure 5.11 will therefore modify the carrier velocities according to their electric field dependence (equations 3.16 and 3.17).

The change in hole and electron velocities at 100 and 1000 μA from the space-charge electric field (figure 5.11) is plotted in figure 5.12. A significant change in both the hole and electron velocities occurs at 1000 μA, suggesting that the NL output has contributions from both carriers at this applied voltage. However, as mentioned before, the sensitivity to the exact electron mobility in the simulated results is weak, as demonstrated by the simulation in figure 5.10, even though the electron contribution to the total NL may be significant.

Previous work[2] has speculated that the load resistance may be the main contributor to the overall NL however, the results in figure 5.10

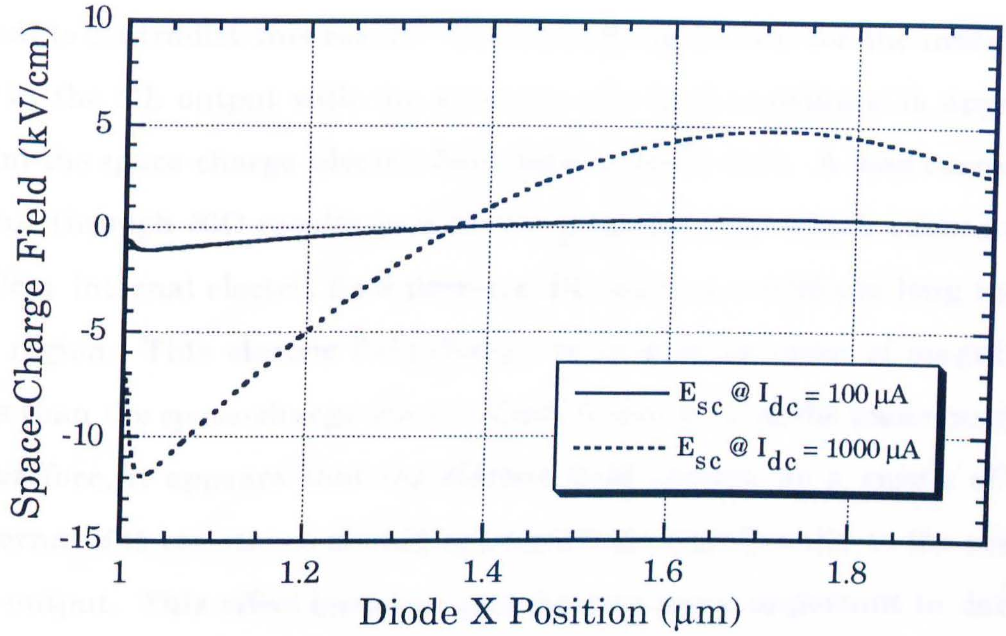

Figure 5.11 The space-charge electric field in the intrinsic region due to the photogenerated carriers. Spot size = 7.0 μm. Applied voltage = -5 V. μ_p = 150 cm^2/Vs. μ_n = 10,000 cm^2/Vs.

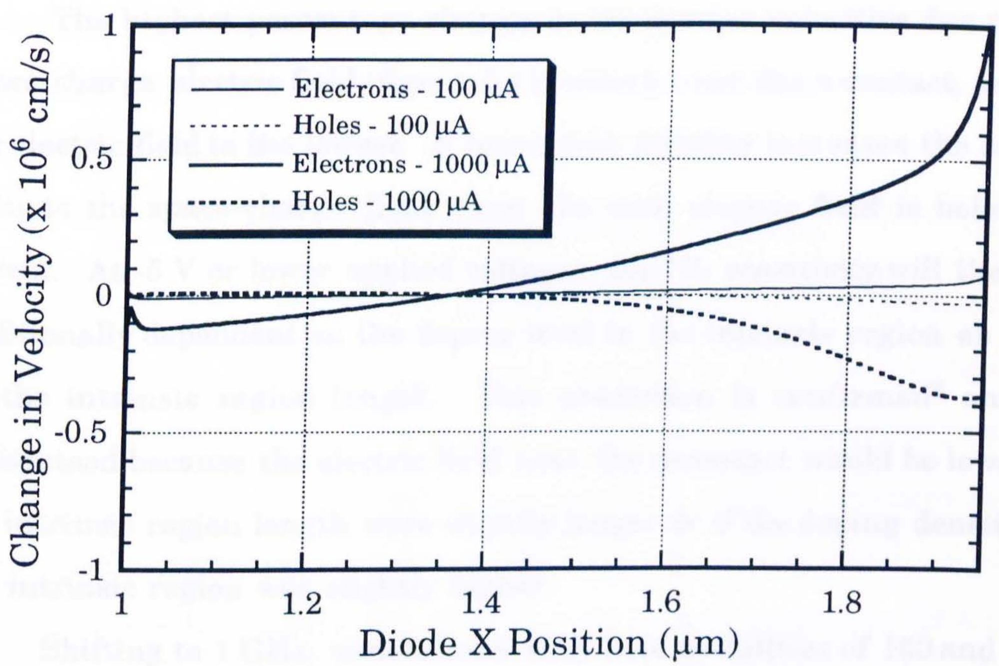

Figure 5.12 The change in carrier velocities in the intrinsic region due to the space-charge fields in figure 5.11. Spot size = 7.0 μm. Applied voltage = -5 V. μ_p = 150 cm^2/Vs. μ_n = 10,000 cm^2/Vs.

seem to contradict this result. The underlying reason for the insensitivity in the NL output with the presence of a load resistance is apparent from the space-charge electric field data in figure 5.11. A load current of 1 mA through 50Ω results in a 50 mV potential drop which causes a 0.5 kV/cm internal electric field decrease throughout a 0.95-μm long intrinsic region. This electric field change is at least an order of magnitude less than the space-charge electric field (figure 5.11) at the same current. Therefore, it appears that the electric field change as a result of and external 50Ω resistance should not contribute significantly to the overall NL output. This effect however, may become more important in devices with 0.1 to 0.2 μm intrinsic region lengths or larger incident spot sizes because, for the same load current, the internal electric field change is inversely proportional to the length and independent of spot size.

The highest percentage change in the carrier velocities due to the space-charge electric field (figure 5.11) occurs near the n-contact, where the electric field is the lowest. A lower hole mobility increases the sensitivity to the space-charge field when the total electric field is below 50 kV/cm. At -5 V or lower applied voltages, the NL sensitivity will then be additionally dependent on the doping level in the intrinsic region as well as the intrinsic region length. This prediction is confirmed[5] and is understood because the electric field near the n-contact would be lower if the intrinsic region length were slightly longer or if the doping density in the intrinsic region was slightly higher.

Shifting to 1 GHz, simulations with hole mobilities of 150 and 175 cm^2/Vs and a simulation spot size of 7 μm, similar to the best-fit simulation parameters utilized in figure 5.9, are plotted in figure 5.13. With the

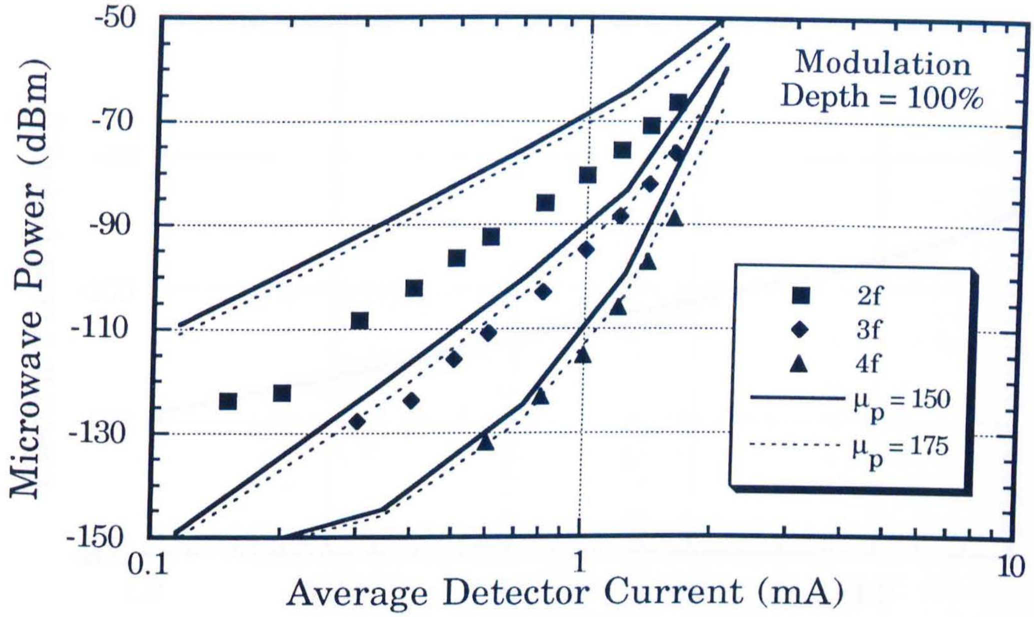

Figure 5.13 Measured and simulated harmonic power vs average PD current at 1 GHz. Applied voltage = -5 V. Fiber pigtailed. μ_p = 150 and 175 cm^2/Vs. Simulated spot size = 7.0 μm.

exception of the second harmonic, the simulated data fits quite well to the measured data. The discrepancy in the second harmonic will be reexamined after simulations and fits to the -10 V NL data.

Ten Volt Measurements and Simulations

Measurements at higher applied voltages and hence higher electric fields should lower the NL dependence on the exact hole mobility of the device, since the hole velocity nearly saturates for electric fields above 50 kV/cm. Higher electric fields thus result in smaller changes in the hole velocity for a given change in the internal electric field. A -10 V reverse bias will increase the electric field by approximately 50 kV/cm over the entire intrinsic region which should be sufficient to saturate the hole velocity given the hole mobility is above 150 cm^2/Vs. The electric field at 100 μA with -10 V applied voltage is plotted in figure 5.14, where the

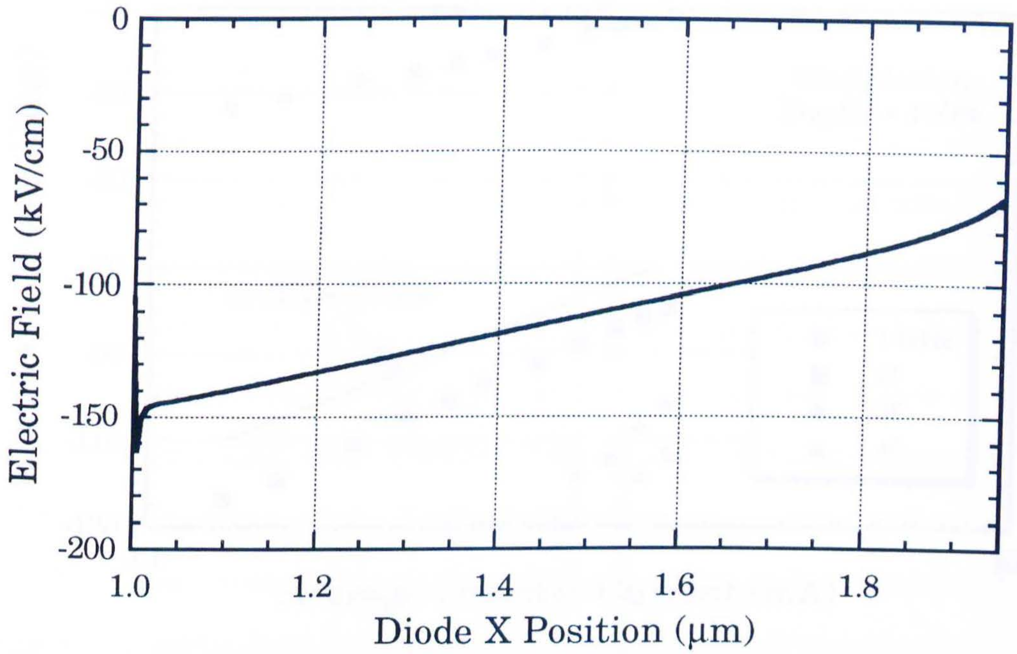

Figure 5.14 Intrinsic region electric field for an intrinsic region doping density of 5.0 x 10^{15} cm^{-3}. Diode applied voltage = -10 V.

electric field is seen to be above 70 kV/cm over the entire intrinsic region.

The measured PD NL at frequencies of 1 and 5 GHz are shown in figures 5.15 and 5.16, respectively. Several differences are observed between the -10 V data (figures 5.15 and 5.16) and the -5 V data (figures 5.5 and 5.6). The individual NL components are 10 to 20 dB lower as expected from the higher electric fields which result in a nearly saturated hole velocity. The frequency dependence is also reduced substantially, for example, the increase in second harmonic at 1 mA between the two frequencies is 15 dB at -5 V applied bias voltage, but reduces to 3 dB at -10 V. Note also that compared to the -5 V data, the -10 V nonlinearities resemble traditional power-law behaviors.

Recall from figures 5.2 and 5.3 that at -10 V applied PD voltage the 1 GHz second harmonic no longer decreases with increasing voltage while

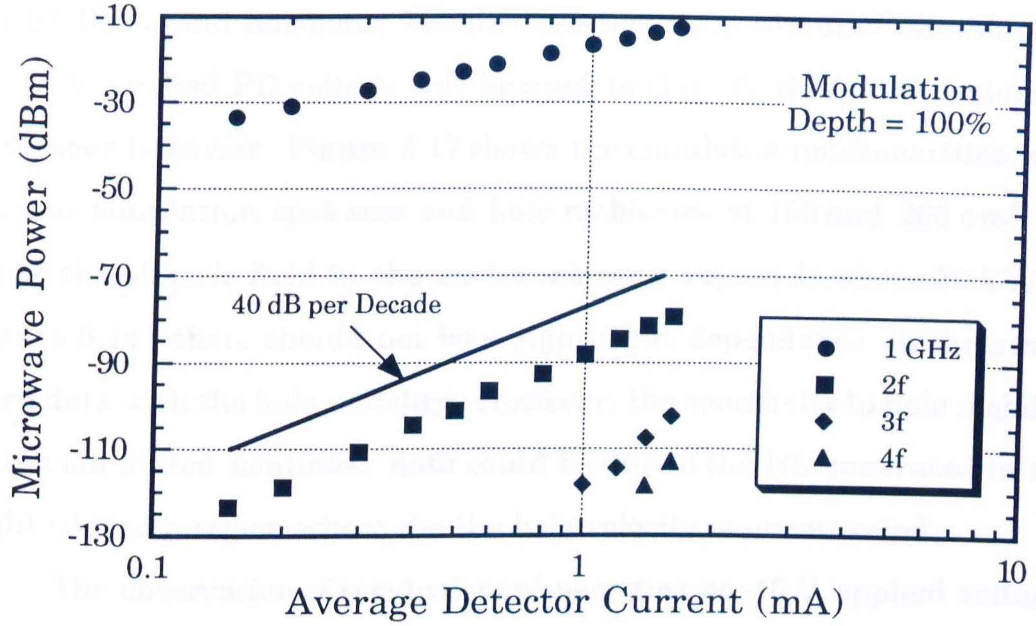

Figure 5.15 Measured fundamental and harmonic power versus input optical power at 1 GHz. Applied voltage = -10 V. Fiber pigtailed. 40 dB per decade tendancy included.

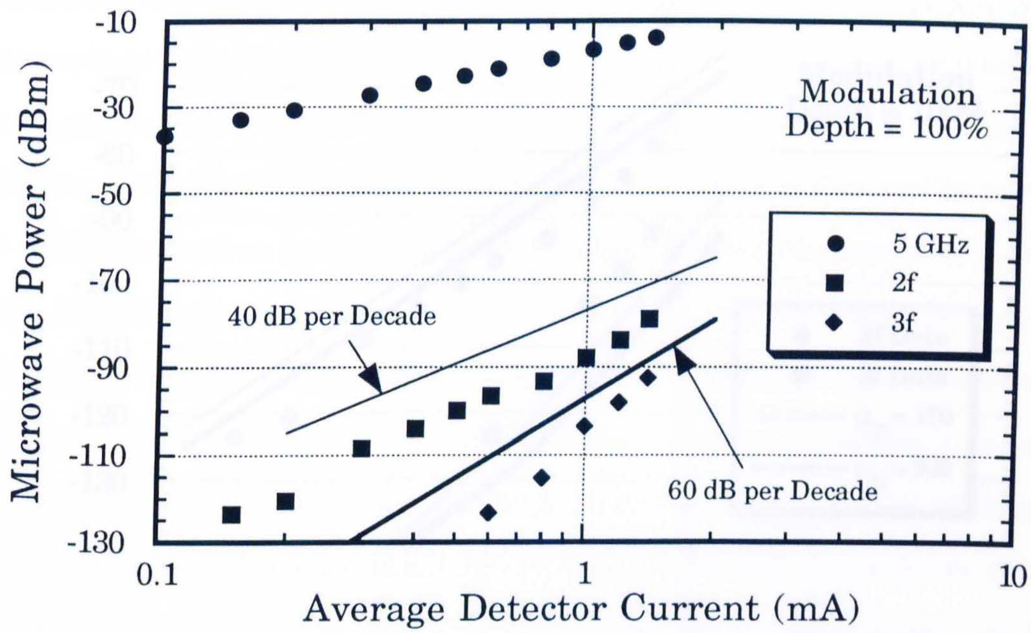

Figure 5.16 Measured fundamental and harmonic power versus incident optical power at 5 GHz. Applied voltage = -10 V. Fiber pigtailed. 40 and 60 dB per decade tendancies included.

the 5 GHz second harmonic has just reached its minimum. Simulations at -10 V applied PD voltage will be used to classify these two regions of nonlinear behavior. Figure 5.17 shows the simulated nonlinearities with a 7 μm simulation spot size and hole mobilities of 150 and 200 cm²/Vs. Since the electric field in the entire intrinsic region is above 70 kV/cm (figure 5.14), there should not be a significant dependence on the simulated data with the hole mobility. However, the sensitivity to hole mobility in the simulated nonlinear data could be due to the NL generated in the highly doped p-region where the the hole velocity is unsaturated.

The observation of residual nonlinearities at -10 V applied voltage, where the electric field in the intrinsic region is sufficient to approximately saturate the hole velocity, is not unexpected due to the many nonlinear mechanisms in the continuity equations (3.3 and 3.4). Several of

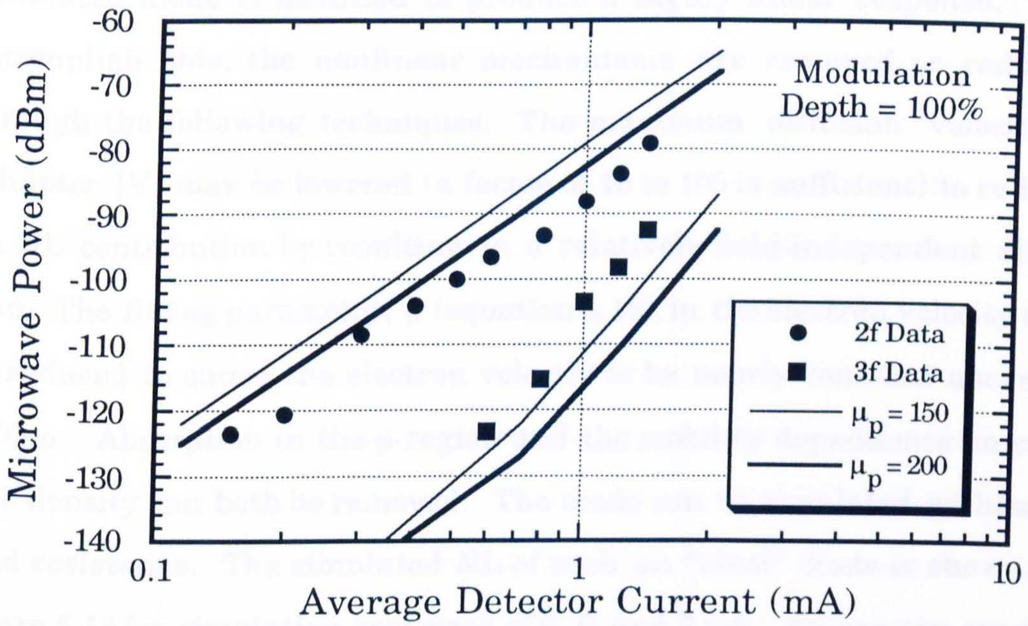

Figure 5.17 Measured and simulated harmonic power vs current at 5 GHz for hole mobilities of 150 and 200 cm^2/Vs. Applied V = -10 V. Spot size = 7 μm. Experimental Data from Figure 5.16.

these mechanisms will be investigated to determine their contribution to the total device NL at high applied voltages. The nonlinear mechanisms under consideration here are:

1) Space charge fields which may modify the carrier velocities.

2) Free carrier scattering which can reduce the carrier mobilities and possibly the carrier velocities.

3) Carriers absorbed in the p-type cap layer (where the electric field is low) may contribute to the total device NL.

4) The diffusion term in equations 3.3 and 3.4 may contain a small non-linear term due to the electric field dependence in the diffusion constant.

5) Loading in the external circuit which may modify the carrier velocities via a reduced internal electric field.

To determine the contribution from the above nonlinear terms, the simulated diode is modified to produce a highly linear response. To accomplish this, the nonlinear mechanisms are removed or reduced through the following techniques. The maximum diffusion "velocities" (Chapter IV) may be lowered (a factor of 10 to 100 is sufficient) to reduce its NL contribution by resulting in a relatively field-independent diffusion. The fitting parameter, β (equation 3.16), in the electron velocity can be reduced to cause the electron velocity to be nearly constant above 20 kV/cm. Absorption in the p-region and the mobility dependence on carrier density can both be removed. The diode can be simulated without a load resistance. The simulated NL of such an "ideal" diode is shown in figure 5.18 for simulation spot sizes of 5, 6, and 7 μm. As one can see the device is very linear producing a -115 dBc second harmonic (dBc implies relative to the fundamental) at 115 μA limited by the FFT window and a -

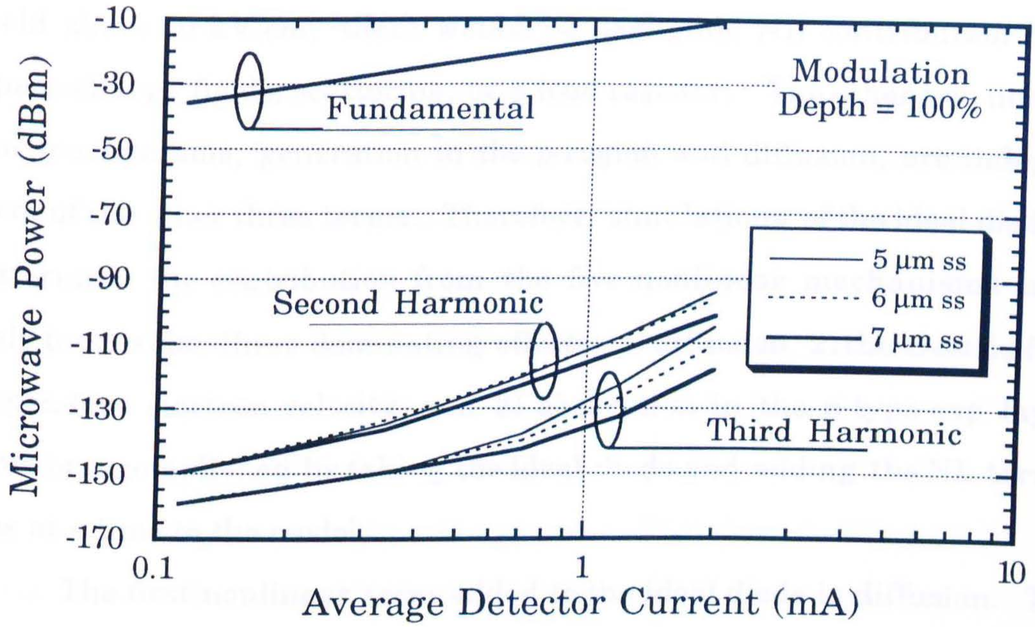

Figure 5.18 Simulated fundamental and harmonic power versus detector current for an "ideal" detector at 5 GHz. Applied voltage = -10 V. μ_p = 200 cm^2/Vs. Simulated spot sizes of 5, 6, and 7 μm.

100 dBc second harmonic at 1 mA. The results above 1 mA are slightly worse, possibly due to the remaining small nonlinearities in carrier velocities or diffusion. Nevertheless, the nonlinear terms may now be added to quantify their relative contributions to the total device NL.

The above five nonlinear mechanisms can be reduced to three basic NL sources, due to the inter-relationships between the nonlinear mechanisms and the carrier velocities. Space-charge electric fields and loading in the external circuit both modify the intrinsic region electric field, and thus, the electron velocity. On the other hand, carrier scattering reduces the carrier mobilities, thus changing the electric field dependence of the carrier velocities. A space-charge induced change in the hole velocity will be determined later to be negligible compared to the electron velocity change. Therefore, if the electron velocity was not a function of electric field above 50 kV/cm, there would be negligible NL contribution from space-charge fields, scattering, or a load resistor. The other two nonlinear mechanisms, generation in the p-region and diffusion, are independent of the other three terms. Therefore, simulations of the ideal diode to determine the contribution from the five nonlinear mechanisms need only to consider three dominating effects: 1) diffusion, 2) the electric field dependent electron velocity, and 3) absorption in the p-type cap layer. This is accomplished by taking the ideal diode and adding the NL terms, one at a time to the model.

The first nonlinear term added to the ideal diode is diffusion. The device NL of the simulated ideal diode with only diffusion added is shown in figure 5.19. There is a slight increase from the ideal diode NL of figure 5.18, although the measured NL in the real device (see figure 5.16) are

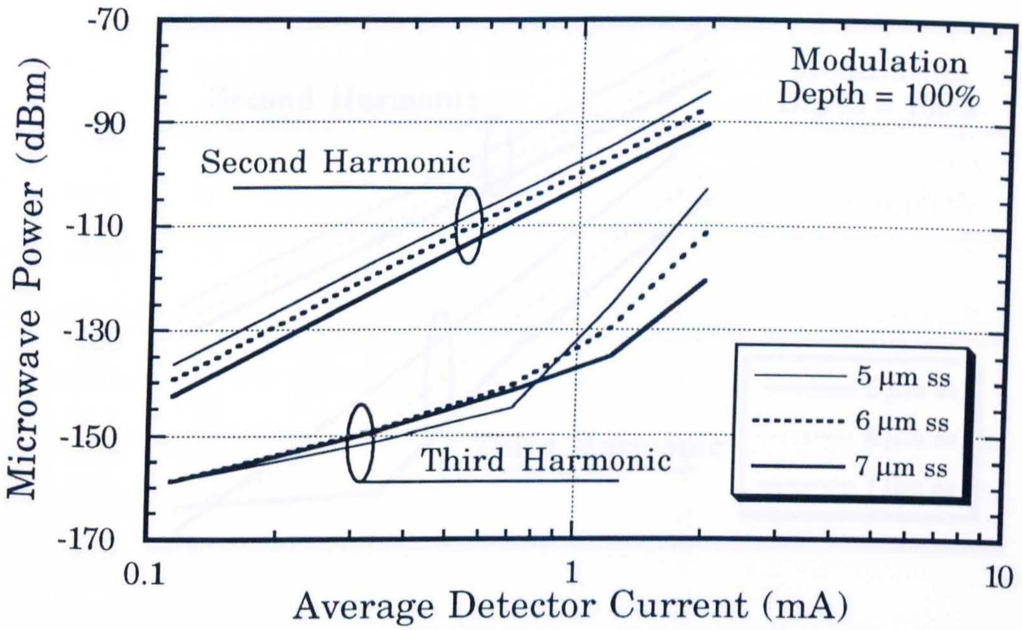

Figure 5.19 Simulated harmonic power versus detector current for an "ideal" detector at 5 GHz including only diffusion. Applied voltage = -10 V. $\mu_p = 200\ cm^2/Vs$.

still 10 to 20 dB higher than the nonlinearities in figure 5.19. Thus, diffusion alone does not account for the observed NL.

The addition of the field dependence of the electron velocity adds NL to the ideal diode whenever there is a space-charge electric field, mobility reduction due to scattering, or loading in the external circuit. The space-charge field cannot be removed from the simulation, but scattering and the load resistance can. Therefore the ideal diode will be modified by adding the electric-field-dependent electron velocity and will affect the NL via space-charge fields only. The simulated ideal diode NL under these conditions is plotted in figure 5.20, where the NL has increased by up to 15 dB over the diffusion-only results of figure 5.19. The simulated NL are now within a few dB of the experimentally observed NL in figure 5.16.

The addition of carrier scattering (mobility reduction) or a load

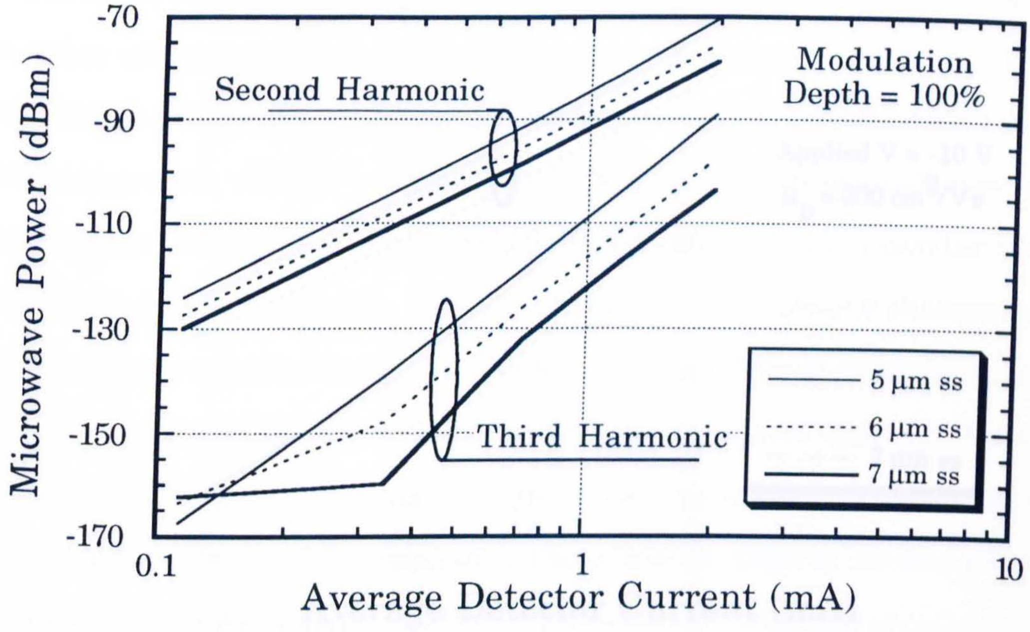

Figure 5.20 Simulated harmonic power vs current for an "ideal" detector at 5 GHz including the field dependent electron velocity with space-charge effects. Applied V = -10 V. $\mu_p = 200\ cm^2/Vs$

resistance will further modify the electric field at high PD currents. The simulated diode leading to the results in figure 5.20 is modified to include both of these additional nonlinear mechanisms and the associated data is plotted in figure 5.21. The results show that the device NL including scattering and a load resistor is about 1 dB less than that simulated diode in figure 5.20, which excluded these two terms. This may happen, since a reduction in the electron mobility can reduce the electric-field-dependence of the electron velocity[4] for electric fields above 20 kV/cm.

A plot of the space-charge electric field (figure 5.22) is identical to the -5 V space-charge electric field. This is expected since the intrinsic region carrier velocities are essentially unchanged, although the NL with the diode biased at -10 V is substantially reduced from the earlier -5 V case. Since the space-charge field has not changed, the drop in the

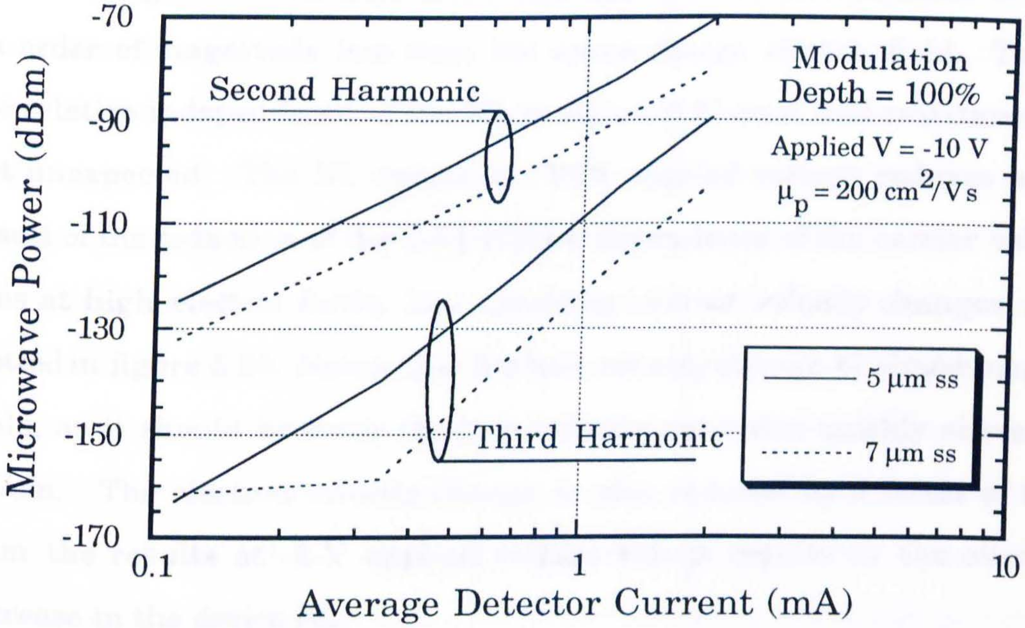

Figure 5.21 Simulated harmonic power vs current for an "ideal" PD at 5 GHz including the field-dependent electron velocity with space-charge effects, scattering, and a 50 Ohm load resistance.

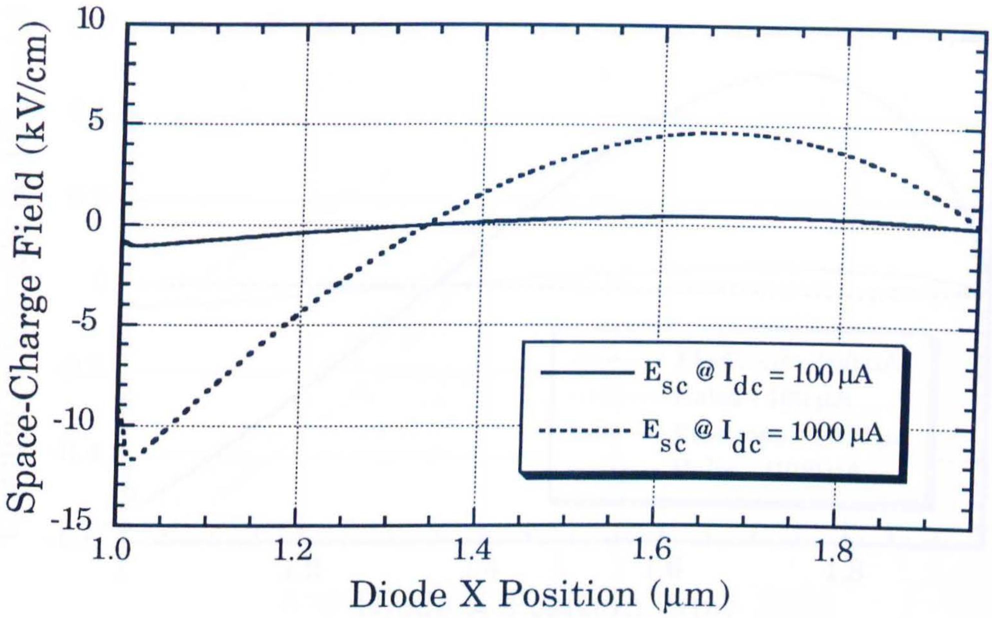

Figure 5.22 The space-charge electric field in the intrinsic region due to the photogenerated carriers. Spot size = 7.0 μm. Applied voltage = -10 V. μ_p = 150 cm^2/Vs. μ_n = 10,000 cm^2/Vs.

intrinsic region electric field associated with a 50Ω load resistance is still an order of magnitude less than the space-charge electric field. Thus, the relative independence of the NL in figure 5.21 on a load resistance is not unexpected. The NL output at -10 V applied voltage reduces as a result of the reduction of the electric field dependence of the carrier velocities at high electric fields. The resulting carrier velocity changes are plotted in figure 5.23. Notice that the hole velocity change is almost negligible, as it should be since the hole velocity saturates quickly above 50 kV/cm. The electron velocity change is also reduced by a factor of ten from the results at -5 V applied voltage which results in the overall decrease in the device NL.

The third nonlinear mechanism under investigation is the addition of absorption in the p-region. This adds to the NL of the ideal diode by

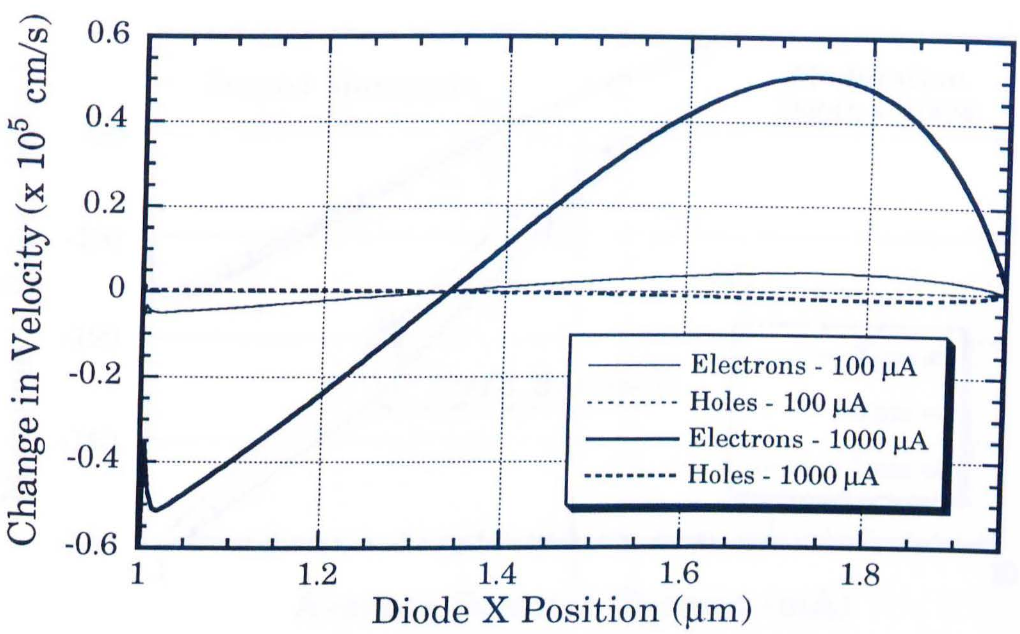

Figure 5.23 The change in carrier velocities in the intrinsic region due to the space-charge field. Spot size = 7.0 μm. Applied voltage = -10 V. μ_p = 150 cm^2/Vs. μ_n = 10,000 cm^2/Vs.

the generation and movement of carriers in a region where the carrier velocities are rapidly changing, even though the carriers may quickly recombine. The simulation results of the ideal diode, modified to include p-region absorption, are plotted in figure 5.24. The nonlinearities in figure 5.24 are approximately 20 dB higher that those obtained when the model diode includes all the nonlinear mechanisms. This overestimation of the device NL is the result of neglecting mobility reduction and diffusion, since the inclusion of these terms contribute to the carrier movement in the p-region. For example, the electron velocity is proportional to the electric field (the electric field is very low so the carrier velocities are equal to μE), which is related to the ratio of electron to hole velocity in the p-region. When mobility reduction is not included in the simu-

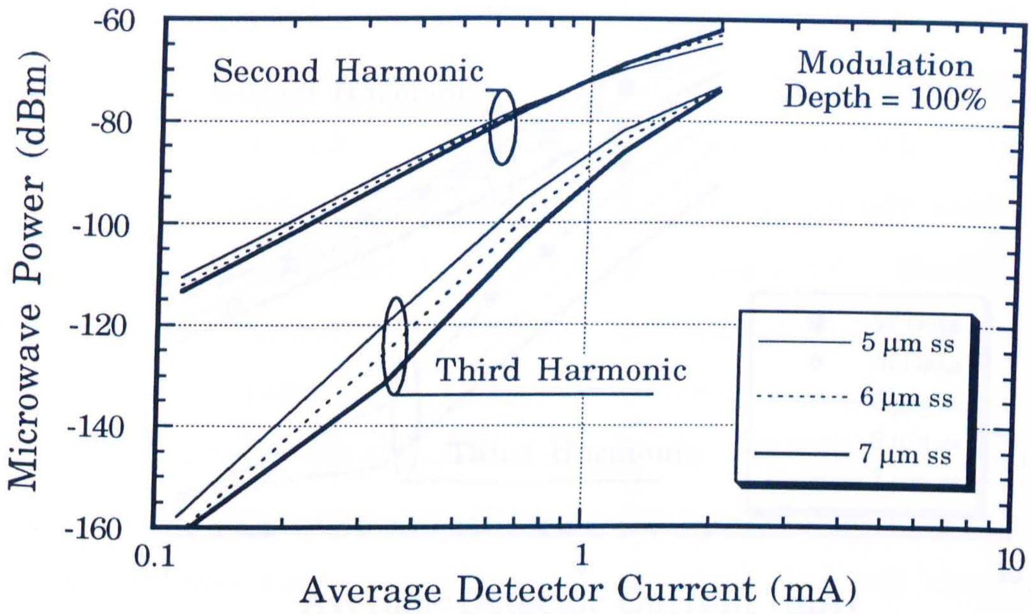

Figure 5.24 Simulated harmonic power versus detector current for an "ideal" detector at 5 GHz including only the p-region absorption nonlinearity. Applied V = -10 V. Spot sizes of 5, 6, and 7 μm.

lation, this ratio increases by a factor of 1.8, since the electron mobility (as compared to the hole mobility) begins to decrease at lower carrier densities. Therefore, the net result is a higher change in electron velocity when scattering is excluded. Enhancement or suppression of the other nonlinear mechanisms may also occur when more than one NL is included in the ideal diode simulations. Therefore, the two dominant terms, the electric field dependence of the electron velocity and the p-region absorption, will be further investigated by excluding each of these two NL from the actual device.

The simulated results for the real diode excluding only p-region absorption and excluding only the electric field dependence in the electron velocity above 20 kV/cm are plotted in figures 5.25 and 5.26, respectively. Both simulations include the mobility as a function of carrier den-

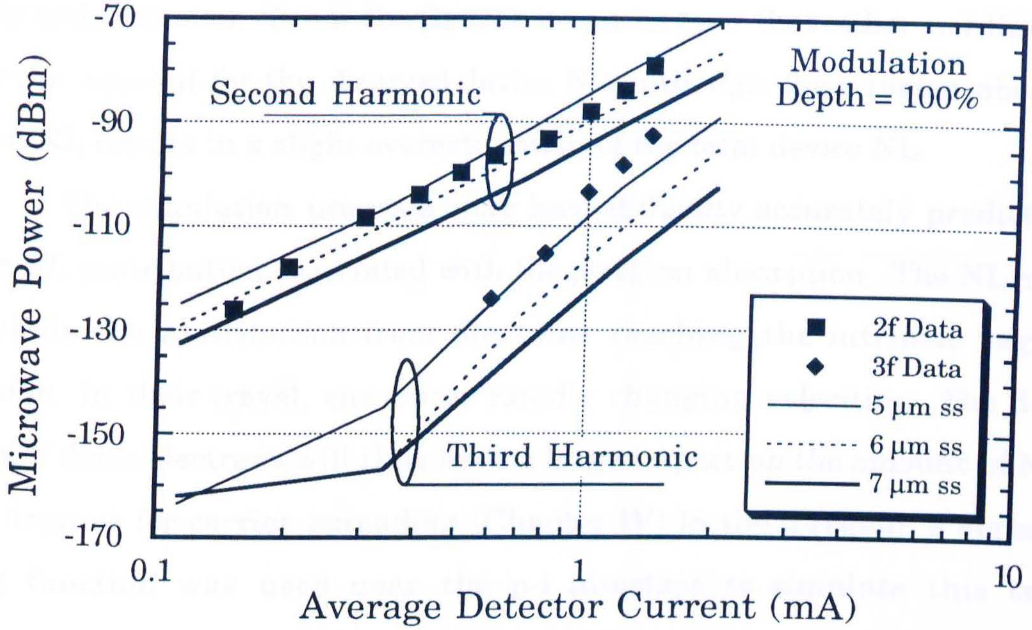

Figure 5.25 Measured and simulated harmonic power vs detector current at 5 GHz excluding p-region absorption. $\mu_p = 200\ cm^2/Vs$. Applied Voltage = -10V. Experimental data from figure 5.16.

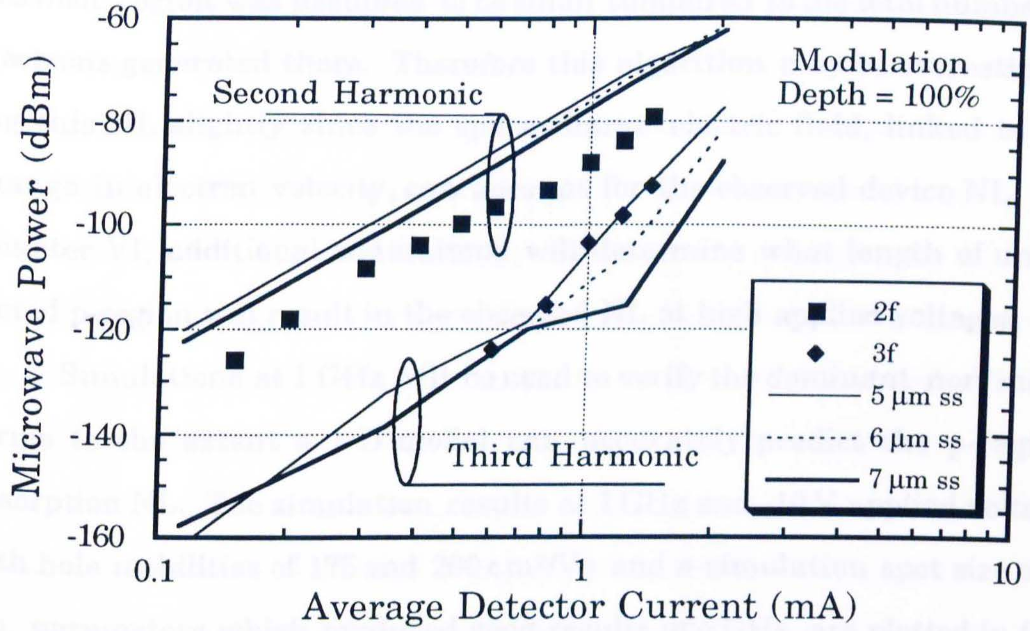

Figure 5.26 Measured and simulated harmonic power vs current at 5 GHz excluding the electron velocity nonlinearity. Applied V = -10V. $\mu_p = 200\ cm^2/Vs$. Experimental data from figure 5.16.

sity and diffusion. From the figures it can be seen that either nonlinearity can account for the observed device NL, although the p-region absorption NL results in a slight overestimation of the total device NL.

The simulation program may have difficulty accurately predicting the NL contribution associated with the p-region absorption. The NL may include the contribution from electrons reaching the intrinsic region which, in their travel, encounter rapidly changing velocities. The density of these electrons will thus have a large impact on the amount of NL. To account for carrier spreading (Chapter IV) in the p-region, a spreading function was used near the p-i interface to simulate this two-dimensional effect for the one-dimensional model. This assumption however resulted in an artificial focusing of p-region-generated electrons traveling into the intrinsic region. The total number reaching the intrinsic region was assumed to be small compared to the total number of electrons generated there. Therefore this algorithm may be overestimating this NL slightly since the space-charge electric field, linked to the change in electron velocity, can account for the observed device NL. In Chapter VI, additional simulations will determine what length of undepleted p-region will result in the observed NL at high applied voltages.

Simulations at 1 GHz will be used to verify the dominant nonlinear terms to the extent a 1-D model can accurately predict the p-region absorption NL. The simulation results at 1 GHz and -10 V applied voltage with hole mobilities of 175 and 200 cm^2/Vs and a simulation spot size of 7 μm, parameters which produced good results at 5 GHz, are plotted in figure 5.27. Notice that at 1 GHz the simulated results do not agree well with the experimental data. The contribution to the NL output at 5 GHz

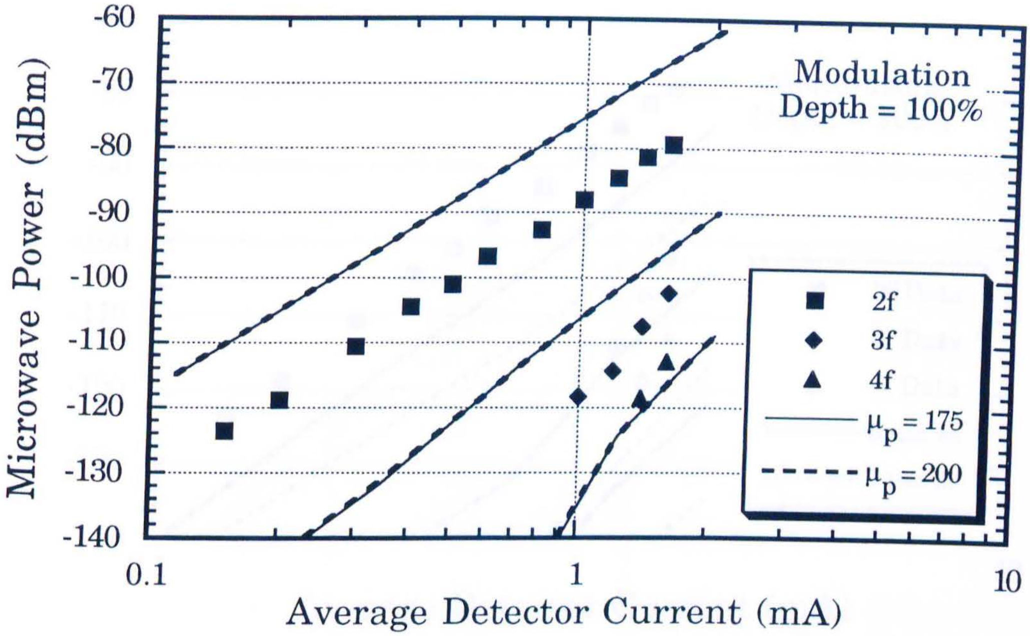

Figure 5.27 Measured and simulated harmonic power vs current at 1 GHz. Applied V = -10 V. Fiber pigtailed. Spot size = 7.0 μm. μ_p = 175 and 200 cm^2/Vs. Measurement data from figure 5.15.

was seen to be influenced the most by two nonlinear mechanisms: a space-charge-induced change in the electron velocity with increasing carrier densities and the absorption in the p-region. It was determined that the NL at 5 GHz could be explained by considering the change in the electron velocity, without including the p-region absorption. In fact, including the p-region absorption, led to an overestimation of the second harmonic by 10 dB at 5 GHz, similar to the results at 1 GHz (figure 5.27).

Therefore the PD is simulated again, this time neglecting p-region absorption, to determine if the electron velocity NL can be used by itself to model the device NL at 1 GHz. The simulated results with a hole mobility of 200 cm^2/Vs and simulation spot sizes of 5 and 7 μm are plotted in figure 5.28, where the NL is now 10 to 15 dB below the measurement data. A lower hole mobility (100 cm^2/Vs) may increase the overall simulated

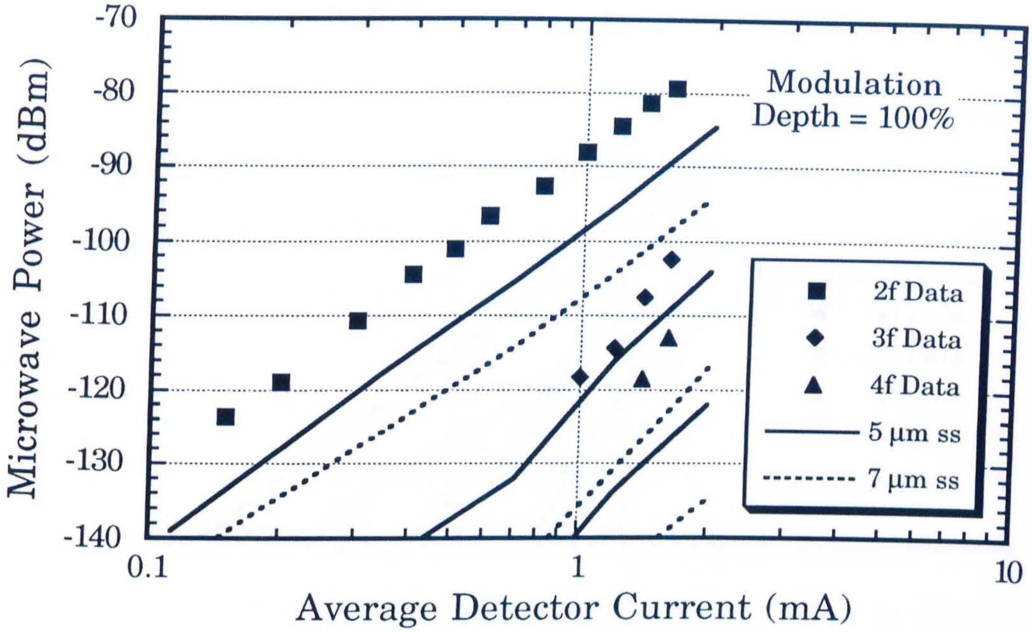

Figure 5.28 Measured and simulated harmonic power vs PD current at 1 GHz neglecting absorption in the p-region. Applied V = -10 V. μ_p = 200 cm^2/Vs. Measurement data from figure 5.15.

device NL, so the PD is simulated again (figure 5.29) without p-region absorption. Here again, the simulated NL is 10 to 15 dB below the measurement data. Therefore, the NL at 1 GHz with -10 V applied voltage is dominated by the p-region absorption and not the space-charge-induced change in the electron velocity.

One question still remains: why does the modeled PD overestimate the NL at -10 V applied voltage at both frequencies of 1 and 5 GHz? From the modeling point of view this question may be alternately phrased as: What influences the NL in the p-region? The answer to this question may not be a simple one, however, it is reasonable to assume that: 1) the minority carrier lifetime in the p-region will determine the extent of which the carriers generated in this region will contribute to the output, 2) the two-dimensional focusing/defocusing approximation at the p-i

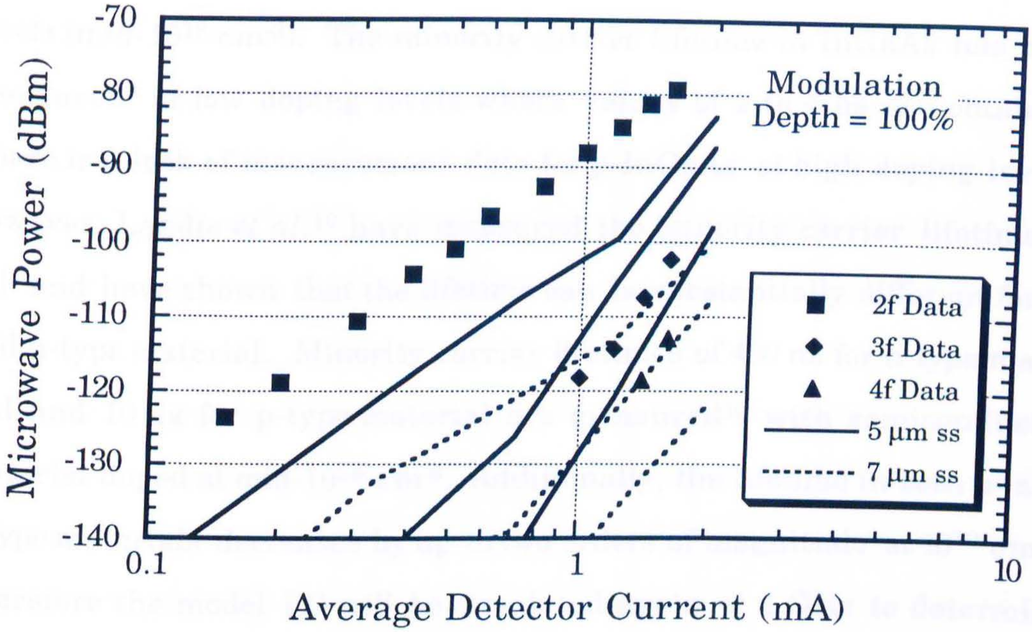

Figure 5.29 Measured and simulated harmonic power vs PD current at 1 GHz neglecting absorption in the p-region. Applied V = -10 V. μ_p = 100 cm^2/Vs. Measurement data from figure 5.15.

interface (Chapter IV) may influence the number of carriers which contribute to the NL, 3) the ratio of carrier mobilities may effect the NL since this ratio determines the electron velocity in the p-region, and 4) the electron mobility (and hence the electron velocity in the p-region) may effect the NL, which is influenced by the functional dependence of the reduction in electron mobility (equation 3.19) with increasing carrier density.

The p-region minority carrier lifetime was assumed to be 500 ps, or about four times smaller than the intrinsic-region lifetime. The simulated NL thus far were not affected by the exact value of the lifetime, however, at high electric fields, the nonlinearities are more subtle. Measurements[6-8] of the minority carrier lifetime in InP, GaAs, and InGaAsP indicate that the lifetimes in these materials are in the 10 to 500 ns range (doping levels of 10^{16} cm^{-3}) with a decrease to 0.1 to 5 ns at higher doping levels (mid-10^{18} cm^{-3}). The minority carrier lifetime in InGaAs has been measured[9] at low doping levels where values of 2 to 4 ns are obtained. There is a lack of measurement data for p-InGaAs at high doping levels, however, Landis *et al.*[10] have measured the minority carrier lifetime in InP and have shown that the lifetime can be substantially different for p- and n-type material. Minority carrier lifetimes of 400 ns for n-type material and 10 ns for p-type material are measured[10] with semiconductor material doped at mid-10^{16} cm^{-3}. Additionally, the lifetime in both n- and p-type materials decreases by up to two orders of magnitude at 10^{19} cm^{-3}. Therefore the model PD will be simulated again at 1 GHz to determine the sensitivity of the device NL to the minority carrier lifetime.

The simulation results are plotted in figure 5.30 with minority carrier lifetimes of 100, 50, and 25 ps, a hole mobility of 200 cm^2/Vs, and a

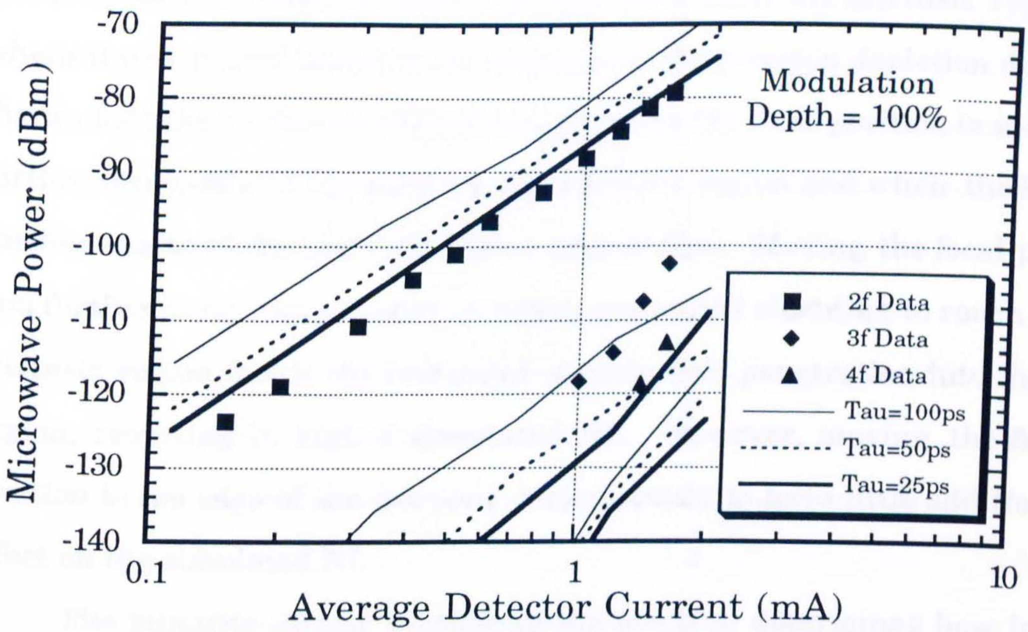

Figure 5.30 Measured and simulated harmonic power vs PD current at 1 GHz. Applied V = -10 V. Spot size = 6.0 μm. Measurement data from figure 5.15. $\mu_p = 200\ cm^2/Vs$. $\mu_n = 10000\ cm^2/Vs$.

simulation spot size of 6 μm. A minority carrier lifetime of 25 ps provides the best-fit to the second harmonic data. A minority carrier lifetime of 25 ps is about two orders of magnitude less than the lifetime in the intrinsic material.[9] Although this value may be slightly low, it is consistent with the reductions (from their value at low doping levels) observed in other materials.[6-8]

The minority carrier lifetime is not the only parameter which influences the p-region absorption NL behavior. Another possible parameter which may influence the NL is the 2-D focusing/defocusing approximation made for the p-region (Chapter IV). The location of the focusing function may be moved closer to or further away from the intrinsic region. The electric field decreases very rapidly just after the focal position due to the high level of p-region doping. Up until now, this focal position has been fixed at approximately 5 nm from the intrinsic region, where it was placed based on an estimate of the p-region depletion depth. Figure 5.31 shows the simulated results when the focal position is moved further away (12 and 19 nm) from the intrinsic region and when the focal position starts at the intrinsic region edge (0 nm). Moving the focal position further away causes more p-region-generated electrons to reach the intrinsic region due to the increased electric field penetration into the p-region, resulting in higher simulated NL. However, moving the focal position to the edge of the intrinsic region seems to have little additional effect on the simulated NL.

The minority carrier lifetime in the p-region determines how long or equivalently how many electrons contribute to the NL. Another parameter which influences the p-region absorption nonlinear behavior

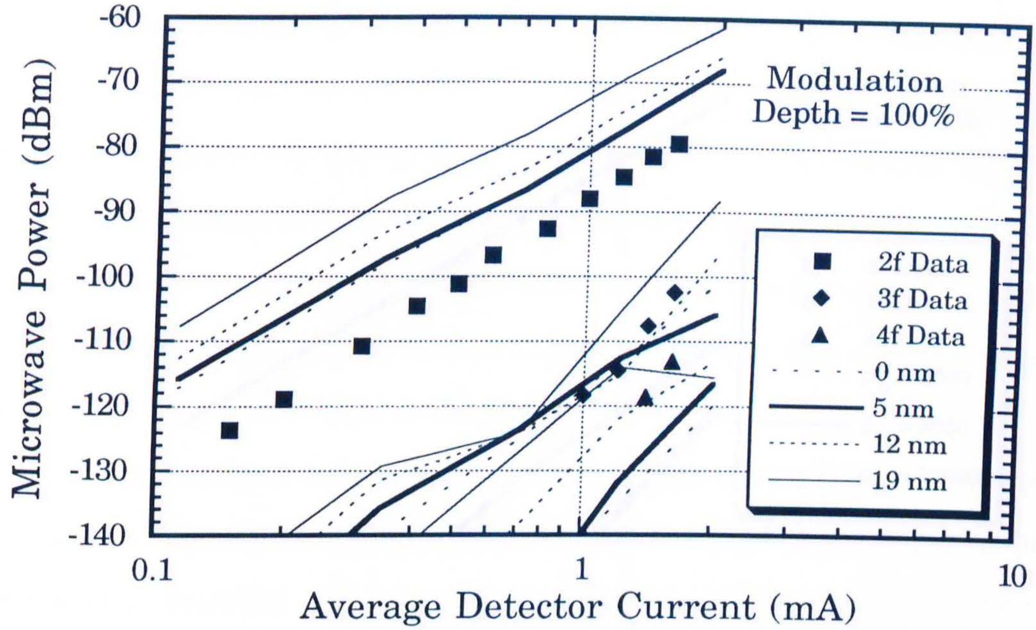

Figure 5.31 Measured and simulated harmonic power vs current at 1 GHz. Applied V = -10 V. Variable positions for hole spreading in the p-region. Spot size = 6.0 μm. Tau_p = 100 ps. μ_p = 200 cm^2/Vs.

is the electron velocity. The electron velocity is determined by the electron mobility in the p-region because the electric field is below 1 kV/cm. The electron mobility is influenced by two parameters: the low-doping-density mobility μ_n and the scattering parameter n_h (equation 3.19) which lowers the electron mobility at high doping levels. To determine the sensitivity in the simulated results to the electron mobility and the scattering parameter, the PD is simulated with a fixed minority carrier lifetime of 100 ps while varying these two parameters.

The NL for electron mobilities of 6000, 8000 and 10000 cm^2/Vs is plotted in figure 5.32. The NL for electron scattering parameters of 0.5, 1, and 2 x 10^{17} cm^{-3} is plotted in figure 5.33 for an electron mobility of 8000 cm^2/Vs. The scattering parameter (Chapter III) was estimated from electrons in uncompensated n-InGaAs.[4] The p-region is composed of

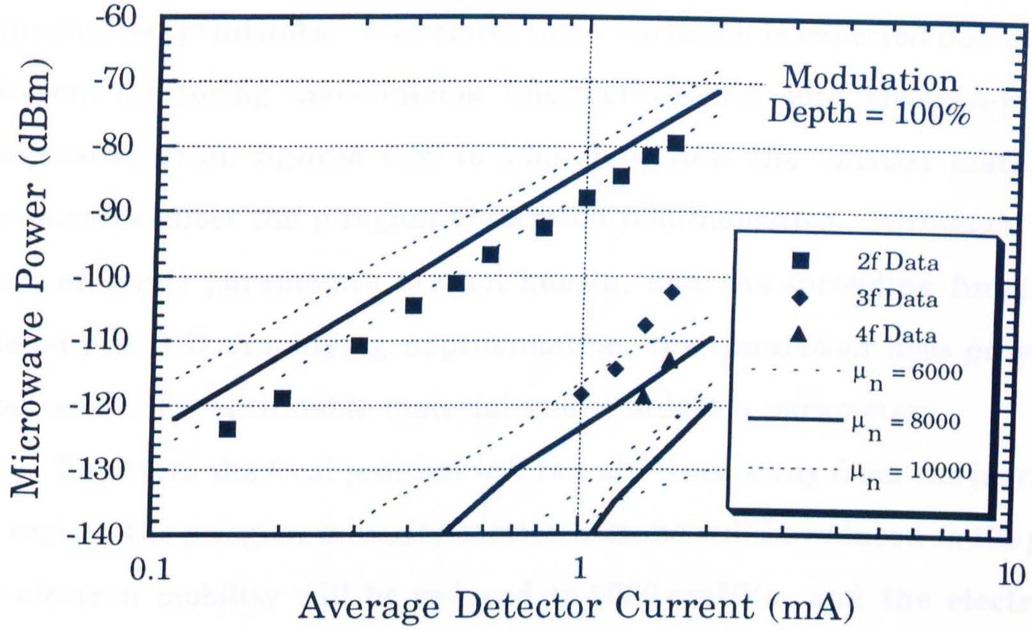

Figure 5.32 Measured and simulated harmonic power versus current at 1 GHz. Applied V = -10 V. Spot size = 6.0 μm. μ_n = 6000, 8000, and 10000 cm^2/Vs. Tau$_p$ = 100 ps. μ_p = 200 cm^2/Vs.

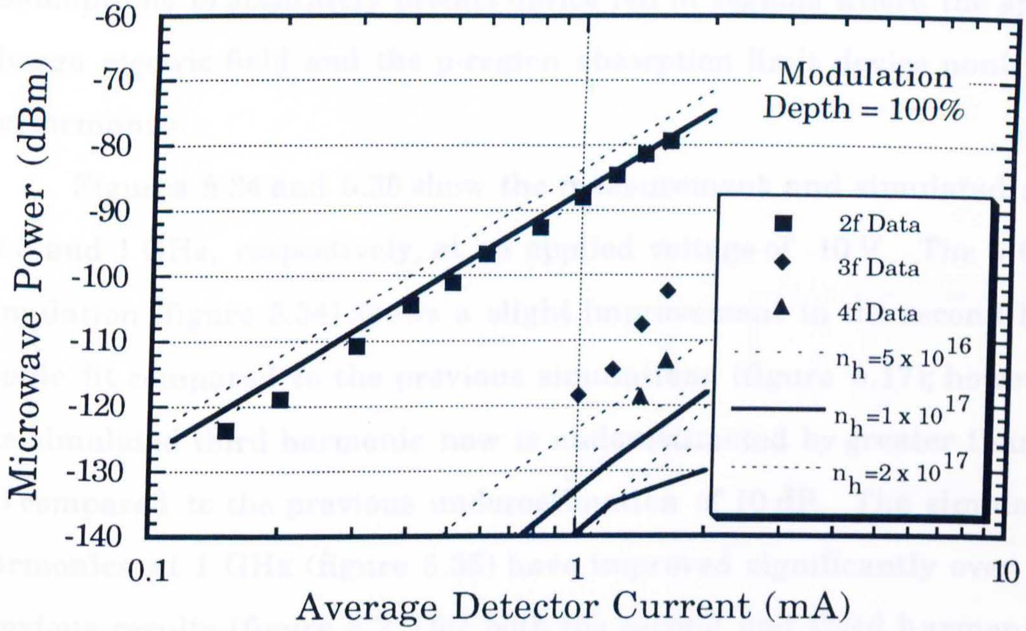

Figure 5.33 Measured and simulated harmonic power vs current at 1 GHz for various electron scattering parameters. V = -10 V. Spot size = 6.0 μm. μ_n = 8000 cm^2/Vs. Tau$_p$ = 100 ps. μ_p = 200 cm^2/Vs.

compensated p-InGaAs. Therefore, some variation is expected due to the different scattering mechanisms (electron-electron and electron-hole). The results from figures 5.30 to 5.33 show how the various material parameters affect the p-region absorption nonlinearities. Although the exact material parameters are not known, and the spreading function was only an 1-D simplifying approximation, the simulation does provide good results for reasonable material and simulation parameters.

Therefore the focal position will remain 5 nm away from the intrinsic region, the p-region minority carrier lifetime will be reduced to 100 ps, the electron mobility will be reduced to 8000 cm^2/Vs, and the electron scattering parameter will be reduced to 0.5×10^{17} cm^{-3}. The simulations at applied voltages of -5 and -10 V and frequencies of 1 and 5 GHz will be recalculated to verify that the simulation contains a reasonable set of assumptions to accurately predict device NL in regions where the space-charge electric field and the p-region absorption limit device nonlinear performance.

Figures 5.34 and 5.35 show the measurement and simulated data at 5 and 1 GHz, respectively, at an applied voltage of -10 V. The 5 GHz simulation (figure 5.34) shows a slight improvement in the second harmonic fit compared to the previous simulations (figure 5.17); however, the simulated third harmonic now is underestimated by greater than 20 dB compared to the previous underestimation of 10 dB. The simulated harmonics at 1 GHz (figure 5.35) have improved significantly over the previous results (figure 5.27) for both the second and third harmonics, with little observed change in the fourth harmonic.

Returning to -5 Volts applied bias, figures 5.36 and 5.37 show the

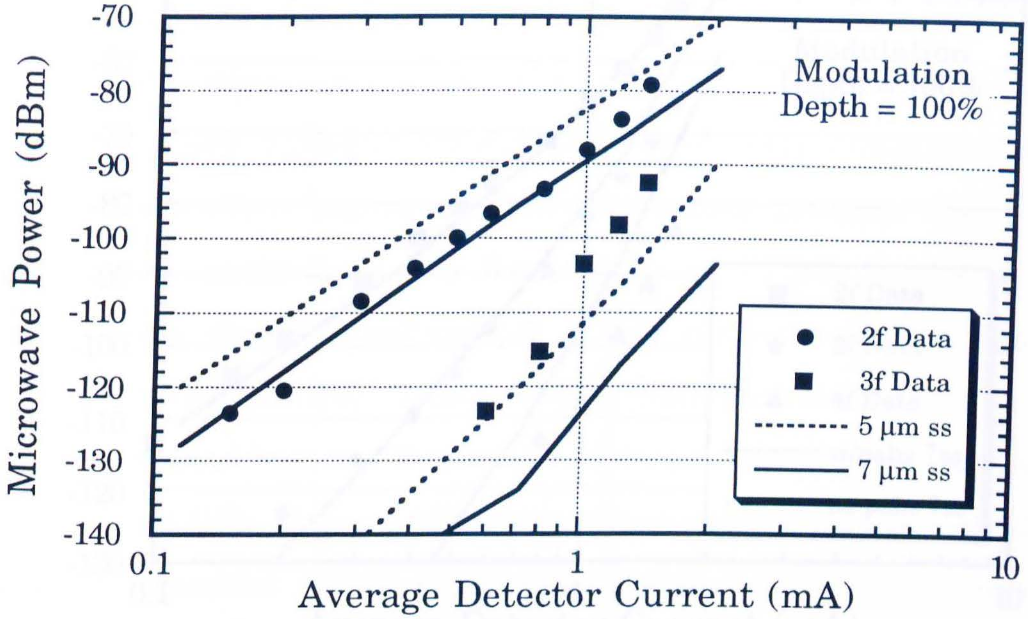

Figure 5.34 Measured and simulated harmonic power vs current at 5 GHz with a hole mobility of 150 cm^2/Vs. Applied V = -10 V. Spot size = 5 and 7 μm. Experimental Data from figure 5.16.

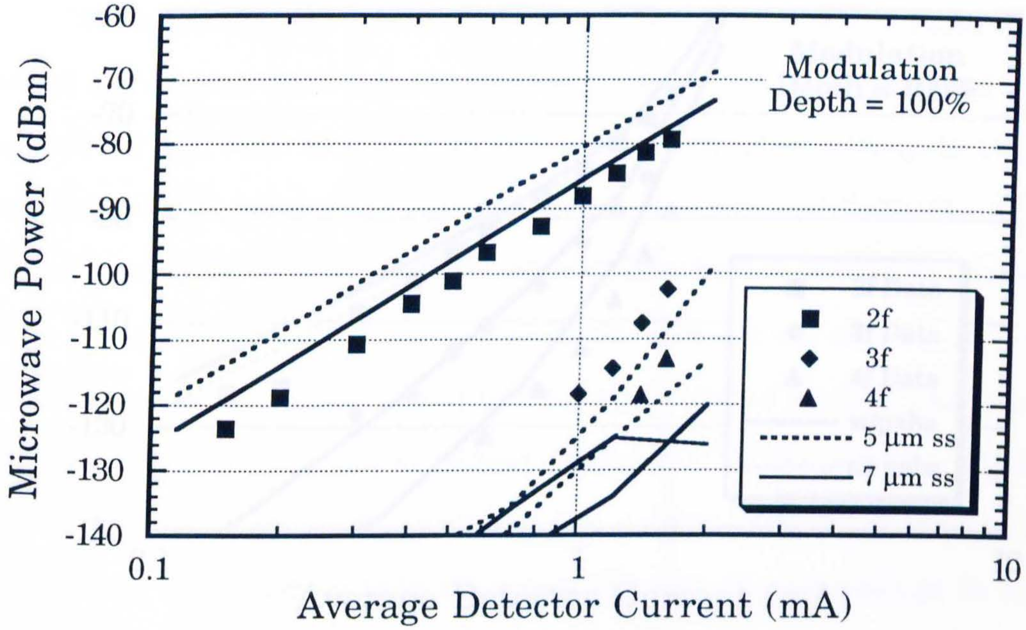

Figure 5.35 Measured and simulated harmonic power versus detector current at 1 GHz. Tau_p = 25 ps. μ_p = 150 cm^2/Vs. Applied voltage = -10 V. Measurement data from figure 5.15.

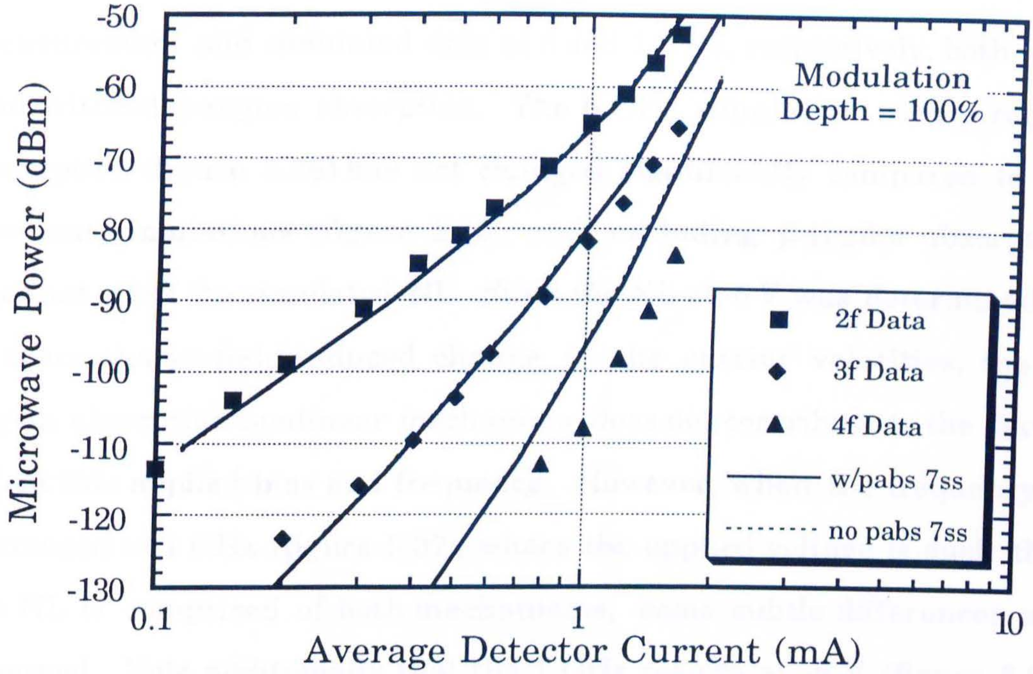

Figure 5.36 Measured and simulated harmonic power at 5 GHz. Spot size = 7 μm with a hole mobility of 150 cm^2/Vs. With and without p-region absorption. Measurement data from figure 5.6.

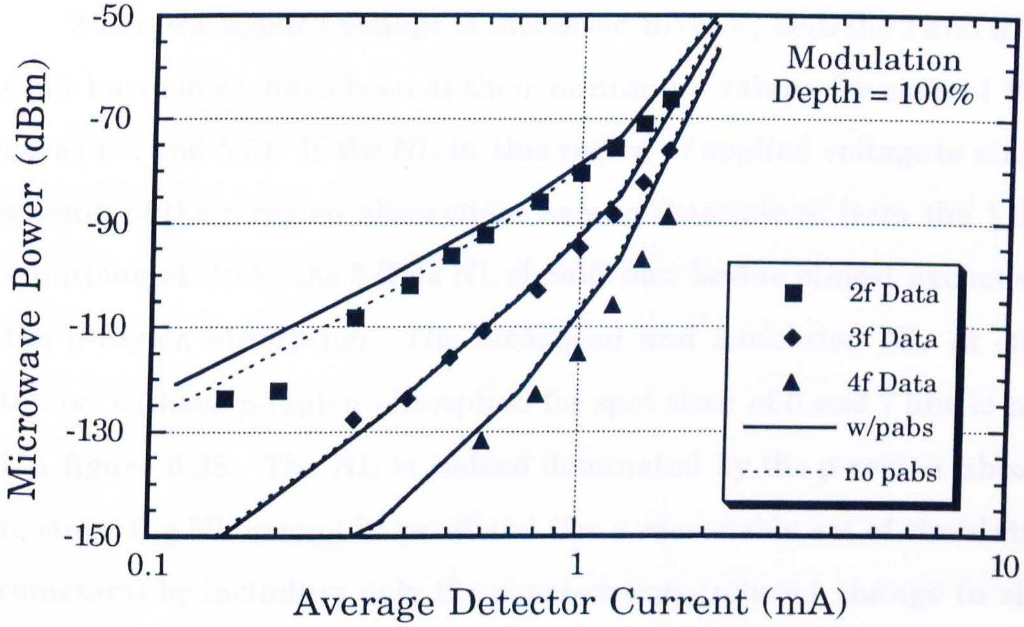

Figure 5.37 Measured and simulated harmonic power vs detector current at 1 GHz. Applied voltage = -5 V. Fiber pigtailed. Spot size = 7.0 μm. μ_p = 150 cm^2/Vs. Measurement data from figure 5.5.

measurement and simulated data at 5 and 1 GHz, respectively, both with and without p-region absorption. The 5 GHz simulation with p-region absorption (figure 5.36) has not changed significantly compared to the previous simulations (figure 5.10), and, excluding p-region absorption does not affect the simulated NL. Since the NL at -5 V was determined by a space-charge-field-induced change in the carrier velocities, the p-region absorption nonlinear mechanism does not contribute to the device NL at this applied bias and frequency. However, when the frequency is decreased to 1 GHz (figure 5.37), where the applied voltage is such that the NL is comprised of both mechanisms, some subtle differences are observed. Note additionally that the 1 GHz results at -5 V (figure 5.37) now agree quite well in contrast to the previous simulations (figure 5.13).

Fifteen Volt Measurements and Simulations

When the applied voltage is increased to -15 V, both the 1 and 5 GHz second harmonics have been at their minimum values for several Volts (figures 5.2 and 5.3). If the NL in this region of applied voltage is strictly the result of the p-region absorption, as was determined from the 1 GHz simulations at -10 V, the 5 GHz NL should now be due almost exclusively to the p-region absorption. The measured and simulated NL at -15 V with and without p-region absorption for spot sizes of 5 and 7 μm is plotted in figure 5.38. The NL is indeed dominated by the p-region absorption, since the NL cannot be predicted (for a reasonable set of simulation parameters) by including only the space-charge-induced change in electron velocity.

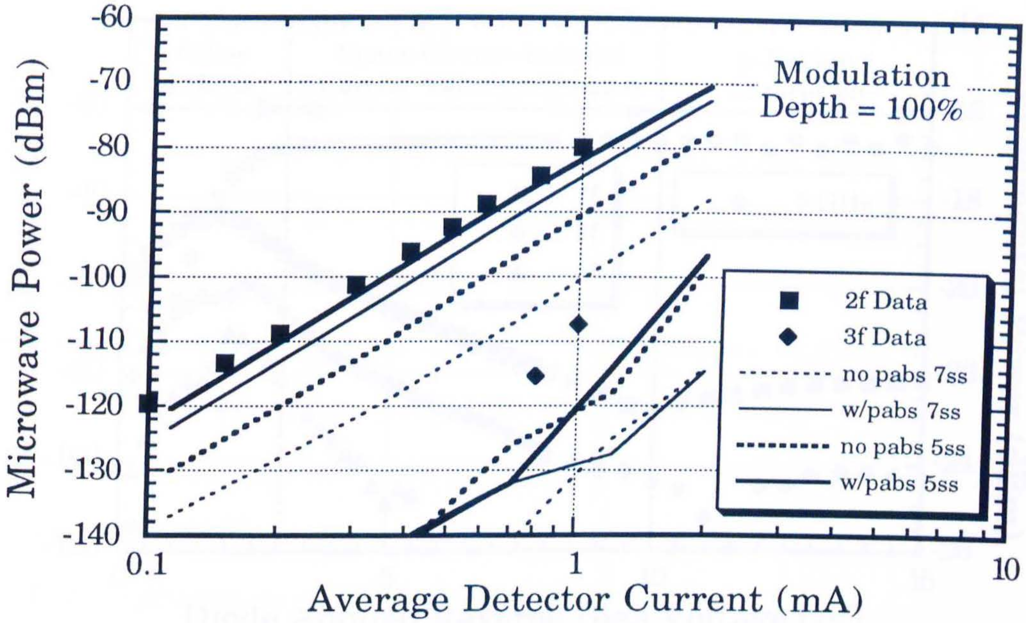

Figure 5.38 Measured and simulated harmonic power vs current at 5 GHz with and without absorption in the p-region. Applied V = -15 V. Spot sizes of 5 and 7 μm. Tau_p = 25 ps. $\mu_p = 150\ cm^2/Vs$.

Summary

In this chapter, we have investigated the origins of nonlinearities in p-i-n PDs and have, for the first time, systematically identified which nonlinear mechanisms are dominant for different applied PD voltages. The PD intrinsic region width, excitation frequency, and incident spot size all influence the exact bias voltage where the transition between the different regimes occur. Typical results are plotted again for convenience in figure 5.39 (same as figure 5.3). Figure 5.39 shows these three regimes: 1) the space-charge-induced change in carrier velocities dominate the NL from the point where the fundamental power saturates (-3 V) to the point where the NL stops decreasing (-10 V), 2) the p-region absorption nonlinear mechanism dominates for applied voltages greater

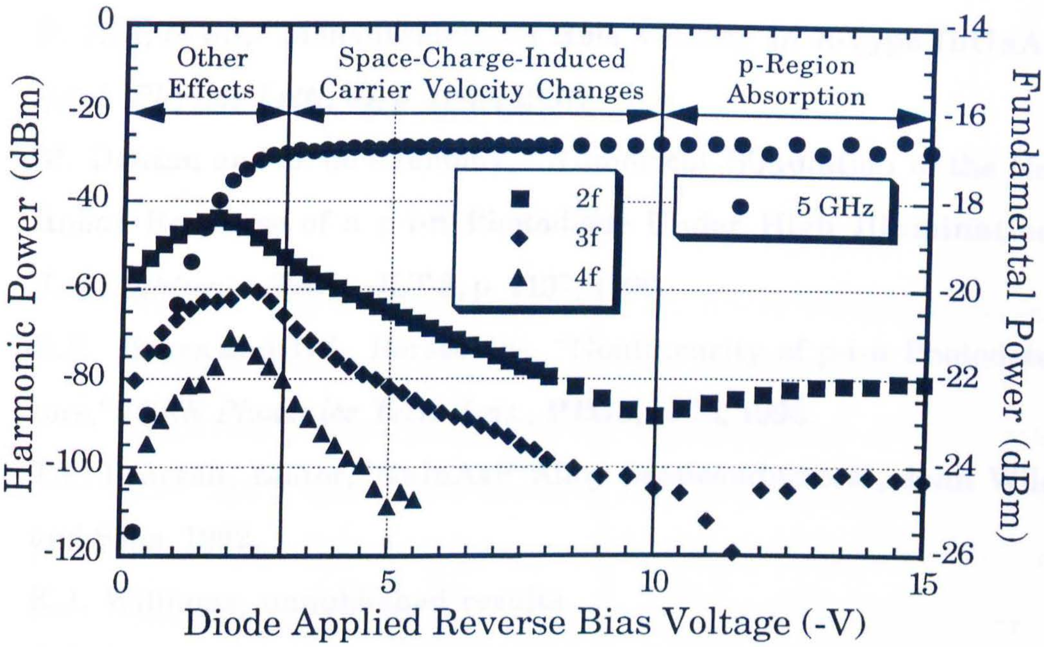

Figure 5.39 Regions of applied bias where different nonlinear mechanisms dominate the second harmonic nonlinear output. Measurement data from figure 5.3.

than -10 V, and 3) at low voltages (< 3 V) where significant two-dimensional carrier flow and electric field redistribution (see Chapter VII) dominate the device NL. The knowledge obtained from the results of this chapter will allow device parameters such as the physical device diameter, intrinsic region length, and intrinsic region doping densities to be investigated to determine if improvements to the inherent device NL can be made. These issues will be covered in Chapter VIII.

1. P. Hill, *et al.*, "Measurement of Hole Velocity in n-Type InGaAs," *Appl. Physics Lett.*, **50**, p. 1260, 1987.
2. M. Dentan and B. de Cremoux, "Numerical Simulation of the Non-linear Response of a p-i-n Photodiode Under High Illumination," *J.of Lightwave Tech.*, **JLT-8**, p. 1137, 1990.
3. R.R. Hayes and D.L. Persechini, "Nonlinearity of p-i-n Photodetectors," *IEEE Photonics Tech. Lett.*, **PTL-5**, p. 70, 1993.
4. T.P. Pearsall, Editor, "GaInAsP Alloy Semiconductors", John Wiley and Sons, 1982.
5. K.J. Williams, unpublished results.
6. G.B. Lush, *et al.*, "Determination of Minority Carrier Lifetimes in n-type GaAs and Their Implications for Solar Cells," 22nd IEEE Photovoltaic Specialists Conference, p. 182, 1991.
7. M. Kot and K. Zdansky, "Measurement of Radiative and Nonradiative Recombination Rate in InGaAsP-InP LED's," *Quantum Electronics Lett.*, **28**, p. 1746, 1992.
8. P. Jenkins, *et al.*, "Minority Carrier Lifetimes in Indium Phosphide," 22nd IEEE Photovoltaic Specialists Conference, p. 177, 1991.
9. A.R. Adams, *et al.*, "The temperature dependence of the Efficiency and Threshold Current of $In_{1-x}Ga_xAs_yP_{1-y}$ Lasers Related to Intervalence Band Absorption," *Jpn. J. Appl. Phys.*, **19**, p. L621, 1980.
10. G.A. Landis, *et al.*, "Photoluminescence Lifetime Measurements in InP Wafers," 22nd IEEE Photovoltaic Specialists Conference, p. 636, 1991.

VI. LOW POWER DENSITY NONLINEARITIES IN DIFFERENT p-i-n STRUCTURES

Introduction

This chapter will investigate p-i-n PD NL under low power density conditions in three devices. Low power density conditions are defined as power densities which generate low enough space-charge electric fields (eqn. 3.35) such that no part of the intrinsic region electric field (eqn. 3.32) collapses. Two basic device structures are under investigation here: one double-heterostructure[1] mesa-type device with a 0.2-μm long intrinsic region fabricated at the University of California Santa Barbara, and two single-heterostructure[2] mesa-type devices with 0.5 and 0.95-μm long intrinsic regions fabricated by GTE Laboratories. These particular devices were chosen because they all have bandwidths over 20 GHz and they cover a range of intrinsic region thicknesses. Since the devices are made by research groups, the layer structure and doping profile are available with reasonable accuracy. At the end of this chapter, data from several additional PDs will be presented for completeness, although these devices will not be modeled.

0.95-μm Device Measurements and Simulations

The 0.95-μm long intrinsic region device is pigtailed with a single mode optical fiber and yields an incident intensity e^{-2} spot size of approximately 10 μm. The doping density versus position for the specific device under investigation was not available; however, data for similar devices was available. Although each device has slightly different characteristics, the doping profile is estimated from a range of available measured devices, with the specific profile utilized for simulation purposes shown in figure 6.1. The simulated device has a 0.95-μm unintentionally-doped lattice-matched n-InGaAs intrinsic region grown on an InP substrate, with a 1.0-μm heavily doped p-InGaAs cap layer.

The bin spacing versus photodiode position is shown in figure 6.2 for the 0.95 μm device. The bin widths were shortened near the p-i and the n-i interfaces to limit the change in the electric field and carrier densities between adjacent bins.

The measured NL at 1 mA of average PD current plotted versus detector applied voltage can be found in figures 5.1 to 5.4 for 100 MHz, 1 GHz, 5 GHz, and 10 GHz, respectively. These curves (figures 5.1 to 5.4) and the information they contain for determining the dominant nonlinear mechanisms was the focus of Chapter V. The simulation results for this device can also be found in Chapter V (figures 5.34 to 5.36) for frequencies of 1 and 5 GHz at applied voltages of -5, -10, and -15 Volts and

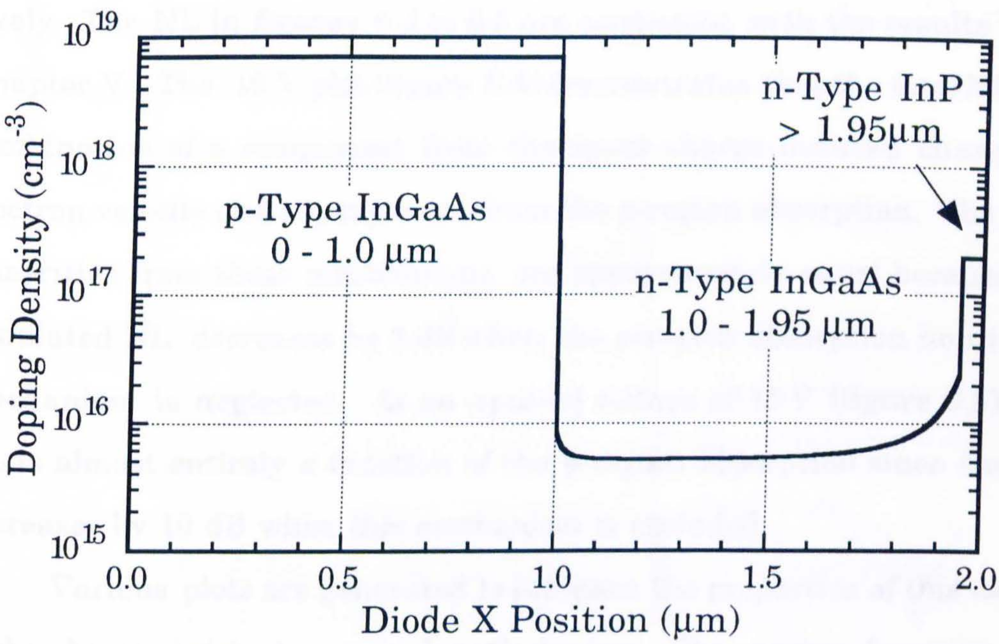

Figure 6.1 Doping profile for the 0.95-μm long intrinsic region device.

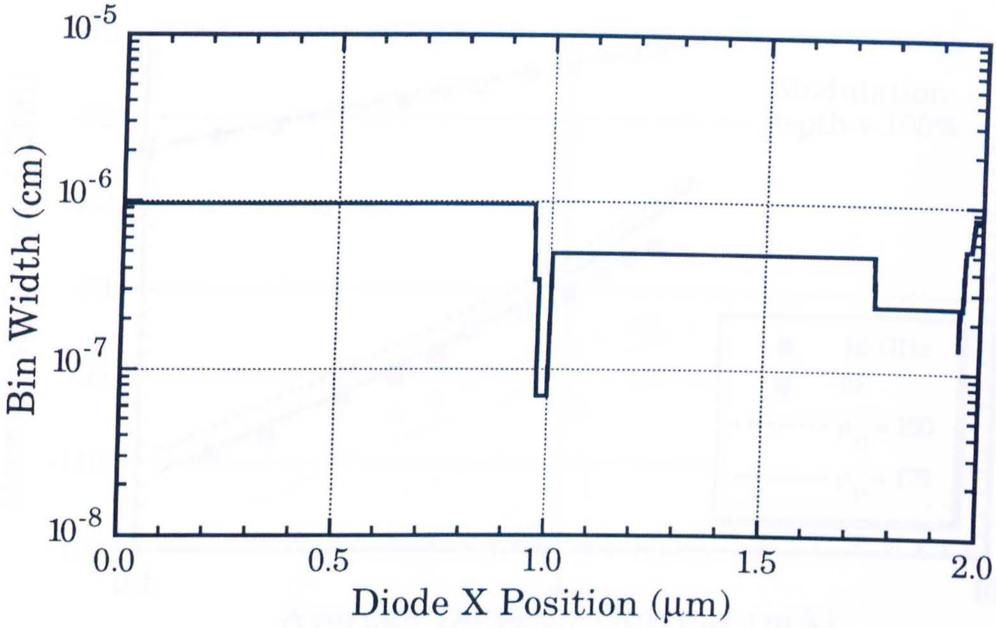

Figure 6.2 Diode bin width versus position, X, utilized in device simulations. 0.95-μm long intrinsic region.

will not be repeated here. The device NL at 10 GHz, with simulation parameters which yielded good results at 1 and 5 GHz, are plotted in figures 6.3, 6.4 and 6.5 for applied voltages of -5, -10, and -15 Volts, respectively. The NL in figures 6.3 to 6.5 are consistent with the results from Chapter V. The -10 V plot (figure 6.4) demonstrates that the total NL is a combination of a component from the space-charge-induced change in electron velocity and a component from the p-region absorption. The nonlinearities from these mechanisms are approximately equal because the simulated NL decreases by 3 dB when the p-region absorption nonlinear mechanism is neglected. At an applied voltage of-15 V (figure 6.5), the NL is almost entirely a function of the p-region absorption since the NL decreases by 10 dB when this mechanism is excluded.

Various plots are generated to compare the properties of this device to the shorter intrinsic region length devices. The carrier densities and

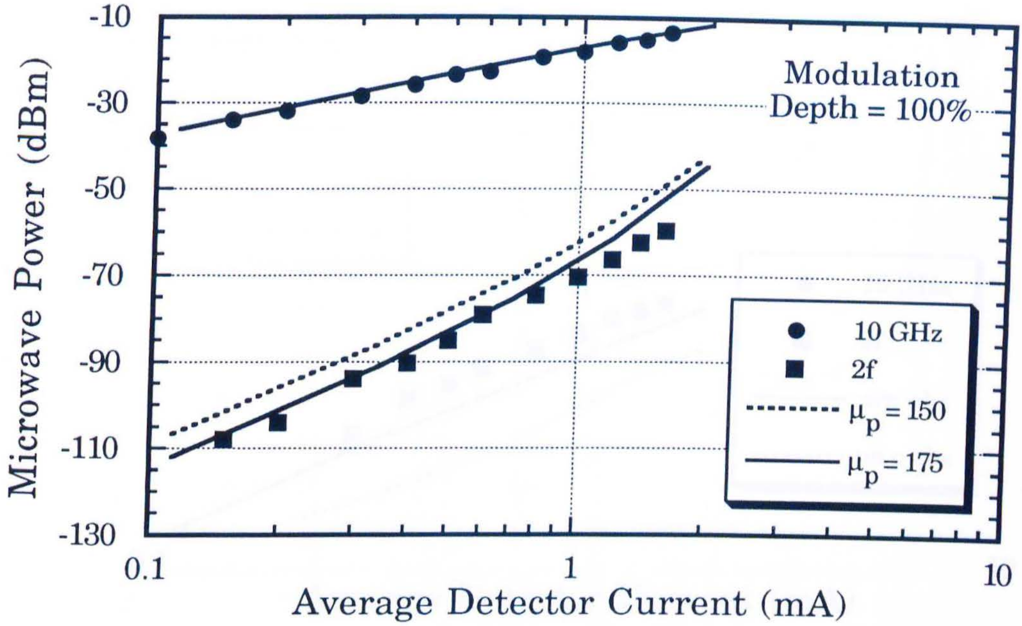

Figure 6.3 Measured and simulated harmonic power versus average detector current at 10 GHz. Applied voltage = -5 V. μ_p = 150 and 175 cm^2/Vs. Spot size = 7.0 μm.

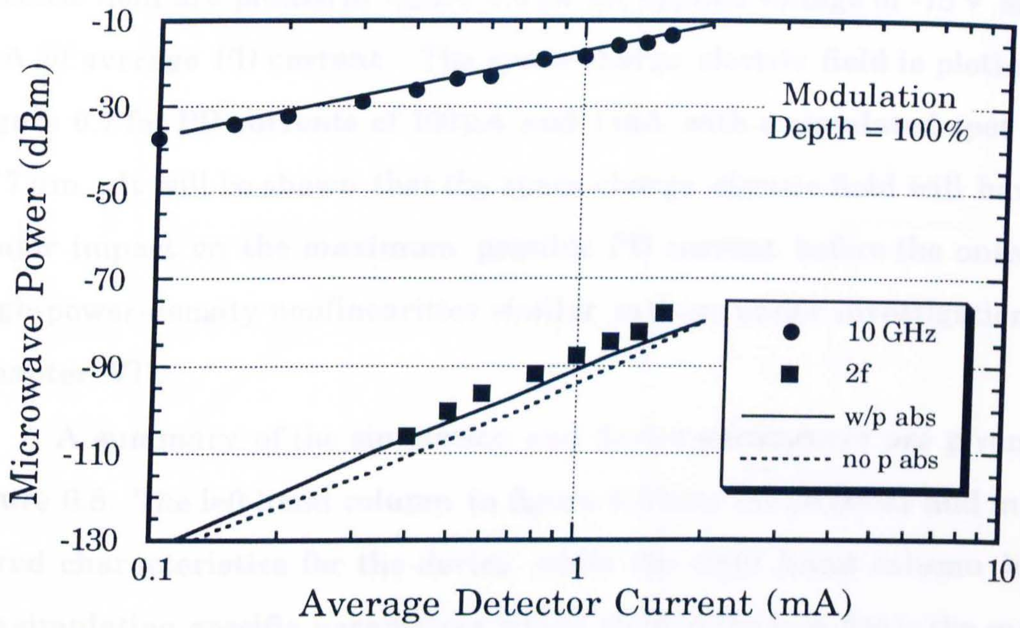

Figure 6.4 Measured and simulated harmonic power versus average detector current at 10 GHz. Applied voltage = -10 V. μ_p = 150 cm^2/Vs. Spot size = 7.0 μm.

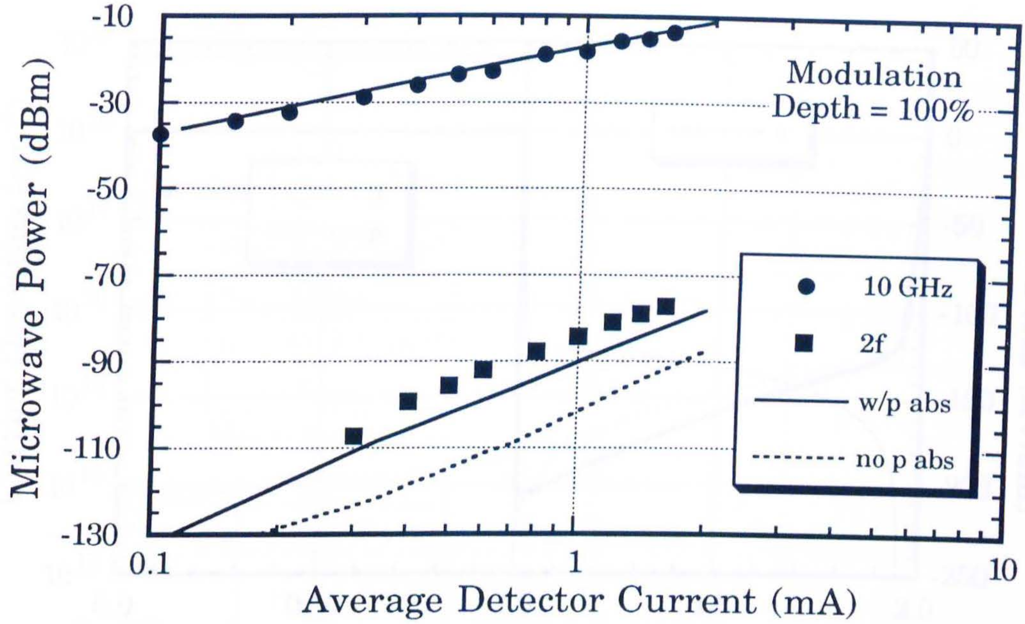

Figure 6.5 Measured and simulated harmonic power versus current at 10 GHz. Applied V = -15 V. With and without p-region absorption. $\mu_p = 150\ cm^2/Vs$. Spot size = 7.0 µm.

electric field are plotted in figure 6.6 for an applied voltage of -15 V and 1 mA of average PD current. The space-charge electric field is plotted in figure 6.7 for PD currents of 100 µA and 1 mA with a simulated spot size of 7 µm. It will be shown that the space-charge electric field will have a major impact on the maximum possible PD current before the onset of high-power-density nonlinearities similar to those under investigation in Chapter VII.

A summary of the simulation and device parameters are given in figure 6.8. The left hand column in figure 6.8 lists the physical and measured characteristics for the device, while the right hand column lists the simulation specific parameters which yielded the best-fits to the measurement data.

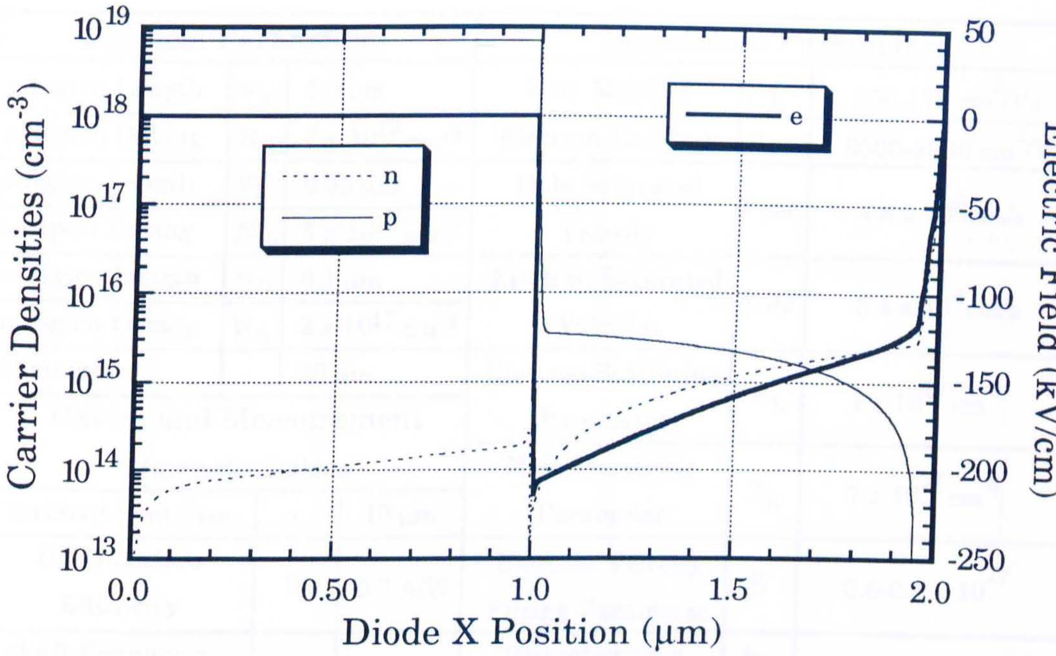

Figure 6.6 Carrier densities and electric field with an average PD current of 1 mA. 0.95-µm long intrinsic region. Applied V = -15 V.

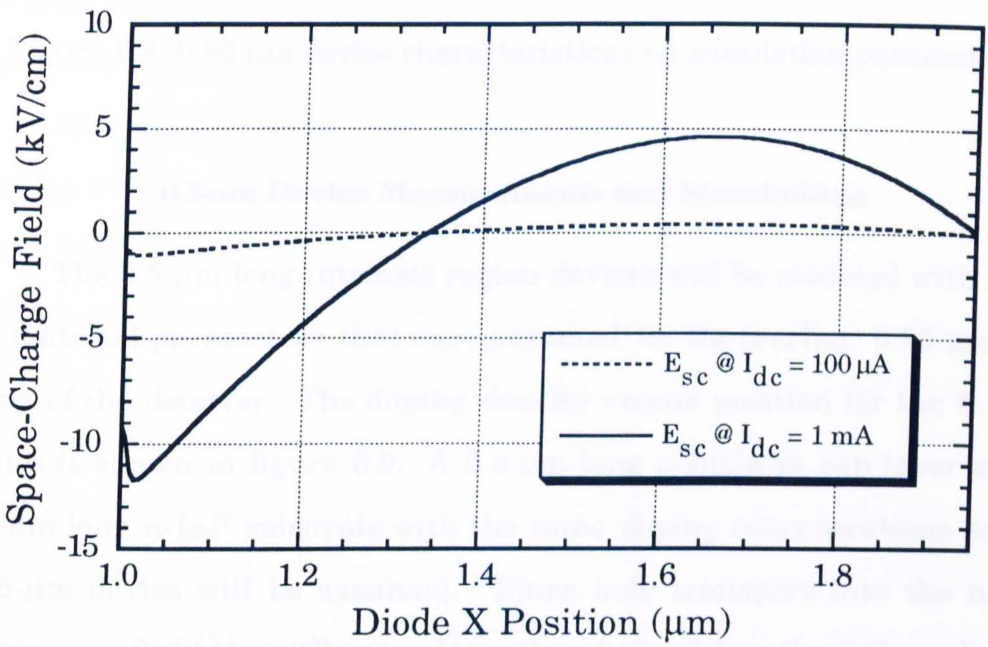

Figure 6.7 The space-charge electric field in the intrinsic region due to the photogenerated carriers. 0.95-µm long intrinsic region. Spot size = 7.0 µm. Applied voltage = -15 V.

Physical Parameters		
p-region Length	w_p	1.0 µm
p-region Doping	N_a	7×10^{18} cm^{-3}
i-region Length	w_i	0.95 µm
i-region Doping	N_{di}	5×10^{15} cm^{-3}
n-region Length	w_n	0.1 µm
n-region Doping	N_d	2×10^{17} cm^{-3}
Diameter	-	30 µm

Device and Measurement Characterisitics		
Incident Spot Size	-	10 µm
DC Quantum Efficiency	η	0.7 A/W
-3 dB Frequency Response	-	20 GHz
Laser Measurement Wavelength	λ	1319 nm

Simulation Parameters		
Hole Mobility	μ_p	150-175 cm^2/Vs
Electron Mobility	μ_n	6000-8000 cm^2/Vs
Hole Saturated Velocity	v_{phf}	4.8×10^6 cm/s
Electron Saturated Velocity	v_{nhf}	5.4×10^6 cm/s
Electron Scattering Parameter	n_h	1×10^{17} cm^{-3}
Hole Scattering Parameter	p_h	7×10^{17} cm^{-3}
Electron Velocity Fitting Parameter	β	$0.6\text{-}0.8 \times 10^{-7}$
Recombination Time, i-region	τ_p τ_n	2 ns
Recombination Time, p-region	τ_p τ_n	100 ps

Figure 6.8 0.95 µm device characteristics and simulation parameters.

0.5-µm Device Measurements and Simulations

The 0.5-µm long intrinsic region devices will be modeled with similar material parameters that were assumed for the (earlier) 0.95-µm versions of the detector. The doping density versus position for the 0.5-µm device is shown in figure 6.9. A 0.4-µm long p-InGaAs cap layer and a 0.1-µm long n-InP substrate with the same doping concentrations as the 0.95-µm device will be assumed. Since hole transport into the n-InP region was forbidden (Chapter III), the physical length of the n-InP is not required so long as enough region is modeled to prevent the depletion region from reaching the n-contact. Any additional transparent InP acts

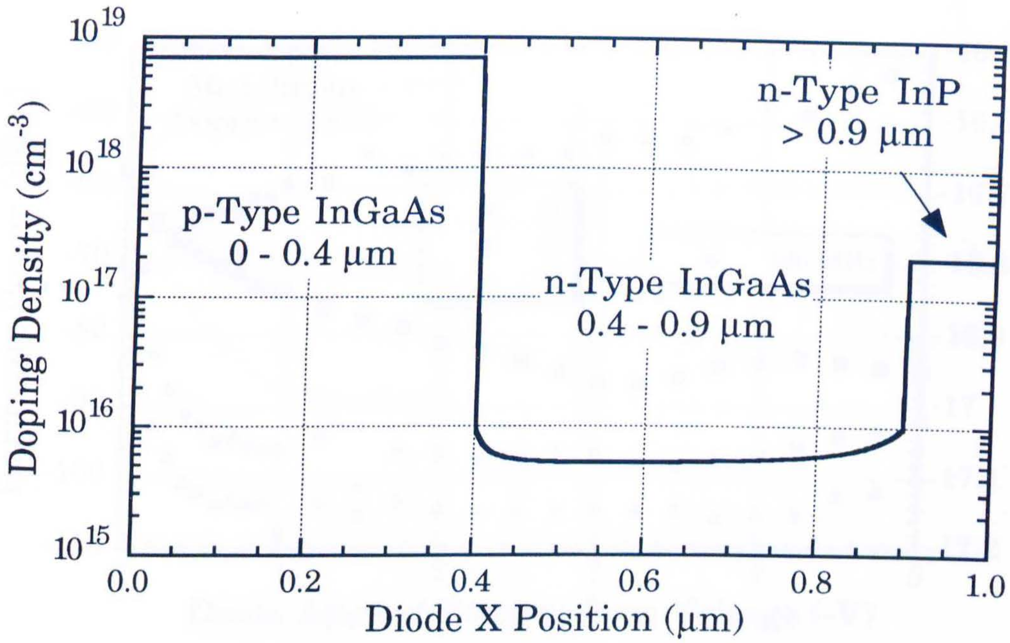

Figure 6.9 Doping profile versus position for the 0.5-μm long intrinsic region device.

like a resistor since the electron current in this region is dominated by the drift current. The simulation bin widths for the 0.5-μm device are about half the size of the bin widths used for the 0.95-μm device.

Figures 6.10 to 6.13 plot the measured NL of this detector with an average PD current of 1 mA and a 100% modulation depth for frequencies of 100 MHz, 1 GHz, 5 GHz, and 10 GHz, respectively. The measurement data shows similar characteristics to the data from the 0.95-μm device (figures 5.1 to 5.4). The NL decreases as the applied voltage increases up to a given voltage where, for higher applied voltages, the NL is approximately unchanged. The transition between these regions are not as distinct compared to the 0.95-μm device; however, the same overall trends are observed. For example, the transition from the two regions should be frequency dependent in such a way that the transition should occur at lower applied voltages for lower frequencies. The transitions occur (fig-

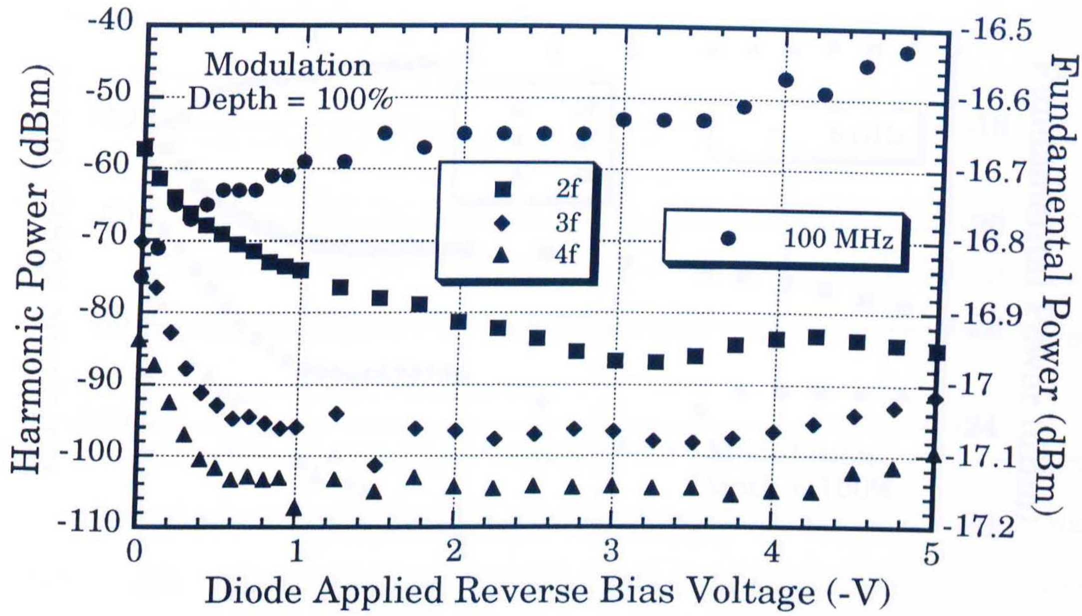

Figure 6.10 Measured fundamental and harmonic power versus detector applied reverse bias voltage at 100 MHz. Fiber pigtailed. Average detector current = 1 mA.

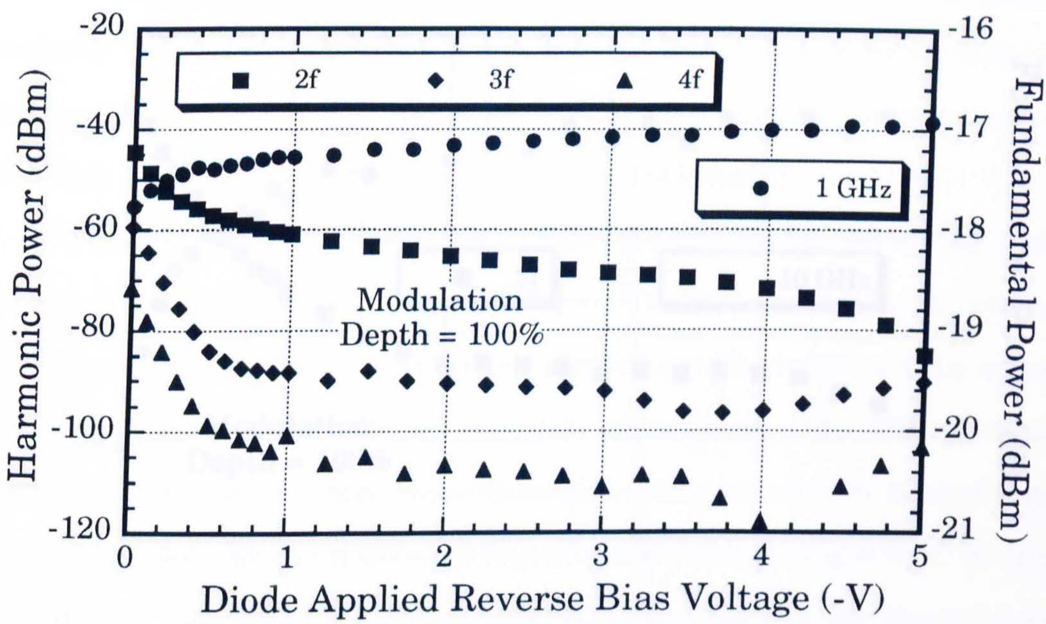

Figure 6.11 Measured fundamental and harmonic power versus detector applied reverse bias voltage at 1 GHz. Fiber pigtailed. Average detector current = 1 mA.

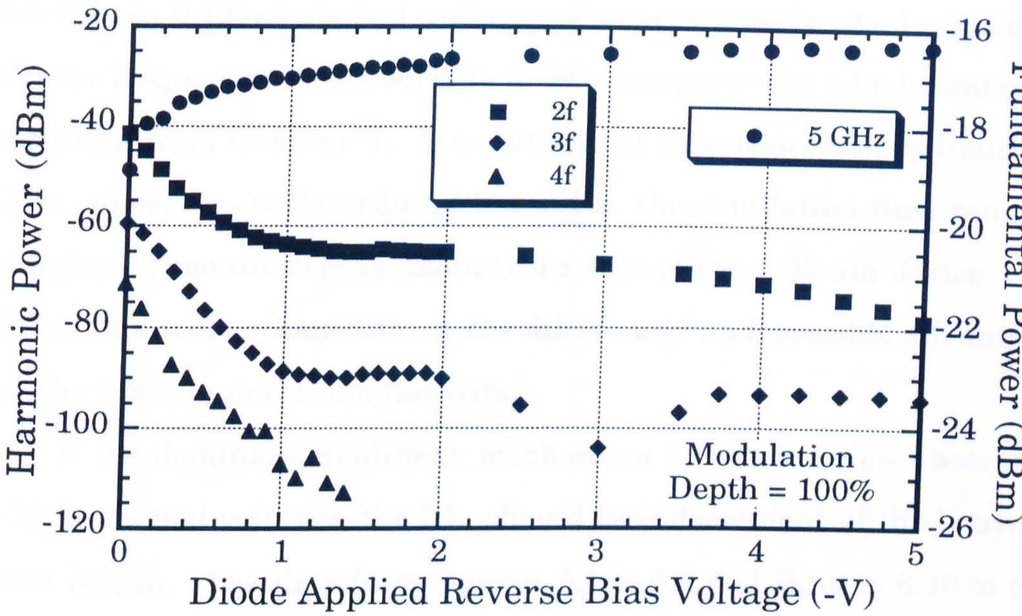

Figure 6.12 Measured fundamental and harmonic power versus detector applied reverse bias voltage at 5 GHz. Fiber pigtailed. Average detector current = 1 mA.

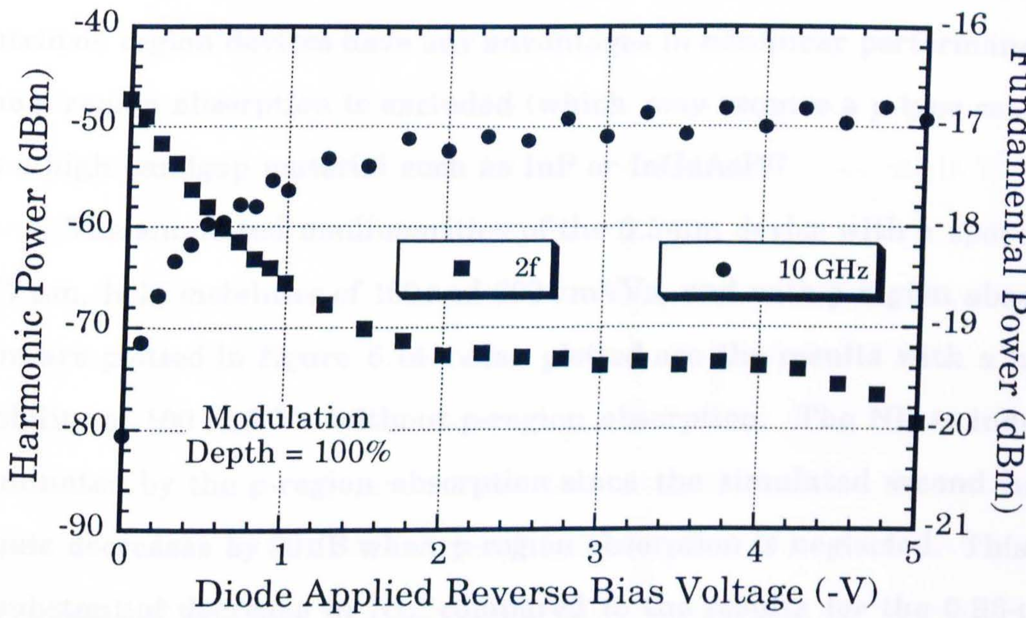

Figure 6.13 Measured fundamental and harmonic power versus detector applied reverse bias voltage at 10 GHz. Fiber pigtailed. Average detector current = 1 mA.

ures 6.10 to 6.13) at applied voltages of approximately -3, -1, -1, and -2 Volts for frequencies of 100 MHz to 10 GHz, respectively, which contradict the results from Chapter V. Simulations on this device will be limited to 5 GHz, since, due to the reduced bin width, the simulation time required for a given time interval is about twice that of the 0.95-μm device. The simulations will concentrate on the differences and possible advantages over the 0.95-μm device nonlinearities.

If the dominant nonlinear mechanism is the p-region absorption for high applied voltages, the NL should be independent of the intrinsic region length. The data from figures 5.1 to 5.4 and figures 6.10 to 6.13 certainly support this hypothesis, with the NL approximately independent of intrinsic region thickness (and frequency) for both devices. Later in this chapter, the 0.2-μm long intrinsic region device will also show similar NL at high applied voltages. A question thus remains: do shorter intrinsic region devices have any advantages in nonlinear performance if the p-region absorption is excluded (which may require a p-type contact in a high bandgap material such as InP or InGaAsP)?

The simulated nonlinearities of the 0.5-μm device with a spot size of 7 μm, hole mobilities of 100 and 200 cm^2/Vs, and with p-region absorption are plotted in figure 6.14. Also plotted are the results with a hole mobility of 100 cm^2/Vs without p-region absorption. The NL is indeed dominated by the p-region absorption since the simulated second harmonic decreases by 60 dB when p-region absorption is neglected. This is a substantial decrease in NL compared to the results for the 0.95-μm device operated at -15 V (figure 5.36) where the decrease was only about 10 dB for the same simulation spot size. The difference in the second har-

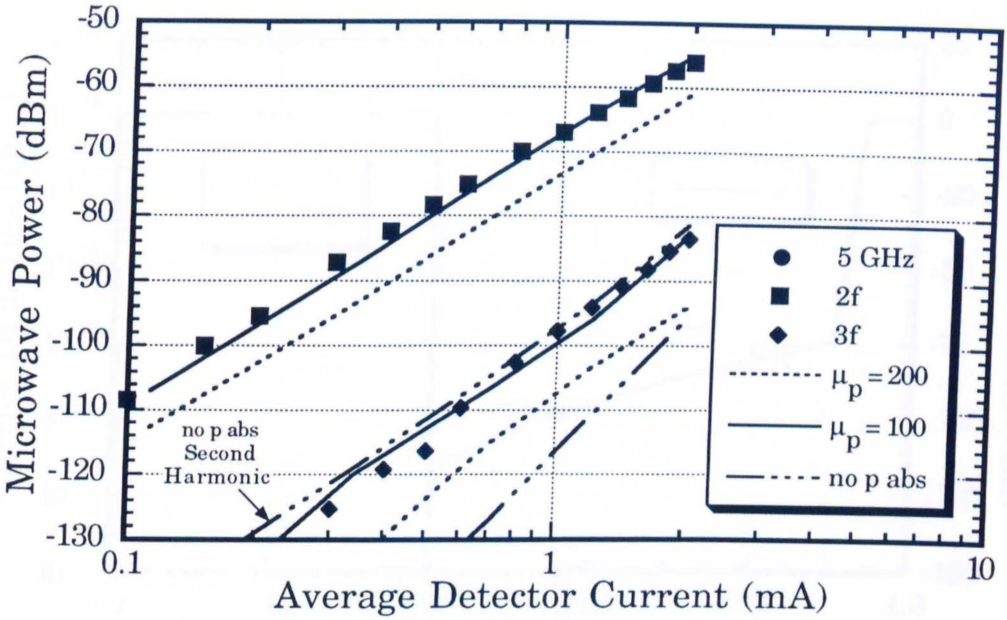

Figure 6.14 Measured and simulated harmonic power versus average detector current at 5 GHz. 0.5-μm long intrinsic region. Applied V = -4 V. Fiber pigtailed. Spot size = 7.0 μm.

monic between the two devices without p-region absorption may be the result of several mechanisms. First, the electric field (figure 6.15) for the 0.5-μm device at -4 V is much flatter across the intrinsic region compared to the electric field (figure 6.6) for the 0.95-μm device at -15 V even though the electric field in the intrinsic region is higher for the 0.95-μm device. Second, the space-charge electric field (figure 6.16) for the 0.5-μm device is about half the space-charge electric field of the 0.95-μm device (figure 6.7) operating with the same current density, since the electrons and holes are separated, on average, by 1/2 the distance in the intrinsic region of the 0.5-μm device compared to the 0.95-μm device. A summary of the simulation and device parameters for the 0.5-μm device are given in figure 6.17.

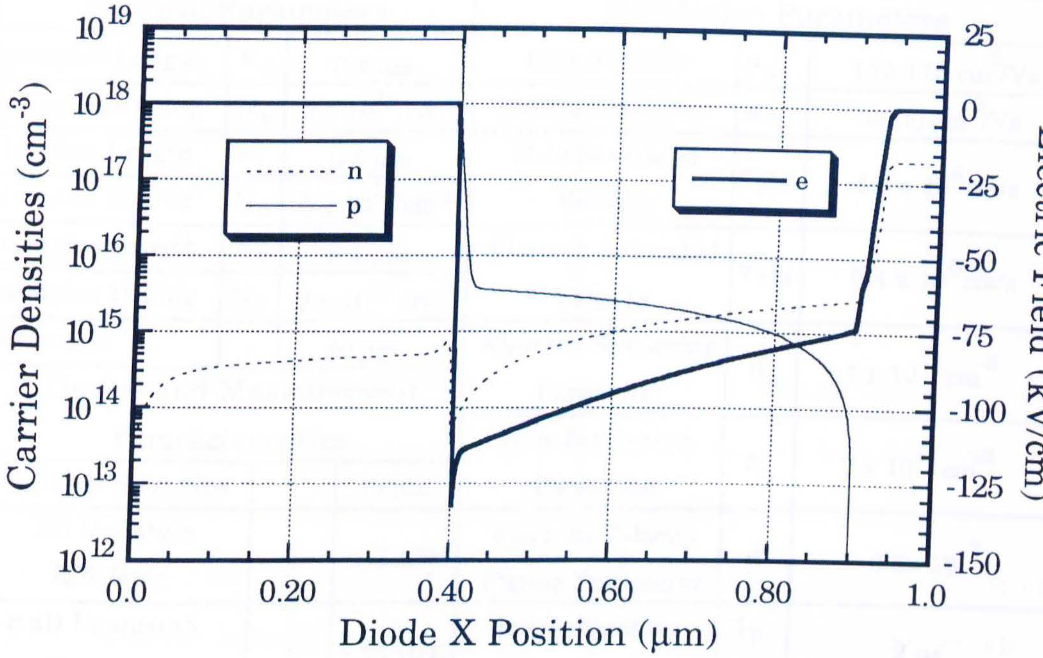

Figure 6.15 Carrier densities and electric field with an average detector current of 1 mA. 0.50-μm long intrinsic region.

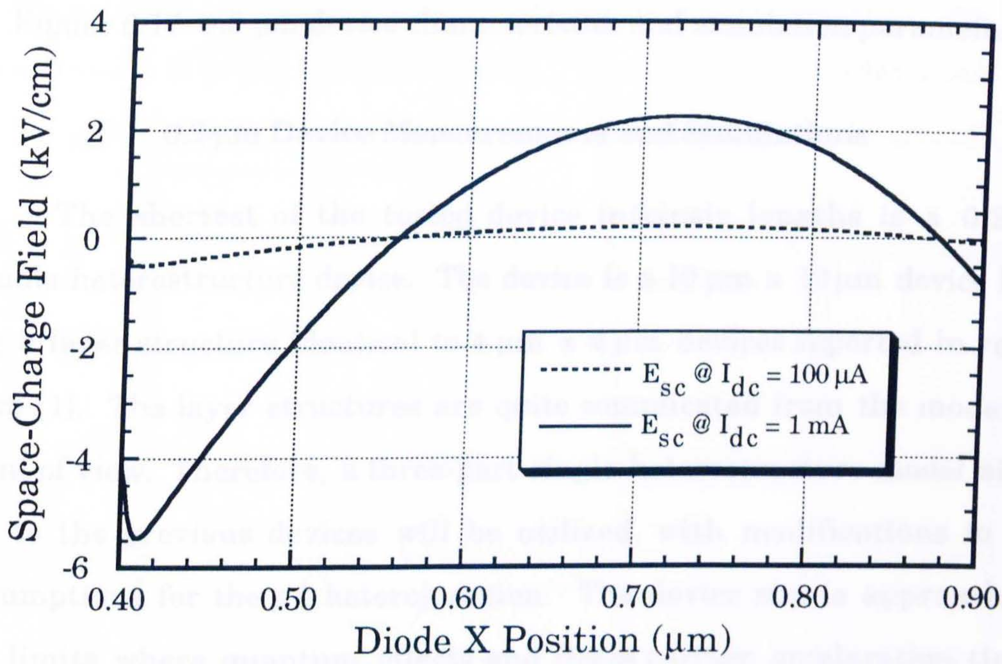

Figure 6.16 Space-charge electric field in the intrinsic region due to the photogenerated carrier densities. Average detector currents of 100 μA and 1 mA. 0.50-μm long intrinsic region.

Physical Parameters		
p-region Length	w_p	0.4 μm
p-region Doping	N_a	7×10^{18} cm^{-3}
i-region Length	w_i	0.5 μm
i-region Doping	N_{di}	5×10^{15} cm^{-3}
n-region Length	w_n	0.1 μm
n-region Doping	N_d	2×10^{17} cm^{-3}
Diameter	-	20 μm

Device and Measurement Characterisitics		
Incident Spot Size	-	10 μm
DC Quantum Efficiency	η	0.3 A/W
-3 dB Frequency Response	-	> 24 GHz
Laser Measurement Wavelength	λ	1319 nm

Simulation Parameters		
Hole Mobility	μ_p	150-175 cm^2/Vs
Electron Mobility	μ_n	8000 cm^2/Vs
Hole Saturated Velocity	v_{phf}	4.8×10^6 cm/s
Electron Saturated Velocity	v_{nhf}	5.4×10^6 cm/s
Electron Scattering Parameter	n_h	1×10^{17} cm^{-3}
Hole Scattering Parameter	p_h	7×10^{17} cm^{-3}
Electron Velocity Fitting Parameter	β	0.8×10^{-7}
Recombination Time, i-region	τ_p τ_n	2 ns
Recombination Time, p-region	τ_p τ_n	100 ps

Figure 6.17 0.5 μm device characteristics and simulation parameters.

0.2-μm Device Measurements and Simulations

The shortest of the tested device intrinsic lengths is a 0.2-μm double-heterostructure device. The device is a 10 μm x 10 μm device having a layer structure identical to 4 μm x 4 μm devices reported in reference [1]. The layer structures are quite complicated from the modeling point of view. Therefore, a three-part single-heterostructure model similar to the previous devices will be utilized, with modifications to the assumptions for the p-i heterojunction. The device size is approaching the limits where quantum effects and finite carrier acceleration times may affect or even dominate carrier transport. Therefore the solutions to the continuity and Poisson's equations with the assumptions made in

Chapters III and IV on such small geometries may not yield accurate results. However, the model will be used to determine just how much information can be obtained without including more difficult (from the modeling point of view) transport mechanisms.

The doping densities[1] for the 0.2-μm device are given in figure 6.18. The heavily-doped p-InP layer, the n-InGaAs intrinsic region, and the n-InP substrate extend from 0 to 0.19 μm, 0.19 to 0.39 μm, and 0.39 to 0.5 μm, respectively. This device differs from the previous two devices by an addition of a second heterostructure consisting of a layer of p-InP between the p-InGaAs cap layer and the n-InGaAs intrinsic region. This additional heterostructure keeps the electrons generated in the p-InGaAs cap layer from traveling into the intrinsic region.[3] The device NL may be characterized by a single heterostructure without absorption in the p-region, since the electrons generated in the p-InGaAs cap layer do not make it to the intrinsic region. The measured fundamental and

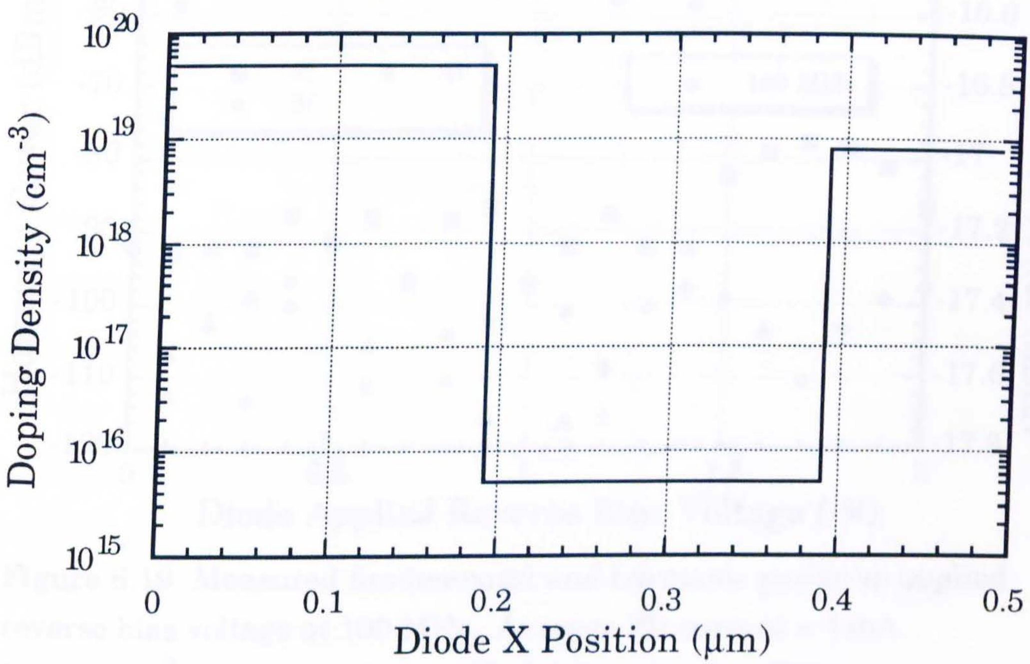

Figure 6.18 Doping density versus position for the 0.2-μm photodiode.

harmonic powers are plotted in figures 6.19 to 6.22 versus applied voltage for frequencies of 100 MHz, 1 GHz, 5 GHz, and 10 GHz, respectively. The nonlinearities are approximately frequency and applied voltage independent, with a second harmonic of -78 dBm for applied voltages greater than 1 V, and slightly better (-80 to -90 dBm) results at 100 MHz. These results are characteristic of the p-region absorption nonlinear mechanism discussed in Chapter V. In Chapter V, the nonlinearity from the p-region absorption was observed to be a function of how many electrons made it to the intrinsic region by moving the focal position of the p-region hole-expansion function and by varying the electron velocity in the p-region. However, the NL may contain a component from the generation and movement of both carriers in the p-InGaAs cap layer, whether or not electrons actually travel into the intrinsic region. Simulations at 5 GHz

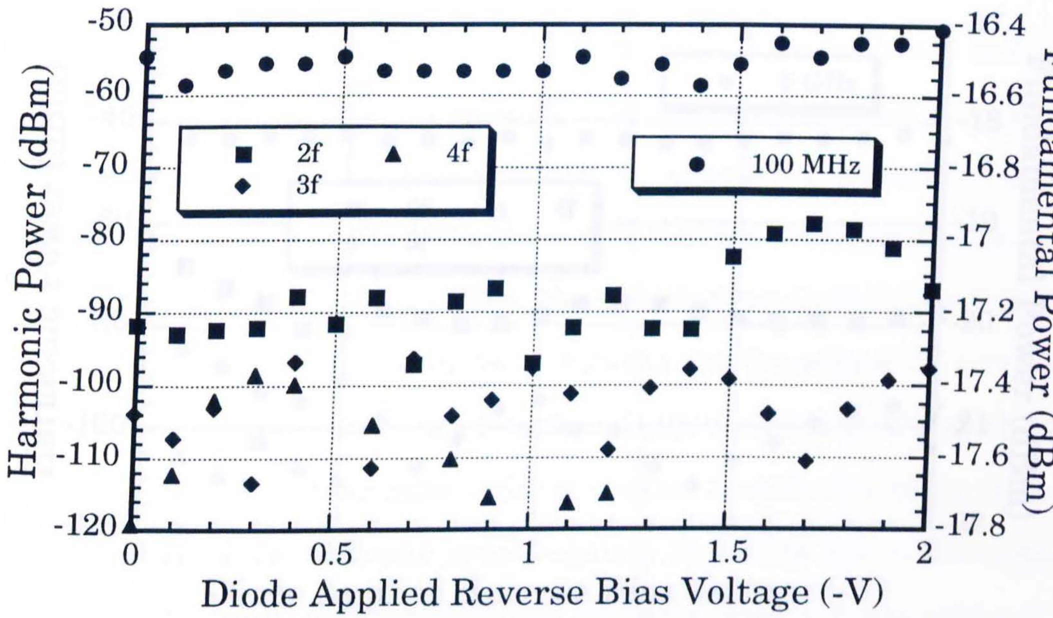

Figure 6.19 Measured fundamental and harmonic power vs applied reverse bias voltage at 100 MHz. Average PD current = 1 mA. Incident e^{-2} spot size = 10 μm. Modulation depth = 100%.

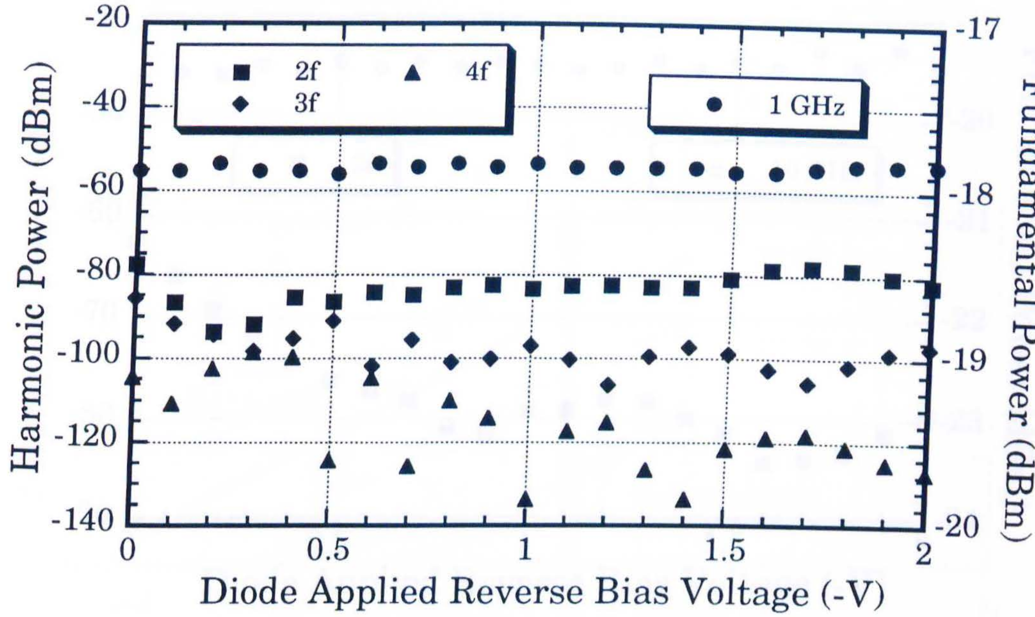

Figure 6.20 Measured fundamental and harmonic power vs applied reverse bias voltage at 1 GHz. Average PD current = 1 mA. Incident e^{-2} spot size = 10 μm. Modulation depth = 100%.

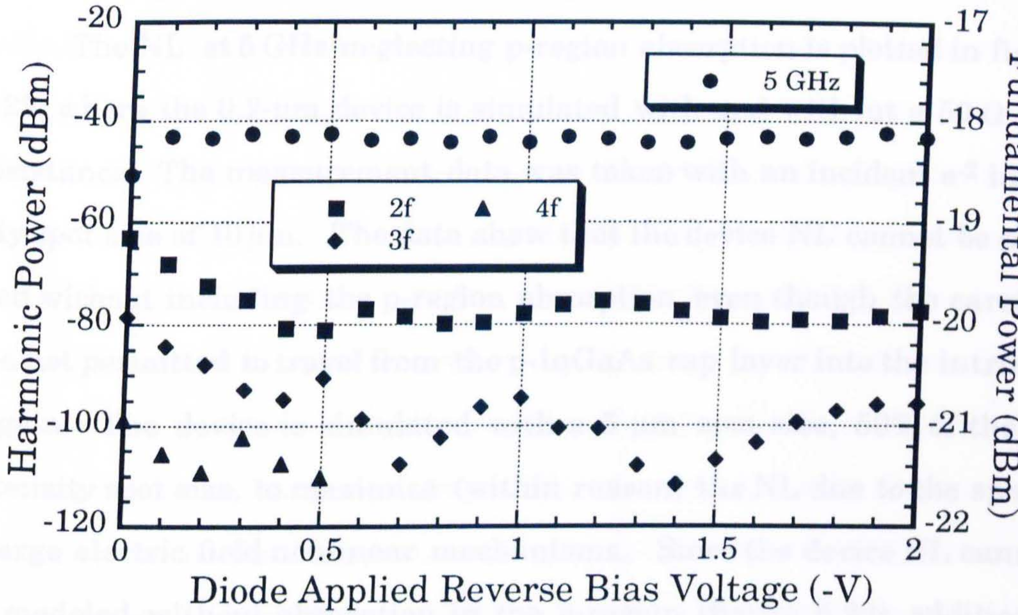

Figure 6.21 Measured fundamental and harmonic power vs applied reverse bias voltage at 5 GHz. Average PD current = 1 mA. Incident e^{-2} spot size = 10 μm. Modulation depth = 100%.

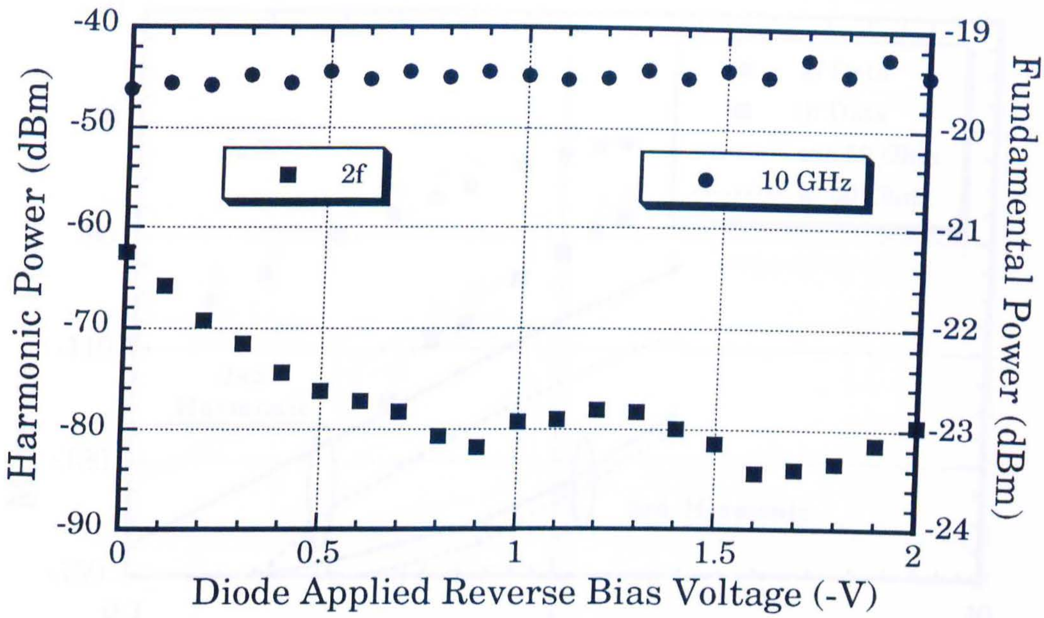

Figure 6.22 Measured fundamental and harmonic power vs applied reverse bias voltage at 10 GHz. Average PD current = 1 mA. Incident e^{-2} spot size = 10 μm. Modulation depth = 100%.

will help to justify or contradict these hypotheses.

The NL at 5 GHz neglecting p-region absorption is plotted in figure 6.23, where the 0.2-μm device is simulated with and without a 50 Ω load resistance. The measurement data was taken with an incident e^{-2} intensity spot size of 10 μm. The data show that the device NL cannot be modeled without including the p-region absorption, even though the carriers are not permitted to travel from the p-InGaAs cap layer into the intrinsic region. The device is simulated with a 5 μm spot size, 50% of the e^{-2} intensity spot size, to maximize (within reason) the NL due to the space-charge electric field nonlinear mechanisms. Since the device NL cannot be modeled without absorption in the p-region (figure 6.23), additional simulations are required to determine the source of the NL behavior.

The nonlinearities may be the result of carrier generation in the p-

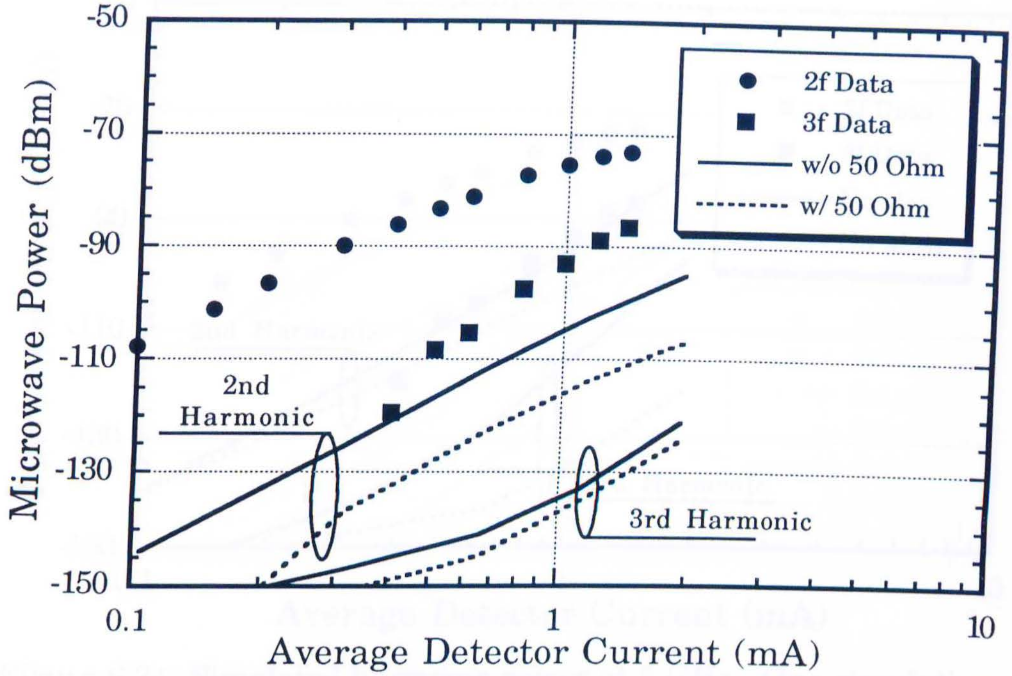

Figure 6.23 Measured and simulated harmonic power vs current at 5 GHz neglecting p-region absorption. Simulated with and without a 50 Ohm load resistor. Spot size = 5 μm. Applied V = -2 V.

InGaAs cap layer even if the electrons do not enter the intrinsic region. To test this hypothesis, two additional simulations are needed. One simulation allows p-region absorption in the entire region except for 20 nm which is nearest to the intrinsic region, allowing the electrons generated in the p-region to recombine before they reach the intrinsic region. The second simulation allows absorption in the entire p-region; however, the electrons are prohibited from leaving the p-region, which is similar to the effect of the second heterojunction. The simulated results (figure 6.24) demonstrate that the NL still cannot be modeled simply by the generation and movement of electrons or holes in the p-region, which implies that the electrons must travel into the intrinsic region to effect the device NL.

A closer look at the device[1] reveals that between the intrinsic region

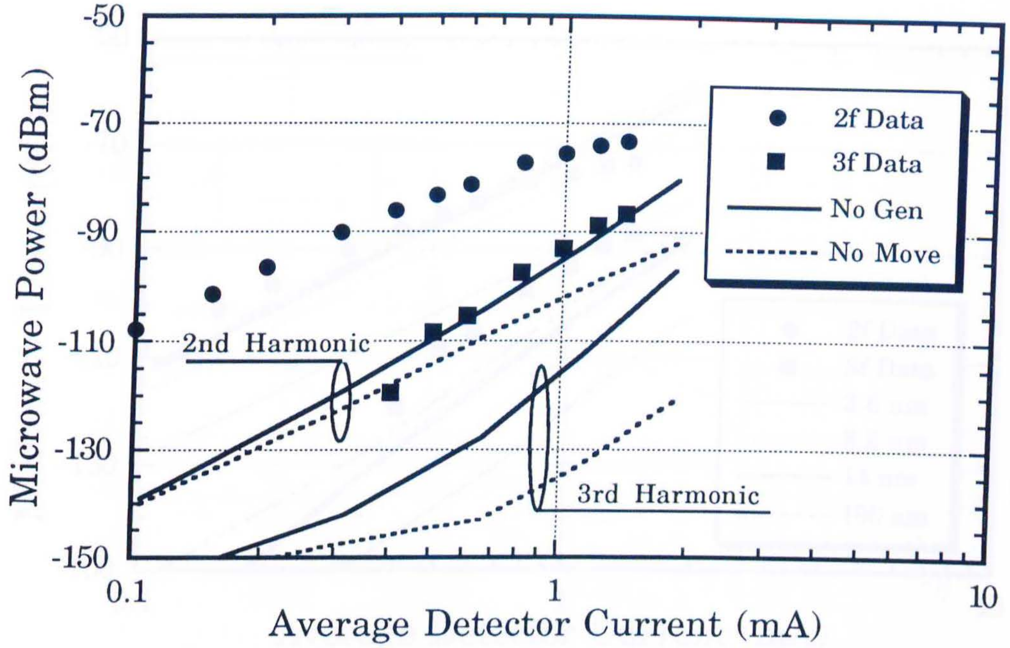

Figure 6.24 Simulated harmonic power at 5 GHz. One simulation excludes genereration in the p-region near the p-i interface, and the second simulation prohibits electron flow from the p- to the i-region.

(n-InGaAs) and the second heterostructure (p-InP), the device contains a graded bandgap layer (GBL). The GBL consists of alternating layers totaling 3.6 nm of InGaAs and InP which help to lower the band discontinuities and prevent hole trapping at the heterojunction interface.[4] The depletion depth into the p-region is only about 1 nm due the high doping level (8 x 10^{18} cm^{-3}) of the InP, therefore much of the InGaAs here may be undepleted. The device cannot be thought of as a simple p-n junction in this region due to the small thicknesses (< 1 nm) of the layers. However, to determine how much undepleted InGaAs is necessary to yield the NL in figure 6.23, the PD is simulated again, this time allowing p-region absorption near the p-i interface. The simulated NL in figure 6.25 consists of four different lengths (3.6, 8.2, 14, and 190 nm) of absorbing p-InGaAs located between the p-InP and the intrinsic region. The results

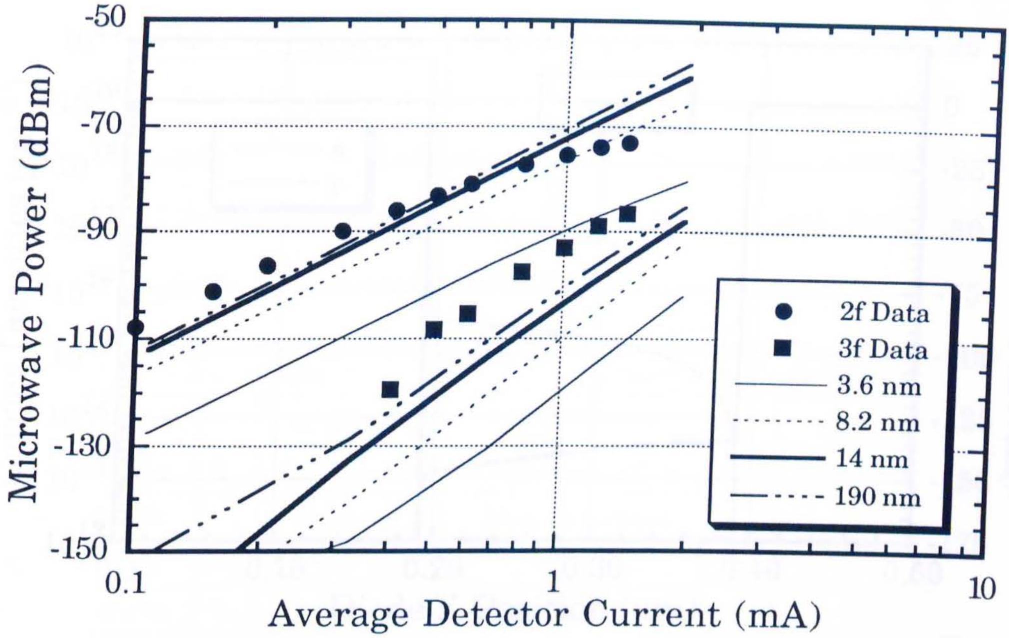

Figure 6.25 Measured and simulated harmonic power vs current at 5 GHz. Simulations for various lengths of absorbing p-InGaAs next to the i-region. 0.2-μm long intrinsic region. Spot size = 7 μm.

in figure 6.25 suggest that only about 8 to 14 nm of essentially undepleted absorbing material next to the intrinsic region is required to model the device nonlinearities.

Although the device only contains 3.6 nm of InGaAs near the intrinsic region, the NL may still be solely from this region. The NL may be enhanced by hole trapping at the heterojunction interface, which may account for the decrease in the second harmonic at higher currents due to filling of the trap sites. However, trapping mechanisms are not considered in the present model. Similar reductions in the second harmonic at higher currents are observed at 100 MHz, 1 GHz, and 10 GHz.

The carrier densities and electric field for this device are plotted in figure 6.26 for an applied voltage of -2 V and 1 mA of average current. The space-charge electric field is plotted in figure 6.27 for PD currents of

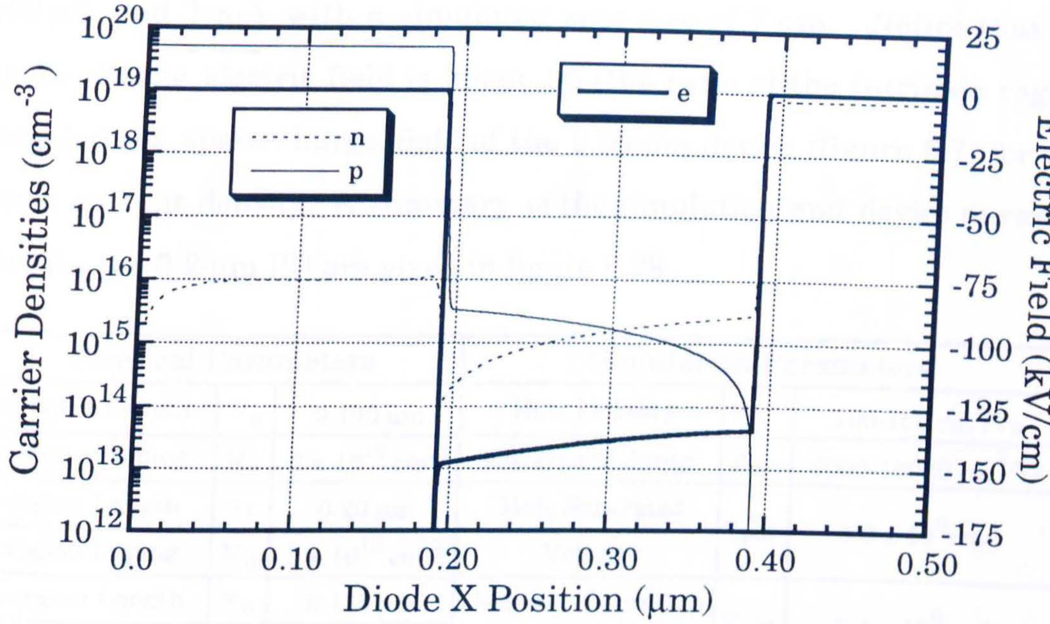

Figure 6.26 Carrier densities and electric field with an average PD current of 1 mA. 0.20-μm long intrinsic region. Simulated spot size = 7 μm. Applied voltage = -2 V.

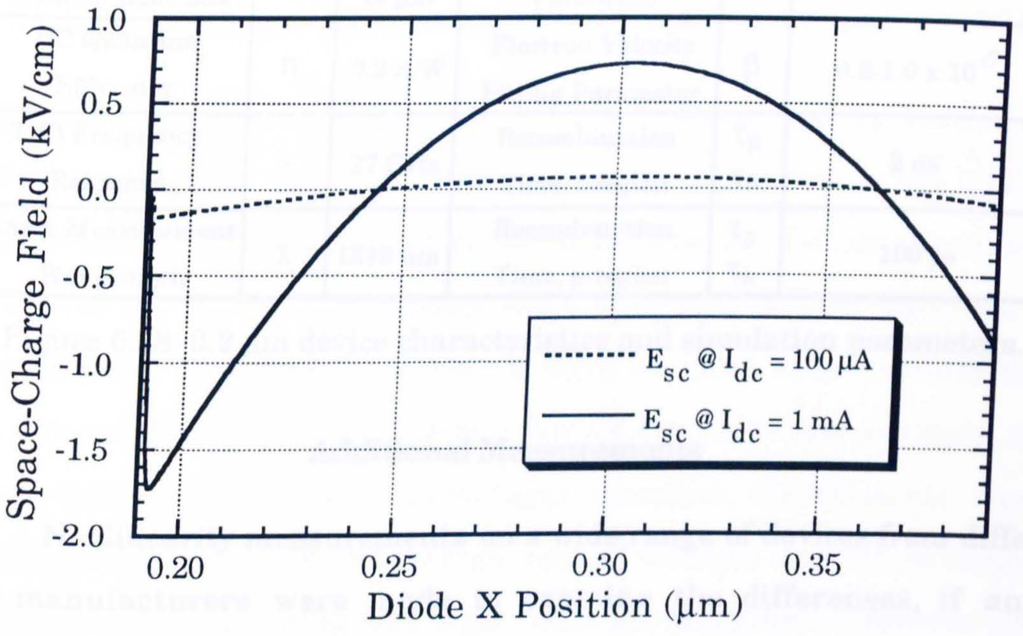

Figure 6.27 Space-charge electric field in the intrinsic region due to the photogenerated carrier densities. Average PD currents of 100 μA and 1 mA. 0.2-μm long intrinsic region. Spot size = 7 μm.

100 μA and 1 mA with a simulated spot size of 7 μm. Notice that the space-charge electric field is about 1/5 (the ratio of the intrinsic region lengths) the space-charge field of the 0.95-μm device (figure 6.7) for the same current density. A summary of the simulation and device parameters for the 0.2-μm PD are given in figure 6.28.

Physical Parameters			Simulation Parameters		
p-region Length	w_p	0.190 μm	Hole Mobility	μ_p	100-150 cm^2/Vs
p-region Doping	N_a	2×10^{19} cm^{-3}	Electron Mobility	μ_n	8000-10000 cm^2/Vs
i-region Length	w_i	0.20 μm	Hole Saturated Velocity	v_{phf}	4.8×10^6 cm/s
i-region Doping	N_{di}	5×10^{15} cm^{-3}			
n-region Length	w_n	0.115 μm	Electron Saturated Velocity	v_{nhf}	5.4×10^6 cm/s
n-region Doping	N_d	2×10^{17} cm^{-3}			
Diameter	-	10 μm	Electron Scattering Parameter	n_h	1×10^{17} cm^{-3}
Device and Measurement Characterisitics			Hole Scattering Parameter	p_h	7×10^{17} cm^{-3}
Incident Spot Size	-	10 μm			
DC Quantum Efficiency	η	0.3 A/W	Electron Velocity Fitting Parameter	β	$0.8\text{-}1.0 \times 10^{-7}$
-3 dB Frequency Response	-	27 GHz	Recombination Time, i-region	τ_p τ_n	2 ns
Laser Measurement Wavelength	λ	1319 nm	Recombination Time, p-region	τ_p τ_n	100 ps

Figure 6.28 0.2 μm device characteristics and simulation parameters.

Additional Measurements

Nonlinearity measurements on a wide range of devices from different manufacturers were made to examine the differences, if any, between devices. Figure 6.29 is a listing of these measurements for eight devices where the measurements have been reduced to seven characteristic numbers. These characteristic numbers are the second and third

Detector	1	2	3	4	5	6	7	8
DC Quantum Efficiency (A/W)	0.71	0.30	0.30	0.78	0.85	0.21	0.70	0.84
50 MHz Quantum Efficiency (A/W)	0.71	0.30	0.30	0.78	0.70	0.10	0.70	0.76
Bandwidth -3 dB (GHz)	20	>24	27	18	14	22	4	12
Bandwidth -6 dB (GHz)	>24	>24	>40	24	20	26	10	16
Applied Voltage (-V) (Min 2f @ 5 GHz)	10	1	0.5	8	15		Not Clear	
100 MHz 2f @ 1 mA (dBc)	-76	-68	-74	-54	-48	-60	-38	-70
100 MHz 3f @ 1 mA (dBc)	-94	-79	-86	-58	-78	-77	-42	-100
1 GHz 2f @ 1 mA (dBc)	-72	-55	-63	-45	-50	-57	-30	-60
1 GHz 3f @ 1 mA (dBc)	-99	-73	-83	-57	-87	-73	-38	-92
5 GHz 2f @ 1 mA (dBc)	-71	-55	-62	-68	-54	-47	-48	-61
5 GHz 3f @ 1 mA (dBc)	-86	-75	-82	-80	-89	-68	-63	-90
10 GHz 2f @ 1 mA (dBc)	-76	-57	-61	-55				-65

Figure 6.29 Measurement data for eight photodetectors. Detectors three through eight are from six different manufacturers.

harmonics of 100 MHz, 1 GHz, and 5 GHz and the second harmonic of 10 GHz, all measured at 1 mA, 100% modulation depth, and at the highest applied detector voltage allowed by the manufacturer. Detectors one, two, and three are the 0.95-μm, 0.5-μm and 0.2-μm long devices discussed in this chapter. Detectors four through eight are from other manufacturers. Variations in the NL of up to a few dB can occur (for example, see figure 6.10 or 6.19) at high bias voltages; therefore, the harmonic levels stated are averages of the NL at high applied voltages and can be considered to have an error of up to ± 5 dB. With the exception of detector one, no device appears to have lower NL at all four frequencies. The results in figure 6.29 help to justify that the NL are intrinsic properties of PDs and not isolated observations in mesa-type devices or devices from a particular manufacturer.

Summary

In this chapter, the device characteristics and best-fit simulation parameters for three intrinsic region length devices were presented. Simulations of the 0.5-μm and 0.2-μm PDs at high applied voltages and 5 GHz confirm that the NL is dominated by p-region absorption near the intrinsic region similar to the results obtained for the 0.95-μm long devices in Chapter V. It was found that only 8 to 14 nm of undepleted absorbing material next to the intrinsic region is sufficient to result in a second harmonic of -60 dBc at 1 mA. The photogenerated space-charge electric field was observed to scale inversely proportional to the intrinsic region thickness for a given incident spot size. This implies that for a given incident optical spot size, shorter intrinsic region PDs will have lower NL associated with the change in carrier velocities. NL measurements from other devices at high applied voltages confirm that these effects are inherent properties of currently available devices.

1. Y.G. Wey, *et al.*, "Ultrafast Graded Double-Heterostructure GaInAs/InP Photodiode," *Appl. Physics Lett.*, **58**, p. 2156, 1991.
2. P. Hill et al., "Measurement of Hole Velocity in n-Type InGaAs," *Appl.Physics Lett.*, **50**, p. 1260, 1987.
3. Y.G. Wey, "High-Speed Double Heterostructure GaInAs/InP p-i-n Photodiodes Theory, Fabrication and Measurement," University of California Santa Barbara Ph.D. Dissertation, 1993.
4. J.G. Wasserbauer, *et al.*, "Specific Contact Resistivity of InGaAs/InP p-Isotype Heterojunctions," *Electron. Lett.*, **28**, p. 1568, 1992.

VII. HIGH POWER DENSITY NONLINEARITIES: A 0.95-μm DEVICE

Introduction

This chapter will study p-i-n photodiode nonlinearities under high power density conditions. High optical power densities obtained from the focusing of light into a PD or from high incident optical powers result in large space-charge densities (~ 10^{16} cm^{-3}), which cause the electric field to redistribute and collapse over part of the intrinsic region. These effects can occur when a 0.95-μm long intrinsic region PD, biased at -5 V, is illuminated with power densities greater than 3 kW/cm^2. The nonlinear effects associated with high power densities can result in additional NL effects distinct from those of Chapter V. At high power densities the PD can cause highly detrimental system characteristics, not only substantially higher harmonic content, but also a reduction in diode high-frequency responsivity and (time domain) phase shifts. This decrease in diode responsivity is shown (below) to be due to an increase in transit across areas within the intrinsic region which have low electric fields and unsaturated carrier velocities. The redistributed intrinsic region electric field also produces a radial electric field component. This is shown to result primarily in electron movement towards the center of the device, thereby increasing the electron density along the axis of the incident signal.

To avoid the high power density conditions, why not just increase the incident optical spot size? To avoid reducing the net quantum efficiency, an increase in spot size must be limited to the active area.

Furthermore, for high frequency devices the active area must be small to achieve low capacitance. For example, 20-GHz devices are limited to maximum device diameters of about 30 microns. With the optical power levels considered here, a 30-μm device diameter is large enough to avoid the high carrier densities under investigation in this chapter. Nevertheless, measurements and simulations will be presented in this chapter for smaller incident spot sizes (< 10 μm) to study and understand the high-power-density characteristics of PDs. The results obtained from measurements and simulations at small spot sizes will thus provide insight into the nonlinear effects which may occur in the next generation of high current (10 to 100 mA) 20-GHz PDs; for ultra-high speed (> 100 GHz), small diameter (< 4 μm) PDs; and in current PDs with excessive incident optical powers (> 100 mW).

Measurement Data

Measurements of the frequency response with increasing levels of optical power reveal the onset of high power nonlinearities. The frequency response of a 0.95-μm PD plotted relative to the response of the device at low average currents is shown in figure 7.1. The average currents in the device are 800 and 1000 μA, the applied bias is -5 V, the modulation depth is 100%, and the measured e^{-2} spot size of the incident optical beam is 5.75 ± 0.25 μm. The response reductions observed in figure 7.1 are very unexpected since the electric field (see figure 5.15 or 7.11) is high enough in the depletion region to nearly saturate the carrier velocities and the load resistance (50 Ω) is too low to result in a sufficient drop of the externally applied bias voltage. Measurements of the low-power-density response confirm the presence of a fully-depleted intrinsic region since

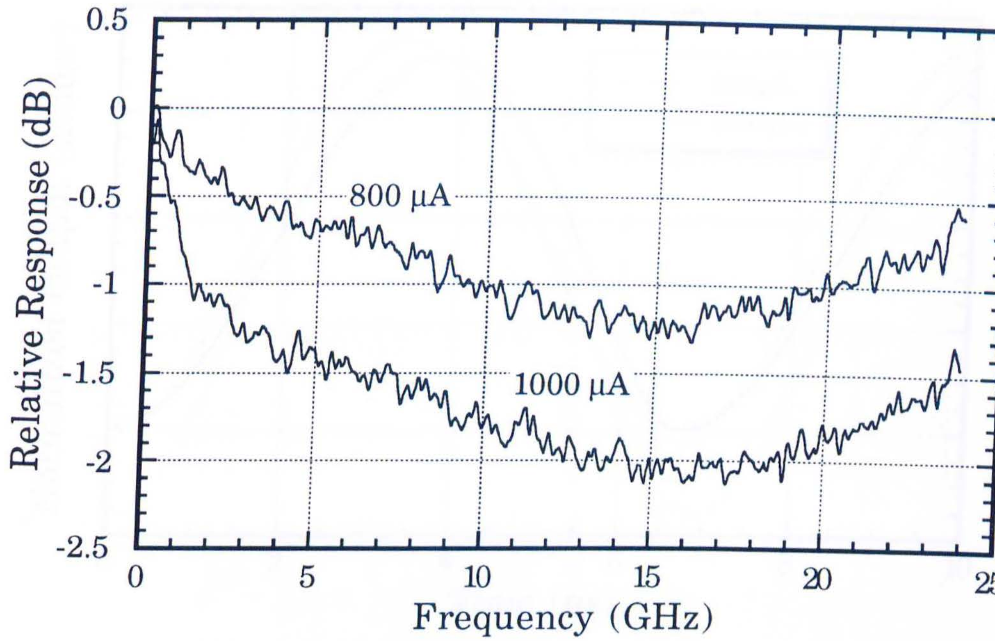

Figure 7.1 Large-signal relative frequency response of a 0.95 μm PD. Average currents of 800 and 1000 μA with an e^{-2} incident spot size of 5.75 ± 0.25 μm. 200 point resolution. 100% modulation depth.

the device response at 20 GHz does not improve by more than 0.5 dB for applied bias voltages above -5 V. From figure 7.1 another anomaly must be explained: the response at frequencies between 10 and 20 GHz are more affected than for frequencies below 10 GHz and above 20 GHz.

To gain insight into this nonlinear behavior, the lasers in figure 2.1 were phased-locked to provide ± 1° phase stability and the time domain output of the PD was observed on an oscilloscope at low and high powers. The frequency response in figure 7.1 shows the response just starting to drop between 100 and 500 MHz. The sinusoidal outputs at 150 MHz with 100 and 1400 μA of average PD current with a 100% modulation depth are plotted in figure 7.2. The amplitudes are normalized such that the sinusoids contained the same energy during a single cycle, since the average PD current is approximately linear (1%) with the average optical power.

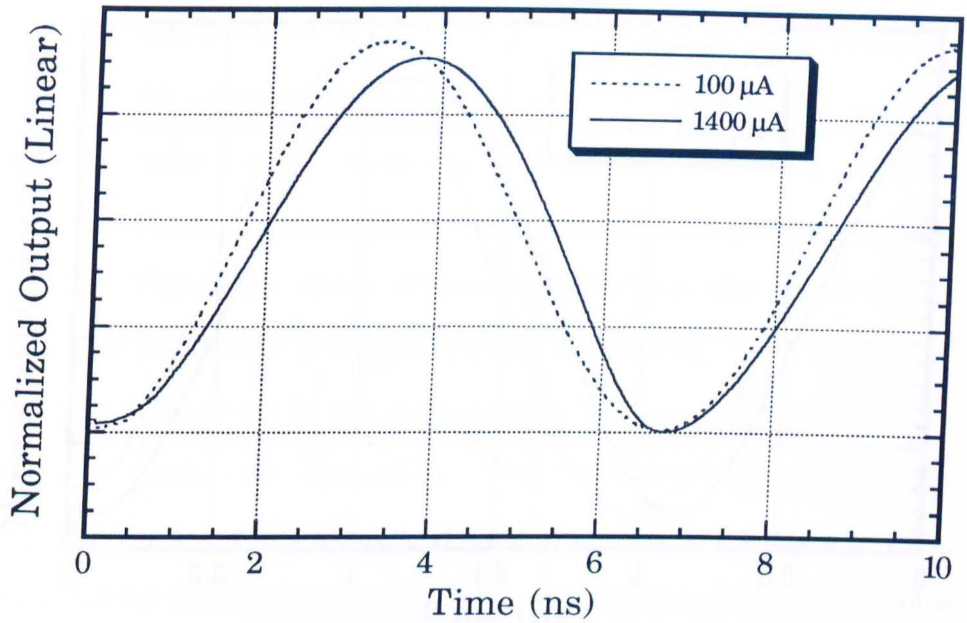

Figure 7.2 Normalized large-signal sinusoidal output of a 0.95-μm -5 V-biased PD at 150 MHz. Average currents of 100 and 1400 μA with an e^{-2} incident spot size of 5.75 ± 0.25 μm. 100% modulation depth.

Figure 7.2 shows that the peak of the high-current sinusoid is delayed from the low-current sinusoid by up to 400 ps, a factor of 20 greater than the low-power transit time of the device. 150 MHz was specifically chosen for this observation because the sinusoidal output was observed to decrease very rapidly and recover just before the start of a new cycle.

When the frequency is increased to 500 MHz, the high-current signal (figure 7.3) shows a large phase shift relative to the low-current signal and some distortion. The distortion is more subtle in this case as compared to the 150 MHz case since the PD response at 500 MHz is 0.5 dB down from the low-power response and no longer recovers before the start of a new cycle. However, it is apparent that the top half of the 500-MHz high-current sinusoid is wider than the lower half. If the incident power density is decreased by keeping the optical power the same and

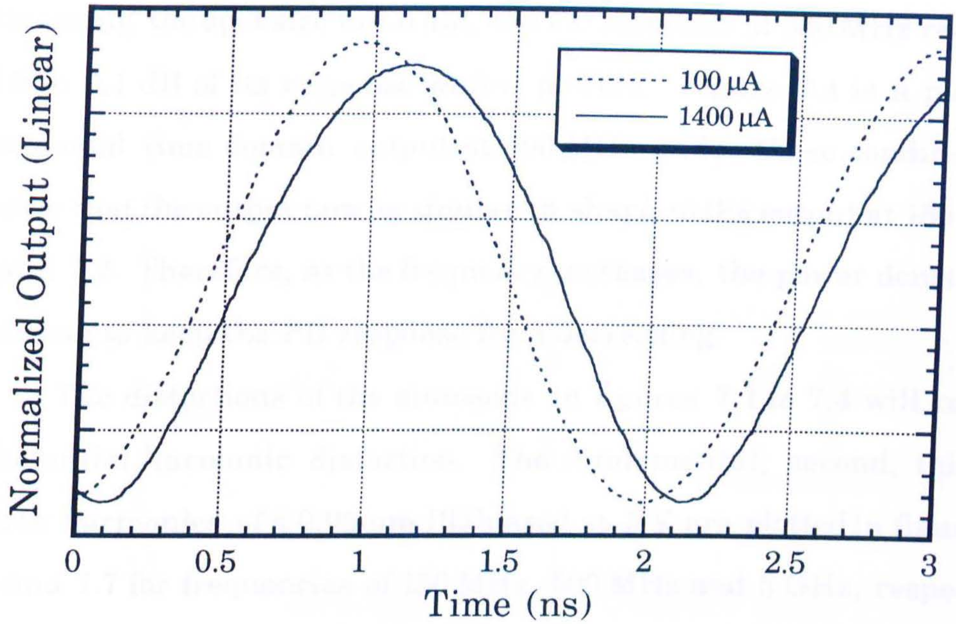

Figure 7.3 Normalized large-signal sinusoidal output of a 0.95-μm -5 V-biased PD at 500 MHz. Average currents of 100 and 1400 μA with a e^{-2} incident spot size of 5.75 ± 0.25 μm. 100% modulation depth.

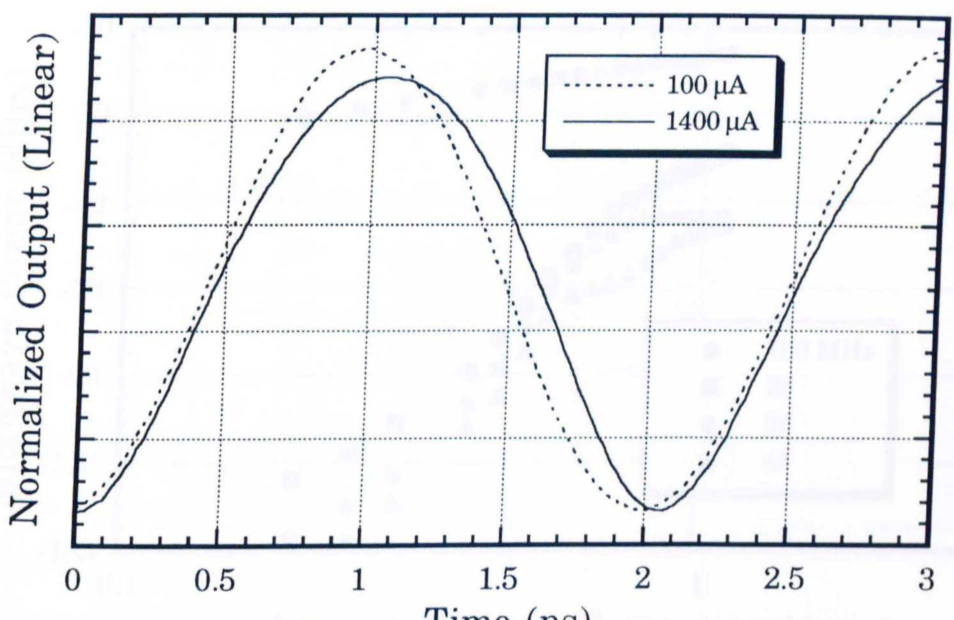

Figure 7.4 Normalized large-signal sinusoidal output of a 0.95-μm -5 V-biased PD at 500 MHz. Average currents of 100 and 1400 μA with an e^{-2} incident spot size of 7.5 ± 0.5 μm. 100% modulation depth.

increasing the spot size to 7.5 μm, the PD response at 500 MHz recovers to within 0.1 dB of its response at low powers. Figure 7.4 is a plot of the sinusoidal time domain output at 500 MHz under these conditions and shows that the output now is similar in shape to the output at 150 MHz in figure 7.2. Therefore, as the frequency increases, the power density must decrease to keep the PD response from decreasing.

The distortions of the sinusoids in figures 7.1 to 7.4 will result in substantial harmonic distortion. The fundamental, second, third and fourth harmonics of a 0.95-μm PD biased at -5 V are plotted in figures 7.5, 7.6 and 7.7 for frequencies of 150 MHz, 500 MHz and 5 GHz, respectively. The growth rate in the harmonic content differs considerably from a power-law dependence. The second harmonic increases from -110 dBm at a current of 100 μA to nearly -40 dBm at 1 mA for all three frequen-

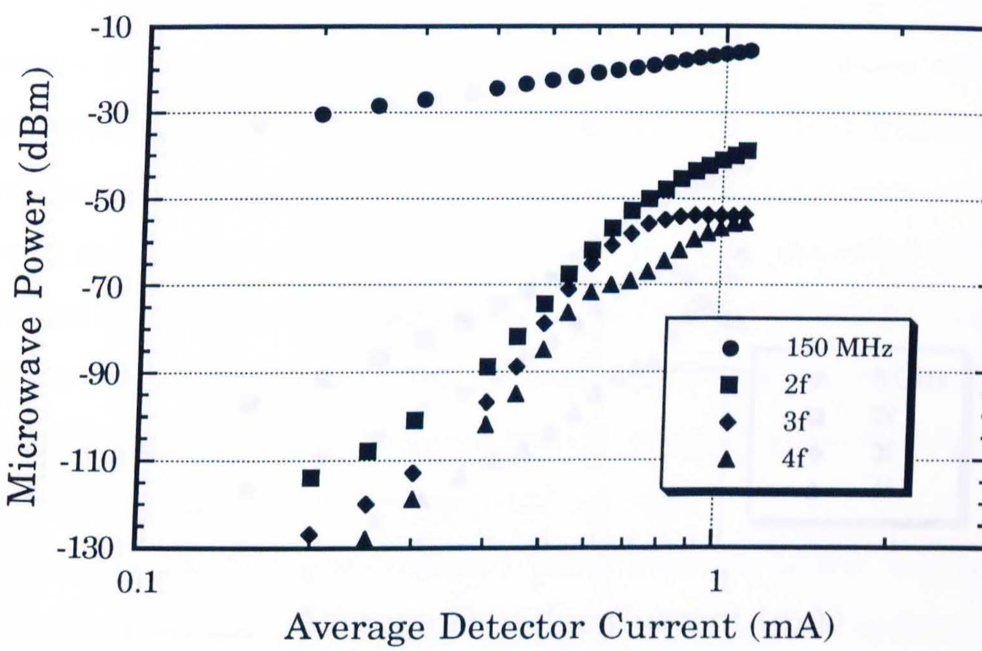

Figure 7.5 Fundamental and harmonic power vs average PD current for a -5 V-biased 0.95-μm PD. 100% modulation depth. Incident e^{-2} spot size of 5.75 ± 0.25 μm. 150 MHz fundamental frequency.

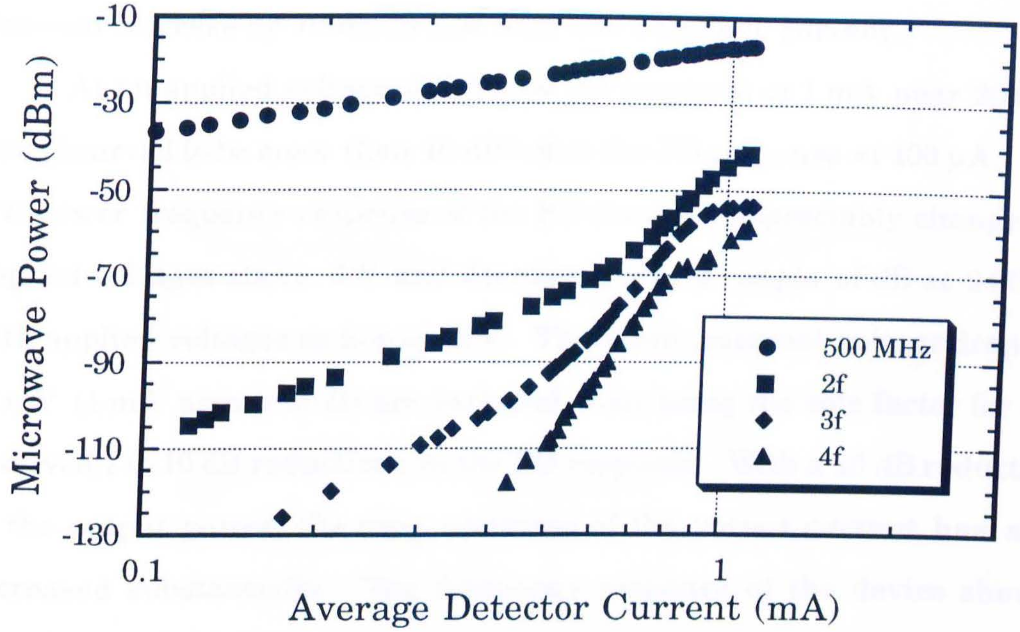

Figure 7.6 Fundamental and harmonic power vs average PD current for a -5 V-biased 0.95-μm PD. 100% modulation depth. Incident e^{-2} spot size of 5.75 ± 0.25 μm. 500 MHz fundamental frequency.

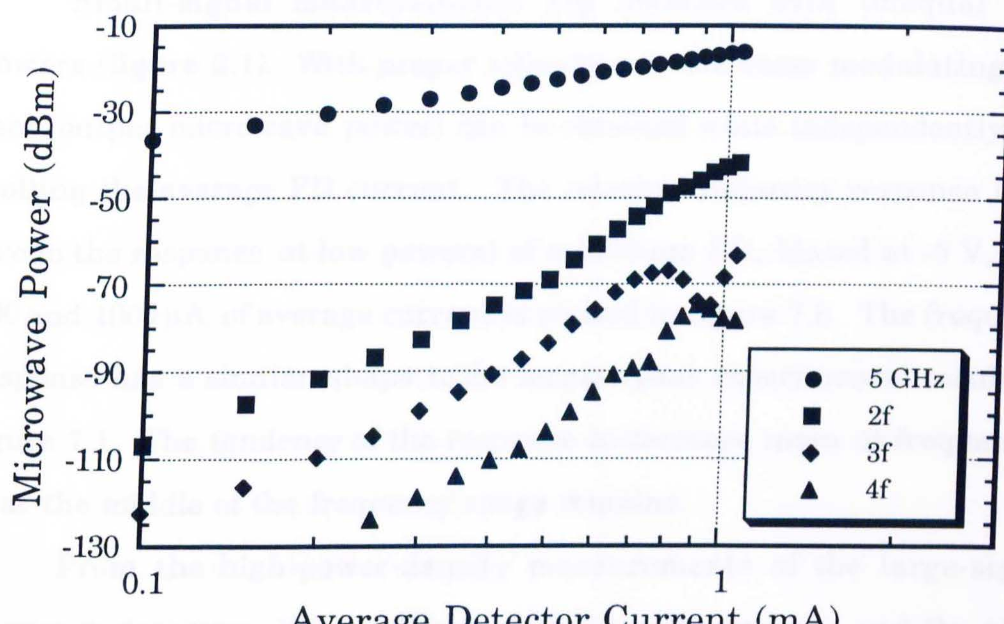

Figure 7.7 Fundamental and harmonic power vs average PD current for a -5 V-biased 0.95-μm PD. 100% modulation depth. Incident e^{-2} spot size of 5.75 ± 0.25 μm. 5 GHz fundamental frequency.

cies—an increase by 70 dB in less than one decade of current.

At an applied voltage of -3 V, the PD response at 1 mA near 20 GHz was observed to be more than 10 dB below the PD response at 100 μA. The low-power frequency response of the PD does not appreciably change for applied voltages above -5 V and decreases only a couple of dB at 24 GHz with applied voltages as low as -2 V. Therefore, external voltage drops of 50 mV (1 mA across 50 Ω) are excluded from being the sole factor for the observed 1 to 10 dB reductions in the PD response. With a 10 dB reduction in the output power, the time variation of the output current has also decreased substantially. The frequency response of the device should therefore be dependent, not on the time varying PD current, but on the average PD current. To verify this hypothesis the frequency response is measured at high power densities under small-signal conditions.

Small-signal measurements are obtained with unequal laser powers (figure 2.1). With proper adjustment, the same modulating current (output microwave power) can be obtained while independently controlling the average PD current. The relative frequency response (relative to the response at low powers) of a 0.95-μm PD, biased at -5 V, with 800 and 1000 μA of average current is plotted in figure 7.8. The frequency response has a similar shape to the large-signal experimental results in figure 7.1. The tendency of the response to decrease more at frequencies near the middle of the frequency range remains.

From the high-power-density measurements of the large-signal frequency response, the small-signal frequency response, and the sinusoidal time domain distortions with the corresponding harmonics, several conclusions can be formulated.

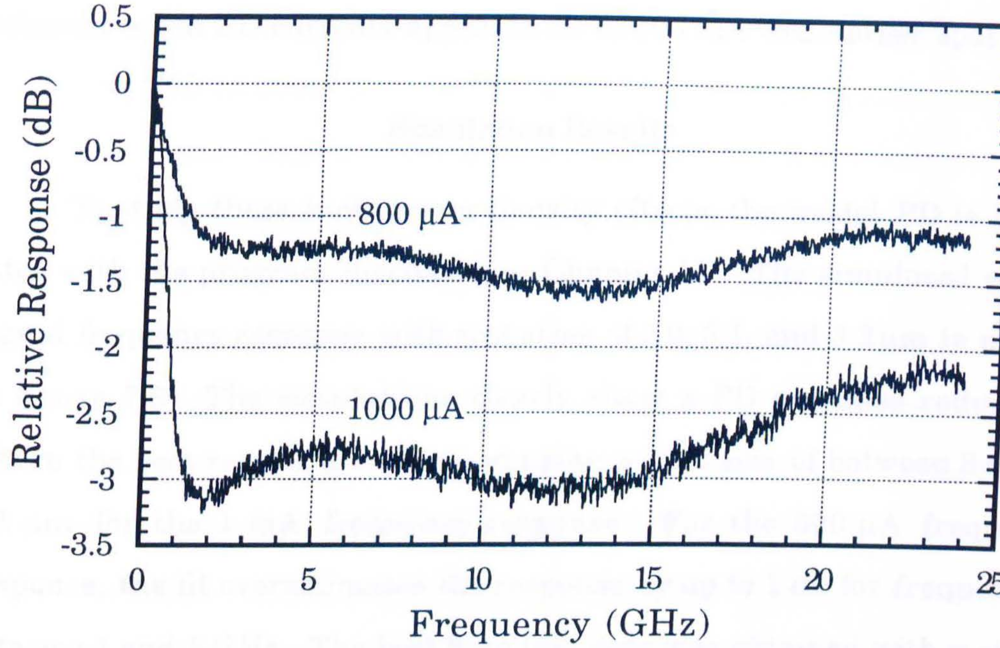

Figure 7.8 Small-signal relative frequency response of a -5 V-biased 0.95-μm PD. Average PD currents of 800 and 1000 μA with an e^{-2} incident spot size of 5.75 ± 0.25 μm. 1000 point resolution.

1) Once the carriers are generated, most exit the intrinsic region before recombining, since measurements of the average current are linear with incident power.

2) The effect must be internal, since the voltage drop in the external circuit is insufficient to explain the observed effects.

3) If most of the generated carriers exit the intrinsic region, with many of them delayed by several hundreds of picoseconds, the intrinsic region electric field must have redistributed sufficiently to cause the observed increase in carrier transit times.

Simulations will provide specific information about the high-power-density carrier dynamics and the electric field distributions in the intrinsic region. This information can then be used for predicting device behavior when PD currents approach 10 to 100 mA with larger spot sizes.

Simulation Results

To study these high power density effects, the model PD is simulated with the program discussed in Chapter I V. The simulated small-signal frequency response with spot sizes of 3.0, 3.1, and 3.2 μm is plotted in figure 7.9. The simulations clearly show a PD response reduction, where the best results are obtained using a spot size of between 3.0 and 3.1 μm for the 1 mA frequency response. For the 800 μA frequency response, the fit overestimates the response by up to 1 dB for frequencies between 1 and 5 GHz. The best fit to this data was obtained with a simulated spot size of only 53% of the e^{-2} spot size, in contrast to the 65 to 75% obtained with the low-power nonlinearities of Chapters V and VI. This

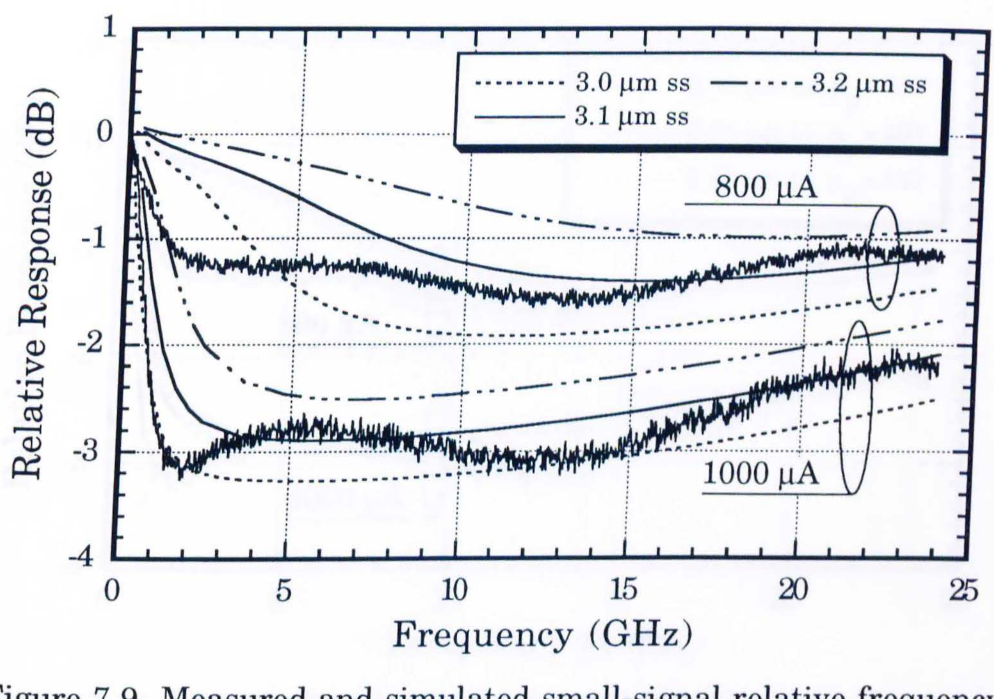

Figure 7.9 Measured and simulated small-signal relative frequency response of a -5 V-biased 0.95-μm PD. Average currents of 800 and 1000 μA. $\mu_p = 230\ cm^2/Vs$. Measurement data from Fig 7.8.

may be needed to account for two-dimensional effects discussed later.

The hole mobility used in the simulated results of figure 7.9 is also about 20% higher than the best-fit hole mobilities of the low-power-density nonlinearities (Chapters V and VI). To compare the sensitivity in the simulated results to hole mobility, figure 7.10 displays the simulated small-signal frequency response for hole mobilities of 150, 200, and 230 cm^2/Vs with the corresponding best-fit spot sizes. The results show slightly better fits at higher frequencies with a higher hole mobility and better fits at lower frequencies with a lower hole mobility. The sensitivity in the simulated results to spot size was about the same as the results in figure 7.9. The results in figure 7.10 show that the PD response reduction is somewhat independent of the hole mobility, given the freedom to vary the spot size. However, for a given spot size, higher hole mobilities (not

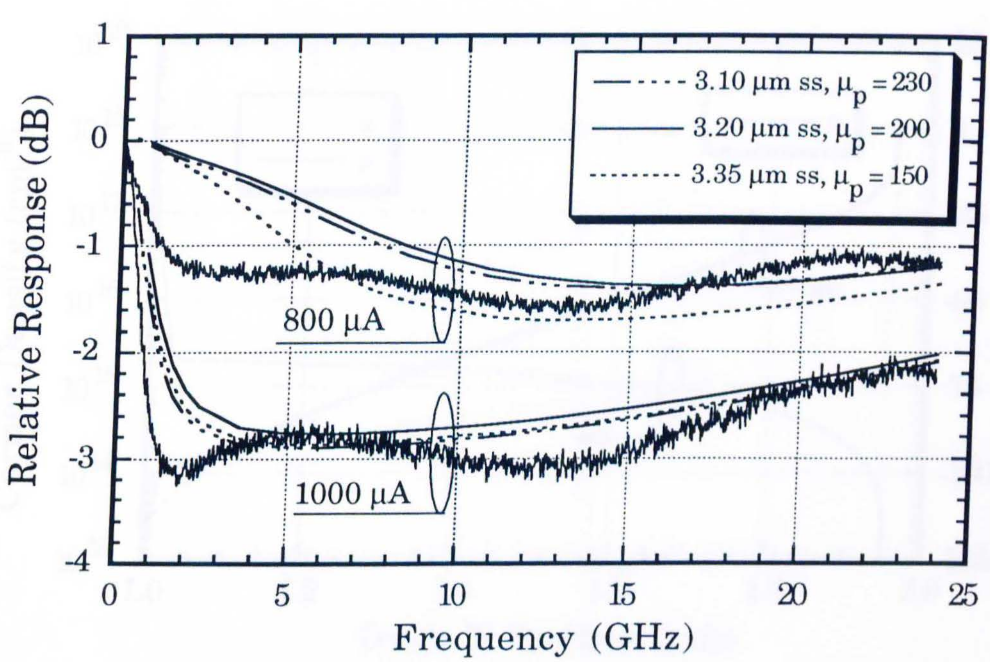

Figure 7.10 Measured and simulated small-signal relative frequency response of a -5 V-biased 0.95-μm PD. Average currents of 800 and 1000 μA. Measurement data from Fig 7.8.

higher saturated hole velocities) result in less response reduction.

Plots of the electric field and the carrier densities for a hole mobility of 230 cm^2/Vs and a spot size of 3.1 μm are given in figures 7.11, 7.12, and 7.13 corresponding to DC photocurrents of 100 μA, 800 μA, and 1000 μA, respectively. At 100 μA, the electric field (figure 7.11) is 15 kV/cm at the edge of the intrinsic region near the n-contact. As the average current increases to 800 μA (figure 7.12) the electric field near the n-contact decreases almost to zero, with the initial observation of an increase of the carrier densities there. When the average current reaches 1 mA (figure 7.13) the electric field has collapsed over 10% (0.1 μm) of the intrinsic region, in the region nearest to the n-contact. Here, the carrier densities have increased to 6.0 to 8.0 x 10^{16} cm^{-3} in a region where the electric field is nearly zero. The electric fields in figures 7.11 to 7.13 establish that the

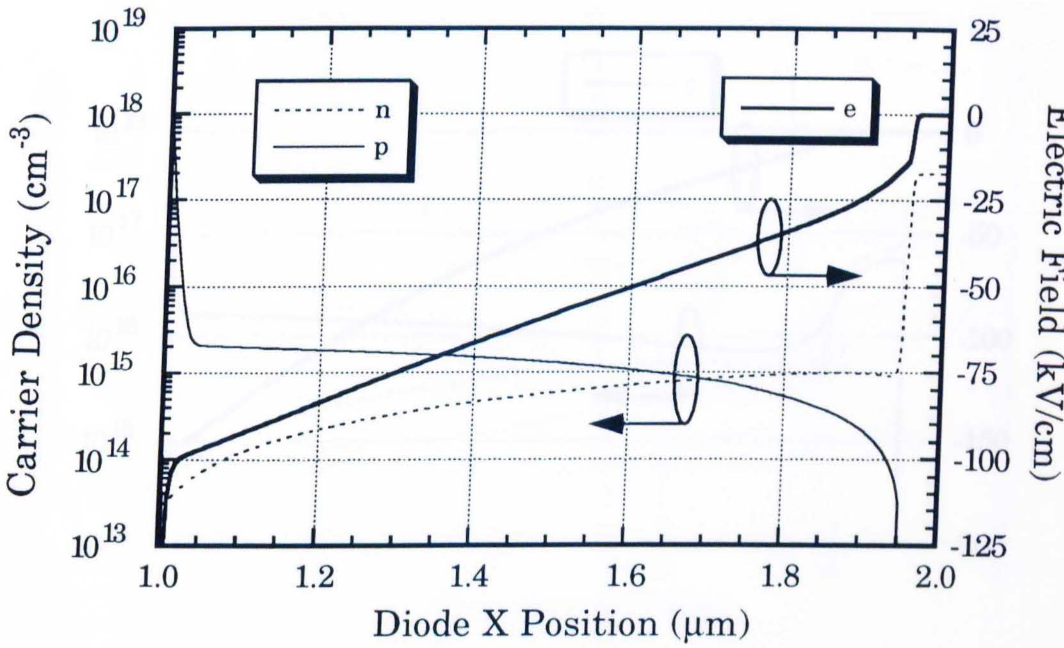

Figure 7.11 Carrier densities and electric field in the intrinsic region at 100 μA. The intrinsic region extends from X = 1.0 μm to X = 1.95 μm. Applied voltage = -5 V. Spot size = 3.1 μm.

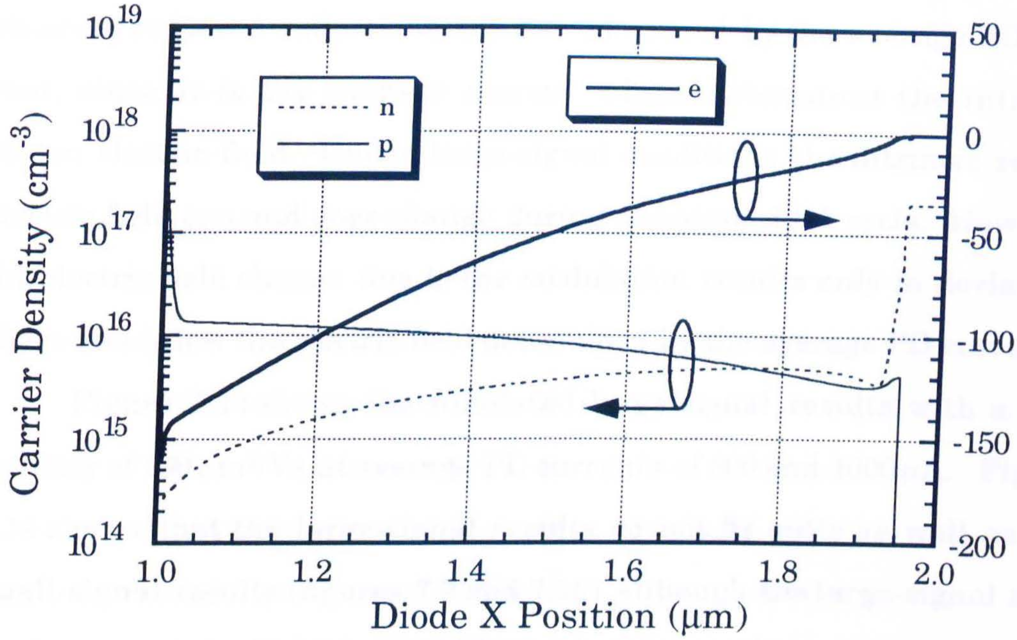

Figure 7.12 Carrier densities and electric field in the intrinsic region at 800 μA. The intrinsic region extends from X = 1.0 μm to X = 1.95 μm. Applied voltage = -5 V. Spot size = 3.1 μm.

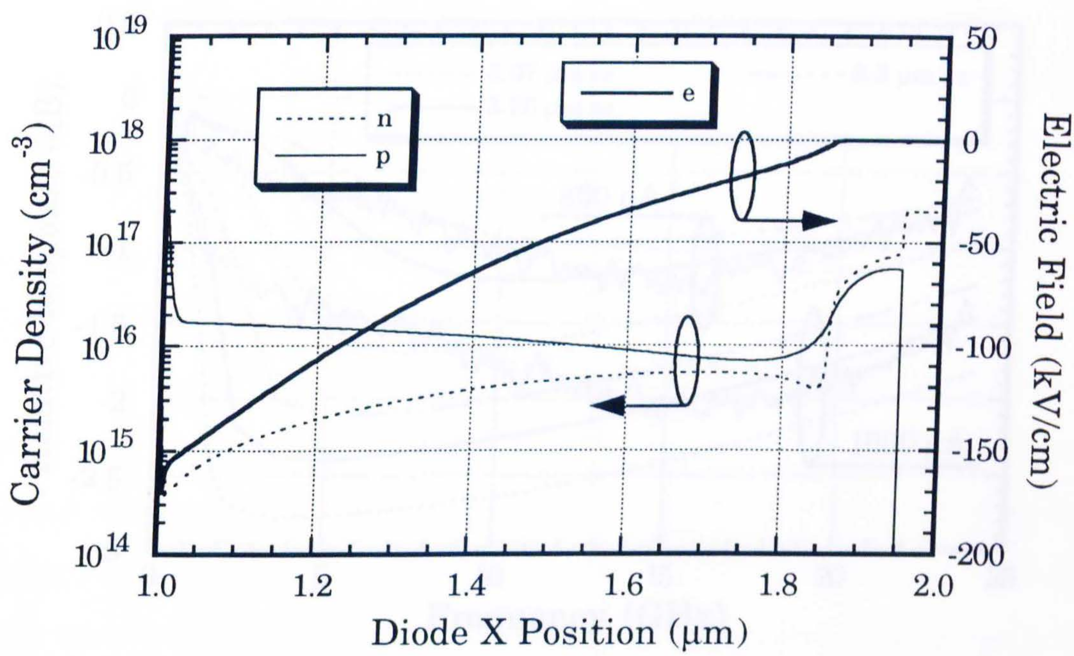

Figure 7.13 Carrier densities and electric field in the intrinsic region at 1000 μA. The intrinsic region extends from X = 1.0 μm to X = 1.95 μm. Applied voltage = -5 V. Spot size = 3.1 μm.

observed response reductions are indeed caused by the average PD current, since it is the average current which determines the intrinsic region electric field. Under large-signal conditions the intrinsic region electric field can and does change during the sinusoidal cycle. However, the electric field change due to the modulation results only in deviations above and below the electric field determined by the average PD current.

Figure 7.14 shows the simulated large-signal results with a hole mobility of 230 cm²/Vs at average PD currents of 800 and 1000 μA. Figure 7.14 shows that the large-signal results do not fit quite as well as the small-signal results (figures 7.9 and 7.10), although the large-signal simulations seem to fit better at 800 μA than 1000 μA, in contrast to the small-signal results which fit better at 1000 μA. The results in figure 7.14 reflect the tendency for the response to remain high until 2 to 6 GHz,

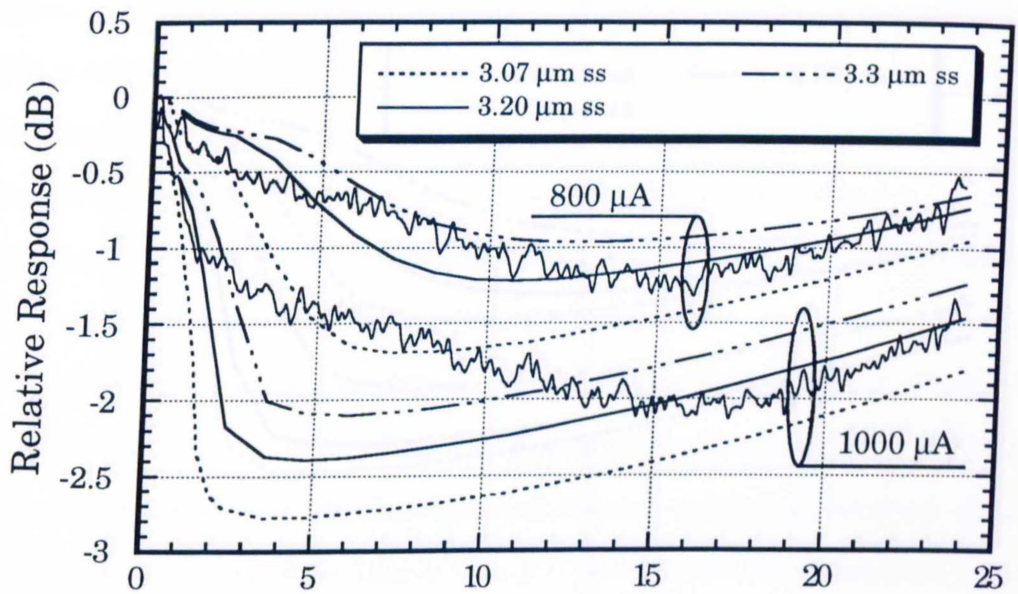

Figure 7.14 Large-signal relative frequency response of a -5 V-biased 0.95-μm PD. Average currents of 800 and 1000 μA. Applied voltage = -5 V. $\mu_p = 230\ cm^2/Vs$. Measurement data from figure 7.1.

where a sudden decrease (0.5 - 1.0 dB) occurs. Simulation results with a hole mobility of 150 cm²/Vs (figure 7.15) show similar characteristics, although the best-fit spot size has increased from 3.2 to 3.5 μm. The spot size for both figures 7.14 and 7.15, are consistent with the results for the best-fit small-signal results, however, both large- and small-signal simulations require approximately 10 to 20% smaller simulation spot sizes than the best-fit results from Chapter V. The fits in figures 7.14 and figure 7.15 suggest that the carrier dynamics under large-signal modulation and collapsing electric fields are being modeled with sufficient accuracy to extend the simulations to the time domain responses.

The simulated sinusoidal output at 150 MHz with a hole mobility of 150 cm²/Vs and a spot size of 3.0 μm is plotted in figure 7.16, where the output of the simulated PD is compared at 100 and 1400 μA. The data in

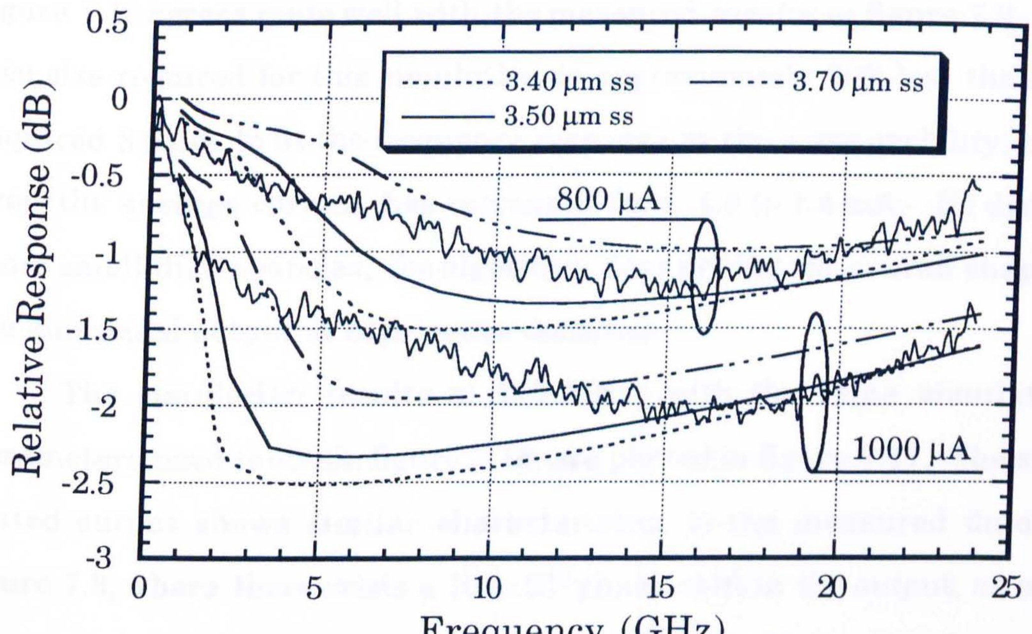

Figure 7.15 Large-signal relative frequency response of a -5 V-biased 0.95-μm PD. Average currents of 800 and 1000 μA. Applied voltage = -5 V. μ_p = 150 cm²/Vs. Measurement data from figure 7.1.

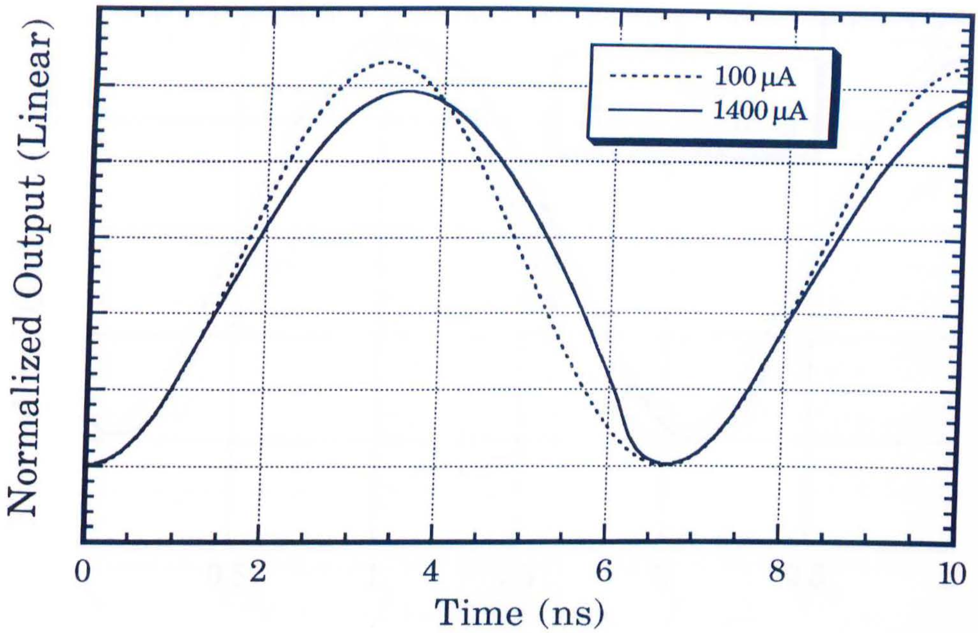

Figure 7.16 Simulated large-signal sinusoidal output of a 0.95-μm PD at 150 MHz. Average currents of 100 and 1400 μA. Spot size = 3 μm. μ_p = 150 cm^2/Vs. Applied V = -5 V. 100% modulation depth.

figure 7.16 agrees quite well with the measured results in figure 7.2. The spot size required for this simulation is approximately 20% less than the required 3.5 μm to fit the frequency response at the same mobility; however, the average current has increased from 1.0 to 1.4 mA. So despite some small discrepancies, the algorithm does predict the overall shape of the sinusoidal output at high power densities.

The simulation results at 500 MHz, with the same simulation parameters used to obtain figure 7.16, are plotted in figure 7.17. The simulated output shows similar characteristics to the measured data in figure 7.3, where there exists a 10 to 25° phase shift in the output, as well as some observable distortion. Rather than normalizing the data, the simulated data can be plotted in an absolute sense and compared to the generation function. The measured data could not be plotted in this way

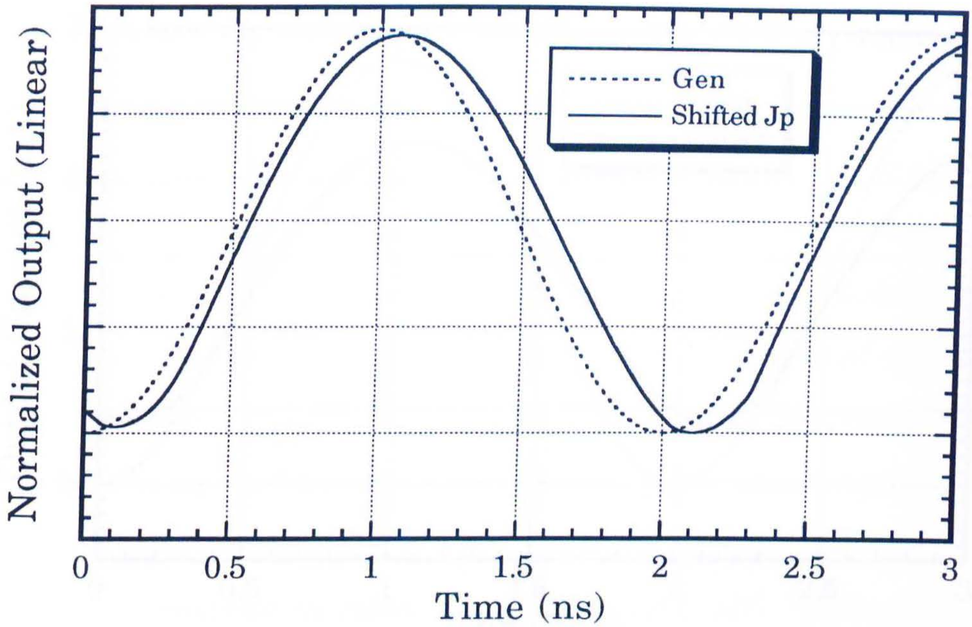

Figure 7.17 Simulated large-signal sinusoidal output of a 0.95-μm PD at 500 MHz. Average currents of 100 and 1400 μA. Spot size = 3 μm. μ_p = 150 cm^2/Vs. Applied V = -5 V. 100% modulation depth.

due to the AC coupling (via the bias tee in figure 2.2) required to bias the PD. The data in figure 7.17 can then be plotted again (figure 7.18) in an absolute sense, where the input signal depicted in figure 7.18 is the output of an ideal PD. Figure 7.18 contains more information about the large-signal carrier dynamics since a direct comparison between the generation function and the output can be made.

Figure 7.3 to 7.4 show that when the spot size is increased by 33%, the PD response at 500 MHz recovers slightly and contains more observable distortion. This is also the case in the modeled PD where the DC-coupled data in figure 7.19 shows a decrease in the phase shift to less than a few degrees and similar distortion characterisitics. Figures 7.16 to 7.19 show that the dynamic nonlinear characteristics occurring in the modeled diode agree with those of the actual device.

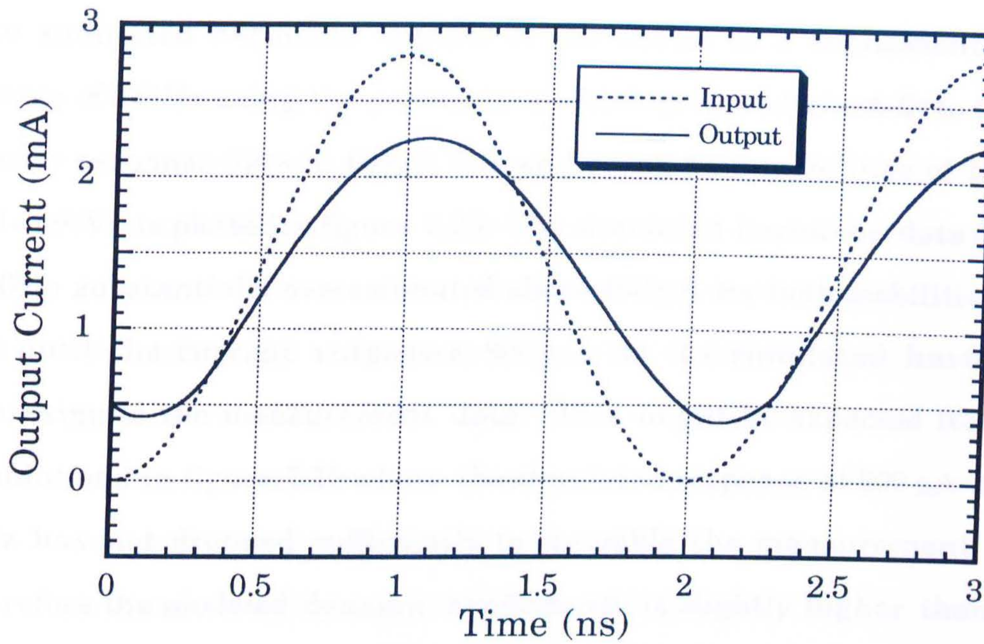

Figure 7.18 DC-coupled simulated large-signal output of a 0.95-μm PD at 500 MHz. Average currents of 100 and 1400 μA. Spot size = 3 μm. μ_p = 150 cm^2/Vs. Applied V = -5 V. 100% modulation depth.

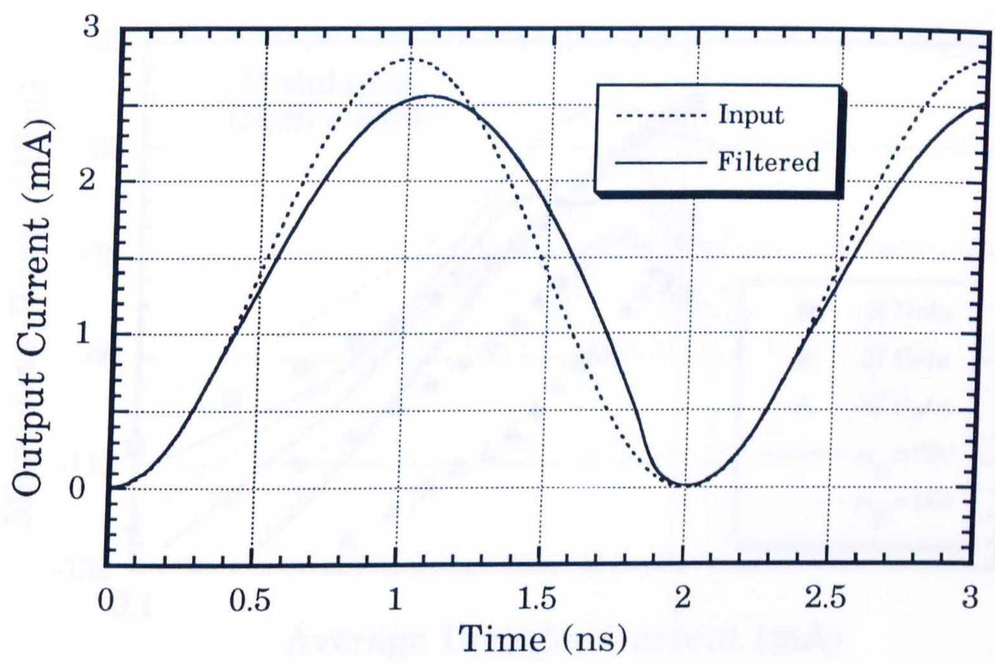

Figure 7.19 DC-coupled simulated large-signal output of a 0.95-μm PD at 500 MHz. Average currents of 100 and 1400 μA. Spot size = 4 μm. μ_p = 150 cm^2/Vs. Applied V = -5 V. 100% modulation depth.

The simulated harmonic content of the device at a fundamental frequency of 5 GHz using the parameters which provided a best-fit to the frequency response data in figure 7.10 and using hole mobilities of 150 and 230 cm^2/Vs is plotted in figure 7.20. The simulated harmonic data (figure 7.20) is substantially overestimated above 400 μA for both mobilities, and not until the current surpasses 900 μA do the simulated harmonics approximate the measurement data. This might be expected from the simulations in figure 7.10 where the simulated response at 800 μA near 5 GHz has not dropped sufficiently to resemble the measurement data. Therefore the modeled dynamic nonlinearity is slightly higher than that which is actually observed. This may be more obvious if one considers the sinusoidal output. If the sinusoid could be acquired on an oscilloscope with sufficient bandwidth, the actual sinusoid at 800 μA would look

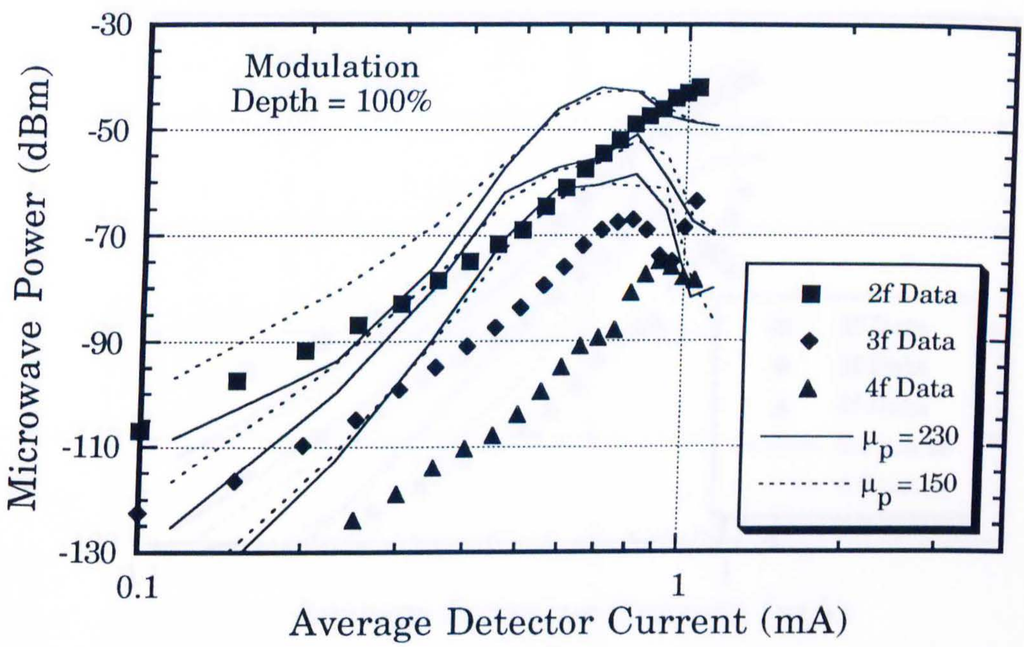

Figure 7.20 Simulated harmonic power versus detector current at 5 GHz. Simulated with parameters leading to best frequency response fits in figure 7.10. Measurement data from figure 7.7.

similar to the sinusoid in figure 7.17, where the response has decreased by only 1 dB from the response at low powers. On the other hand, the simulated sinusoid would look similar to the sinusoid in figure 7.19, since the simulated response has decreased less than 0.2 dB from the low power response. The sinusoid in figure 7.19, however, has more discernible distortion than the sinusoid in figure 7.17 and thus should also have higher harmonic content. Therefore, to fit the harmonic data, the spot size will be reduced to 60 to 70% of the e^{-2} spot size which provided the best-fits to harmonic data in Chapters V and VI.

The simulated results using a hole mobility of 200 cm^2/Vs with spot sizes of 3.6 and 4.0 μm are plotted in figure 7.21. The data shows that the simulated third harmonic has a reasonable fit to measurement data, with the second harmonic slightly underestimated and the fourth har-

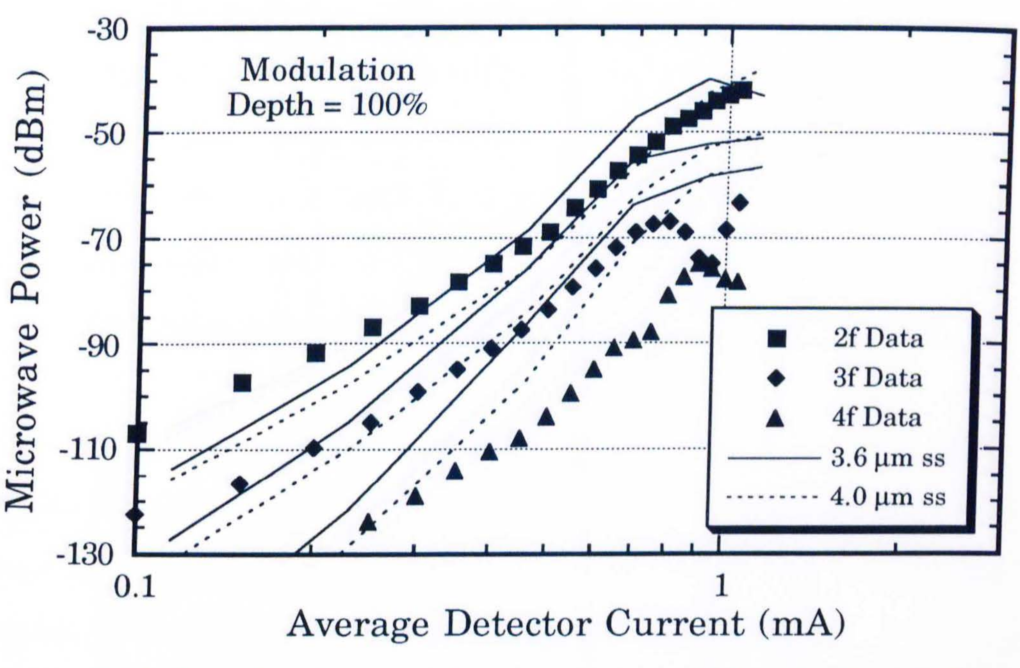

Figure 7.21 Simulated harmonic power versus PD current at 5 GHz. Simulated with spot sizes of 3.6 and 4.0 μm. Applied voltage = -5 V. μ_p = 200 cm^2/s. Measurement data from figure 7.7.

monic slightly overestimated, similar to the simulation tendencies in Chapter V (figure 5.13). Better fits in Chapter V were obtained by decreasing the hole mobility and the spot size. Simulation results for hole mobilities of 175 and 150 cm²/Vs are plotted in figures 7.22 and 7.23, respectively. A best-fit is obtained with a hole mobility of 150 cm²/Vs and a spot size of 4.5 μm (75% of the incident e^{-2} spot size) which agrees with the best-fit simulation parameters in Chapter V.

The frequency dependence in the NL output (figures 7.5 to 7.7) has two distinct regions of comparison. At 200 μA, there exists a 22 dB difference in the second harmonic between the 150 MHz and the 5 GHz data, while at 1 mA the difference is less than 3 dB. The simulated NL at 500 MHz is plotted in figure 7.24 using a hole mobility of 150 cm²/Vs with spot size of 4.5 μm, values which produced the best-fits at 5 GHz (figure 7.23).

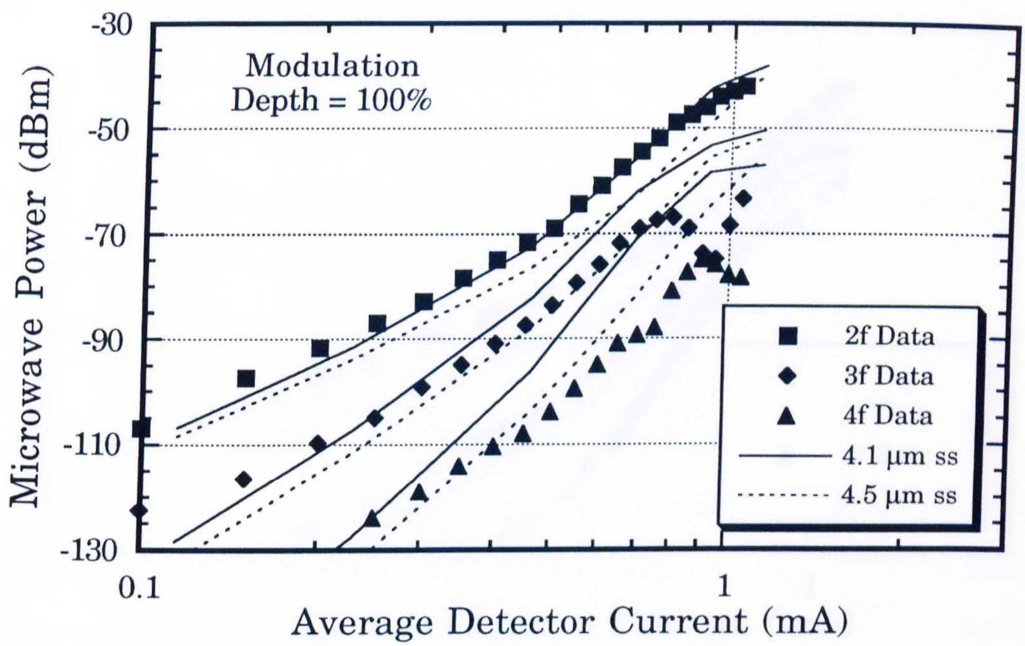

Figure 7.22 Simulated harmonic power versus PD current at 5 GHz. Simulated with spot sizes of 4.1 and 4.5 μm. Applied voltage = -5 V. μ_p = 175 cm²/s. Measurement data from figure 7.7.

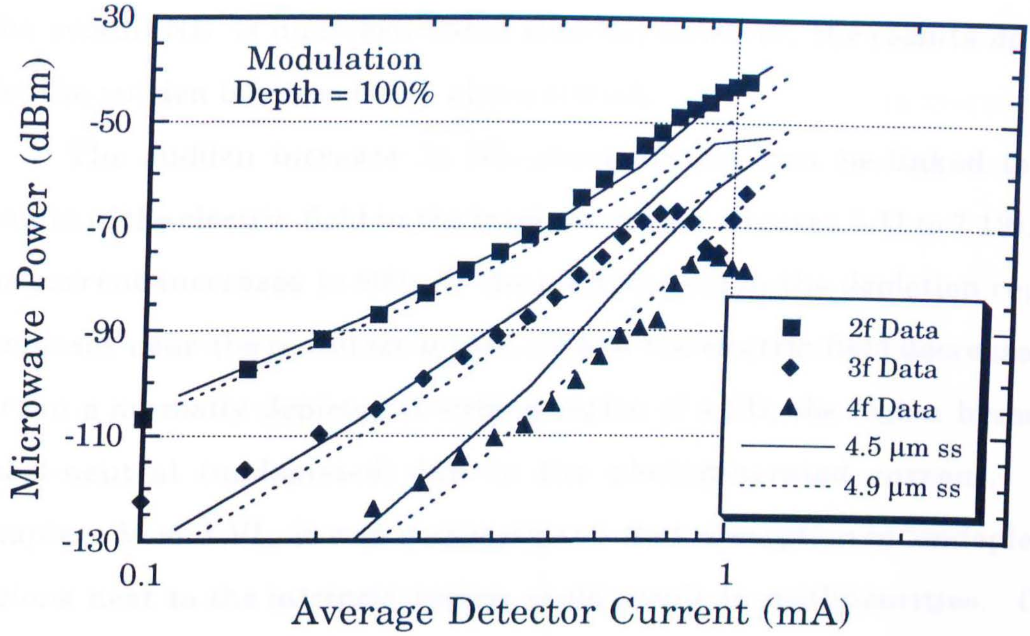

Figure 7.23 Simulated harmonic power versus PD current at 5 GHz. Simulated with spot sizes of 4.5 and 4.9 μm. Applied voltage = -5 V. μ_p = 150 cm^2/s. Measurement data from figure 7.7.

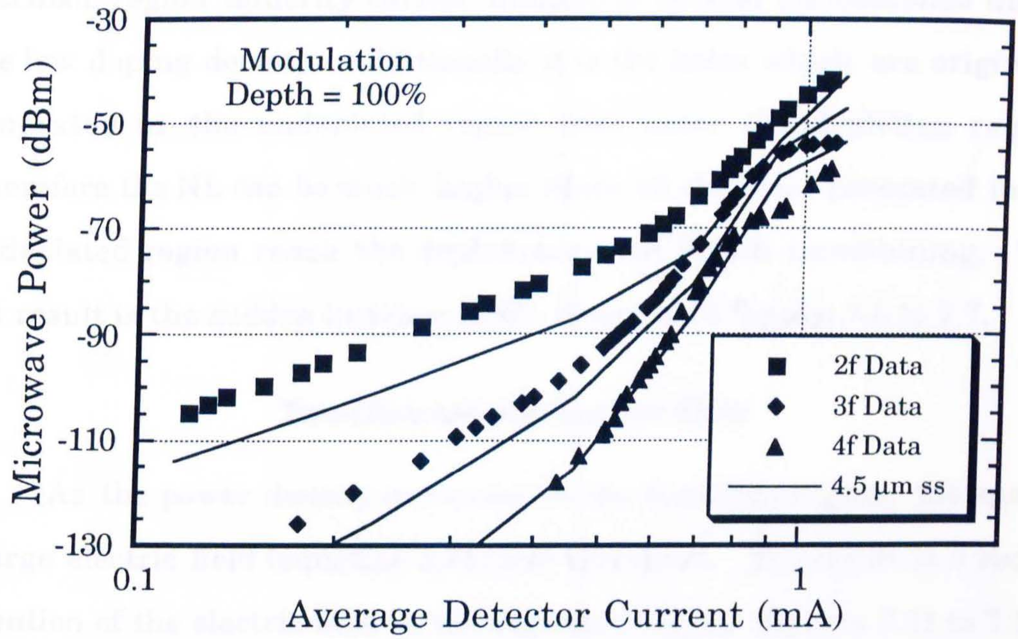

Figure 7.24 Simulated harmonic power vs PD current at 500 MHz. Simulated with a spot size of 4.5 μm. Applied voltage = -5 V. μ_p = 150 cm^2/s. Measurement data from figure 7.6.

The overall NL is underestimated slightly; however, the results do predict the sudden increase in NL above 500 μA.

The sudden increase in NL above 500 μA can be linked to the results of the electric field in the intrinsic region (figures 7.11 to 7.13). As the current increases to 800 μA, the electric field in the depletion region decreases near the n-contact to zero. When the electric field decreases to zero in a normally depleted absorbing region of a PD, the region becomes quasi-neutral (undepleted) due to the photogenerated current. In Chapters V and VI, it was demonstrated that absorption in undepleted regions next to the intrinsic region could result in nonlinearities. One factor controlling the amount of NL was the minority carrier lifetime, where longer lifetimes resulted in higher nonlinearities. In contrast to the highly-doped undepleted regions simulated in Chapter V, the intrinsic region minority carrier lifetime is several nanoseconds due to the low doping density. Additionally it is the holes which are originally generated in the undepleted region that enter the depletion region. Therefore the NL can be much higher since all the holes generated in the undepleted region reach the depletion region before recombining. The net result is the sudden increase in NL observed in figures 7.5 to 7.7.

Two-Dimensional Carrier Flow

As the power density increases in the depletion region, the space-charge electric field (equation 3.35) also increases. The result is a redistribution of the electric field in the depletion region (figures 7.11 to 7.13). The PD thus far has been considered to have exclusively one-dimensional carrier movement in the intrinsic region. This was assumed since the dark electric field in the intrinsic region is independent of the radial coordinate, neglecting edge effects or other device asymmetries. This is a good approximation because the intrinsic region, as far as the electric field is concerned, is a parallel plate capacitor which has a diameter (35 μm) that is sufficiently larger than its width (1 μm). However, when the electric field in the depletion region is perturbed according to the localized carrier densities and the localized carrier densities are not uniform, then the electric field may contain radial components. Carrier movement, which was assumed to be exclusively axial, may now contain a component in the radial direction.

A qualitative argument for the existence of a radial component of electric field is undertaken here with the help of the low and high power electric fields from figures 7.11 and 7.13, plotted on the same graph (figure 7.25). Assume that the device operating under dark conditions

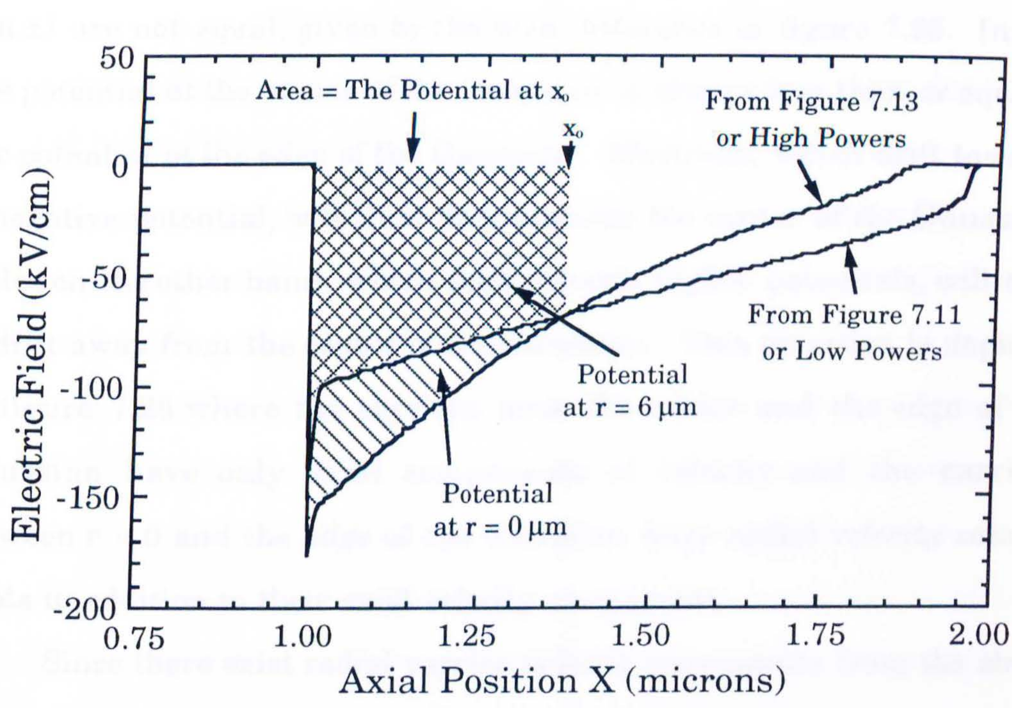

Figure 7.25 Representation of the potential in the intrinsic region versus radial position.

has an internal electric field given in figure 7.11. Since there are no generated carriers anywhere in the depletion region, the potential, $\Psi(r,x)$, at an arbitrary radial coordinate is just the integration of the electric field in figure 7.11 from $x = 0$ to $x = x$. When light is incident on the PD equivalent to 1 mA of average current, with a e^{-2} spot size of 6 μm, the number of generated carriers at $r = 6$ μm is low enough that the electric field at $r = 6$ μm is unchanged from its value under dark conditions. The potential, $\Psi(r=6\ \mu m,x)$, is given by the integration of the dark electric field in figure 7.25 from $x = 0$ to x. On the other hand, the intensity of the light at the center of the Gaussian is enough to perturb the electric field, given by the high-power curve in figure 7.25. The potential, $\Psi(r=0,x)$, is therefore given by the integration of the redistributed electric field (figure 7.25) from $x = 0$ to x. For any value of x, the potentials $\Psi(r=0,x)$ and $\Psi(r=6\ \mu m,x)$ are not equal, given by the area difference in figure 7.25. In fact the potential at the center of the Gaussian is always less than or equal to the potential at the edge of the Gaussian. Electrons, which drift towards a negative potential, will thus drift towards the center of the Gaussian. Holes on the other hand, which drift towards higher potentials, will tend to drift away from the center of the Gaussian. This situation is depicted in figure 7.26 where the carriers near the center and the edge of the Gaussian have only axial components of velocity and the carriers between $r = 0$ and the edge of the Gaussian have radial velocity components in addition to their axial velocity components.

Since there exist radial carrier velocity components from the above arguments, the remaining problem is to determine how important the radial velocity is compared to the axial velocity. Without a 2-D solution to

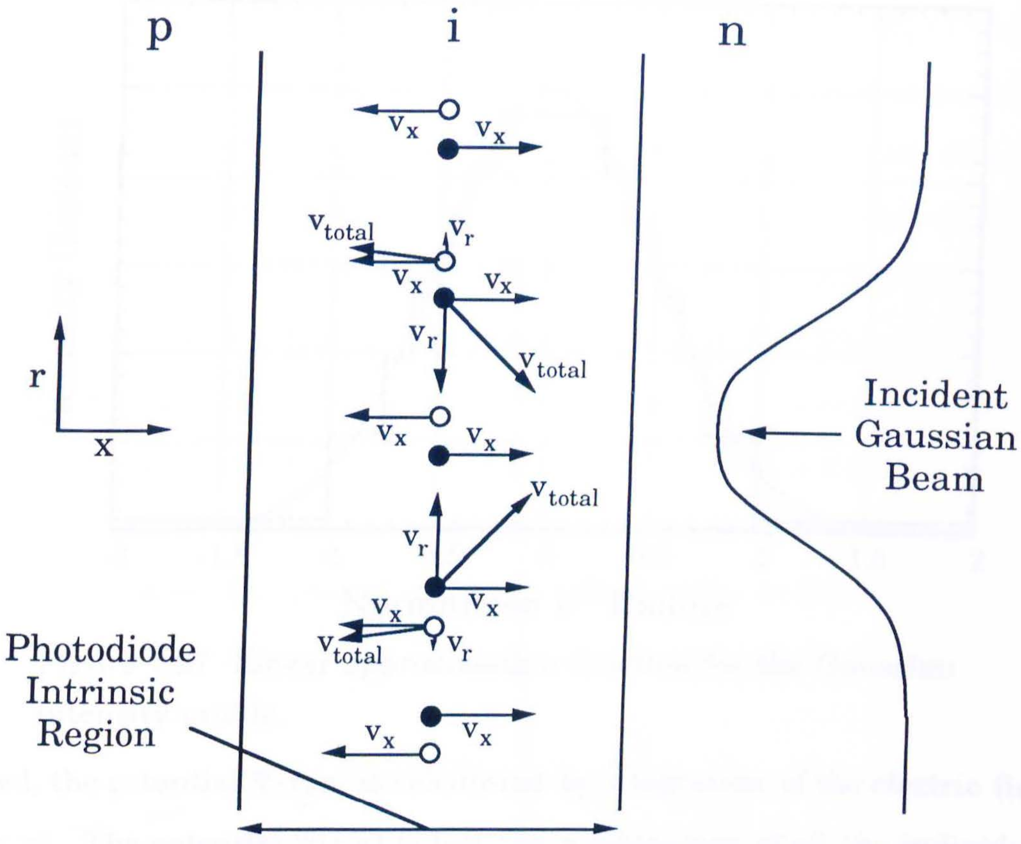

Figure 7.26 Representation of two-dimensional carrier flow due to the radial potential from figure 7.25.

the transport equations (eqns 3.2 to 3.4), an estimation of the axial electric field can be obtained from the solution of many 1-D problems with intensities equal to the intensities along the radial coordinate of the Gaussian. The 1-D solutions assume, by definition, that radial currents do not exist. From the 1-D results, this assumption can be proved or disproved by estimating the magnitude of the expected radial carrier velocities.

The simulations begin with an approximation to the Gaussian radial intensity with j = 7 linear intensities (figure 7.27). A simulation for each intensity, j, corresponding to a given radius r_j, is performed to obtain the electric field, $E_x(r_j,x)$. Once the electric field has been com-

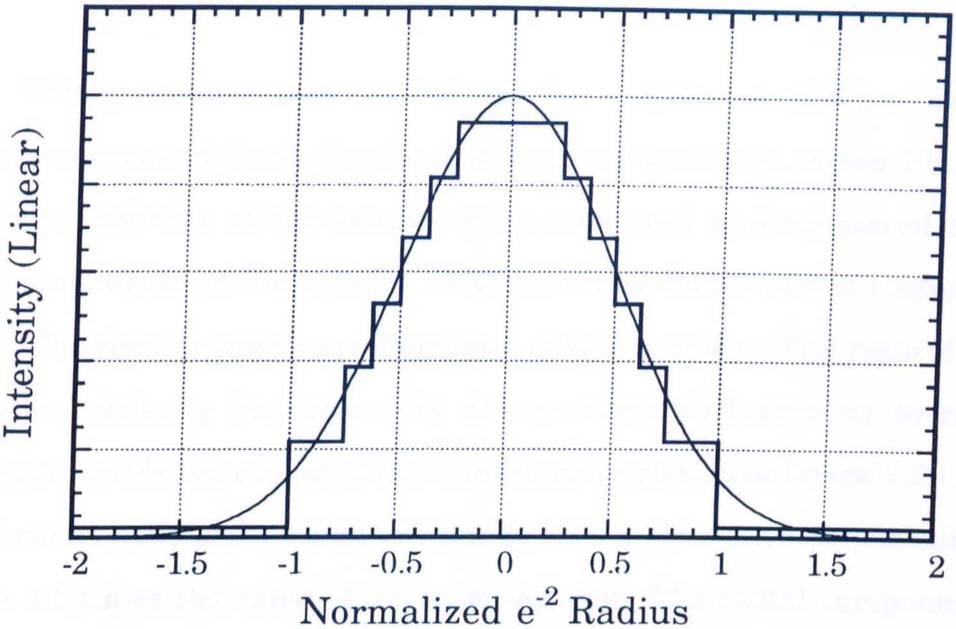

Figure 7.27 Linear approximation function for the Gaussian intensity profile.

puted, the potential $\Psi(r_j,x)$ is calculated by integration of the electric field $E_x(r_j,x)$. The potential $\Psi(r,x)$ is just the combination of all the individual terms $\Psi(r_j,x)$. The radial component of the electric field, $E_r(r,x)$, is then calculated by taking the negative gradient of the potential $\Psi(r,x)$, which can be used to estimate the radial carrier drift velocities from their relationships to the electric field (equations 3.16 and 3.17). This procedure is outlined in figure 7.28.

Simulation:	Solutions	=>	$E_x(r_i,x)$	$i = 1,\ldots,j$
Integration:	$\int_0^x E_x(r_i,\hat{x})\,dx$	=>	$\Psi(r_i,x)$	$i = 1,\ldots,j$
Interpolation:	$\Psi(r_i,x)$	=>	$\Psi(r,x)$	
Gradient:	$-\nabla\Psi(r,x)$	=>	$E_r(r,x)$	

Figure 7.28 Procedure for obtaining a radial electric field estimate.

This procedure was carried out for a spot size of 6 μm and an average current of 1 mA for the 0.95-μm long intrinsic region PD. The radial components of the velocity were computed and compared to the axial components of the velocity. A three-dimensional plot is required to display the results which are functions of both x and r. The ratio of electron axial velocity (movement is always towards larger x) to radial velocity (towards the center of the Gaussian) is plotted in figure 7.29. The radial component of the electron velocity near x = 1.4 μm has peaked and is over 1.5 times the value of the axial velocity. The radial component of the electron velocity near x = 1.95 μm (near the i-n junction) is also over

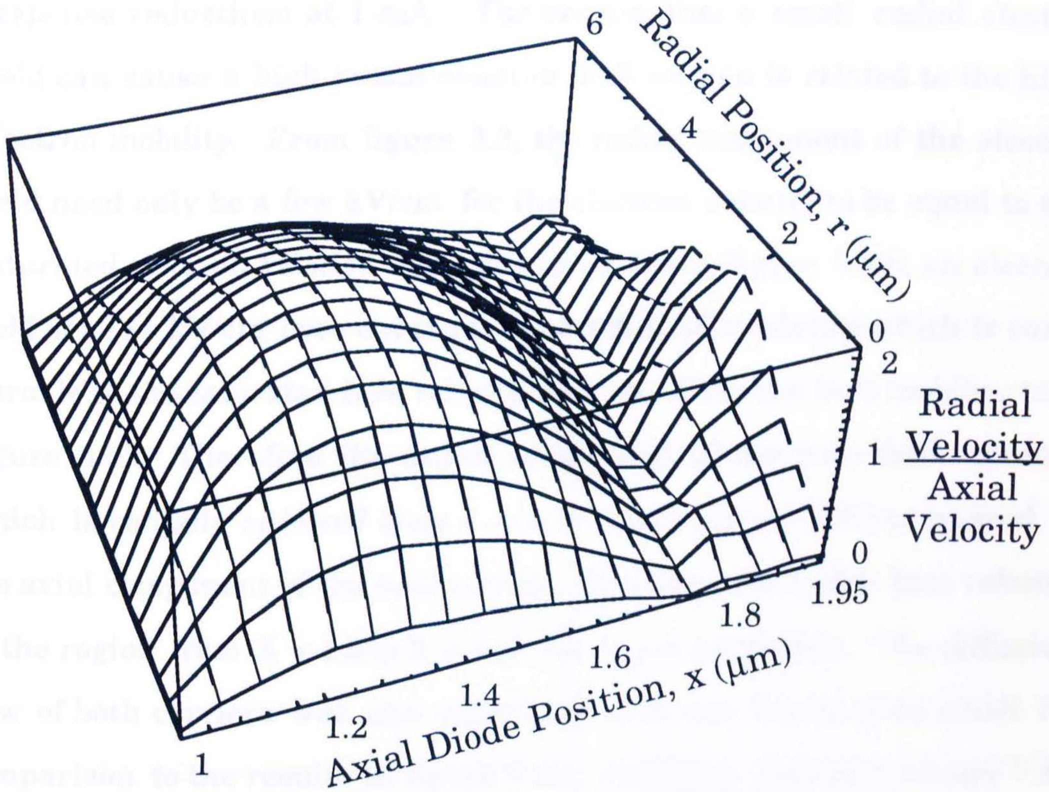

Figure 7.29 Ratio of the estimated electron radial velocity to the electron axial velocity.

1.5 times the size of the axial component. Thus an electron velocity in the intrinsic region, near the steepest part of the Gaussian, has more radial movement than axial movement in any given time interval. The average ratio of the radial component of velocity relative to the axial component is approximately one from figure 7.29.

The result is an electron movement in the radial direction which is nearly equal to the electron movement in the axial direction. With an intrinsic region width of 0.95 μm, the electrons can move (radially) up to 1 μm. This results in a 10 to 20% overall decrease in the spot size, accounting for the discrepancies in the simulation results earlier in the chapter which required 10 to 20% smaller spot sizes to agree with response reductions at 1 mA. The reason that a small radial electric field can cause a high radial electron drift motion is related to the high electron mobility. From figure 3.3, the radial component of the electric field need only be a few kV/cm for the electron velocity to be equal to the saturated electron velocity. Conversely for holes (figure 7.30), an electric field of a few kV/cm does not result in a radial hole velocity which is comparable to the saturated hole velocity because of the low hole mobility (see figure 3.4). Therefore the radial component of the hole drift velocity, which is radially outward from r = 0, is small (figure 7.30) compared to the axial component of the hole velocity. However, the radial hole velocity in the region from X = 1.8 to X = 1.95 μm is not negligible. The diffusive flow of both carriers was also calculated and was found to be small in comparison to the results in figure 7.29. Although figures 7.29 and 7.30 were calculated for a PD where the response had already started to decrease, the effects of a radial electric field will occur whenever there

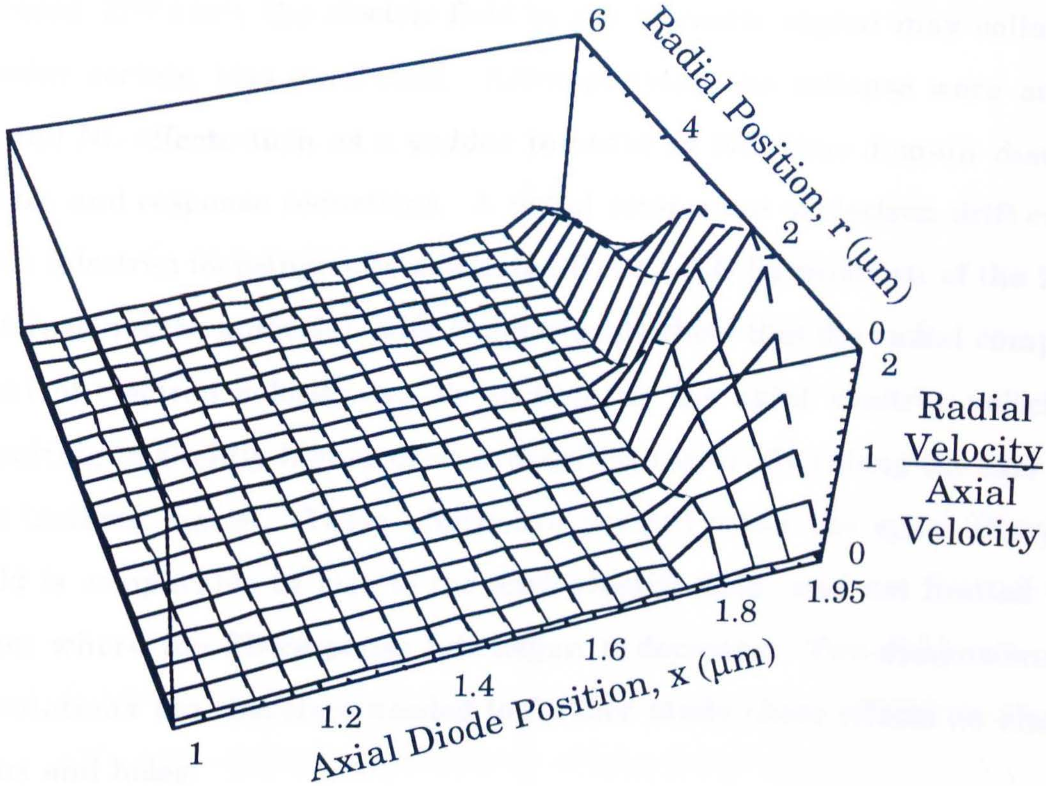

Figure 7.30 Ratio of the estimated hole radial velocity to the hole axial velocity.

are space-charge fields which are comparable to the dark electric field. This is apparent from figure 7.29 where most of the radial electron movement occurs over the portion of the intrinsic region which is still depleted.

Summary

The measurements and simulations in this chapter demonstrated that several additional effects need to be included to fully understand the nonlinear behavior of p-i-n PDs at power densities greater than 3 kW/cm^2. It was observed that when the hole and electron densities exceed 10^{16} cm^{-3}, the electric field in the intrinsic region may collapse under certain bias conditions. Accompanying the collapse were additional NL effects such as a sudden increase in NL, time domain distortions, and response reductions. A radial component of electron drift current (electron focusing) was estimated from a 1-D formulation of the 2-D intrinsic region potential. The estimation predicts that the radial component of electron velocity can be as high as the axial electron velocity resulting in slightly higher carrier densities (up to 30%) along the axis of the incident signal. These effects are present when the space-charge field is comparable in size to the dark electric field, and not limited to cases where the PD response has begun to decrease. Two-dimensional simulations are therefore needed to further study these effects on electrons and holes.

VIII. REDUCTION IN NONLINEAR OUTPUT AND EXTRAPOLATION TO HIGHER POWERS

Introduction

If a PD can be made with a p-type cap layer from a semiconductor material which is transparent to the detection wavelength, it has been demonstrated in Chapters V and VI that significant improvement (> 60 dB) can be obtained in the second harmonic. This chapter will assume that it is possible to make a device with a transparent p-type cap layer and further investigate ways to decrease device NL. Additionally, this chapter will include simulations to determine proper PD design (from the NL point of view) to achieve up to 50 mA of detector current while maintaining low NL and avoiding the nonlinear effects observed in Chapter VII.

0.95-μm Long Intrinsic Region Devices

For equivalent intrinsic-region electric fields and incident spot sizes, the 0.5-μm device displayed lower nonlinearities (see Chapter VI) when the p-region absorption was neglected. One possible reason for the nonlinear suppression was that the intrinsic region electric field in the 0.5-μm device deviated from its average value less compared to electric field in the 0.95-μm device. To investigate whether an approximately constant (under dark conditions) intrinsic region electric field results in lower NL, the intrinsic region doping density can be reduced since the slope of the electric field is proportional to the doping density. The intrinsic region electric field under dark conditions for intrinsic region doping densities of 1×10^{14}, 1×10^{15}, and 5×10^{15} cm^{-3} is plotted in figure 8.1.

The simulated device NL for the above three intrinsic region doping

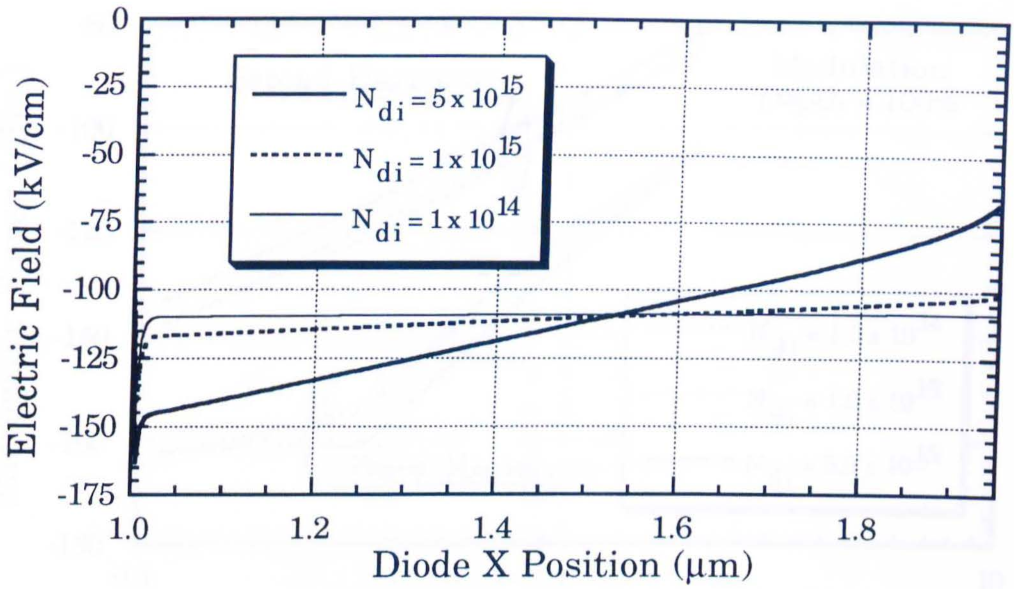

Figure 8.1 Intrinsic region electric field for intrinsic region doping densities of 1×10^{14}, 1×10^{15}, and 5×10^{15} cm^{-3}. Applied voltage = -10 V.

densities is plotted in figure 8.2 for a simulated spot size of 7 μm where the p-region absorption is neglected. A marginal improvement in the second harmonic of 5 dB is achieved with lower intrinsic region doping densities while the third harmonic actually increases by 5 dB for currents below 1 mA. A closer look at the resulting electron velocity change versus doping density may help to clarify this result.

When the carrier velocities are approximately saturated in the intrinsic region, the current (not current density) is proportional to the carrier density, the carrier velocity, and the incident spot size. This implies that, for basically linear devices, the space-charge electric field is independent of the intrinsic region doping level. The space-charge electric field for intrinsic region doping densities of 1×10^{14} and 5×10^{15} cm^{-3} with a PD current of 1 mA are plotted in figure 8.3, where little difference is observed. Since the doping density determines the intrinsic region

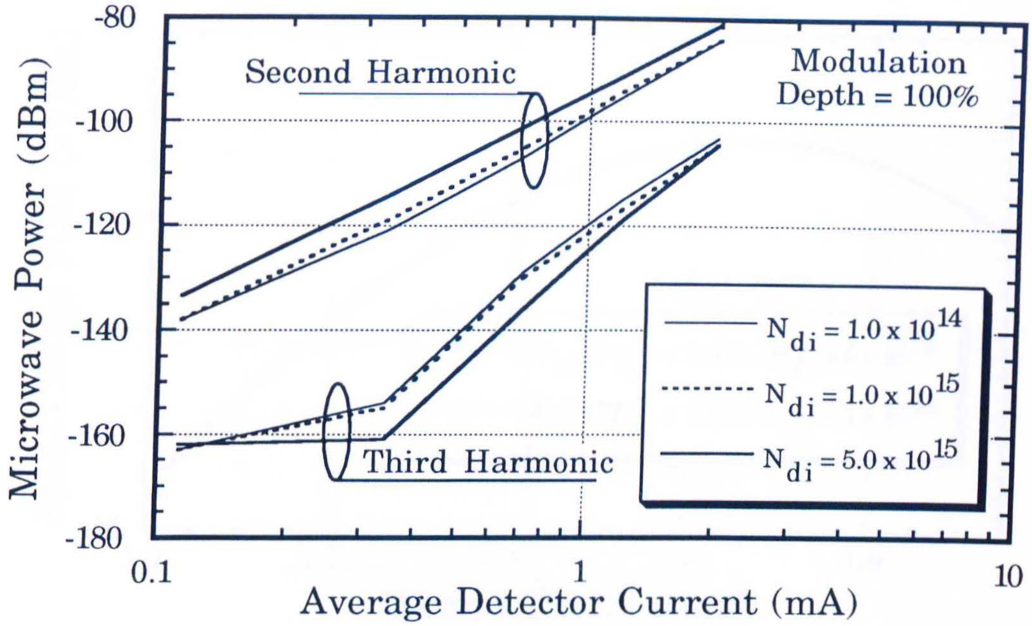

Figure 8.2 Simulated harmonic power vs detector current at 5 GHz neglecting p-region absorption for various intrinsic region doping densities. Spot size = 7 μm. Applied Voltage = -10 V.

electric field (figure 8.1), the resulting difference in the device NL (figure 8.2) is due to the change of the electron velocity versus position (recall from figure 5.23 that the hole velocity change is negligible when the electric field is greater than 50 kV/cm) from its electric field dependence.

The change in electron velocity, due to the space-charge electric field in figure 8.3, is plotted in figure 8.4. The results in figure 8.4 are not conclusive, since there does not seem to be a significantly lower change in the electron velocity for the lower intrinsic region doping levels. The higher intrinsic region doping level does however have a larger average velocity change compared to the low intrinsic region doping level, although this may not be the underlying parameter which determines the device NL. Nevertheless, the results in figure 8.2 do predict that a slight decrease in the second harmonic can be obtained with a slight

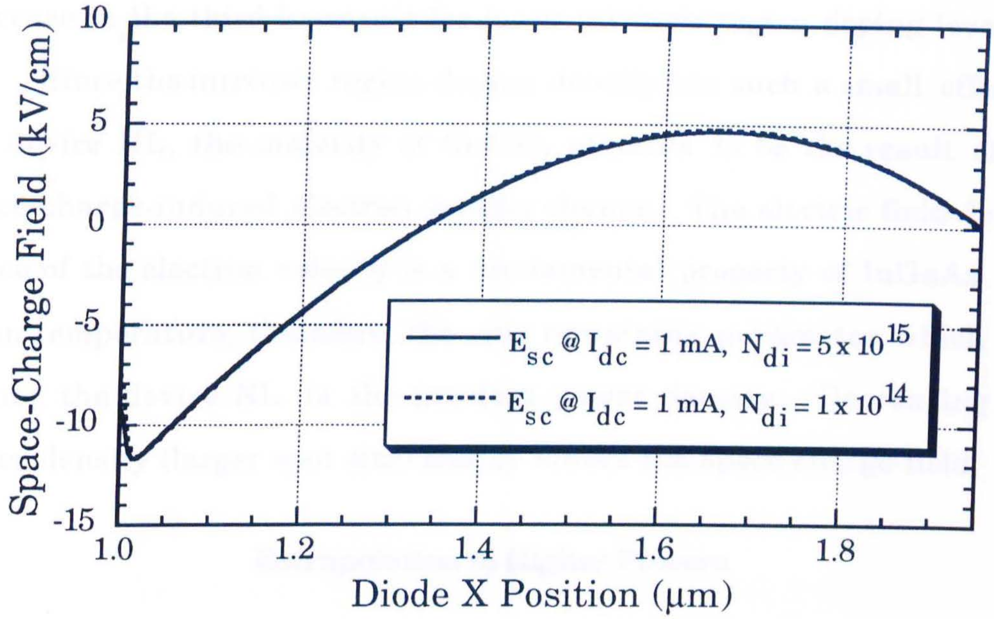

Figure 8.3 The space-charge electric field in the intrinsic region. Intrinsic region doping densities of 1 x 10^{14} and 5 x 10^{15} cm^{-3}. Spot size = 7.0 μm. Applied voltage = -10 V.

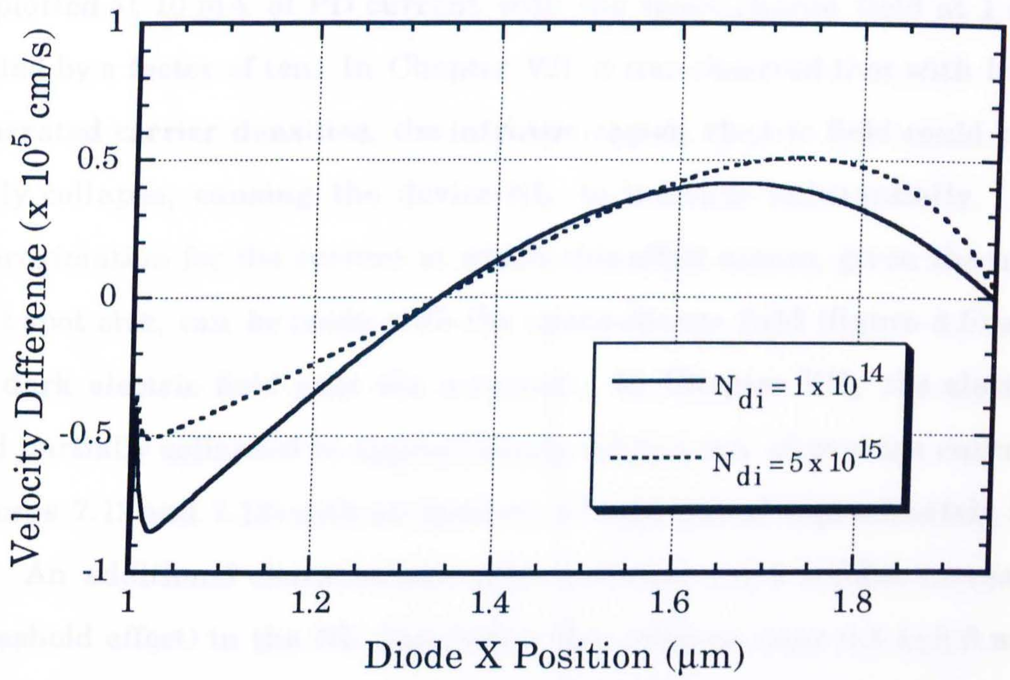

Figure 8.4 Difference in electron velocities from 10 μA to 1000 μA average currents. Intrinsic region doping densities of 1 x 10^{14} and 5 x 10^{15} cm^{-3}. Spot size = 7.0 μm. Applied voltage = -10 V.

increase in the third harmonic for lower intrinsic region doping levels.

Since the intrinsic region doping density has such a small effect on the device NL, the majority of the NL remains to be the result of the space-charge-induced electron velocity change. The electric field dependence of the electron velocity is a fundamental property of InGaAs at a given temperature; therefore, the only remaining parameter which can reduce the device NL is the incident power density. Decreasing the power density (larger spot size) simply lowers the space-charge field.

Extrapolation to Higher Powers

When the carrier velocities are approximately saturated, the space-charge electric field is simply proportional to the current in the intrinsic region. This is shown in figure 8.5 where the space-charge electric field is plotted at 10 mA of PD current with the space-charge field at 1 mA scaled by a factor of ten. In Chapter VII it was observed that with large generated carrier densities, the intrinsic region electric field could partially collapse, causing the device NL to increase substantially. An approximation for the current at which this effect occurs, given the incident spot size, can be made with the space-charge field (figure 8.5) and the dark electric field near the n-contact. In Chapter VII, the electric field partially collapsed at approximately 0.8 to 1 mA of average current (figures 7.12 and 7.13) with an incident e^{-2} spot size of approximately 5.7 μm. An additional characteristic of the collapse was a sudden increase (threshold effect) in the NL just before this collapse near 0.5 to 0.6 mA (figures 7.6 and 7.7). With an e^{-2} spot size of 5.7 μm, approximately one-half the 10 μm e^{-2} spot size, the space-charge electric field is approxi-

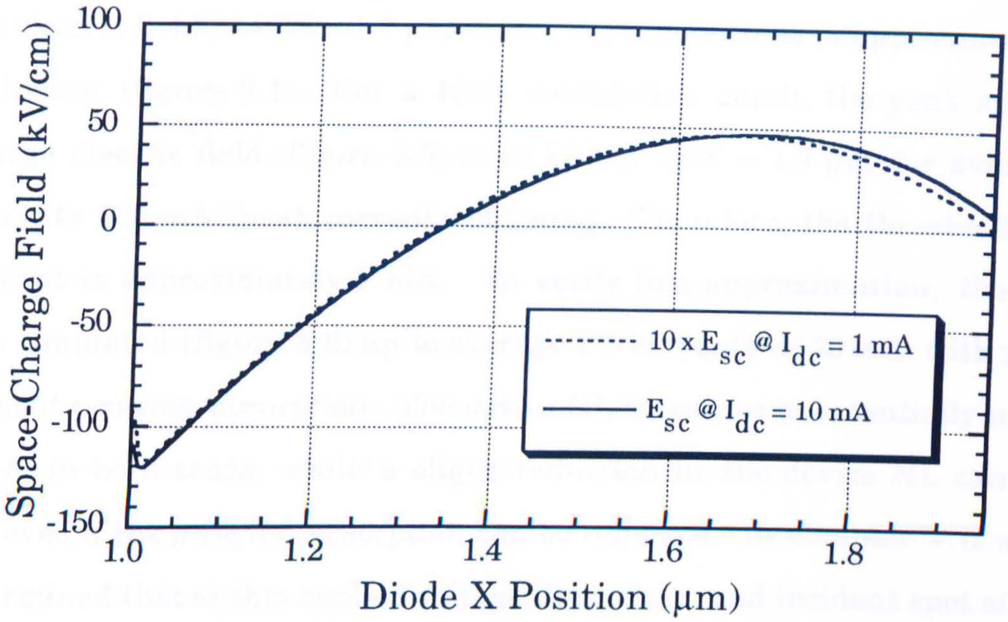

Figure 8.5 The space-charge electric field in the intrinsic region due to the photogenerated carriers. Spot size = 7.0 μm. 0.95-μm long intrinsic region. Applied voltage = -10 V.

mately four times the space-charge field at 1 mA. An additional factor of two arises if one considers the peak current under large signal conditions. Eight times the space-charge electric field at 1 mA (figure 8.5) yields an opposing space-charge electric field of 40 kV/cm at X = 1.7 μm, while the dark electric field at X = 1.7 μm (the position of the peak space-charge field) is 35 to 40 kV/cm (figure 7.11). Therefore, the opposing space-charge field is sufficient to collapse the intrinsic region electric field in this region. This electric field collapse is responsible for the threshold in the device NL, noticeable at approximately 1/2 the field-collapsing current. We will define this current where the NL suddenly increases as the threshold PD current, 0.5 mA for the above example.

With an incident e^{-2} spot size of 10 μm, the threshold PD current can be approximated in a similar way. Given an applied voltage of -10 V, the electric field near X = 1.7 μm under dark conditions is approximately 95 kV/cm (figure 8.1). For a 100% modulation depth, the peak space-charge electric field (figure 8.5) is 10 kV/cm at X = 1.7 μm for average currents of 1 mA (peak currents of 2 mA). Therefore, the threshold PD current is approximately 5 mA. To verify this approximation, the PD was simulated (figure 8.6) up to average PD currents of 20 mA with and without p-region absorption. The device NL increases substantially near 5 mA in both cases, while a slight reduction in the device NL can be achieved if the p-region absorption can be removed. In Chapter V it was determined that at this applied voltage, frequency, and incident spot size, the p-region absorption and the space-charge field induced change in electron velocity resulted in approximately equal device NL. Therefore, no significant improvement in NL was expected from excluding the p-

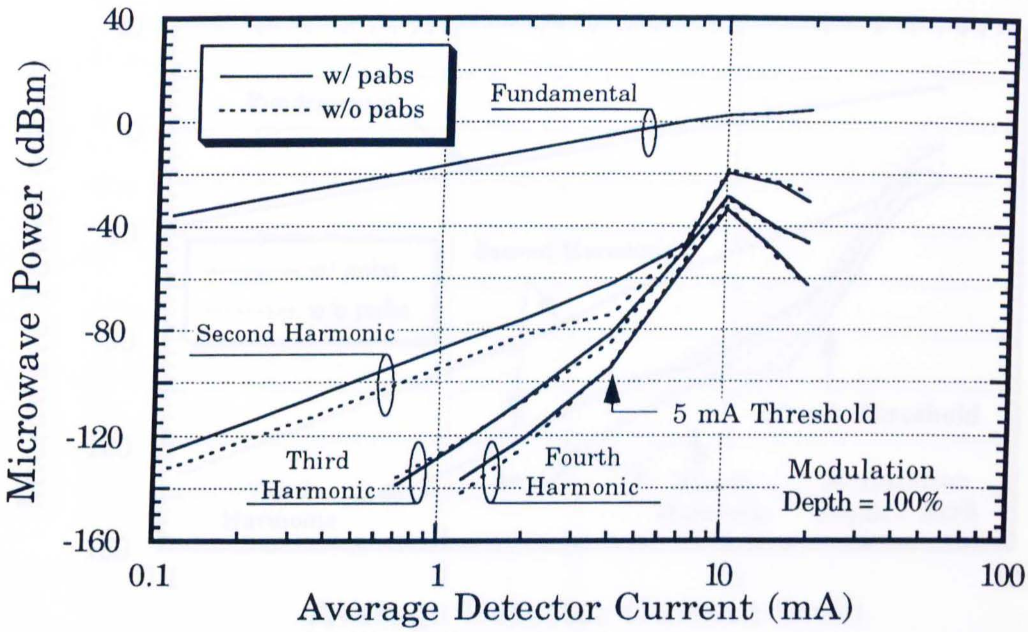

Figure 8.6 Simulated fundamental and harmonic power vs current at 5 GHz with and without p-region absorption. 0.95-μm long intrinsic region. Spot size = 7 μm. μ_p = 150 cm^2/Vs. Applied V = -10 V.

region absorption. The tendency for the NL to decrease above 10 mA is an artifact of the response reduction. For PD currents above the current where the peak in the NL occurs, the PD response decreases (see Chapter VII). When the PD response drops, the dynamic NL also decreases (for example, see figures 7.16 and 7.17) resulting in less distortion.

To increase the threshold PD current and reduce the contribution to the device NL from the space-charge electric field, the incident e^{-2} spot size can be increased from 10 to 20 μm. This should increase the threshold PD current by a factor of four. The simulated device NL under these conditions with and without p-region absorption is plotted in figure 8.7. The figure shows that the second harmonic increases sharply at approximately 20 mA, thus defining a threshold PD current of 20 mA, or four times the previous threshold PD current of 5 mA. Figure 8.7 also demon-

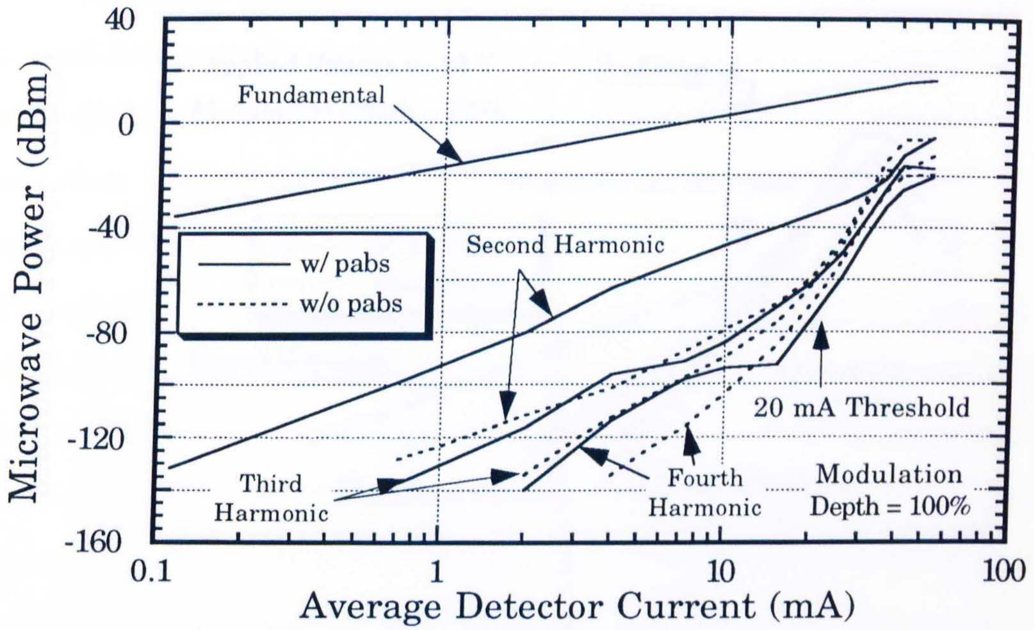

Figure 8.7 Simulated fundamental and harmonic power vs current at 5 GHz with and without p-region absorption. Spot size = 14 μm. 0.95-μm long intrinsic region. $\mu_p = 150\ cm^2/Vs$. Applied V = -10 V.

strates that the p-region absorption nonlinear mechanism now dominates the device NL since larger spot sizes result in lower space-charge fields. The second, third, and fourth harmonics decrease by approximately 30, 10, and 10 dB, respectively, for average PD currents below 20 mA. Above 20 mA, the device NL is dominated by the high power density nonlinearities studied in Chapter VII, which are independent of the p-region absorption conditions.

Since the space-charge electric field has decreased by a factor of four with the increase in spot size from 7 to 14 μm, the device NL caused by a 50 Ω output resistance may no longer be negligible. A 50 Ω resistive load will drop the PD voltage by 1 V when the PD current reaches 20 mA. Therefore, the device is simulated again (figure 8.8) with the load resistor. For PD currents below 10 mA, the device NL is now dominated by the

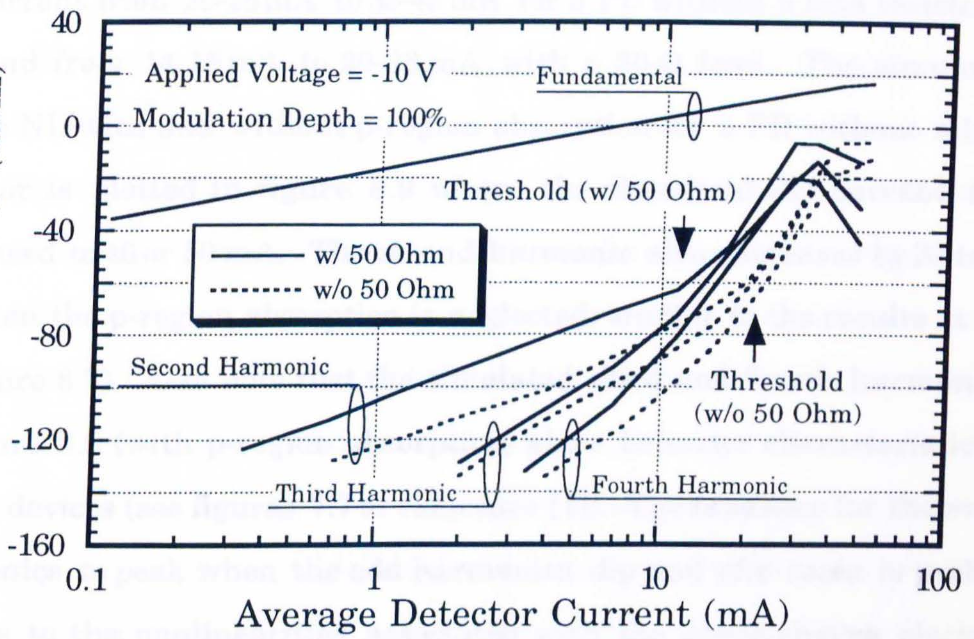

Figure 8.8 Simulated fundamental and harmonic power at 5 GHz with and without a 50 Ohm load. No p-region absorption. 0.95-μm long intrinsic region. Spot size = 14 μm. μ_p = 150 cm^2/Vs.

potential drop from the load resistor, which results in an 18 dB increase of the second harmonic. The resistor also lowers the threshold PD current from 20 mA to 14 mA, although this may be compensated for with a higher applied voltage. At 14 mA of PD current, the intrinsic region electric field drops by 7 kV/cm due to the resistor, which is equivalent to a 7 mA space-charge field (spot size of 14 μm = 1/4 of figure 8.5), accounting for the reduction in the threshold PD current. The tendency for the NL to decrease above 20 mA (figure 8.8 w/ 50 Ω) is an artifact of the response reduction as described for the results in figure 8.6. In this figure, the presence of a resistor simply decreases the current where the NL peaks as compared to the PD with a zero Ohm load.

Increasing the applied voltage from -10 to -15 V raises the electric field by 50 kV/cm near the n-contact which should increase the threshold PD current from 20-25 mA to 35-45 mA for a PD without a load resistor (0 Ω), and from 14-18 mA to 20-28 mA with a 50 Ω load. The simulated device NL with and without p-region absorption for a PD without a load resistor is plotted in figure 8.9 where the threshold PD current has increased to 40 or 50 mA. The second harmonic also decreases by 20 to 30 dB when the p-region absorption is neglected, similar to the results at -10 V (figure 8.7). Also note that the simulated third and fourth harmonics in figure 8.9 (with p-region absorption) show behavior characteristic of actual devices (see figures 7.7 or reference [1]). The tendency for the even harmonics to peak when the odd harmonics dip and *vice versa* is probably due to the nonlinearities associated with the space-charge electric field and the p-region absorption adding constructively and destructively. This is the most likely explanation since the ripple is absent when the p-

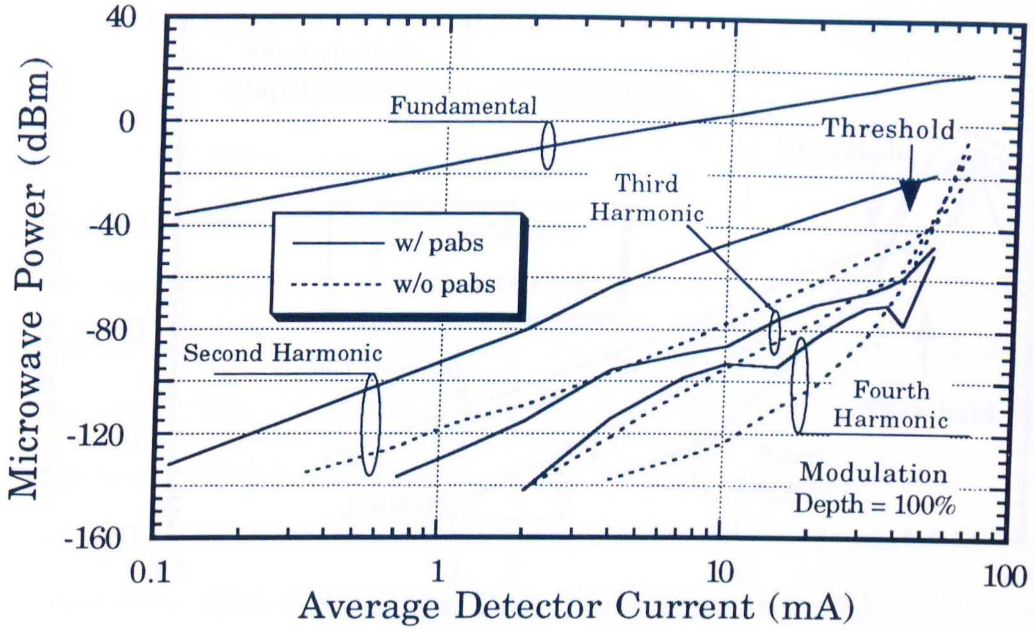

Figure 8.9 Simulated fundamental and harmonic power vs current at 5 GHz with and without p-region absorption. 0.95-μm long intrinsic region. Spot size = 14 μm. μ_p = 150 cm^2/Vs. Applied V = -15 V.

region absorption is neglected. Similar characteristics are also observed in figure 8.7.

The nonlinear output excluding p-region absorption for a PD with and without an external resistor is plotted in figure 8.10 where the threshold PD current decreases to 30 mA when the external resistor is included. The device NL is still higher with the presence of the resistor; however, the increase in the second harmonic is only 7 dB, compared to the 18 dB observed increase when the applied voltage was -10 V. This was not unexpected because a higher average intrinsic region electric field results in a smaller electron velocity change from a fixed electric field decrease due to the load resistor. From the results in figure 8.10, a conventional 0.95-μm long intrinsic region 20 GHz p-i-n PD could achieve a

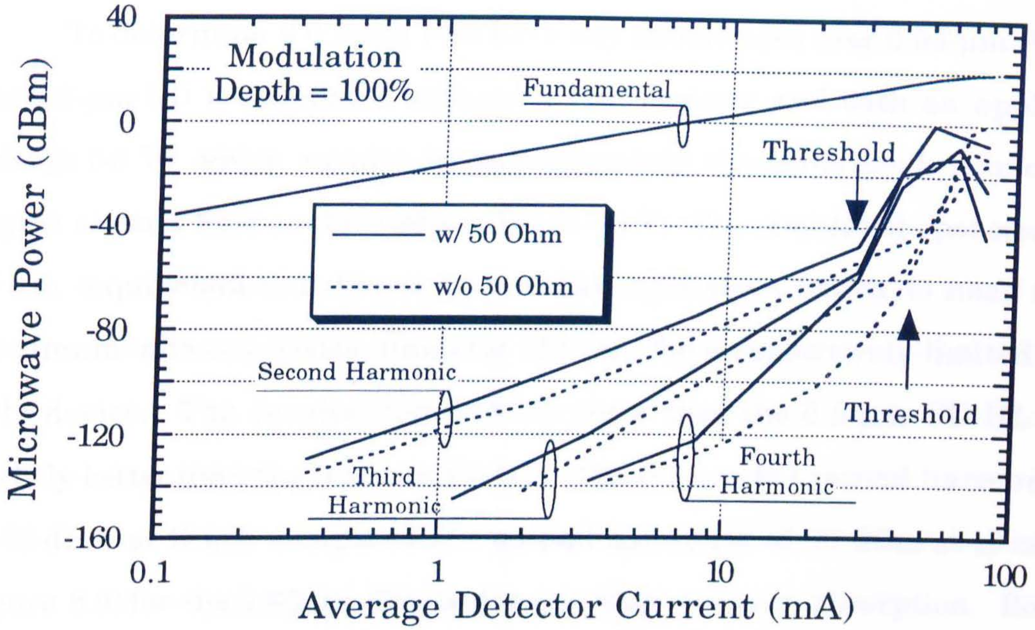

Figure 8.10 Simulated fundamental and harmonic power at 5 GHz with and without a 50 Ohm load. No p-region absorption. 0.95-μm long intrinsic region. Spot size = 14 μm. $\mu_p = 150\ cm^2/Vs$.

maximum threshold PD current of 50 to 60 mA. This is because the device area cannot be increased beyond 35 μm (figure 8.8 assumes a 20 μm e^{-2} spot size) to achieve the desired bandwidth. Therefore, the incident spot size cannot be increased beyond 30 μm resulting in a factor of two decrease in the power density. Furthermore, the applied voltage cannot be increased since the electric field at 60 mA is approaching 300 kV/cm near the p-i interface, where the device may begin to display avalanche gain (resulting in a lower frequency response) or break down (device failure). Also, filling the entire PD area with light may introduce additional NL from nonuniform electric fields present near the edge of the device. Two-dimensional carrier flow (Chapter VII) may further reduce the threshold PD current from an increase in the electron density near the center of the incident signal.

To determine if 0.5-μm PDs have any advantages over 0.95-μm PDs, the 0.5-μm PD is simulated without a load resistor and with an applied voltage (-5 V) which results in approximately the same peak intrinsic region electric field as the 0.95-μm PD at -10 V. The simulated spot size is 10 μm (equivalent to a 14 μm e^{-2} incident spot size), which is near the maximum allowed device diameter (20 μm) for a capacitively-limited 20 GHz device. The results (figure 8.11) show that the 0.5-μm PD NL is slightly better than the 0.95-μm PD NL. The 0.5-μm PD second harmonic is -85 dBm at 10 mA compared to a second harmonic of -77 dBm at 10 mA (figure 8.9) for the 0.95-μm PD, both neglecting p-region absorption. Both devices yield threshold PD currents of approximately 30 mA.

The insignificant improvement in nonlinear performance for the 0.5-μm device is the result of the smaller incident spot size resulting in a

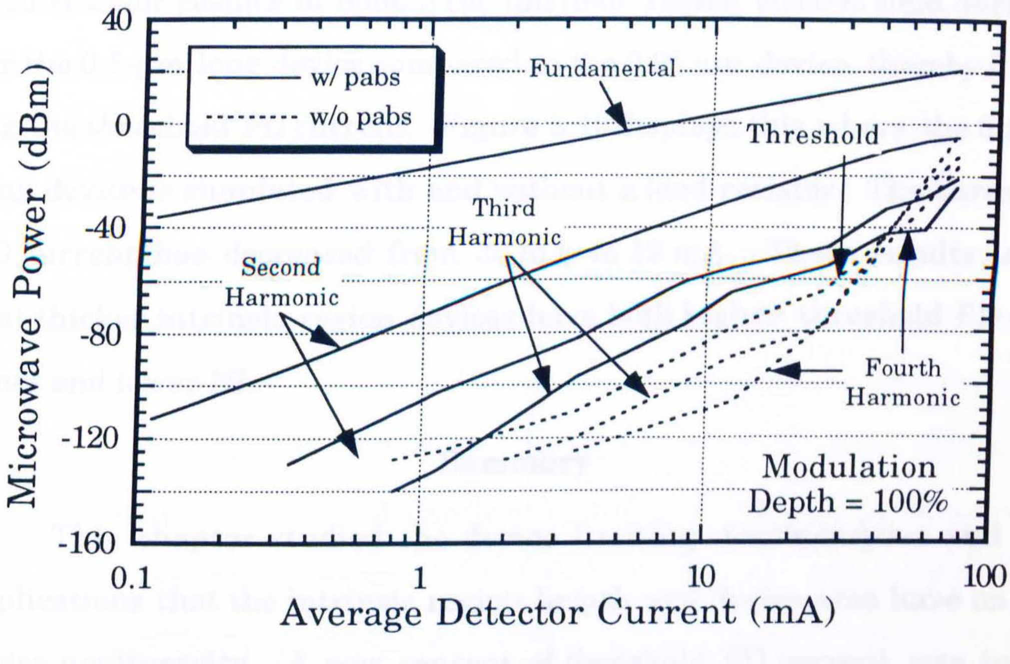

Figure 8.11 Simulated fundamental and harmonic power vs current at 5 GHz with and without p-region absorption. 0.5-μm long intrinsic region. Spot size = 10 μm. μ_p = 150 cm^2/Vs. Applied V = -5 V.

higher space-charge electric field. In general, for capacitively-limited devices, the capacitance is proportional to the area divided by the intrinsic region thickness. Recall also that the space-charge electric field is inversely proportional (Chapter VI) to the intrinsic region thickness. Therefore, for capacitively-limited devices, the space-charge electric field is independent of intrinsic region thickness. So although the 0.5-μm long device exhibits 1/2 the space charge electric field (figure 6.16) as the 0.95-μm long device (figure 6.6), the device area, and hence the incident spot size, must also be twice as small for the 0.5-μm long device as the 0.95-μm long device, accounting for the similarities in the device NL.

Actual microwave PDs experience an equivalent 50 Ω load resistor (transmission line) which results in lower threshold PD currents for shorter intrinsic region devices. The same potential drop across a 50 Ω load resistor results in double the intrinsic region electric field decrease for the 0.5-μm long device compared to the 0.95 μm device, thereby lowering the threshold PD current. Figure 8.12 displays this where the 0.5-μm long device is simulated with and without a load resistor. The threshold PD current has decreased from 30 mA to 12 mA. These results imply that thicker intrinsic region devices have both higher threshold PD currents and lower NL.

Summary

This chapter studied the device limiting nonlinearities and the implications that the intrinsic region length and device area have on the device nonlinearity. A new concept of threshold PD current was introduced and utilized to compare PD nonlinear behavior between devices with different intrinsic region lengths at high PD currents. It was

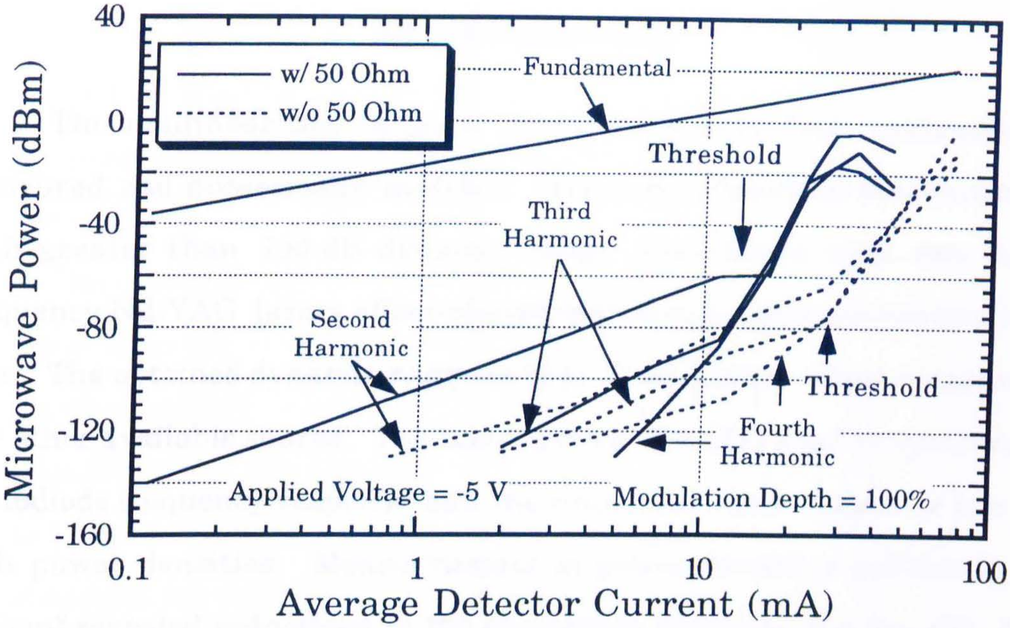

Figure 8.12 Simulated fundamental and harmonic power at 5 GHz with and without a 50 Ohm load. No p-region absorption. 0.5-μm long intrinsic region. Spot size = 10 μm. $\mu_p = 150\ cm^2/Vs$.

shown that the intrinsic region doping density has very little effect on the total device NL, while longer intrinsic region lengths lower device NL for PDs with capacitively-limited bandwidths. Therefore, a high-power high-frequency low-nonlinearity device should be designed with three main considerations. The intrinsic region should be as thick as possible, within the allowed transit time frequency response, to minimize the nonlinearities caused by a 50 Ω load resistor and to maximize the quantum efficiency. The device area should be as large as possible, within the allowed capacitively-limited bandwidth, to minimize the nonlinearities from the space-charge electric field. The device should also be fabricated without absorbing regions (undepleted) near the intrinsic region, to substantially lower the nonlinearities generated in this region.

IX. CONCLUSION

The nonlinearities in p-i-n photodiodes have been systematically measured and numerically modeled. Harmonic distortion measurements with greater than 130 dB dynamic range were made with two single-frequency Nd:YAG lasers offset-phased-locked to a stable microwave reference. The obtained dynamic range is 50 to 70 dB higher when compared to any other available source. The laser system was also used to measure the photodiode frequency response and the sinusoidal time output for low and high power densities. Measurements at power densities greater than 3 kW/cm^2 revealed reductions in the photodiode response of a few dB. Measurements of the sinusoidal time output at power densities of 4 kW/cm^2 revealed easily discernible distortions such as second harmonics of -20 dBc and frequency dependent phase shifts of 10 to 25°.

A semi-classical approach to solving photodiode carrier transport was conducted. This approach required the simultaneous solution of three coupled nonlinear differential equations: Poisson's equation and the hole and electron continuity equations. These transport equations were numerically solved in the case of a one-dimensional InGaAs/InP p-i-n structure, including the undepleted p- and n-regions for completeness.

Several transport properties and characteristics specific to InGaAs were included in the model. The electric field dependence of both the hole and electron velocity were included to account for velocity saturation (both carriers) and velocity overshoot (electrons only). Mobility reduction at high carrier densities due to scattering mechanisms was included to describe the carrier movement in the bulk regions where the carrier densities are approaching 10^{19} cm^{-3}. Diffusion was included in the model. Particular attention was given to the electric field dependence of the diffusion constants and to limiting the diffusion currents using a physical argument rather than artificially limiting the numerical solution to avoid numerical oscillations.

The effects of the heterojunction(s) were included by neglecting hole transport from the intrinsic region into the n-type substrate where the heterojunction appears as a 0.5 eV barrier to hole flow. The 0.1 eV barrier to electron flow from the intrinsic region into the n-type substrate was neglected due to the high velocity of the electron towards the barrier combined with its low effective mass. A second heterojunction, if present, was included with similar assumptions.

After a discussion of the transport mechanisms, the transport equations were expanded to explain how nonlinear terms enter the equations. Nonlinear terms arise when the carrier velocities are a function of the carrier densities. However, this does not restrict the carrier velocities from being functions of position or time alone, as long as these functions do not have an underlying carrier-density dependence. Additional nonlinear terms arise when the diffusion terms and the recombination terms have underlying carrier-density dependencies.

Nonlinearities caused by carrier-dependent carrier velocities are shown to be due to several intermediate mechanisms. Space-charge electric fields, lower mobilities due to scattering, loading in the external circuit, and absorption in undepleted regions next to the intrinsic region all contribute to the nonlinear output through the carrier-density-dependent carrier velocity. As the generated carriers drift towards their respective bulk regions, they induce a space-charge electric field. As the space-charge field increases, a redistributed electric field results in changing hole and electron velocities via Poisson's equation and their respective electric-field dependencies. Since the electron velocity does not fully-saturate for electric fields below 200 kV/cm, this nonlinear mechanism can never be fully removed from the transport equations. Potential drops in the external circuit result in lower intrinsic region electric fields causing additional changes in the hole and electron velocities. Another carrier velocity change occurs from the decrease in the carrier mobilities as a result of carrier-carrier scattering mechanisms. An empirical relationship is used to incorporate these effects in the transport equations. Absorption in undepleted regions next to the intrinsic region were shown to introduce nonlinearities since the electric field in this region is proportional to the total current. Therefore, the carriers generated in these regions travel with velocities which are directly proportional to the current and hence the carrier densities.

Using a very powerful, high dynamic range, photodiode nonlinearity measurement set-up and resorting to numerical analysis to simulate carrier transport in a p-i-n diode structure, a systematic study into photodiode nonlinearities was conducted. Numerical modeling of the photodiode response was performed to investigate and isolate the various nonlinear mechanisms. The simulation results were first used to methodically reduce the set of possible nonlinear mechanisms to smaller, manageable subsets.

To reduce the set of possible nonlinear mechanisms, three regions of applied voltage and two frequencies were used. The voltages and frequencies were chosen to emphasize the dominant nonlinear mechanisms and their region of importance. It was determined that for intrinsic region electric fields below 50 kV/cm (-5 V across a 0.95-μm long intrinsic region photodiode), the nonlinearities were influenced primarily by the space-charge electric-field-induced change in the hole and electron velocities. Best-fit simulation results were obtained in this region of applied voltage with a simulation spot size 70% of the e^{-2} incident intensity spot size and a hole mobility of 150 cm^2/Vs. For intrinsic region electric fields between 50 kV/cm and 100 kV/cm, the contribution to the overall nonlinearity was shown to be influenced primarily by two mechanisms. The electron velocity change was shown to account for the nonlinear behavior at frequencies above 5 GHz, while the p-region absorption was shown to account for the nonlinear behavior at frequencies below 1 GHz. When the intrinsic region electric field increases to greater than 100 kV/cm, only the p-region absorption could explain the observed nonlinear behavior for frequencies below 10 GHz. It was determined that only 8 to 14 nm of undepleted absorbing material next to the intrinsic region was sufficient to cause second harmonic distortion levels of -60 dBc at 1 mA of average photodiode current. This is the first time that this region was shown to dominate the nonlinearities at high electric fields.

After determining the origins of basic nonlinearities at low intensities, simulations were performed at high power densities. These simulations provided valuable insight into the dynamics of carrier movement under high power density operation. To predict the observed response reductions and sinusoidal time-output distortions, 20 to 30% smaller spot sizes were required. This was explained in terms of a two-dimensional carrier motion in the intrinsic region. An approximation for the radial electric field was implemented to determine the importance of the radial flow. This approximation established the existence of a radial component of electron velocity towards the center of the incident Gaussian beam. Under certain operating conditions, the magnitude of the average radial electron velocity was estimated to be the same size as the axial electron velocity. Two-dimensional movement (electron focusing) thus accounted for the 20% decrease in spot size required to fit the measurement data. Very good agreement at high power densities between measurement and simulation results were obtained.

The model was extended to predict the maximum current a photodiode can handle before a sharp increase in nonlinear output occurs. For capacitively-limited devices operating with the largest allowable incident spot size, it was shown that the nonlinearities induced by the space-charge electric field were independent of the intrinsic region length. However, loading in the external circuit was determined to result in higher nonlinearities as the intrinsic region length decreases. It was thus concluded that the photodiode with the lowest possible nonlinearities should be constructed without undepleted absorbing regions near the intrinsic region, with the longest intrinsic region allowed from transit time considerations, and with an incident spot size which fills the capacitively-limited device area. With such a device, an improvement in the second harmonic of 40 to 60 dB can be obtained compared to currently available devices. It was also determined that maximum photodiode currents of 30 to 50 mA should be attainable in a p-i-n photodiode structure, with minimum nonlinearities.

Although this study significantly advances our understanding of photodiode nonlinearities, more work remains. At high applied voltages, the nonlinearities are dominated by the p-region absorption. Absorption in undepleted regions is common to many photodiode types. Waveguide designs, p-i-n designs, and MSM designs all utilize p-contacts to lower contact resistances. Double heterostructure designs offer the most promising hope for eliminating this source of nonlinearity, however, the grading layers utilized near the p-i interface and the specifics concerning carrier movement in this region require further investigation to determine whether this nonlinear mechanism can be effectively reduced. Some advantage may be gained by using a heterostructure material which has only a slightly higher bandgap than the absorbing material. Although this will limit the useful wavelength range which attains high linearity, it may lessen the requirements on the grading layers.

Specific issues related to material properties of InGaAs also needs to be investigated. Material properties in highly-doped regions such as the minority carrier lifetime and carrier velocities versus doping density are not well known and require additional work. Measurements of the hole velocity below 50 kV/cm are also needed. Additional work is needed concerning carrier flow near the p-i junction. This will help to determine which specific mechanisms control the nonlinearities associated with the p-region absorption. As devices are designed to handle currents greater than 10 mA, additional work is needed to determine if two-dimensional carrier movement places any additional limitations on the maximum possible photogenerated currents.

REFERENCES

A.R. Adams, *et al.*, "The temperature dependence of the Efficiency and Threshold Current of $In_{1-x}Ga_xAs_yP_{1-y}$ Lasers Related to Intervalence Band Absorption," *Jpn. J. Appl. Phys.*, **19**, p. L621, 1980.

R.B. Adler, *et al.*, "Introduction to Semiconductor Physics," John Wiley and Sons, pp. 173-180, 1964.

U. Ascher, *et al.*, "Conditioning of the Steady State Semiconductor Device Problem," *SIAM J. of Applied Math.*, **49**, p. 165, 1989.

H. Baher, "Analog and Digital Signal Processing," John Wiley and Sons, 1990.

R.E. Bank, *et al.*, "Numerical Methods for Semiconductor Device Simulation," *IEEE Trans. on Electron Devices*, **ED-30**, p. 1031, 1983.

P.E. Bauhahn, *et al.*, "Comparison of the Hot Electron Diffusion Rates for GaAs and InP," *Electron. Lett.*, **9**, p. 460, 1973.

G. E. Bodeep and T. E. Darcie, "Comparison of Second- and Third-Order Distortion in Intensity Modulated InGaAsP Lasers and a $LiNbO_3$ External Modulator," OFC 89, Paper WK2.

K.W. Boer, "High-Field Carrier Transport in Inhomogeneous Semiconductors," *Ann. der Physik*, p. 371, 1985.

K.W. Boer, "Survey of Semiconductor Physics," Van Nostrand Reinhold, New York, Volume I, 1990.

K.W. Boer, "Survey of Semiconductor Physics," Van Nostrand Reinhold, New York, Volume II, 1992.

J.E. Bowers and C.A. Burrus,"Ultrawide-Band Long-Wavelength p-i-n Photodetectors," *J. of Lightwave Tech.*, **JLT-5**, p. 1339, 1987.

C. H. Bulmer, "Sensitive, Highly Linear Lithium Niobate interferometers for Electromagnetic Field Sensing,"*Appl. Phys. Lett.*, **53**, p. 2368, 1988.

P.S. Cheung and C.J. Hearn, "The Diffusion of Electrons in Semiconductors in High Electric Fields," *J. of Physics C: Solid State Physics*, **5**, p. 1563, 1972.

R. B. Childs and V. A. O'Byrne, "Predistortion Linearization of Directly Modulated DFB Lasers and External Modulators for AM Video Transmission," OFC 90, Paper WH6.

C. H. Cox, *et al*,. "An Analytic and Experimental Comparison of Direct and External Modulation in Analog Fiber-Optic Links," *IEEE Trans. on Microwave Theory and Tech.*, **MTT-38**, p. 501, 1990.

M. Dentan and B. de Cremoux, "Numerical Simulation of the Nonlinear Response of a p-i-n Photodiode Under High Illumination," *J. of Lightwave Tech.*, **JLT-8**, p. 1137, 1990.

S. Dushman, *Rev. Modern Physics*, **2**, p. 381, 1930.

R.D. Esman and K.J. Williams, "Measurement of Harmonic Distortion in Microwave Photodetectors," *IEEE Photon. Tech. Lett.*, **PTL-2**, p. 502, 1990.

W. Fawcett and G. Hill, "Temperature Dependence of the Velocity-Field Characteristic of Electrons in InP," *Electron. Lett.*, **11**, p. 80, 1975.

A. H. Gnauck, *et al.*, "Comparison of Direct and External Modulation for CATV Lightwave Transmission at 1.5μm Wavelength," *Electron. Lett.*, **28**, p. 1875, 1992.

H.K. Gummel, "A Self-Consistent Iterative Scheme for One-Dimensional Steady State Transistor Calculations," *IEEE Trans. on Electron Devices*, , **ED-11**, p. 455, 1964.

C. Hammar and B. Vinter, "Diffusion of Hot Electrons in n-Indium Phosphide," *Electron. Lett.*, **9**, p. 9, 1973.

R. R. Hayes and D.L. Persechini, "Nonlinearity of p-i-n Photodetectors," *IEEE Photonics Tech. Lett.*, **PTL-5**, p. 70, 1993.

O. Heinreichsberger, *et al.*, "Fast Iterative Solution of Carrier Continuity Equations for Three-Dimensional Device Simulation," *SIAM J. of Sci. Stat. Comput.*, **13**, p. 289, 1992.

P. Hill, *et al.*, "Measurement of Hole Velocity in n-Type InGaAs," *Appl. Physics Lett.*, **50**, p. 1260, 1987.

P. Jenkins, *et al.*, "Minority Carrier Lifetimes in Indium Phosphide," 22nd IEEE Photovoltaic Specialists Conference, p. 177, 1991.

B. H. Kolner and D. W. Dolfi, "Intermodulation Distortion and Compression in an Integrated Electrooptic Modulator," *Applied Optics*, **26**, p. 3676, 1987.

M. Kot and K. Zdansky, "Measurement of Radiative and Nonradiative Recombination Rate in InGaAsP-InP LED's," *Quantum Electronics Lett.*, **28**, p. 1746, 1992.

D. Kuhl, et al., "Influence of Space Charges on the Impulse Response of InGaAs Metal-Semiconductor-Metal Photodetectors," *J. of Lightwave Tech.*, **JLT-10**, p. 753, 1992.

G.A. Landis, *et al.*, "Photoluminescence Lifetime Measurements in InP Wafers," 22nd IEEE Photovoltaic Specialists Conference, p. 636, 1991.

G. Lucovsky, *et al.*, "Transit-Time Considerations in p-i-n Diodes," *J. of Appl. Physics*, **35**, p. 622, 1964.

G.B. Lush, *et al.*, "Determination of Minority Carrier Lifetimes in n-type GaAs and Their Implications for Solar Cells," 22nd IEEE Photovoltaic Specialists Conference, p. 182, 1991.

T. Ozeki and E. H. Hara, "Measurements of Nonlinear Distortion in Photodiodes," *Electron. Lett.*, **12**, p. 80, 1976.

T.P. Pearsall, *et al.*, "Electron and Hole Mobilities in GaInAs," *Gallium Arsenide and Related Compounds 1980*, p. 639, 1981.

T.P. Pearsall, Editor, "GaInAsP Alloy Semiconductors", John Wiley and Sons, p.456, 1982.

S.J. Polak, *et al.*, "Semiconductor Device Modeling from the Numerical Point of View," *Intl. J. for Numerical Methods in Eng.*, **24**, p. 763, 1987.

W.H. Press, *et al.*, "Numerical Recipes The Art of Scientific Computing," Cambridge University Press, pp. 397-407, 1989.

C.S. Rafferty, *et al.*, "Iterative Methods in Semiconductor Device Simulation," *IEEE Trans. on Electron Devices*, **ED-32**, p. 2018, 1985.

L.B. Rall, "Computational Solution of Nonlinear Operator Equations," Krieger Publishing, Huntington, NY, 1979.

R. Sabella and S. Merli, "Analysis of InGaAs p-i-n Photodiode Frequency Response," *IEEE J. of Quantum Elec.*, **JQE-29**, p. 906, 1993.

W. E. Stephens and T. R. Joseph, "System Characteristics of Direct Modulated and Externally Modulated RF Fiber-Optic Links," *IEEE J. of Lightwave Tech.*, **LT-5**, p. 380, 1987.

R.H. Stolen and E.P. Ippen, "Raman Gain in Glass Optical Waveguides," *Appl. Physics Lett.*, **22**, p. 276, 1973.

W. Susaki, "Recent Progress in superlinear InGaAsP Laser Diodes," OFC 91, Paper WG5, p. 92.

S.M. Sze, "Physics of Semiconductor Devices," 2nd Edition, John Wiley and Sons, pp. 35-51, 1981.

J.G. Wasserbauer, *et al.*, “Specific Contact Resistivity of InGaAs/InP p-Isotype Heterojunctions,” *Electron. Lett.*, **28**, p. 1568, 1992.

Y.G. Wey, *et al.*, "Ultrafast Graded Double-Heterostructure GaInAs/ InP Photodiode," *Appl. Physics Lett.*, **58**, p. 2156, 1991.

Y.G. Wey, "High-Speed Double Heterostructure GaInAs/InP p-i-n Photodiodes Theory, Fabrication and Measurement," University of California Santa Barbara Ph.D. Dissertation, 1993.

A. R. Williams, *et al.*, "High Frequency Saturation Measurements of an InGaAs/InP Waveguide Photodetector," *Electron. Lett.*, **29**, p. 1298, 1993.

K. J. Williams, "Offset Phase Locking of Nd:YAG Nonplanar Ring Lasers," MS Thesis, Univ. of Maryland, 1989.

K.J. Williams, *et al.*, "6-34 GHz Offset Phase Locking of Nd:YAG 1319 nm Nonplanar Ring Lasers," *Electron. Lett.*, **25**, p. 1242, 1989.

K. J. Williams and R. D. Esman, "Observation of Photodetector Nonlinearities," *Electron. Lett.*, **28**, p. 731, 1992.

T.H. Windhorn, *et al.*, "The Electron Velocity-Field Characteristic for n-InGaAs at 300K," *IEEE Electron Device Lett.*, **EDL-3**, p. 18, 1982.

A. Yariv, "Optical Electronics," Holt, Rinehart and Winston, 1985.

H. Yi, *et al.*, "Novel Method to Control Numerical Solution Oscillation of Diffusion-Drift Equation," *Electron. Lett.*, **26**, p. 1487, 1990.

A. Yoshii, *et al.*, "Investigation of Numerical Algorithms in Semiconductor Device Simulation," *Solid State Elec.*, **30**, p. 813, 1987.

J.M. Zhang and D.R. Conn, "State-Space Modeling of the PIN Photodetector," *J. of Lightwave Tech.*, **JLT-10**, p. 603, 1992.